

**Mechanochemical Behaviour of Solid  
Pharmaceuticals during Milling: Experimental  
and Modelling Studies**

**Hanane Abouhakim**

**Submitted in accordance with the requirements for the degree of Doctor of Philosophy**

**The University of Leeds  
School of Chemical and Process Engineering**

**September 2020**

## Declaration

The candidate confirms that the work submitted is her own, except where work which has formed part of jointly authored publications has been included. The contribution of the candidate and the other authors to this work has been explicitly indicated below. The candidate confirms that appropriate credit has been given within the thesis where reference has been made to the work of others. The details of joint authors are as follows;

Chapter 4 involves sections that were obtained from collaboration work with Dr Christopher Pask from the University of Leeds who conducted the single crystal diffraction measurements. Also, Chapter 4 consists of computational work which was performed by Dr Sten Nilsson from AstraZeneca. Example of computation includes the validation of the hydrogen positions, the calculation of the attachment energy, the energy of the slip planes, and the mechanical properties. The outcome of this collaboration was published in the journal *Crystal Engineering and Materials*.

Chapter 5 encompasses the computational work which was performed in AstraZeneca by Dr Sten Nilsson including the growth morphology by attachment energy model, the calculation of the mechanical properties, and the quantification of interactions for the slip plane assessment.

Chapter 6 consists of a section outlining the quantification the amount of amorphous DABOMD formed with planetary ball mill using chemometric analysis of the FTIR which was performed by Dr Maryam Asachi from the University of Leeds. Also, the computational modelling of the FTIR spectra of DABOMD was conducted by Dr Sten Lill. The outcome of this collaboration was also published in publication in the journal of *Crystal Growth & Design*.

Chapter 8 consists of DEM simulation work which was carried out by Dr Mohammadreza Alizadeh Behjani at the University of Leeds.

1) Title of publication: The Crystal Structure, Morphology and Mechanical Properties of Diaqua-bis(Omeprazole)-Magnesium Dihydrate

Name of authors: H. Abouhakim, A. Hassanpour, M.J. Quayle, S. T. Norberg, S.O. Nilsson Lill, Christopher M. Pask

Date of publication: January/2020

Journal details: *Acta Crystallographica Section B Structural Science, Crystal Engineering and Materials*. Volume 76, issue 2, pages, 275-284

<http://scripts.iucr.org/cgi-bin/paper?rm5029>

2) Mechanically Induced Amorphisation of Diaqua-bis(Omeprazole)-Magnesium Dihydrate

Name of authors: H. Abouhakim, A. Hassanpour, M.J. Quayle, S. T. Norberg, S.O. Nilsson Lill, Maryam Asachi, Sven Schroeder, Frans Muller

Date of publication: July/2020

Journal details: Crystal Growth & Design

Name of authors: H. Abouhakim, A. Hassanpour, M.J. Quayle, S. T. Norberg, S.O. Nilsson Lill, F. Muller, S. Schroeder, M. Asachi.

<https://pubs.acs.org/doi/abs/10.1021/acs.cgd.0c00770>

This copy has been supplied on the understanding that it is copyright material and that no quotation from the thesis may be published without proper acknowledgement.

2020

University of Leeds

Hanane Abouhakim

## **Acknowledgements**

First and foremost, praise to Allah, the creator who blessed me and enabled me to reach this stage. Special thanks to my main academic supervisor Dr Ali Hassanpour for his continuous support and encouragement. Thanks to my other academic supervisors Professor Frans Muller and Professor Sven Schroeder. I am very grateful to my industrial supervisor's Dr Mike Quayle, Dr Sten Nilsson, and Dr Stefan Norberg at New Modalities and Parenteral Development, Pharmaceutical Technology & Development, Operations, AstraZeneca, Gothenburg, Sweden for their tremendous support with this project. A huge thanks to Dr Mohammadreza Alizadeh Behjani for his help with DEM simulation. Special thanks to Prof. Mojtaba Ghadiri and Prof. Kevin Roberts and their teams for their help with various aspects of the project.

I would like to thank the Centre of Doctoral Training CDT for giving me the opportunity to undertake my PhD in Complex Particulate and Processes CP3. Thanks to the centre manager Anoushka Kulikowski for being a great supporter. Special thanks to EPSRC, AstraZeneca, and the University of Leeds who have jointly contribute to the funding of CDT. I would like to acknowledge the significant role of AstraZeneca throughout my PhD and during my placement. I am very grateful to my colleagues in the School of Chemical and Process Engineering who helped me in multiple occasions including Dr Jabbar Gardy, Mozhddeh Mehrabi, Svetlana Bibiceva, Dr Mohammadreza Alizadeh Behjani, Dr Umair Zafar, Dr Maryam Asachi, Muhammad Najib, Dr Alex Moldovan, Dr Thokozile Kathyola, and Dr Muzammil Ali.

I extend my thanks to Ben Douglas and George Dowson for their help in the particle's labs in engineering. Thanks to the team in LEMAS for their help with the microscopic techniques. Special thanks to Christopher Pask for his tremendous support with single-crystal analysis in the School of Chemistry. I want to extend my thanks to Lesley Neve for her help with XRPD analysis in the School of the Earth.

I am very grateful to my family, my parents Amina Ait El Bouhali and Abdehai Abouhakim for their supports and prayers throughout my project. A big thanks to my sisters Merieme Abouhakim and Salma Abouhakim, particularly Merieme for being very close support.

Special thanks to my everyday companion, my husband Zahir Melko, for supporting me from the beginning of my PhD. I am sincerely grateful to my son Bassam Melko for being understanding and cheering despite his young age. A warm thanks to my baby boy Yunus Melko for accompanying me during my writing up period and being my best cutie friend.

Without their support completing my PhD would not be possible

## **Dedication**

I dedicate this thesis to my parents, Amina Ait El Bouhali and Abdelhai Abouhakim who were dreaming to see me accomplishing my PhD. I also dedicate it to my grandmother Reikia Ait El Bouhali, who seen the potential in me from my childhood and always advised me to grasp on the path of knowledge.

## Abstract

Milling is a commonly used technique in the processing of active pharmaceutical ingredients (APIs) or excipients to control the size and dissolution rate of poorly soluble drugs. However, one of the major challenges of the milling process is the physical and chemical changes arising from the mechanical treatment (mechanochemistry) of the material which might adversely impact the pharmaceutical performances. The common practice to optimise the milling of a specific solid pharmaceutical is to conduct extensive trial and error experiments. However, this method is costly and ineffective, particularly in the early drug development stage, where, a limited amount of API is available. Hence, a methodology that allows anticipating the milling behaviour of particular pharmaceutical solids would be highly desirable.

The review section is set to identify the knowledge gap to enable designing a methodology that can address the lack of understanding of the mechanistic behaviour of solid pharmaceutical during milling including the extent of particles size reduction (comminution), and potential mechanochemistry (i.e. amorphisation). This is achieved through determining the key material properties that influence the milling behaviour of the sample, such as the mechanical properties which are controlled by their underlying crystal structure and molecular properties. And through evaluating the critical milling parameters that control the level of the energy available for the treatment of particles during milling, including the type of mill, speed, and time of milling.

The material properties influencing the mechanistic behaviour of solid pharmaceuticals were predicted using computational chemistry through studying the sample intrinsic characteristics at the molecular level. The key predicted properties include crystal habit, mechanical properties, and any potential slip plane/system. Two solid pharmaceutical candidates were used in the modelling work, L-Glutamic Acid ( $\beta$ -LGA) and Diaqua-bis(Omeprazole)-magnesium(II) dihydrate (DABOMD) which are employed for cancer inhibition and stomach acid reflux applications respectively. The outcome of the properties prediction indicates that DABOMD is anticipated to experience large comminution and amorphisation due to its propensity to brittle failure and plastic deformation owed to its moderate elastic modulus and hardness, presence of slip plane and the allocation of water molecules near its slip system. Whereas,  $\beta$ -LGA is expected to experience a larger comminution and lower amorphisation compared to DABOMD which is related to the prevailing hydrogen network holding its crystal structure, higher elastic modulus and hardness values, and to the lack of slip planes in its structure.

To verify the results of the predicted work, milling was performed on DABOMD using a planetary ball mill and a single ball mill and on  $\beta$ -LGA using a planetary ball mill at different times. The outcome of the empirical work shows that DABOMD undergoes a prominent comminution and amorphisation processes that occur parallel to each other, with planetary ball mill causing slightly higher comminution and amorphisation compared to the single ball mill.

Whereas, milling of  $\beta$ -LGA shows that it undergoes larger dominant comminution followed by partial amorphisation and recrystallisation.

To establish a relationship between the degree of comminution, amorphisation, and the intensity of milling. The energies of planetary ball mill and a single ball mill were quantified using a collision model derived from the literature, and through tracking the milling jar with high speed-camera respectively and were validated through the DEM simulations of the mills. It was found that the planetary ball mill produces higher energy than single ball mill which explains the difference in the comminution and amorphisation obtained in the two mills. The energy produced using DEM simulation of the planetary ball mill agrees with the calculated energies from the collision model. However, the energy calculated from the DEM simulation is lower than that generated from tracking the milling jar in the single ball using a high-speed camera since the DEM tracks the movement of the ball and the powder instead of the movement of the jar. This methodology will enable determining the type and amount of changes that raise with the milling of a solid (i.e. comminution, amorphisation), the time at which it occurs, and the energy required to cause this change.

## Table of Contents

Declaration.....	ii
Acknowledgements .....	iv
Dedication.....	iv
Abstract .....	v
Table of Contents .....	vii
Table of Figures .....	xi
List of Tables .....	xvii
List of Equations .....	xix
Abbreviations.....	xx
Nomenclature.....	xxi
1. Chapter 1 Introduction.....	1
1.1. Background of Research .....	2
1.2. Scope of Work.....	3
1.3. Project Management .....	5
1.4. Structure of the Thesis.....	7
2. Chapter 2 Literature Review on Milling and its Impact on the Solid Pharmaceuticals.....	1
2.1. Introduction.....	2
2.2. Milling .....	3
2.2.1. Theory of Particle Size Reduction .....	4
2.2.2. Milling Techniques.....	5
2.3. Materials Properties Affecting the Milling Process.....	10
2.3.1. Solid State.....	10
2.3.2. Mechanical Properties .....	12
2.3.3. Effects of Flaws and Imperfections .....	19
2.3.4. Effect of Crystal Structure on Mechanical Properties .....	24
2.3.5. Particle Shape and Size.....	26
2.4. Mechanochemistry .....	27
2.4.1. Milling Conditions Related to Mechanochemistry .....	30
2.4.2. Mechanism of Mechanochemistry.....	33
2.5. Summary.....	38
3. Chapter 3 Materials and Method .....	40

3.1.	Introduction.....	41
3.1.1.	L- Glutamic Acid .....	41
3.1.2.	Selection of a Material Candidate.....	44
3.1.3.	Diaqua-bis(Omeprazole)-magnesium(II) dihydrate (DABOMD) .....	47
3.2.	Material Properties Predicting Methods .....	47
3.2.1.	Crystal Habit Prediction.....	47
3.2.2.	Slip Plane Prediction .....	49
3.2.3.	Mechanical Properties Prediction .....	50
3.3.	Milling Method.....	50
3.3.1.	Planetary Ball Mill .....	50
3.3.2.	Vibratory Mill .....	51
3.4.	Characterisation Techniques.....	51
3.4.1.	X-Ray Powder Diffraction XRPD .....	51
3.4.2.	Single Crystal X-ray Diffraction .....	52
3.4.3.	Differential Scanning Calorimeter DSC.....	53
3.4.4.	Thermal Gravimetric Analysis TGA.....	54
3.4.5.	Fourier Transform Infra-Red FTIR.....	55
3.4.6.	Laser Diffraction .....	58
3.4.7.	Scanning Electron Microscope SEM .....	59
3.5.	Conclusion .....	60
4.	Chapter 4 Predicting the Material Properties of DABOMD by Modelling.....	61
4.1.	Introduction.....	62
4.2.	Crystal Structure .....	63
4.2.1.	Crystallisation .....	63
4.2.2.	Solving Crystal Structure of DABOMD .....	63
4.2.3.	Crystal Solvent Contents.....	70
4.3.	Crystal Habit .....	72
4.3.1.	BFDH .....	72
4.3.2.	Attachment Energy.....	73
4.4.	Slip Plane .....	74
4.5.	Mechanical Properties of DABOMD .....	77
4.6.	Conclusion .....	81

5.	Chapter 5 Predicting the Material Properties of $\beta$ -LGA by Modelling .....	82
5.1.	Introduction .....	83
5.2.	Crystal Structure .....	84
5.2.1.	Crystallisation .....	84
5.2.2.	Crystal Structure .....	84
5.3.	Crystal Habit .....	86
5.3.1.	BFDH .....	86
5.3.2.	Attachment Energy .....	86
5.4.	Slip Plane .....	88
5.5.	Mechanical Properties .....	91
5.6.	Conclusion .....	92
6.	Chapter 6 Milling of DABOMD .....	94
6.1.	Introduction .....	95
6.2.	Milling DABOMD with Planetary Ball Mill .....	96
6.2.1.	Experimental Setup .....	96
6.2.2.	Power Characterisation of DABOMD .....	96
6.3.	Milling DABOMD with Single Ball Mill .....	121
6.3.1.	Experimental Setup .....	121
6.3.2.	Powder Characterisation of DABOMD .....	122
6.4.	Conclusion .....	135
7.	Chapter 7 Milling of $\beta$ -LGA .....	137
7.1.	Introduction .....	138
7.2.	Planetary Ball Mill .....	138
7.2.1.	Experimental Setup .....	138
7.2.2.	Powder Characterisation .....	138
7.2.3.	Crystalline Properties .....	142
7.2.4.	Thermodynamic Properties .....	145
7.2.5.	Intermolecular Properties .....	146
7.2.6.	Quantification of Amorphous .....	148
7.3.	Discussion .....	149
7.3.1.	Comminution Amorphisation Relation .....	149
7.3.2.	Mechanism of Milling of $\beta$ -LGA .....	151

7.4 Conclusion .....	154
8. Chapter 8 Quantification of the Energy of the Mills .....	155
8.1. Introduction .....	156
8.2. Calculating the Energy in Planetary Ball Mill .....	157
8.3. Calculating the Energy Transferred to the Single Ball Mill .....	160
8.4. Compression Test .....	162
8.5. Verification of Energy Using DEM Simulation .....	164
8.5.1. Simulation Parameters .....	165
8.6. DEM Simulation of the Planetary Ball Mill.....	166
8.7. DEM Single ball mill .....	167
8.8. Summary .....	170
8.9. Conclusion .....	171
9. Chapter 9 Conclusion and Future Recommendation .....	173
9.1. Conclusion .....	173
9.2. Future Work Recommendations .....	175
9.3. Reference .....	177

## Table of Figures

Figure 1-1: Project map showing how objectives are met in the thesis .....	5
Figure 1-2: Structure of the thesis illustrating brief contents on each chapter .....	7
Figure 2-1: Physical transformation of drugs along with the pharmaceutical industry. (modified from (Abramov, 2016)) .....	2
Figure 2-2: Types of stress modes generated inside the mills. a) compression, b) shear (attrition), c) impact (stroke) and d) impact (collision). With circles illustrating milling media, square for the milled material and rectangles represent the mill wall (amended from (Alex <i>et al.</i> , 2016)).....	5
Figure 2-3: Schematic diagram of a ball mill. (modified from (Loh, Samanta and Sia Heng, 2015)) .....	7
Figure 2-4: Milling parameters for ball mill.....	7
Figure 2-5: Milling chamber of the fluid jet mill (Chauruka, 2015) .....	10
Figure 2-6 Stress-strain curve (adapted from ( <i>Cyberphysics - Young's Modulus</i> , 2009)).....	13
Figure 2-7: Schematic diagram of nanoindentation (modified from (Arteaga <i>et al.</i> , 1993)).....	17
Figure 2-8: Vickers hardness model (reprinted from (INSTRON, 2020)).....	18
Figure 2-9: Schematic shows point defect in a crystal (reprinted from (Science, 2016)) .....	20
Figure 2-10: Deformation generated by an edge dislocation moving through the crystal (reprinted from (Roberts, 2016))....	21
Figure 2-11: Deformation caused by (a) edge and, (b) screw dislocation motion in a crystal (Babu, 2008).....	21
Figure 2-12: a) twin boundary, b) tilt boundary and, c) and grain boundary (Babu, 2008) .....	22
Figure 2-13: Schematic illustrating the nature of deformation by slip (reprinted (Roberts, 2016)).....	22
Figure 2-14: Schematic shows dislocation glide and climb dislocations (modified from (Yuan <i>et al.</i> , 2018)) .....	23
Figure 2-15: Schematic shows jog and kink dislocations (reprinted from (Babu, 2008)).....	23
Figure 2-16: Schematic shows crystalline packing of Magnesium steroid anhydrous and dihydrates form (modified from (Byrn, Zografis and Chen, 2017)) .....	25
Figure 2-17 The crystal structure of Aspirin along with the modelled Young's modulus in x and y directions, (modified from (Storey and Ymen, 2011)) .....	25
Figure 2-18: The crystal structure of Primidone A along with the calculated Young's modulus in x and y directions, (modified from (Storey and Ymen, 2011)).....	26
Figure 2-19: The basic shapes of a crystal/particle (modified from (Storey and Ymen, 2011)) .....	27
Figure 2-20: X-ray powder diffraction patterns for budesonide rerecorded at room temperature before milling (a) and after 15 h milling process (b). DSC heating curves of crystalline budesonide before milling (c) and after 15 h milling process (d), the inset depicts a near view of the glass transition domain appearing in MDSC reversible heat flow (reprinted from (descamps et al. 2007)).....	32
Figure 2-21: Schematic shows the magma-plasma model, where; E –exo-electrons, N – undeformed solid, D – highly deformed surface layer, P – plasma (modified from (Baláz <i>et al.</i> , 2013)).....	34
Figure 2-22: Mechanical pulses varies by varying the intensity or frequency of the pulse (reprinted (Boldyreva, 2013)) .....	35
Figure 2-23: Different relaxation channels of the stress field (modified from (Boldyrev, 2006)).....	36
Figure 3-1: Microscopic image of two polymorphic forms of glutamic acid; (a), $\alpha$ form, (b) $\beta$ form.(reprinted from (Borissova <i>et al.</i> , 2009)) .....	42
Figure 3-2: SEM images of $\beta$ glutamic acid.....	42
Figure 3-3: Crystallisation of $\beta$ -(LGA) experimental setup.....	43
Figure 3-4: SEM images for the as-received powder of DABOMD .....	47
Figure 3-5: Planetary ball mill PM100 ((RETSCH, 2019)).....	51

Figure 3-6: Schematic shows ball and powder motion in the single ball mill ( modified from (Chauruka, 2015))	51
Figure 3-7: Derivation of Bragg's Law ( amended from (Storey and Ymen, 2011))	52
Figure 3-8: Single-crystal X-ray diffractometer (reprinted from(Byrn, Zografis and Chen, 2017))	53
Figure 3-9: a) DSC cell, b) DSC sensor (reprinted from (Bibi et al., 2015))	54
Figure 3-10: Key Components of the TGA instrument (modified from (Roberts, 2016))	55
Figure 3-11: Vibrational modes of a methylene group (modified from (El-Azazy, 2019))	55
Figure 3-12: Schematic diagram of Infrared dispersive spectrometer (modified from (Barth, 2007))	56
Figure 3-13: Fourier transform infrared spectrometer ( modified from (Byrn, Zografis and Chen, 2017))	57
Figure 3-14: a) Diffuse reflectance infrared instrument with KBr sample cells and b) Attenuated total reflectance sample cell (modified from (Roberts, 2016))	57
Figure 3-15: Infrared spectroscopy correlation chart (reprinted from (Jakobs et al., 2000))	58
Figure 3-16: Schematic diagram of the laser diffraction particle size apparatus (reprinted from (Malvern Instruments Ltd, 2012))	59
Figure 3-17: Schematic shows light scattered from large and small particles (Malvern, 2015)	59
Figure 3-18: Schematic diagram of SEM (reprinted from (Purdue Univesrity, 2010))	60
Figure 4-1: Scanning Electron Microscopy image of a single crystal of DABOMD. (Reproduced with the permission of the International Union of Crystallography (IUCr) (Abouhakim <i>et al.</i> , 2020a))	63
Figure 4-2: Molecular structure of diaqua-bis(Omeprazole)-magnesium dihydrate (DABOMD). Thermal ellipsoids are shown at the 50% level with intermolecular hydrogen bonding between the molecules in the lattice shown in blue dotted lines Mg: green, S: yellow, N: blue, O: red, C: grey, H: white. (Reproduced with the permission of the International Union of Crystallography (IUCr) (Abouhakim <i>et al.</i> , 202a))	65
Figure 4-3: Crystal packing arrangement of DABOMD viewed down the crystallographic b axis. Thermal ellipsoids are shown at the 50% level. Additional W2 water molecules are omitted for clarity. Intermolecular hydrogen bonding between the molecules in the lattice shown in dotted lines Mg: green, S: yellow, N: blue, O: red, C: grey, H: white. (Reproduced with the permission of the International Union of Crystallography (IUCr) (Abouhakim <i>et al.</i> , 2020a))	67
Figure 4-4: CASTEP optimized DABOMD crystal structures with different hydrogen bond directions. (Reproduced with the permission of the International Union of Crystallography (IUCr) (Abouhakim <i>et al.</i> , 2020a))	69
Figure 4-5: XRD pattern of DABOMD, simulated from single crystal; experimental – single ground crystals, and experimental – bulk powder. (Reproduced with the permission of the International Union of Crystallography (IUCr) (Abouhakim <i>et al.</i> , 2020a))	70
Figure 4-6: Thermal Gravimetric Analysis plot of DABOMD crystalline powder heated from 25 to 250 °C at a rate 5°C/min. (Reproduced with the permission of the International Union of Crystallography (IUCr) (Abouhakim <i>et al.</i> , 2020a))	71
Figure 4-7: Differential Scanning Calorimetry plot of DABOMD crystalline powder heated from 25 to 290 °C at a rate 5°C/min. (reproduced with the permission of the International Union of Crystallography (IUCr) (Abouhakim <i>et al.</i> , 2020a))	71
Figure 4-8: Hot stage microscope image of DABOMD heated from 25°C to 190°C at a rate of 10°C/min. a) at 25°C, b) at 180 °C	72
Figure 4-9: DABOMD; a) Predicted morphology using BFDH Model, b) Predicted morphology using <i>Eatt</i> growth morphology model c) Morphology from experimentally grown single crystal (Reproduced with the permission of the International Union of Crystallography (IUCr) (Abouhakim <i>et al.</i> , 2020a))	72
Figure 4-10: DABOMD; Plot of Zingg diagram, where L is the longest dimension, I is the intermediate dimension, and S is the shortest dimension. Dimensions obtained from morphologies derived from BFDH (red triangle), attachment energy (blue	

circles), and experiment (back square) (Reproduced with the permission of the International Union of Crystallography (IUCr) (Abouhakim <i>et al.</i> , 2020a).....	74
Figure 4-11: Visualisation of the potential slip plane in DABOMD crystal (100) the major face of BFDH and the attachment energy (Reproduced with the permission of the International Union of Crystallography (IUCr) (Abouhakim <i>et al.</i> , 2020a).....	75
Figure 4-12: Visualisation of (011) and (11-1) planes the second and third major face from attachment energy shows that slip is rather difficult in these planes since it requires breaking of the strongest hydrogen and ionic bonds in DABOMD (Reproduced with the permission of the International Union of Crystallography (IUCr) (Abouhakim <i>et al.</i> , 2020a).....	75
Figure 4-13: Quantification of interactions along (100) plane visualized as green lines. (Reproduced with the permission of the International Union of Crystallography (IUCr) (Abouhakim <i>et al.</i> , 2020a).....	76
Figure 4-14: Proposed slip direction in a crystal in a) a flat layer structure and b) corrugated structure (reprinted from (Halme <i>et al.</i> , 2019)).....	77
Figure 4-15: Classification of materials based on mechanical properties (adapted from Roberts <i>et al.</i> (1995)).....	79
Figure 4-16: Anisotropy of elastic moduli of DABOMD in different directions and planes. Highest Young's modulus is found along the z-axis. (Reproduced with the permission of the International Union of Crystallography (IUCr) (Abouhakim <i>et al.</i> , 2020a).....	80
Figure 4-17: Hydrogen bonding in DABOMD crystal mainly along z-direction as visualized by red lines. (Reproduced with the permission of the International Union of Crystallography (IUCr) (Abouhakim <i>et al.</i> , 2020a).....	80
Figure 5-1: SEM shows a grown single crystal of $\beta$ -LGA.....	84
Figure 5-2: $\beta$ -LGA molecular structure. N: blue, O: red, C: grey, H: white.....	85
Figure 5-3: Crystal structure of $\beta$ -LGA viewed from b axis. Where, N: blue, O: red, C: grey, H: white, and Hydrogen bonds in red.....	85
Figure 5-4: $\beta$ -LGA: a) Morphology from experimentally grown crystals, b) Predicted morphology using BFDH Model c) Predicted morphology using <i>Eatt</i> growth morphology.....	87
Figure 5-5: $\beta$ -LGA Zingg diagram, where L is the longest dimension, I is the intermediate dimension, and S is the shortest dimension. Dimensions obtained from morphologies derived from BFDH (red triangle), attachment energy (blue circles), experiment (back square).....	88
Figure 5-6: (1) Visualisation of the crystal packing of $\beta$ -LGA shows that no slip plane is present due to the extensive hydrogen bonds interactions including charged assisted hydrogen bonds shown in yellow.....	89
Figure 5-7: Qualitative Visualisation of the different interacting forces in $\beta$ -LGA. The longer the line the stronger the interaction. Where, long yellow represents the strongest interactions, and long pink represent the medium interactions, whereas, short pink represents weak interactions. N: blue, O: red, C: grey, H: white.....	89
Figure 5-8: Visualisation of the a) 3*3 crystal packing of $\beta$ -LGA and b) its corresponding pattern of the strongest hydrogen assisted interactions.....	90
Figure 5-9: Visualisation of the interactions within (002) face.....	91
Figure 5-10: Anisotropy of elastic moduli of $\beta$ -LGA in different directions and planes. Highest Young's modulus is found along X-axis (1visualised in (Romain Gaillac, 2016)).....	92
Figure 6-1: Schematic of a planetary ball mill (Reproduced with the permission of American Chemical Society (ACS) (Abouhakim, <i>et al.</i> , 2020b).....	96
Figure 6-2: Particle size distribution of non-milled and milled DABOMD in planetary ball mill from 1min to 300 min (Reproduced with the permission of American Chemical Society (ACS) (Abouhakim <i>et al.</i> , 2020b).....	97
Figure 6-3: Cumulative distribution of non-milled and planetary ball milled DABOMD from 1min to 300 min (Reproduced with the permission of American Chemical Society (ACS) (Abouhakim <i>et al.</i> , 2020b).....	98

Figure 6-4: SEM used for quantitative image analysis .....	99
Figure 6-5: SEM images show the morphology of DABOMD, a-Non-milled ( $\times 800$ ), b- Non-milled ( $\times 25000$ ), c-300 min milled ( $\times 800$ ), d-300 min milled ( $\times 25000$ ). Figures are shown for easier comparison of the feed and product DABOMD. 100	100
Figure 6-6: SEM images show the morphology of DABOMD particles (left) and their surfaces (on the right), a-Non-milled, b- 1min milled, c-5min milled, d-15min milled, e-30min planetary ball mill (Reproduced with the permission of American Chemical Society (ACS) (Abouhakim et al., 2020b).....	101
Figure 6-7: SEM images show the morphology of DABOMD's particles (left) and their surfaces (on the right), f-60min milled, g- 120min milled, h-180min milled, i-240min milled, j-300min planetary ball mill (Reproduced with the permission of American Chemical Society (ACS) (Abouhakim et al., 2020b).....	102
Figure 6-8: XRPD of DABOMD before milling and after milling with planetary ball mill from 1 min to 300min (Reproduced with the permission of American Chemical Society (ACS) (Abouhakim et al., 2020b) .....	103
Figure 6-9: TGA Profile of DABOMD for the non-milled and milled in planetary ball mill at a temperature 25 to 250 °C and a rate of 5°C/min (Reproduced with the permission of American Chemical Society (ACS) (Abouhakim et al., 2020b) .....	104
Figure 6-10: DSC Profile of DABOMD for the non-milled and milled samples in a planetary ball mill at a temperature 25 to 250 °C and a rate 5°C/min. (Reproduced with the permission of American Chemical Society (ACS) (Abouhakim et al., 2020b) .....	105
Figure 6-11: FTIR-ATR of non-milled and milled DABOMD in planetary ball mill showing scan from a- 600 to 950 $\text{cm}^{-1}$ , b- from 950 to 1200 (Reproduced with the permission of American Chemical Society (ACS) (Abouhakim et al., 2020b) .....	106
Figure 6-12:FTIR-ATR of non-milled and milled DABOMD in planetary ball mill showing scan from c-1200 to 1600 $\text{cm}^{-1}$ and d from 2600 to 3700 $\text{cm}^{-1}$ (Reproduced with the permission of American Chemical Society (ACS) (Abouhakim et al., 2020b).....	107
Figure 6-13: A model system of DABOMD for calculation of molecular IR-spectra, especially highlighting the hydrogen bond network. Fixed atomic positions are marked with larger balls .....	109
Figure 6-14: Calibrated Curve of the area under the curve of different ratios of standard crystalline and amorphous DABOMD measured by XRPD.....	110
Figure 6-15: Percentage amorphous of DABOMD forming during different milling time in the planetary ball mill by XRPD (Reproduced with the permission of American Chemical Society (ACS) (Abouhakim et al., 2020b) .....	110
Figure 6-16: Identification of planes involved in the crystalline disorder of DABOMD (Reproduced with the permission of American Chemical Society (ACS) (Abouhakim et al., 2020b).....	114
Figure 6-17: Thermal Controlled XRPD of DABOMD from 25 to 170 °C (Reproduced with the permission of American Chemical Society (ACS) (Abouhakim et al., 2020b).....	115
Figure 6-18: The kinetic of comminution of DABOMD in planetary ball mill(Reproduced with the permission of American Chemical Society (ACS) (Abouhakim et al., 2020b).....	118
Figure 6-19: The kinetic of amorphisation of DABOMD in planetary ball mill derived from; XRPD analysis and from FTIR Chemometric analysis(Reproduced with the permission of American Chemical Society (ACS) (Abouhakim et al., 2020b) 119	119
Figure 6-20: The kinetic of the water present in DABOND during milling fitted model using XRPD and Chemometric FTIR .....	120
Figure 6-21: A proposed mechanistic model for the milling process of DABOMD. Where the ordered particles represent the comminution, and the disordered particles represent the amorphisation (Reproduced with the permission of American Chemical Society (ACS) (Abouhakim et al., 2020b).....	121
Figure 6-22: Pictures illustrating a) Single ball mill MM200 and b) milling jar with milling media (Chauruka, 2015) .....	122
Figure 6-23: Particle size distribution of non-milled and milled DABOMD in single ball mill from 1min to 300 min .....	123

Figure 6-24: Cumulative distribution of non-milled and single ball-milled DABOMD from 1min to 300 min.....	124
Figure 6-25: SEM images show the Morphology of DABOMD particles (left) and their surfaces (on the right), a-Non-milled, b- 1min milled, c-5min milled, d-15min milled, e-30min Single Ball Mill.....	126
Figure 6-26: SEM images show the morphology of DABOMD's particles (left) and their surfaces (on the right), f-60min milled, g- 120min milled, h-180min milled, i-240min milled, j-300min single ball mill.....	127
Figure 6-27: XRPD of DABOMD before milling and after milling with single ball mill from 1 min to 300min .....	128
Figure 6-28: DSC Profile of DABOMD for the non-milled and milled samples in a single ball mill at a temperature 25 to 250 °C and a rate 5°C/min.....	129
Figure 6-29: FTIR-ATR of non-milled and milled DABOMD in single ball mill showing scan from a- 600 to 950 cm <sup>-1</sup> , b- from 950 to 1200 .....	130
Figure 6-30: FTIR-ATR of non-milled and milled DABOMD using single ball mill showing scan from c-1200 to 1600 cm <sup>-1</sup> and d from 2600 to 3700 cm <sup>-1</sup> .....	131
Figure 6-31: Percentage amorphous of DABOMD forming during different milling time in single ball mill .....	132
Figure 6-32: The kinetic of comminution of DABOMD in single ball mill presented by <i>D</i> <sub>90</sub> and <i>D</i> <sub>50</sub> .....	134
Figure 6-33: The kinetic of amorphisation of DABOMD in single ball mill.....	135
Figure 7-1: Average particle size distribution of non-milled $\beta$ -LGA with error bars.....	139
Figure 7-2: Particle size distribution of non-milled and milled $\beta$ -LGA in planetary ball mill from 15min to 300 min .....	139
Figure 7-3: Cumulative Distribution of non-milled and planetary ball milled $\beta$ -LGA from 1min to 300 min.....	140
Figure 7-4: SEM images of $\beta$ -LGA, a) Non-milled, b) 15 min milled, c) 30 min, d) 60 min milled.....	142
Figure 7-5: SEM images of $\beta$ -LGA, e) 120 min milled, f) 180 min milled, g) 240 min milled, h) 300 min milled .....	142
Figure 7-6: XRPD of $\beta$ -LGA before milling and after milling from 1 min to 300min.....	144
Figure 7-7: Assigning the planes to the peaks of $\beta$ -LGA .....	144
Figure 7-8: TGA of non-milled $\beta$ -LGA at 10°C/min .....	145
Figure 7-9: DSC Profile of $\beta$ -LGA for the non-milled and milled samples from 25 to 250 °C and 10°C/min.....	146
Figure 7-10: Glass transition temperature the 60 min milled $\beta$ -LGA.....	146
Figure 7-11: FTIR-ATR of non-milled and milled $\beta$ -LGA in planetary ball mill showing scan from 1600 cm <sup>-1</sup> to 3700 cm <sup>-1</sup> .....	147
Figure 7-12: FTIR-ATR of non-milled and milled $\beta$ -LGA in planetary ball mill showing scan from 600 cm <sup>-1</sup> to 1800 cm <sup>-1</sup> .....	147
Figure 7-13: The kinetic of comminution of $\beta$ -LGA presented by <i>D</i> <sub>90</sub> .....	150
Figure 7-14: The kinetic of amorphisation of $\beta$ -LGA in planetary ball mill derived from; XRPD analysis .....	151
Figure 7-15: Proposed mechanistic model for the milling process of $\beta$ -LGA, ordered blue particle represents comminution partially disordered particles represents partial amorphisation.....	153
Figure 7-16: Hot stage microscope image of $\beta$ -LGA heated from at a rate of 10°C/min. a) at 25°C, b) at 210 °C .....	153
Figure 8-1: Total energy transferred to the system in a planetary ball mill and the amount of generated amorphous .....	160
Figure 8-2: Experimental setup for measuring the speed of the milling jar in the single ball mill using high-speed Camera .....	160
Figure 8-3: Trajectory of the vibratory mill jar .....	161
Figure 8-4: Schematic shows the compression of DABOMD.....	162
Figure 8-5: Load versus extension graph for compression test.....	163
Figure 8-6: XRPD profile of DABOMD after compression.....	163
Figure 8-7: Schematic shows forces applied to three arbitrarily interacting particles (reprinted from (Behjani, 2018)).....	164

Figure 8-8: Schematic diagram representing the coefficient of sliding friction, with (a) is the surface at rest, (b) particle-particle sliding friction and (c) particle-wall sliding friction (reprinted from (Behjani, 2018)) .....	165
Figure 8-9: DEM simulation of planetary ball mill .....	167
Figure 8-10: Kinetic energy after the Collision of the balls in planetary ball mill .....	167
Figure 8-11: DEM simulation of single ball mill.....	169
Figure 8-12: Kinetic energy after the collision in single ball mill.....	169

## List of Tables

Table 2-1: Mills employed in size reduction of pharmaceutical powders (adapted from (Aulton, 2007)).....	6
Table 2-2: Properties which may be impacted by solid (reprinted from (Abramov, 2016)) .....	12
Table 2-3: The value of the young's modulus of some known materials and pharmaceuticals (Byrn, Zografı and Chen, 2017) .....	14
Table 2-4: The value of the shear modulus of some materials (Byrn, Zografı and Chen, 2017).....	15
Table 2-5: Value of brittleness index for some APIs and excipients (Byrn, Zografı and Chen, 2017).....	19
Table 2-6: Table summarising the mechanical treatment, mechanochemistry and the influenced properties of some pharmaceuticals (modified from (Abouhakim, 2016)).....	28
Table 2-7: Excitation processes and their relaxation times occurring in mechanically activated solids derived from the hierarchy model (Baláz, 2008).....	37
Table 3-1: Example of thermodynamically stable amorphous (for 22 days and their properties (Graeser <i>et al.</i> , 2009; Baird, Van Eerdenbrugh and Taylor, 2010; Mahlin and Bergström, 2013).....	45
Table 3-2: List of drugs with predicted stable amorphous along with hazard category and cost .....	46
Table 4-1: DABOMD crystal data. (Reproduced with the permission of the International Union of Crystallography (IUCr) (Abouhakim <i>et al.</i> , 2020a).....	65
Table 4-2: Selected Bond Angles for DABOMD. (Reproduced with the permission of the International Union of Crystallography (IUCr) (Abouhakim <i>et al.</i> , 2020a).....	66
Table 4-3: Selected Bond Angles for DABOMD (IUCr) (Abouhakim <i>et al.</i> , 2020a) .....	66
Table 4-4: DABOMD results from attachment energy( <i>E<sub>att</sub></i> ) calculations of growth morphology (Reproduced with the permission of the International Union of Crystallography (IUCr) (Abouhakim <i>et al.</i> , 2020a) .....	73
Table 4-5: Young's Modulus along different crystal axis for DABOMD (Reproduced with the permission of the International Union of Crystallography (IUCr) (Abouhakim <i>et al.</i> , 2020a) .....	78
Table 5-1: $\beta$ –LGA crystal data information (Hirokawa, 1955; M. S. Lehmann, Koetzle and Hamilton, 1972).....	85
Table 5-2: $\beta$ –LGA results from attachment energy ( <i>E<sub>att</sub></i> ) calculations of growth morphology.....	87
Table 5-3: Table shows the calculated interactions in $\beta$ –LGA crystal .....	90
Table 5-4: Young's Modulus along different crystal axis for $\beta$ –LGA .....	92
Table 6-1: Characteristic sizes ( <i>D</i> 10, <i>D</i> 50, and, <i>D</i> 90) of non-milled and milled DABOMD samples in planetary ball mill from 1min to 300 min (Reproduced with the permission of American Chemical Society (ACS) (Abouhakim <i>et al.</i> , 2020b) .....	98
Table 6-2: Measurement of the non-milled DABOMD powder using SEM and laser diffraction .....	99
Table 6-3: Median diameter of DABOMD non-milled and milled with planetary ball mill, measured using image analysis .	99
Table 6-4: Table shows the mode of vibration for the main functional groups in DABOMD (Reproduced with the permission of American Chemical Society (ACS) (Abouhakim <i>et al.</i> , 2020b).....	108
Table 6-5: Percentage amorphous of DABOMD forming during different milling time in planetary ball mill measured by XRPD (Reproduced with the permission of American Chemical Society (ACS) (Abouhakim <i>et al.</i> , 2020b) .....	110
Table 6-6: Percentage amorphous formed with planetary ball mill quantified using FTIR chemometric method of milled DABOMD and equivalent % water content from TGA.....	112
Table 6-7: Planes of the significant XRPD peaks of DABOMD obtained from Mercury (Mercury User Guide and Tutorials 2018 CSD Release, 2017) (Reproduced with the permission of American Chemical Society (ACS) (Abouhakim <i>et al.</i> , 2020b) .....	114

Table 6-8: The amount of water present in DABOMD detected by TGA (Reproduced with the permission of American Chemical Society (ACS) (Abouhakim et al., 2020b).....	116
Table 6-9: Table shows the outcome of the model fit of the kinetics of comminution amorphisation in the planetary ball mill and water loss in DABOMD.....	118
Table 6-10: Characteristic sizes ( $D_{10}$ , $D_{50}$ , and, $D_{90}$ ) of non-milled and milled DABOMD samples in planetary ball and single ball mill from 1min to 300 min.....	124
Table 6-11: Median diameter of DABOMD non-milled and milled with single ball mill, measured using image analysis...	125
Table 6-12: Vibrations of the main functional groups in non-milled crystalline and milled DABOMD in planetary and single ball mills .....	129
Table 6-13: Percentage amorphous of DABOMD quantified from XRPD forming during different milling time in single ball mill.....	132
Table 6-14: Percentage amorphous formed with single ball mill quantified using FTIR chemometric method of milled DABOMD and equivalent % water content from TGA.....	133
Table 6-15: Table shows the outcome of the model fit of the kinetics of comminution amorphisation in the single ball mill .....	133
Table 7-1: Characteristic sizes ( $D_{10}$ , $D_{50}$ , and, $D_{90}$ ) of non-milled and milled $\beta$ –LGA samples in planetary ball mill from 1min to 300 min.....	140
Table 7-2: FTIR-ATR of non-milled and milled $\beta$ –LGA in planetary ball mill .....	148
Table 7-3: The amount of amorphous $\beta$ –LGA quantified from XRPD.....	148
Table 7-4: Table shows the outcome of the model fit of the kinetics of comminution and amorphisation of $\beta$ –LGA .....	150
Table 8-1: Planetary ball mill variables .....	157
Table 8-2: Planetary ball mill geometrical parameters.....	157
Table 8-3: Values of calculated energies in planetary ball mill .....	159
Table 8-4: Single ball mill variables.....	161
Table 8-5: Energies from single ball mill compared to planetary ball mill.....	161
Table 8-6: Calculated energy from compression test compared to a single ball mill and planetary ball mill .....	162
Table 8-7: DEM simulation parameters for PBM.....	166
Table 8-8: Impact energy of the planetary ball mill simulated using DEM and literature .....	167
Table 8-9: DEM simulation parameters for SBM.....	168
Table 8-10: Impact energy of the single ball mill simulated using DEM and literature .....	170
Table 8-11: The amount of energies used to generate different size, and amount of amorphous in planetary ball mill and single ball mill .....	171

## List of Equations

Equation 2.1.....	3
Equation 2.2.....	4
Equation 2.3.....	4
Equation 2.4.....	4
Equation 2.5.....	13
Equation 2.6.....	14
Equation 2.7.....	14
Equation 2.8.....	16
Equation 2.9.....	16
Equation 2.10.....	16
Equation 2.11.....	16
Equation 2.12.....	17
Equation 2.13.....	17
Equation 2.14.....	19
Equation 3.1.....	48
Equation 3.2.....	50
Equation 3.3.....	52
Equation 6-1.....	111
Equation 6-2.....	111
Equation 6-3.....	111
Equation 6-4.....	111
Equation 6-5.....	117
Equation 6-6.....	117
Equation 6-7.....	117
Equation 6-8.....	117
Equation 8-1.....	158
Equation 8-2.....	158
Equation 8-3.....	158
Equation 8-4.....	158
Equation 8-5.....	158
Equation 8-6.....	159
Equation 8-7.....	159
Equation 8-8.....	159
Equation 8-9.....	159
Equation 8-10.....	159
Equation 8-11.....	161
Equation 8.12.....	164
Equation 8.13.....	164
Equation 8.14.....	166
Equation 8.15.....	168

## Abbreviations

BFDH	Bravais, Friedel, Donnay and Harker
BPR	Ball-to-Powder Ratio
CASTEP	Cambridge Serial Total Energy Package
CCDC	Cambridge Crystallographic Data Centre
<i>CoR</i>	Coefficient of Restitution
DABOMD	Diaqua-bis (omeprazole)-magnesium dihydrate
DEM	Discrete Element Method
DFT	Density Functional Theory
DSC	Differential Scanning Calorimetry
FF	Force Field
FTIR	Fourier Transformed Infra-Red
FTIR-ATR	Attenuated Infrared Fourier Transform
FWHM	Full Width A Half Maximum Intensity
GGA	Generalized Gradient Approximation
IR	Infra-Red
K.E.	Kinetic Energy
LGA	L Glutamic Acid
PSD	Particle Size Distribution
RMSD	Root-Mean-Square
SBM	Single ball mill
SEM	Scanning Electron Microscopy
<i>SOS</i>	Sum of Squares
TGA	Thermogravimetric analysis
<i>VHN</i>	Vicker Hardness
XRD	X-ray diffraction
XRPD	X-ray powder diffraction

## Nomenclature

<b>Roman Letter</b>		<b>Units</b>
A	Surface area of the drug particle	<i>m</i>
$A_0$	Initial area	<i>m</i>
$A_f$	Area straight after the fracture	<i>m</i>
AAC	Apparent amorphous content	%
AR	Maximum area reduction before disruption	%
C	Drug concentration in the solution	$kg/m^3$
C	Stiffness matrix	$kg/m^3$
$C_s$	Drug's concentration at the surrounding of the solid	$kg/m^3$
<i>d</i>	Spacing between the crystals	<i>m</i>
$d_b$	Diameter of the ball	<i>m</i>
$D_0$	Powder diameter at the start of milling	<i>m</i>
D(t)	Powder diameter at time (t)	<i>m</i>
$D_v$	Diameter of the pot	<i>m</i>
$D_\infty$	Powder diameter at the end of the milling	<i>m</i>
$D_{10}$	Particle size diameters represent 10% of the total volume distribution in a measured sample	$\mu m$
$D_{50}$	Particle size diameters represent 50% of the total volume distribution in a measured sample	$\mu m$
$D_{90}$	Particle size diameters represent 90% of the total volume distribution in a measured sample	$\mu m$
$dm/dt$	The dissolution rate	$kg\ m^2/s$
<i>E</i>	Young's modulus/ Modulus of Elasticity	<i>GPa</i>
$E_{att}$	Attachment energy	$kcal\ mol$
$E_b$	Kinetic energy	$kcal\ mol$
<i>EL</i>	Percentage maximum elongation	%
$E_m$	Energy of the mill	<i>J/s</i>
$E_s$	Residual $E_s$ energy within the balls after the hit	<i>J/g.s</i>
$E_{lattice}$	Lattice energy	$kcal\ mol$
$E_{slice}$	Energy released from the formation of a growth-slice	$kcal\ mol$
F	Applied force	<i>N</i>
$F_{ij}^c$	Contact force exerted on particle	<i>N</i>
$F_{ij}^{nc}$	Non-direct forces imposed on particles <i>i</i> and <i>j</i> by particle <i>k</i> or other forces	<i>N</i>
$f_{AAC}(t)$	Apparent amorphous content at time t	%
$f_b$	Frequency of collisions	
$f_c$	Strength of the material	<i>Pa</i>
H	Hardness	<i>MPa</i>
$H_v$	Height of the pot	<i>m</i>
$I_i$	Motion of inertia	$Kg\ m^2$
G	Shear modulus	<i>GPa</i>
<i>K</i>	Dissolution constant	$mol\ dm^{-3}$
$K_c$	Critical intensity factor	$MPa\ m^{-2}$
<i>k</i>	Rate of kinetics	$min^{-1}$
$K_R$	Rittinger constant	

L	Length of the indenter diameter	<i>m</i>
<i>n</i>	Integer representing the order of reflection	
<i>N<sub>b</sub></i>	Number of balls	
P	Total power transferred to the system	<i>J/s</i>
PW	Powder weight	<i>Kg</i>
<i>R<sub>p</sub></i>	Distances from the centre of the mill to the centre of the vial	<i>m</i>
<i>R<sub>v</sub></i>	Distances from the centre of the vial and from the centre of the vial to its periphery	<i>m</i>
<i>S</i>	Compliance matrix	
<i>w<sub>i</sub></i>	Angular velocity	<i>rad s<sup>-1</sup></i>
<i>W<sub>p</sub></i>	Angular velocity of the plate	<i>rad s<sup>-1</sup></i>
<i>W<sub>v</sub></i>	Absolute angular velocity of the vial	<i>rad s<sup>-1</sup></i>
<i>x<sub>Cryst</sub></i>	Extend of crystallinity	%
<i>X<sub>p</sub></i>	Primary size of the particle	<i>μm</i>
<i>X<sub>f</sub></i>	Final size of the particle	<i>μm</i>
<i>x<sub>com</sub></i>	Extent of comminution	%

### Greek Letters

$\alpha$	Alpha
$\alpha_{\text{rpd\_com}}$	Extent of rapid comminution
$\alpha_{\text{rpd\_amp}}$	Extent of rapid amorphisation
$\alpha_{\text{slw\_com}}$	Extent of slow comminution
$\alpha_{\text{slw\_com}}$	Extent of slow amorphisation
$\beta$	Beta
$\gamma$	shear strain
$\varepsilon$	Geometry parameter
$\eta_v$	Geometry parameter
$\theta$	$\theta$ is the angle between the X-ray incident beam
$\xi$	Strain
$\xi_{\text{max}}$	maximum strain
$\sigma$	Stress
$\tau$	Shear stress
$\varphi_b$	Geometry parameter
$\Delta E_b$	impact energy which causes deformation to the powder

## **Chapter 1 Introduction**

**1.1. Background of Research**

**1.2. Scope of Work**

**1.3. Project Management**

**1.4 Structure of The Thesis**

**This chapter provides a brief introduction to the thesis background, aims, and objective of the work and structure followed for thesis.**

## 1.1. Background of Research

The majority of pharmaceuticals are manufactured in particulate solid forms (almost 80%) (Byrn, Zografi and Chen, 2017). Many of these solid pharmaceuticals require size reduction to deliver specific requirements. Size reduction by mechanical means also referred to as milling, is a commonly used process in the pharmaceutical industry to control the size and uniformity of the solid drug or dosage (Storey and Ymen, 2011). It is also used to enhance the dissolution rate of poorly soluble drugs via increasing the surface area to the volume ratio of the particles (Parrott, 1974).

The micronisation can lead to unwanted changes in the physical characteristics of the material, including poor control of the particle size and morphology. In some cases, it can lead to the emergence of new polymorph, amorphisation, and chemical changes; this is known as mechanochemistry (Baláž, 2008). The resultant changes can influence the desired products attributes and clinical performances of the pharmaceutical API such as the dissolution rate, bioavailability and stability (Snow, Richard H. Luckie, 1979; Chieng *et al.*, 2009; I. Colombo, Grassi and Grassi, 2009; Descamps and Willart, 2016). The behaviour of the solid pharmaceutical, particularly, the process of mechanochemistry remains unanticipated due to the lack of understanding of the fundamental science of the material properties of the feed API or excipient and due to the insufficient knowledge of the milling parameters that influence the milling process. For instance, a critical material property which impact the milling behaviour is the mechanical properties which arise from the molecular interactions in the crystalline lattice of the compound (Storey and Ymen, 2011). Hence, it is tremendously vital to relate the intrinsic properties at the molecular level to the extrinsic properties at the bulk level. These properties can be influenced by the level of energy produced in milling, which is dictated by certain parameters which require thorough analysis.

There is a gap in the literature about the properties that dictate the mechanistic behaviour of the solid at the bulk level and their underlying intrinsic properties at the molecular level which requires addressing. Moreover, insufficient work has been conducted to the link between the different milling parameters and the generated energy. Therefore, the impact of the different milling energies on the physicochemical characteristics of solids, particularly, pharmaceutical solids has not yet been established. With regards to the physicochemical changes arising with milling; a remarkable deficiency is present in the literature corresponding to the mechanochemistry of pharmaceutical solids, and its underlying mechanism which makes this phenomenon one the most unanticipated behaviour of the sample. To study the process of mechanochemistry, one needs an in-depth knowledge of the solid-state techniques that are capable to detect the produced changes, such as formation of amorphous phase with milling.

Addressing these knowledge gaps will enable developing a relationship between the feed properties, the energy of mill and the produced change and allows the anticipation of the API characteristics and performances which is the main motivation of this work. This approach will

allow the reduction of the amount of trial and error experiments, save time, cost, and optimise the quality of the pharmaceutical product.

## 1.2. Scope of Work

The milled product characteristics and performance is theoretically associated with the feed material properties (i.e. size, morphology, mechanical properties, crystalline properties) which can be influenced by the variable milling energies that arise from different conditions/parameters. This gives rise to the following research question which will be addressed in this thesis:

“Why solid pharmaceuticals exhibit different behaviour during milling, and how can we anticipate it?”

In an attempt to address the question in this thesis, the following objectives are implemented ;

- 1) Predict the material properties influencing the milling behaviour of the solid pharmaceutical
- 2) Mill at different conditions using critical milling parameters
- 3) Identify the impact of milling on the physicochemical characteristics of the samples
- 3) Compare the predicted and the experimental outcome
- 4) Calculate the energy of the mills associated with the physicochemical changes
- 5) Formulate a relationship between the milling conditions, the feed properties and the product characteristics.

The implication of these steps is as follows;

- Predict the crystal habit, mechanical and slip plane from the crystal structure of the pharmaceutical compound by the aid of computational chemistry.
- Anticipate the propensity of the solid pharmaceutical to fracture and to plastic deformation based on the predicted properties.
- Mill the solid pharmaceutical in planetary ball mill and single ball mill at different times.
- Characterise the feed and milled product size, morphology, crystalline, thermodynamic and intermolecular properties. The characterisation techniques employed include laser diffraction, scanning electron microscope (SEM), X-ray powder diffraction (XRPD), differential scanning spectroscopy (DSC) and Fourier transform infrared (FTIR) spectroscopy.
- Compare the predicted and the experimental behaviour of the milled samples.
- Calculate the energy of the mills. The energy of the mills is calculated from literature derived model for the planetary ball mill, and from tracking the jar of single ball mill using a high-speed camera. The energy is validated using the Discrete Element Method (DEM) simulation of the mills.

- Outline the relationship between material properties, milling energy and product characteristics.

This study adopts a novel area of research called Quality by Design (QbD) which relates the product characteristics to the milling conditions and Critical Attributes (CA) (material properties) of the feed. Figure 1-1 shows a project map of how the objectives will be fulfilled. Two pharmaceuticals are employed in this work DABOMD and  $\beta$ -LGA . The focus on DABOMD is attributed to the predicted stability of its amorphous form, whereas the focus on  $\beta$ -LGA is related to its availability and safety.

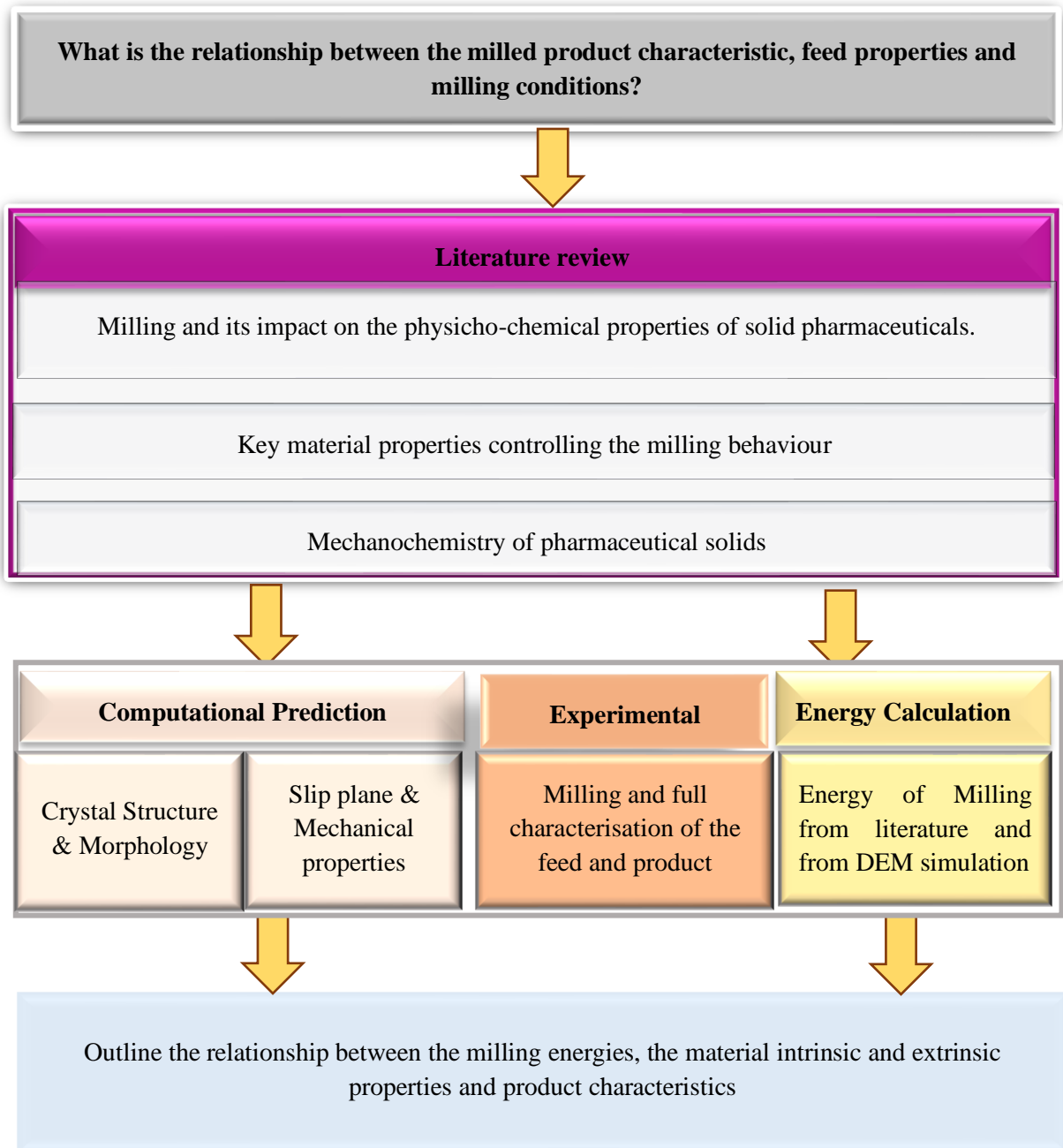


**Figure 1-1: Project map showing how objectives are met in the thesis**

### 1.3. Project Management

This research work is mainly funded by the Engineering and Physical Science Research Council EPSRC while AstraZeneca and the University of Leeds have also contributed to part of the project funding. The project is part of the Centre of Doctoral Training CDT for Complex Particulate and Product Cp3 at the University of Leeds. This work was supervised by academic and industrial supervisors. The main academic supervisor was Dr Ali Hassanpour while Prof Frans Muller and Prof Sven Schroeder act as co-supervisors. The industrial supervisors from

AstraZeneca are Dr Mike J. Quayle, Dr Stefan. T. Norberg and Dr Sten.O. Nilsson Lill as. A biweekly telephone/skype meeting was arranged with the main academic and industrial supervisors to present and to discuss the progress of the work. The majority of the experimental work was carried out at the University of Leeds while part of the experimental work such as powder characterisations were conducted at AstraZeneca. The computational chemistry works such as the predicted mechanical properties of the samples were carried out in AstraZeneca by Dr Sten.O. Nilsson Lill. The DEM simulations of the planetary ball mill and the single ball mill were carried out by Dr Mohammadreza Alizadeh Behjani at the University of Leeds.

## 1.4. Structure of the Thesis

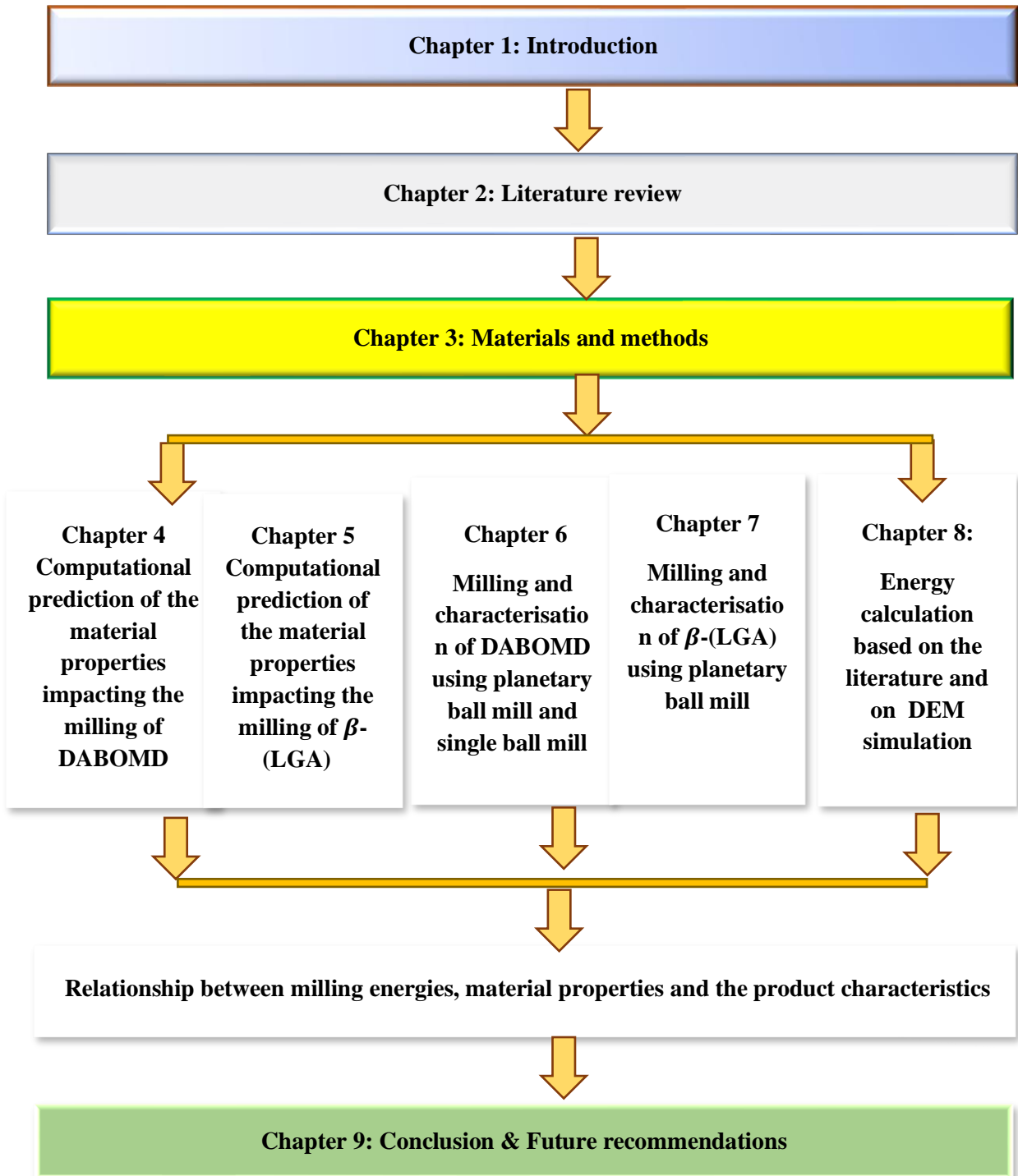


Figure 1-2: Structure of the thesis illustrating brief contents on each chapter

A summary of the thesis structure is shown in Figure 1-2 is listed below:

Chapter 1 outlines the background of the research, research question, scope, and objectives.

Chapter 2 outlines reviews of topic areas related to the research project, including the following: a review on milling and its application in the pharmaceutical industry, review on the critical material properties that dictate the mode of breakage/failure during milling. A review of the mechanochemistry of pharmaceuticals arises from the process of milling.

*Chapter 3* outlines the materials employed for the rest of the thesis including Diaqua-bis(Omeprazole)-magnesium(II) dihydrate (DABOMD) and  $\beta$  L glutamic acid  $\beta$ -(LGA) and the rationale for the selection. It also outlines the milling techniques, solid-state characterisation techniques, and modelling approaches that are employed to predict the critical material properties influencing the drug from the molecular level using computational chemistry. The derived characteristics include crystal structure, habit, and mechanical properties and the potential presence of a slip plane.

*Chapter 4* involves the application of computational chemistry for the prediction of the underlying material properties that impact the milling behaviour of DABOMD.

*Chapter 5* involves the application of computational chemistry for the prediction of the underlying material properties that impact the milling behaviour of  $\beta$ -(LGA).

Chapter 6 outlines the milling process of (DABOMD) carried out using a planetary ball mill and a single ball mill and provides a comparison between the selected mills. Furthermore, this chapter also depicts the effect of milling on the material characteristics, including size and morphology, thermodynamic, structural and, intermolecular properties. This chapter investigates the mechanism of milling of DABOMD with particular attention to the process of comminution and amorphisation.

*Chapter 7* involves the milling process of  $\beta$ -(LGA) carried out using a planetary ball mill. This chapter also illustrates the effect of milling on the material physiochemical changes characteristics including size and morphology, thermal and structural properties, and intermolecular properties. This chapter investigates the mechanism of milling of  $\beta$ -(LGA) with particular attention to the process of comminution and amorphisation.

*Chapter 8* determines the milling energies generated from planetary ball mill and single ball mill using models derived from the literature, and high-speed camera tracking of the milling jar respectively; and were validated using DEM simulation. A relationship between the milling energy and the observed changes on the milled materials is derived.

Chapter 9: Provides an overall conclusion of the entire project which liaise between the material properties of the solid pharmaceuticals, the milling behaviour observed during the milling experiments, and the energies utilised in the milling process. This chapter also sets out the future work needed and recommendations.

## **Chapter 2 Literature Review on Milling and its Impact on the Solid Pharmaceuticals**

### **2.1. Introduction**

### **2.2. Milling**

### **2.3. Material Properties Affecting the Milling Process**

### **2.4 Mechanochemistry**

### **2.5 Summary**

A summary of the literature is provided in this chapter including the process of milling and its impact on the solid pharmaceuticals. The material properties that influence the milling of solids are also outlined in this chapter. Moreover, a review is provided in this chapter which covers the process of mechanochemistry of pharmaceuticals .

## 2.1. Introduction

In the pharmaceutical industry, the development of successful drugs depend mainly on two factors; the production of an effective API, and the administration of the API to the desired site at an appropriate rate. The first factor is related to the chemical structure of the drug molecule, which has been a research focus for a while in the pharmaceutical filed (Byrn, Zografis and Chen, 2017; Yihong Qiu, Yisheng Chen, Geoff G.Z. Zhang, Lawrence Yu, 2017). Whereas, The second factor is associated with the nature of the dosage form employed for the drug administration (Craig, 1997). Figure 2-1 shows a workflow presenting the evolution of a solid pharmaceutical. The drug initially starts as a single-molecule then, developed into an active component (API) which becomes a part of the solid API particle (Abramov, 2016). The manipulation of the dosage form can alter the biological activity of the drug API including the drug's solubility and bioavailability, and can impact the drug's stability, flow, compression, and hygroscopicity (Byrn, Zografis and Chen, 2017). The nature of the dosage form depends strongly on the formulation and manufacturing process. Since the majority of drugs are commonly manufactured as solid dosage forms, the drug performances are influenced by their physical characteristics (De Gussemé *et al.*, 2008).

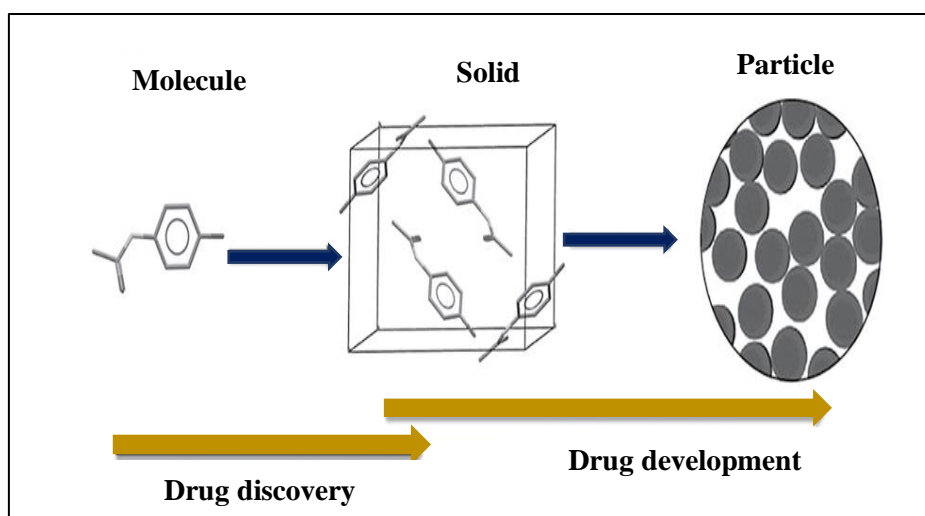


**Figure 2-1: Physical transformation of drugs along with the pharmaceutical industry. (modified from (Abramov, 2016))**

Although the chemical structure of the dosage forms is usually well recognised, the physical characteristics of many of these systems remain unknown. Hence the study of the physical and material properties of drugs solid dosage forms is undoubtedly an area that requires further research (Abramov, 2016). Also, the pharmaceutical industry is facing tremendous pressure from regulations to implement a thorough understanding of the solid drug development stage (Abramov, 2016; Byrn, Zografis and Chen, 2017). The drug development stage is composed of multiple processes, including crystallisation, milling, granulation, etc. This project focuses on the milling process and its effect on the drug's physical and chemical characteristics.

Milling is a top-down process used to reduce the size of coarse particles. In pharmaceutical processing, milling is often employed to enhance the solubility and dissolution of poorly soluble drugs by reducing the size and creating large surface area available for dissolution following the Noyes-Witney formula (Equation 2.1). Therefore, enhancing the dissolution rate and the bioavailability of the drug (Abramov, 2016; Byrn, Zografis and Chen, 2017).

$$\frac{dm}{dt} = K_A(C_s - C) \quad \text{Equation 2.1}$$

Where,  $dm/dt$  is the dissolution rate,  $C_s$  is the drug's concentration at the surrounding of the solid,  $C$  is the drug concentration in the solution,  $K$  is the dissolution constant which dependants on the thickness of the dissolution layer and the diffusion coefficient and,  $A$  is the surface area of the drug particle. The size reduction process is also desired in respiratory drugs, since it improves the drug aerodynamics in the respiratory system and, facilitates the drug's deposition on the lungs. In addition to the micronisation process, milling was reported to be responsible for phase transformation, i.e. formation of polymorphs and/or amorphous as well as solid-state reaction. This process is referred to as mechanical activation of the material, and the physico-chemical change caused by milling is referred to as mechanochemistry (I Colombo, Grassi and Grassi, 2009). The produced pharmaceutical solid exhibits different solubility, hardness, density, stability, and melting points which directly influence the product performances. The behaviour of the material inside the mill including the mode of failure, breakage propensity, and phase transformation or any other mechanochemistry is all dependant on the solid material properties of the feed and on the milling conditions which result in specific milling energy. However, there is a substantial gap in the literature that links the material properties (material science field), milling process (engineering field) to the physical and chemical changes (field of mechanochemistry) of the product which is primarily due to the complexity and extensive work needed in each field.

Therefore, this literature review will tackle three main areas. Firstly, the milling process, particularly, milling of solid pharmaceuticals, and the critical milling parameters that impact the solid material. Secondly, the key material properties responsible for the mechanistic behaviour of the powder during milling and their underlying intrinsic properties at the molecular level. Thirdly, the process of mechanochemistry in pharmaceutical solids and its underlying conditions and mechanisms.

## 2.2. Milling

The particle size reduction process is achieved as a result of the applied energy by mechanical mean. In general, it is difficult to evaluate the amount of energy required for particle fracture due to the complexity of the stress and strain field that every single particle experience in the mill. It has been reported that the energy employed for size reduction is equal to 10% of the

total energy consumed by the mill, whereas, the rest of the energy is dissipated in the form of friction, noise, and heat (Backhurst, J. R. Harker, J.H. Richardson, 2002).

### 2.2.1. Theory of Particle Size Reduction

Few comprehensive theories were developed to explain the size reduction or comminution process during milling. Since milling utilizes energy to induce fracture to the particles, few models were developed to predict the energy consumption for the size reduction process including Rittinger (1867), Kick (1885), and Bond (1952) (Rhodes, 2008).

Rittinger stated that the energy required to reduce the size of a particle is proportional to the new surface area produced or, inversely proportional to the diameter of the produced particle, as shown in Equation 2.2.

$$E_m = C \left( \frac{1}{X_p} - \frac{1}{X_f} \right) = K_R f_c \left( \frac{1}{X_p} - \frac{1}{X_f} \right) \quad \text{Equation 2.2}$$

Where,  $E_m$  is the energy of the mill,  $X_p$  is the primary size of the particle and  $X_f$  is the final size of the particle,  $K_R$  is Rittinger constant and  $f_c$  is the strength of the material. Rittinger model is more convenient to fine particles where a large increase in the surface area per unit mass is applied. However, milling is inefficient since a large amount of energy is required to produce new surfaces due to its dissipation in other forms besides comminution.

Kicks proposed that the energy involved in the size reduction process is proportional to the reduction ratio (size of the initial particle to that of the final particle), as shown in Equation 2.3.

$$E_m = C \ln \left( \frac{X_f}{X_p} \right) = K_k f_c \ln \left( \frac{X_f}{X_p} \right) \quad \text{Equation 2.3}$$

Where,  $K_k$  is the Kick's constant. This model suggests that the energy required to reduce the size of a particle from  $500 \mu m$  to  $100 \mu m$  is equal to that needed to reduce a particle size from  $50 \mu m$  to  $10 \mu m$  which oversimplified the particle size reduction process.

Bond came up with a formula that combines both Rittinger's and Kick's models which states that the energy needed for milling is inversely proportional to the square root of the diameter of the product (Equation 2.4).

$$E_m = 2C \left( \frac{1}{\sqrt{X_p}} - \frac{1}{\sqrt{X_f}} \right) = 2C \frac{1}{\sqrt{X_p}} \left( 1 - \frac{1}{\sqrt{q}} \right) \quad \text{Equation 2.4}$$

Where  $q = \frac{X_f}{X_p}$ . Bond's model is useful for the preliminary evaluation of milling. However, none of the stated models is practical in the process development of the mill. Nonetheless, Kicks has been found suitable for larger particles, whereas Rittinger's model can be employed for fine particles (Rhodes, 2008).

### 2.2.2. Milling Techniques

Wet milling and dry milling are two different approaches to the size reduction process. However, dry milling is most commonly used in the pharmaceutical industry. The method of size reduction varies from mill to mill depending on the mode of stress associated with the specific mill which can be in the form of; compression, impact, collision, shear, or a combination of these modes as shown in Figure 2-2. The selection of the dry mill for the particle size reduction depends on the desired size of the particle, the type of stress generated by the mill, the mode of operation, the milling efficiency, the ease to clean and sterilise, the abrasion of the mill, and the interaction between the feed and the material of the mill (Table 2-1) (Müller and Polke, 1999).

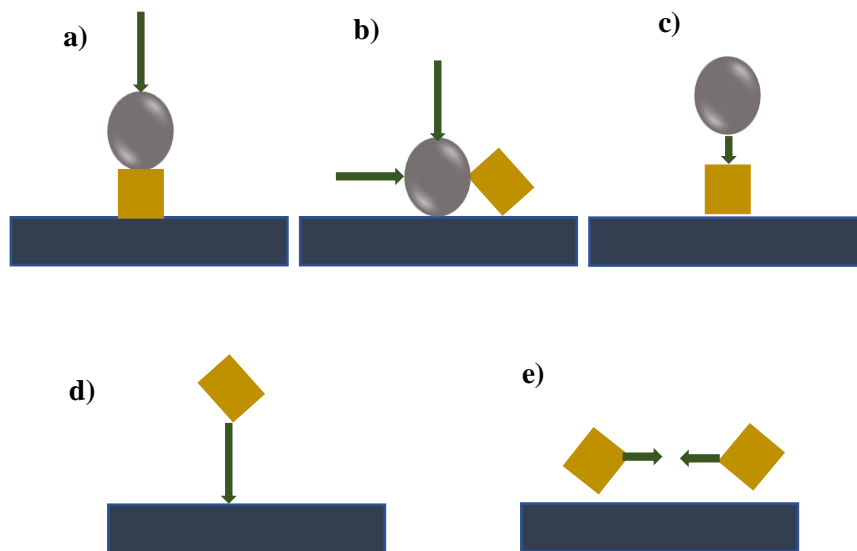


**Figure 2-2: Types of stress modes generated inside the mills. a) compression, b) shear (attrition), c) impact (stroke) and d) impact (collision). With circles illustrating milling media, square for the milled material and rectangles represent the mill wall (amended from (Alex *et al.*, 2016))**

To achieve particle sizes in the micron range desired in most pharmaceutical applications, ball mills, vibratory mills and, fluid jet mills are commonly employed due to their high efficiency and capacity (Aulton, 2007). Ball mills are classified on the top lists of high energy mills since they provide high impact energy per contact area (Varin *et al.*, 2009). For this study, high energy mills including a single ball mill and planetary ball mill are selected owing to their ability to dissipate a large amount of energy which suggests that they can contribute to a remarkable change in the milled product such as mechanochemistry.

**Table 2-1: Mills employed in size reduction of pharmaceutical powders (adapted from (Aulton, 2007))**

<b>Mills</b>	<b>Mode of size reduction</b>	<b>Product size (<math>\mu m</math>)</b>	<b>Used for</b>	<b>Not applicable for</b>
<b>Cutter mill</b>	Fracture by cutting	> 1000	Soft and tough materials	Friable materials
<b>Edge runner mill</b>	Compression and attrition	> 1000	Soft and fibrous materials	Abrasive materials
<b>Hammer mill</b>	Impaction	50 - > 1000	Almost all materials	Abrasive materials
<b>Vibration mill</b>	Repeated impaction	1 - 1000	Almost all materials	Abrasive materials
<b>Roller mill</b>	Attrition	50 - > 1000	Almost all materials	Abrasive materials
<b>Fluid energy mill</b>	Impaction and attrition	< 50	Moderately hard and friable materials	Soft and sticky materials
<b>Ball mill</b>	Impaction and attrition	< 50	Abrasive materials	Soft materials

### **2.2.2.1. Ball Mill**

Ball mill is commonly employed for particle size reduction of pharmaceuticals. Ball mill involves a cylinder milling vessel filled with a single or multiple balls or rods synthesised from materials such as porcelain or alloys (Figure 2-3). There are various types of ball mill, including shaker, tumbler, attritor, stirred canon and planetary ball mill (Neikov, 2009b). Impact and shear stresses are the prevailing stresses present in this type of mill. Shear stress arises from the collision of the balls with each other and with the wall, whereas, impact stress is generated when the balls drop down as a result of gravitational force (Varin *et al.*, 2009). The ball mill can be cleaned and sterilised easily. The key factors influencing the amount of energy generated inside the mill are the mass of the ball and the velocity. The mass of the ball varies with the size of the ball as well as with its composite material, whereas, the velocity is associated with the intensity of the mill (Neikov, 2009). The vessel, the material of the ball, the size of the ball, and the number of balls can generate different levels of energy on the milled powder as was reported by (Chauruka, 2015).

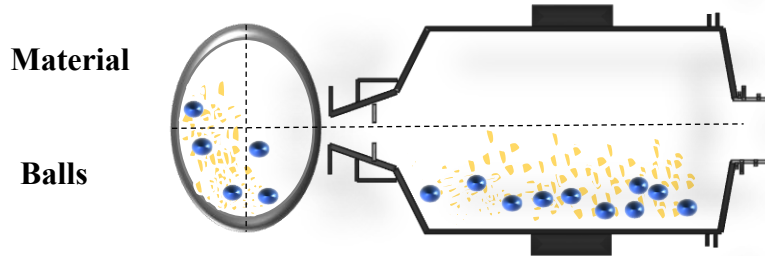


**Figure 2-3: Schematic diagram of a ball mill. (modified from (Loh, Samanta and Sia Heng, 2015))**

#### 2.2.2.2. Ball Milling Process Variables

Ball mill involves various process variables that require a careful consideration upon designing a method for milling since they can impact on the product properties. The Ball mill variables include milling speed, milling material, milling media, filling of the jar, ball to powder ratio (BPR), milling duration, milling temperature, milling atmosphere and, process control agents (Figure 2-4) (Parrott, 1974).

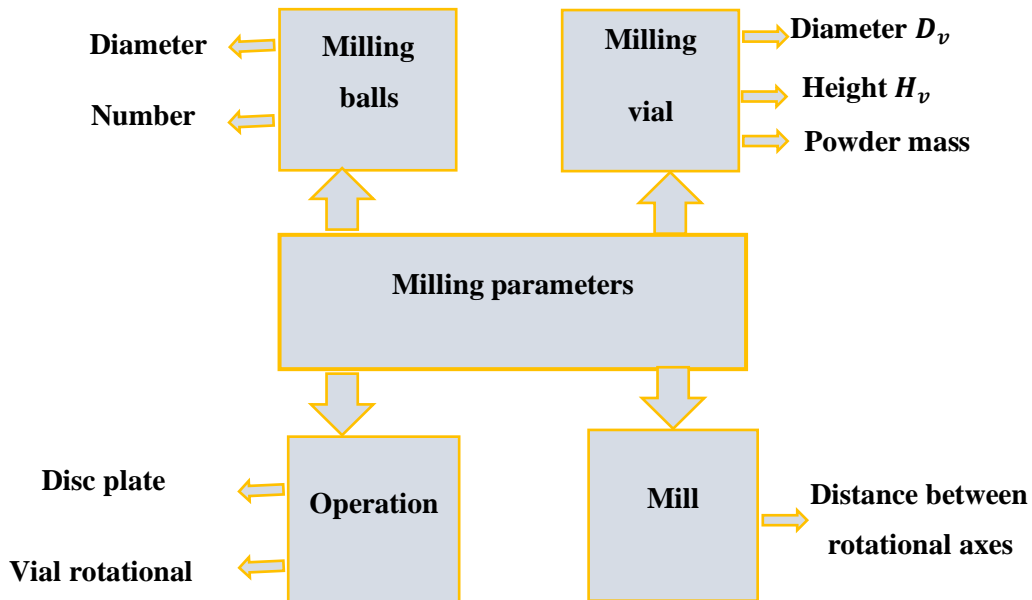


**Figure 2-4: Milling parameters for ball mill**

##### 2.2.2.2.1. Milling Speed

Milling speed controls, the amount of energy available in the mill, in general, high milling speed or frequency provides a large amount of energy available for particle fracture. However, a ball mill (vibratory mill) involves a critical milling speed above which the milling media

cannot move adequately inside the milling jar which implies that less or no input energy is available for the milled sample (Kwan *et al.*, 2004).

#### **2.2.2.2.2. Milling Material**

Different type of milling materials generates variable amounts of energy due to their distinct density and hardness. Materials with high density can contribute to smaller size particles as opposed to those with lower density and hardness. It is of paramount importance to consider the nature of milling material making the milling media or the balls and the milling jar since not only do they depict the amount of energy but also can result in the contamination of the product. A range of materials is available, including zirconia, stainless steel, steel, agate, and carbide. Chauruka carried out milling experiments on Gamma-Alumina using various materials. She found that material such as agate and stainless steel deliver higher energy for particle breakage (Chauruka, 2015).

#### **2.2.2.2.3. Milling Duration**

The time of milling is an important parameter that requires controlling during the process of milling; since it can severely influence the product characteristics such as size, morphology, and crystal structure as well as the level of contamination. The time required for milling is chosen based on the desired product properties and the nature of the feed material; for instance, friable materials might require a longer time of milling as opposed to hard materials. Time intervals are required during the milling process to prevent the temperature increase of the system since it can lead to the decomposition of the product (Kocich and Lukáč, 2015).

#### **2.2.2.2.4. Milling Media**

Milling media such as balls can vary in size, material, and number. In terms of the ball's size, a large diameter can dissipate more energy available for the fracture of particles (Hasegawa, Honma and Kanda, 1990). The material of the milling media is a vital parameter to consider since different materials exhibit variable density and hardness as mentioned earlier and hence can generate different amounts of energies. Also, the number of balls employed in the milling process has a considerable effect on the processed material. Multiple balls can yield a higher amount of energy compared to a single ball. It is essential to consider the size of the milling jar and the amount of milled powder when choosing the size and the number of milling media (Baláž, 2008).

#### **2.2.2.2.5. Ball to Powder Ratio**

Ball to powder ratio (BPR) refers to the mass of the balls to that of the powder. BPR can vary from 1:1 to 220:1. The higher the ball to powder ratio, the more energy inputs available to the system. A higher BPR ratio is usually employed in processes where mechanical activation is required. 10:1 ratio is the most commonly used during milling for the desired product characteristics (i.e. size) (Kocich and Lukáč, 2015).

#### **2.2.2.2.6. Milling Temperature**

The milling temperature parameter is associated with various factors in the mill, such as milling intensity/speed of milling, duration of milling, milling material and, BPR. The temperature of the milling process can be monitored and controlled by allowing regular break intervals during the milling process. Thermally unstable materials can be milled using cryomills. While the temperature of the bulk in the milling vessel can be controlled and measured, it is difficult to measure the localised temperature on the surface of the milled particles. For instance, it has been reported that the highest temperature increase in planetary ball mill is 443K, whereas, the localised temperature on the surface of inorganic materials can exceed 1273K (Baláž, 2008). However, no technique is yet available that enables quantifying the temperature of the micron regions of the particle. Higher temperatures within the mill can lead to thermal decomposition of the material. Also, the temperature rise was suggested to be one of the contributors to mechanochemistry through the local melt of sub-micron regions on surface material (Baláž, 2008).

#### **2.2.2.2.7. Milling Environment**

Milling is employed for various applications, some of which require specific environments such as the cryogenic environment. Wet milling is used to achieve finer particles using mediums such as water or other solvents or via using various lubricants such as steric acid to facilitate the friction process (Kocich and Lukáč, 2015).

#### **2.2.2.3. Vibratory Mill**

Vibratory mill involves the same components and milling mechanism as that of a conventional ball mill. Aside, it has an additional cascading or mixing action imposed on the milling media and milling vessel. The additional vibration motion promotes higher movements and collisions of the milling media and ultimately contributes to higher impacts and shear for efficient particle size reduction (Parrott, 1974).

#### **2.2.2.4. Air Jet Mill**

The fluid jet mill is commonly employed in the pharmaceutical industry for dry micronization. The size reduction in this type of mill is achieved through the collision of particles with each other and with the wall as a result of a flowing air at high velocity inside the mill. The compressed air enters the chamber from different inlets and circulates at high speed. The speed of the air is controlled by the pressure, which is set depending on the desired product size. Fluid jet mill by design has a centrifugal force that pushes the particles to rotate in a circular motion around the chamber (Hui et al., 2015). The particles circulate the milling chamber and exit through a classifier for screening, whereby, particles with the desired size exit the chamber, and others circulate back for further milling (Figure 2-5) (Abouhakim, 2016).

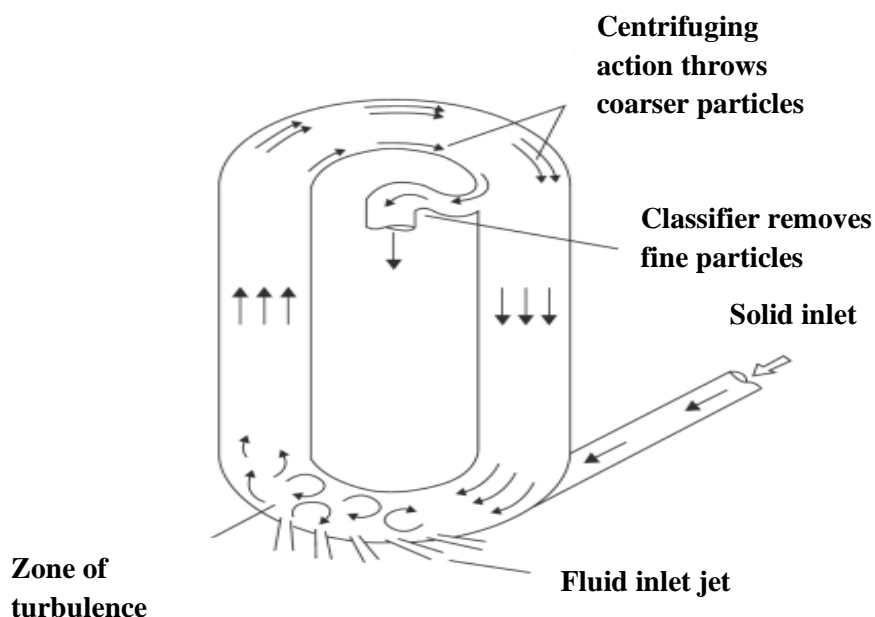


Figure 2-5: Milling chamber of the fluid jet mill (Chauruka, 2015)

## 2.3. Materials Properties Affecting the Milling Process

### 2.3.1. Solid State

#### 2.3.1.1. Type of Solid States of Pharmaceuticals

Pharmaceutical solids exist in different forms depending on their crystalline structure and arrangements. They can be in the form of crystalline, amorphous, polymorphs, anhydrous, solvates, cocrystals, and salts.

- **Crystalline:** Crystalline solid is characterised by molecules packed in an arranged array while displaying a long-range order in three-dimensional direction.
- **Amorphous:** Amorphous or glassy material is referred to as a disordered crystalline system caused by randomness in molecules conformation and lattice disorder. An amorphous material usually lacks any long-range transitional orientation symmetry that characterise the crystalline structure. Amorphous is also characterised by the glass transition temperature (instead of melting temperature) which represents its transition from solid-state to a rubbery state. The glass transition temperature of the material varies depending on the nature and thermodynamic stability of the amorphous (Guinot and Leveiller, 1999; Birju, Kumar Kakumanu and Bansal, 2006).
- **Polymorph:** Polymorph refers to the crystalline solid encompassing the same chemical composition but different internal structures such as different molecular packing, different molecular conformation, tautomeric, or combination of these. Different crystalline implies

different lattice parameters (h, k, l) (Lefebvre *et al.*, 2008). Polymorphs of the same drug exhibit variable melting points, hardness, and solubility (Florence and Attwood, 2011).

- **Solvates:** solvates are crystals comprising molecules of the same solid crystal which has solvent molecules integrated into its crystal structure.
- **Cocrystals:** Cocrystals are multicomponent crystals formed by API or intermediate.
- **Salts:** Salts are multicomponent held by ionic interactions.

### 2.3.1.2. Impact of Changing Solid State

Understanding the solid-state characteristic is a critical strategic component for designing a successful active pharmaceuticals API and excipient. A great emphasis has been placed on discovering a new pharmaceutical API. However, it is now established that to design a successful pharmaceutical drug; it is vital to develop a firm understanding of the solid-state formulation and manufacturing since, any altering of the solid-state can lead to significant impact on pharmaceutical product properties and performances (Byrn, Zografis and Chen, 2017). Table 2-2 summarises some critical material properties that can be influenced as a result of changing the solid-state form, which can arise from processes such as milling (Abramov, 2016). Therefore, the efficiency of the pharmaceutical drug is not limited to a single molecule; instead, it is a complex material with physical and chemical characteristics. Some of the vital properties for pharmaceutical performance are solubility and dissolution rate, which can be altered by changing the solid form. For instance, the difference in solubility between crystalline and amorphous compounds can reach two orders of magnitudes. Also, solvates possess higher solubility compared to anhydrous. Another important characteristic of pharmaceuticals is its chemical stability which is directly related to drug degradation. Drug degradation is highly dependent on surface characteristics. For instance, amorphous has a higher surface area and molecular mobility compared to crystalline which makes it more prone to drug degradation. Also, amorphous exhibits higher surface energy which render it more hygroscopic (Byrn, Zografis and Chen, 2017). A change in the crystalline solid form can lead to changes in the morphology, for instance, particles with needle shapes are more complicated for the processing which make them undesirable in the pharmaceutical industry. A change in the crystalline form can lead to the emergence of a metastable polymorph which is prone to degradation and has lower stability compared to the stable form (Baláž, 2008). For example, Ritonavir form I, a drug developed to treat patients with HIV was launched in the market in 1998 and was sooner withdrawn due to its lower dissolution and variable stability. The investigation of this phenomenon revealed that a new form II precipitated from the formulation which exhibits different dissolution and stability (Datta and David J W Grant, 2004). A change in the solid-state can also influence the mechanical properties as will come in detail later.

**Table 2-2: Properties which may be impacted by solid (reprinted from (Abramov, 2016))**

<b>Chemical</b>	<b>Physical</b>	<b>Mechanical</b>	<b>Surface</b>	<b>Thermodynamic</b>	<b>Kinetic</b>
Chemical stability/reactivity	Stability	Compatibility	Surface free energy	Solubility	Dissolution rate
Photochemical reactivity	Hygroscopicity	Hardness	Stickiness	Free energy of Fusion	Nucleation and crystal growth rates
	Morphology	Powder flow tableting	Interfacial tension	Melting point	Solid-state reaction rates
	Density	Tensile strength	Surface area	Heat of Fusion	
	Colour	Cleavage		Vapour pressure	
	Refractive index				

### 2.3.2. Mechanical Properties

Mechanical properties of a solid material refer to its resistance to mechanical force. The material behaviour can be elastic, plastic, brittle, or a combination of these deformations. The main parameters that depict the mechanical behaviour are Young's modulus, hardness, and critical intensity factor. Young's modulus is the resistance of a material to elastic deformation; hardness refers to the resistance of a material to plastic deformation while the critical intensity factor is the resistance of a material to crack propagation (Ghadiri, Kwan and Ding, 2007). This section will outline the underlying physics of mechanical properties. The mechanical properties are fundamentally based on the correlation between stress and strain. Stress refers to the mechanical force applied to an area of a solid body. The strain is the dimensional change, motion, or any deformation of a solid as a result of stress (Fayed and Otten, 1997).

There are two main types of stresses, namely axial stress, and shear stress. The axial stress refers to the stress applied vertically on a body that can be compressive or tensile. Compressive stress arises from a pushing force, and tensile stress is a resultant of a pulling force and, shear stress refers to a sliding force applied in a horizontal direction. Stress-strain relationship of a solid compound or particle experiencing mechanical force can be illustrated by the stress-strain curve shown in Figure 2-6. The initial region of the stress-strain curve is linear, representing an elastic deformation where the material obeys the hooks law. In this region, the material tends to deform and return to its original shape upon the relief of stress and, any change occurring in

this region is reversible. If the stress continues increasing, it reaches a point representing the elastic limit which is referred to as the yield point. The material is said to deform plastically, and any changes occurring in the material is irreversible. Further increase of stress leads to a material failure or fracture (Byrn, Zografis and Chen, 2017). Tensile strength represents the maximum stress that a material can withstand before the breakage as a result of stretch or pulling, and is considered as an essential mechanical property particularly for compression or tableting (Storey and Ymen, 2011).

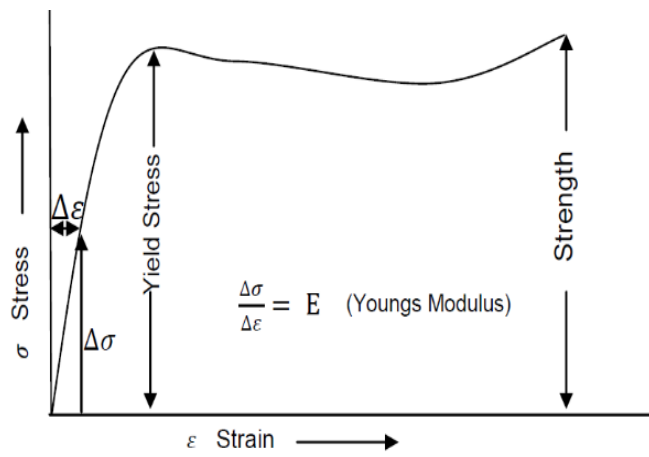


**Figure 2-6 Stress-strain curve (adapted from (Cyberphysics - Young's Modulus, 2009))**

Based on the stress-strain curve, materials can be classified as brittle, semi brittle, or ductile. A brittle material is a high elastic material which undergoes little or no plastic deformation before failure. A ductile, or tough material exhibits extensive plastic deformation before failure with no evidence of crack propagation. Semi brittle material is limited by local plastic flow whereby, cracks initiate at plastic zones and propagates elastically to the rest of the body (Kwan *et al.*, 2005).

### 2.3.2.1. Elasticity

Elasticity represents the ability of a particle or a body to return to its original shape or size upon the removal of the forces causing the deformation. Elasticity (the modulus of elasticity) is represented by the slope of the line in first region of the stress-strain curve. For material experiencing compression or tensile stress, the modulus of elasticity is referred to as Young's modulus, which can be expressed according to Equation 2.5. Where,  $\sigma$  and  $\epsilon$  represent stress and strain respectively (Byrn, Zografis and Chen, 2017).

$$E = \frac{\sigma}{\epsilon} \quad \text{Equation 2.5}$$

A material which exhibits a large modulus of elasticity and modulus of rigidity has a lower stiffness, for example, steel ( $E= 220$  GPa), Whereas, a material with a lower modulus of elasticity has high stiffness, for example, rubber ( $E= 0.002$  GPa).

Table 2-3 shows Young's modulus of some known materials including pharmaceuticals for example starch is more elastic than microcrystalline cellulose.

**Table 2-3: The value of the young's modulus of some known materials and pharmaceuticals** (Byrn, Zografı and Chen, 2017)

Material	Young's modulus (GPa)
Steel	220
Calcium carbonate	88
Glass	60
Calcium phosphate	48
Sorbitol	45
Lactose monohydrate	24
Spray-dried lactose	14
Theophylline	13
Acetaminophen	12
Caffeine	8.7
Aspirin	7.5
Ibuprofen	5.0
Microcrystalline cellulose	8-10
Stearic acid	3.8
Starch	3.7
High-density polyethylene	0.8
Rubber	0.002

For materials experiencing shear stress, the modulus of elasticity is referred to as the shear modulus  $G$  and is represented Equation 2.6.

$$G = \frac{\tau}{\gamma} \quad \text{Equation 2.6}$$

Where  $\tau$  is the shear stress and,  $\gamma$  is the shear strain.

The Young's modulus and the shear modulus can be related to each other using the formula shown in Equation 2.7.

$$E = 2(1 + \nu_p)G \quad \text{Equation 2.7}$$

Whereas,  $\nu_p$  is the Poisson's ratio,  $E$ , and  $G$  represent the axial strain and the transverse shear strain respectively. When the material is subjected to compress stress in one direction, it usually expands perpendicularly in two directions to the direction of compression. Whereas, if the material is stretched, it shrinks in the transverse direction, this is known as Poisson's effect (Byrn, Zografı and Chen, 2017).

**Table 2-4: The value of the shear modulus of some materials (Byrn, Zografi and Chen, 2017)**

Material	Shear modulus (GPa)
Steel	77
Glass	26
Polyethylene	0.13
Rubber	0.0003

#### **2.3.2.1.1. Evaluation of the Modulus of Elasticity**

The modulus of elasticity is experimentally determined using various compressibility tests performed on powder compacts with different porosity. The data is then extrapolated to zero porosity to infer for a single particle. However, several factors can adversely influence the mechanical testing process. A large amount of sample is required to make powder compact which poses a problem for the pharmaceuticals in the early development stage and makes specimen preparation costly for the expensive APIs. Furthermore, the data interpretation involves various assumptions which can contribute to unreliable results. For instance, it is assumed that the powder compacts have uniform porosity which might not hold as a result of the non-uniform distribution of stress or forces applied on the compact specimen (Olusanmi *et al.*, 2011). Also, the formation of the compacts might involve some degree of fragmentation of particles as well as plastic deformation depending on the nature of the pharmaceutical compound making the compact, since the powder compaction involves particle rearrangements, elastic and plastic deformation as well as fragmentation. The correlations employed for the data extrapolation do not account for the fragmentation and binding process results (Prasad, Sheen and Sherwood, 2001). A better approach is to carry out the mechanical testing on single crystals of the pharmaceutical, which can be achieved using a nanoindentation test. Nanoindentation requires a crystal with a size of at least 100 microns, and the specimen should encompass a flat surface to allow for applying the load of the indenter tip, which can be challenging.

#### **2.3.2.1.2 Evaluating the Elasticity from Molecular Structure.**

To determine the elasticity of a solid pharmaceutical compound, single crystals are required for this experiment. In some cases, it is difficult to grow single crystals of adequate size and quality. Alternatively, the elasticity can be evaluated from computational work at the molecular level since it is associated with the intermolecular forces. The elastic constant is evaluated from the compliance matrix  $S$  which is equal to the inverse of the stiffness matrix  $C^{-1}$ . For a single crystal, the elastic constants in  $I, j$  direction are presented as three orthogonal components of

Young's modulus can be derived according to Equation 2.8 and Equation 2.9 (Storey and Ymen, 2011).

$$E_x = \frac{1}{S_{11}}, \dots \dots E_y = \frac{1}{S_{22}}, \dots \dots E_z = \frac{1}{S_{33}} \quad \text{Equation 2.8}$$

$$E_{mean} = \frac{E_x + E_y + E_z}{3} \quad \text{Equation 2.9}$$

### 2.3.2.2. Plasticity

The plasticity of material is defined as the ability of a material to permanently deform plastically without breakage or rupture. This is an important property for pharmaceutical processing since it can dramatically impact processes such as grinding, compaction, and, extrusion. The extent of plasticity is referred to as ductility, and it can be quantified using Equation 2.10 and Equation 2.11 (Byrn, Zografis and Chen, 2017).

$$\%EL = \xi_{max} \times 100 \quad \text{Equation 2.10}$$

Where  $\%EL$  represents the percentage maximum elongation and  $\xi_{max}$  is the maximum strain due to plastic deformation.

$$\%AR = \frac{A_0 - A_f}{A_0} \quad \text{Equation 2.11}$$

Where,  $\%AR$  is the maximum area reduction before disruption,  $A_0$  and  $A_f$  represent the initial area and the area immediately after the fracture, respectively.

The plasticity of solid material is usually represented by the hardness, which is the resistance to plastic deformation. According to Mohs hardness scale, a material with a high value of hardness can scratch other materials for example diamond, as opposed to talc which encompasses a lower hardness value which classifies it at the lower Mohs hardness scale (Chamayou and Dodds, 2007; Ghadiri, Kwan and Ding, 2007).

Hardness can be evaluated experimentally using nanoindentation (Figure 2-7) of single crystals where indentation force is used to place compression stress on the surface of a single crystal aiming to create an indentation on the crystal's surface (Byrn, Zografis and Chen, 2017). The depression generated from indentation is measured, and the hardness is rescaled depending on the force applied and the extent of depression.

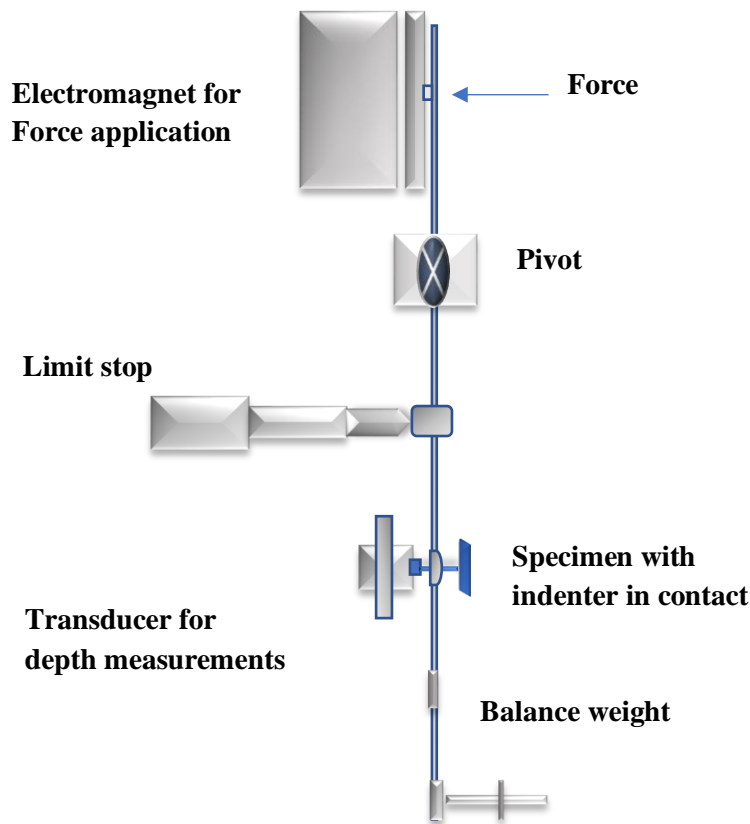


**Figure 2-7: Schematic diagram of nanoindentation (modified from (Arteaga *et al.*, 1993))**

Various methods of indentation are available, including Brinell, Rockwell, and Vickers. Vickers (Figure 2-8) is the most commonly used method since the Vickers hardness test can measure a broad hardness scale. The Vickers hardness test involves a diamond indenter with a square-based pyramid shape, of which the angles of the opposite faces are equal to  $136^\circ$ . The value of the hardness following this method is referred to as the Vickers hardness number (VHN), which can be calculated from the surface area of the indenter and the applied load following Equation 2.12.

$$VHN = \frac{2F \sin \frac{\theta}{2}}{L^2} \quad \text{Equation 2.12}$$

Where,  $L$  is the length of the indenter diameter, and  $F$  is the applied force. If  $\theta$  is set to  $136^\circ$ , the VHN It is expressed in Equation 2.13.

$$VHN = \frac{1.854F}{L^2} \quad \text{Equation 2.13}$$

*VHN* is characterised by its continuous hardness scale covering materials from very soft to very hard materials. For instance, the *VHN* of soft metal such as aluminium is equal 25 whereas that of a hard material such as hard steel is about 1000 (Byrn, Zografı and Chen, 2017).

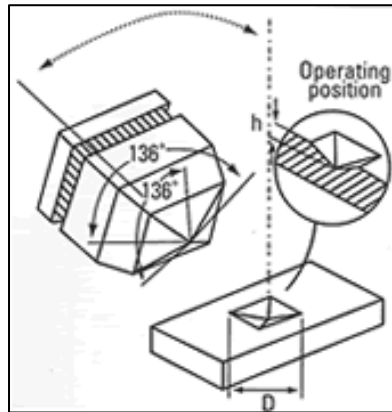


**Figure 2-8: Vickers hardness model (reprinted from (INSTRON, 2020))**

At the molecular level, the plastic deformation is associated with the breakage and formation of intermolecular interactions arising from hydrogen bonds, Van der Waals, and ionic interactions. For plastic material, large numbers of molecules are displaced to new positions upon the removal of stress. Therefore, for crystalline material the plastic deformation at the microscale level is associated with the motions generated around the crystal dislocations, grain boundaries, and long slip planes material (Byrn, Zografı and Chen, 2017).

Plastic deformation of material can contribute to the formation of regions of strain hardening and strain softening. At the strain hardening regions, as the stress increases the strain increases leading to a brittle fracture as the material shows resistance to plastic deformation, for example, in metals. Conversely, in the strain-softening regions, as the stress decreases the strain increases as a result of non-homogeneous yielding at some local area which promotes the formation of voids. Hence the material deforms plastically, for example, polymers (Byrn, Zografı and Chen, 2017).

### 2.3.2.3. Brittleness

Brittleness refers to the fracture of materials without experiencing plastic deformation. Examples of brittle materials include glass, ceramics, which tend to absorb a fraction of energy before fracture. Different researches have tried to develop different models to measure the brittleness. For instance, Law and Marshall established the brittleness index, which can be calculated according to Equation 2.14 (Ghadiri, Kwan and Ding, 2007). Where  $H$  is the hardness which can be obtained from indentation testing, and  $K_c$  is the critical intensity factor which can be determined from single edge notched beam and the nanoindentation test. Where,  $K_c$  is derived from the applied force, the geometry of the beam, and the geometry of the notch or the indenter. Table 2-5 shows values of the brittleness of some pharmaceuticals, for instance,

it can be seen that paracetamol and sucrose are much more brittle than avicel PH101 which makes the avicel a preferred excipient for compressibility.

$$\text{Brittleness index} = \frac{H}{K_c} \quad \text{Equation 2.14}$$

**Table 2-5: Value of brittleness index for some APIs and excipients** (Byrn, Zografi and Chen, 2017)

<b>Material</b>	<b>Brittleness index</b>
<b>Avicel PH0101</b>	0.22
<b>Lactose beta anhydrous</b>	0.33
<b>Ibuprofen</b>	0.34
<b>Sodium chloride</b>	0.45
<b>Aspirin</b>	0.56
<b>Adipic acid</b>	0.88
<b>Paracetamol, direct compressible</b>	1.08
<b>Alpha lactose monohydrate</b>	1.45
<b>Sucrose</b>	2.88
<b>Paracetamol</b>	3.65

### 2.3.3. Effects of Flows and Imperfections

Pharmaceutical drugs come with inherited imperfections such as impurities, irregularities, and dislocations that arise from pharmaceutical processing, including crystallisation. Crystal imperfections can be in the form of point defects, line defects, planar defects, and surface defects. Crystal imperfections and purities can have a significant impact on the crystal growth and particle size reduction process via the effects of slip and shearing, which can potentially influence the mechanistic behaviour of the pharmaceutical during milling (Storey and Ymen, 2011).

#### 2.3.3.1. Point Defects

Point defect refers to a foreign molecule (impurity) which becomes trapped within a regular site in the crystalline lattice. If the impurity molecule substitutes an original one, this is called substitutional point defects. However, if the space in the crystalline lattice remains unoccupied, it is referred to as a vacancy (Figure 2-9).

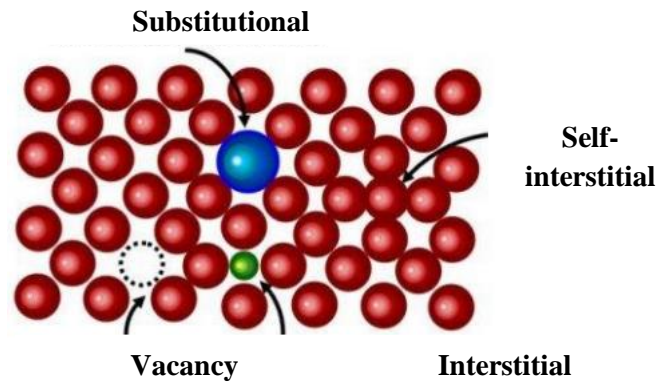


**Figure 2-9: Schematic shows point defect in a crystal (reprinted from (Science, 2016))**

### 2.3.3.2. Line Defects

Line defects or dislocations are defects occurring to the crystalline lattice, which can be found in three forms; edge dislocation, line dislocation, and mixed dislocation. Edge dislocation can be described as an additional half-plane of atoms introduced to the crystalline structure. The upper half of the plane consists of perfectly arranged atoms as opposed to the bottom half of the plane which incorporates atoms that are displaced from the original positions. When the crystal is subject to stress, the molecules along with the slip plane propagate over the dislocation line. Thus, the dislocation is a linear defect and coincides with the edge of the introduced half-plane (Hull and Bacon, 2011). Figure 2-10 shows a schematic of an edge dislocation motion during plastic deformation. The row of the bonds is ruptured at point A, and rebound with the introduced half-plane, here the dislocation is set to move by one lattice spacing as this process is replicated, eventually, the dislocation shifts through the entire crystal and leads to the displacement of both the upper and the lower parts of the crystal by one lattice spacing with respect to each other. This process of displacement is described as a slip. Despite that the movement dislocation is small, the displacement of multiple dislocations throughout the crystal can contribute to significant plastic deformation. Since individual row of bonds is broken at a time at each stage instead of all the bonds across all the layers, thus, the required stress to cause a plastic deformation is lower (Hull and Bacon, 2011; Roberts, 2016). The movement of dislocations in this manner is described as glide.

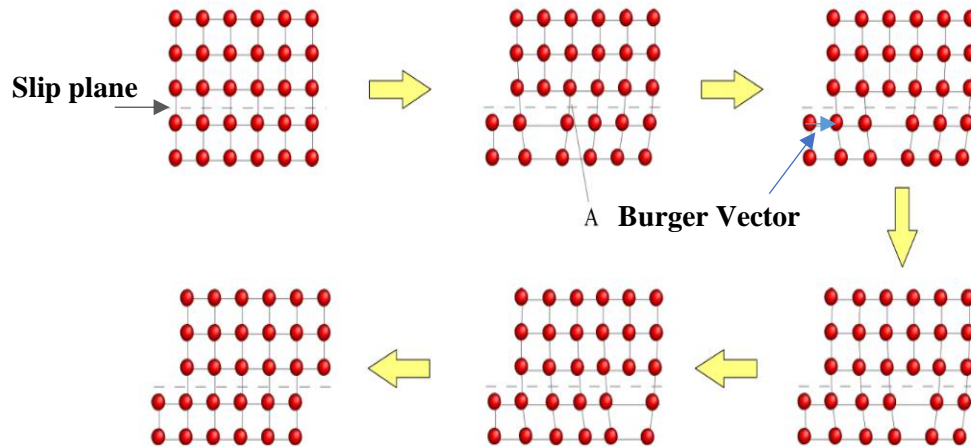


**Figure 2-10: Deformation generated by an edge dislocation moving through the crystal (reprinted from (Roberts, 2016))**

The dislocation is characterised by three components, the slip plane, the line direction, and the Burgers vector. The slip plane is where the dislocation is moving. The slip plane incorporates a line direction and a burger vector of the dislocation. The line direction is the line of distorted material along the edge of the introduced half-plane of atoms. The burger vector controls the slip direction. The magnitude of the burger vector is one lattice spacing. In the edge dislocation, the Burger vector and line direction are perpendicular to each other. Whereas, in screw dislocation, the burger vector and the line direction are parallel to each other. In a screw dislocation, one part of the plane moves to the right the other part moves to the left (Figure 2-11 b). Mixed dislocations are more complex compared to the edge and screw dislocations, in this type of dislocation, the angle between the burger vector and the line direction is in the range from 0 to 90° (Roberts, 2016).

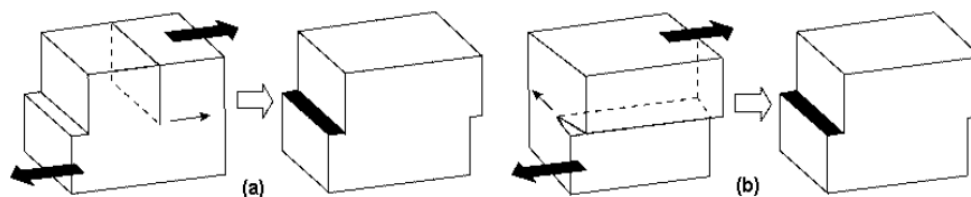


**Figure 2-11: Deformation caused by (a) edge and, (b) screw dislocation motion in a crystal (Babu, 2008)**

### 2.3.3.3. Planar Defect

Planar boundaries arise from changes in the lattice orientation and involve twin boundary, tilt boundary, and grain boundary (Figure 2-12). Twinning occurs as a result of deformation, which causes the lattice volume to transform into an orientation mirror-symmetrical to the parent lattice. When dislocations of the same polarity aligned, they formed a tilt boundary. This

generates small energy on rotation and causes the parent lattice to split into sub-grains. Twist boundaries are similar to tilt boundaries; however, they are twisted in a normal direction boundary plane. Grain boundaries are formed when two different phases or lattices share an interface plane but have different orientations (Babu, 2008).

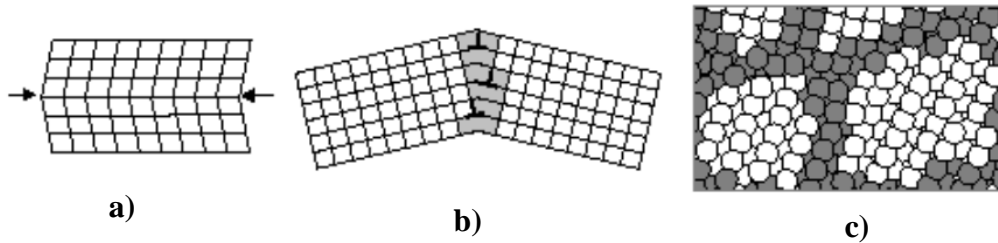


**Figure 2-12: a) twin boundary, b) tilt boundary and, c) grain boundary (Babu, 2008)**

#### 2.3.3.4. Plastic Deformation

Plastic deformation occurs as a result of layers of atoms sliding past each other. The plastic flow in crystalline solid is attributed to the movement of dislocations, including edge and screw dislocations, and planar defect. The motion occurs in the crystalline lattice by slip mechanism across specific directions (Perry, Green and Maloney, 1997). For a material experiencing plastic deformation, a microscopic examination of its surface shows that the sample exhibits lines and steps which indicate plastic deformation. Each step comprises a series of smaller steps that arise from the motion of the planes of atoms sliding past each other (Hull and Bacon, 2011; Roberts, 2016). The plastic deformation contributes to the formation of ductile materials. The sliding process comprises of bonds breaking between neighbouring layers, followed by the displacement of these layers and finally, the formation of new bonds between the layers as shown in schematics a, b, c, and d respectively in Figure 2-13.

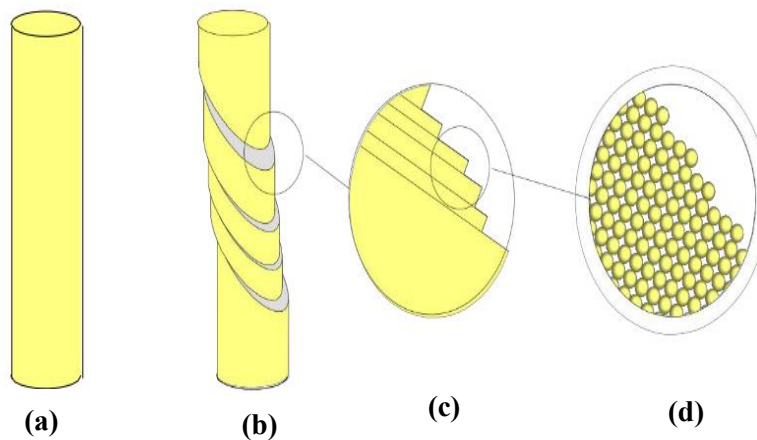


**Figure 2-13: Schematic illustrating the nature of deformation by slip (reprinted (Roberts, 2016))**

The dislocation can take place in the form of glide or climbs (Figure 2-14). (Bandyopadhyay and Grant, 2002; Hull and Bacon, 2011). Glide dislocation is the most common dislocation where the Burgers vector and the dislocation line tend to align in the same slip plane; this process is referred to as glissile. The glide dislocation occurs at high temperature in a direction that is tangential to slip plane which enables the preservation of interplanar spacing between the plane. Once the system encounters higher temperature at a longer time scale, the dislocation tends to move out of the slip plane, this is known as climb dislocation which renders the dislocation and the Burgers vector perpendicular to each other. The climb dislocation that moves from one plane to the other is known as jog dislocation, whereas, that involving step is referred to as kink dislocation (Figure 2-15).

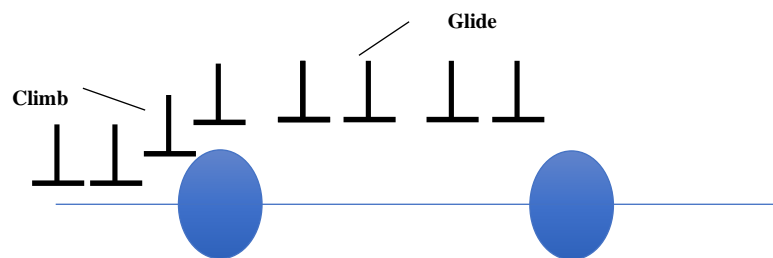


**Figure 2-14: Schematic shows dislocation glide and climb dislocations (modified from (Yuan *et al.*, 2018))**

The extent of the plastic deformation of a material is associated with the strength of the intermolecular bonds and the width of the dislocations. An example of the application of plastic deformation is manifested in the process of work hardening. Whereby, an increase in the dislocation density limits the flow of deformation, which leads to material straightening and ultimately work hardening. For example, when a paper clip is subjected to stress it bends, during this process, the dislocations move towards the bending tip and become locked, which hinders further movement. Any additional stress-energy is dissipated through breakage or fracture mechanism (Natlson, 2015).

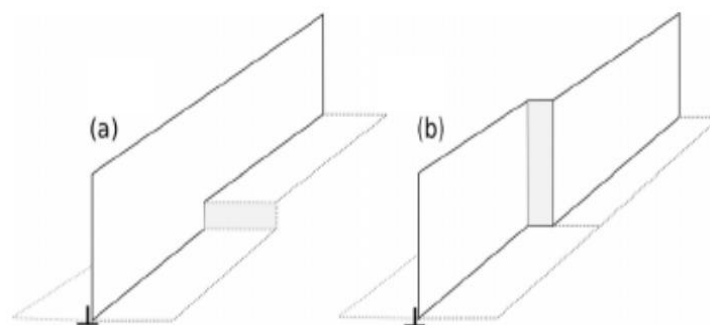


**Figure 2-15: Schematic shows jog and king dislocations (reprinted from (Babu, 2008))**

#### **2.3.4. Effect of Crystal Structure on Mechanical Properties**

As was mentioned earlier, pharmaceutical materials exist in a wide range of solid forms, including crystalline, amorphous, polymorphs, solvates, and hydrates. Each of these solid forms exhibits its unique internal structure and mechanical properties. The material internal structure involves molecular structure, molecular interactions, molecular conformations, and molecular mobility. Hydrogen bonds and Van der Waals are the dominant forces that hold the crystal together and contribute to the formation and backing of the crystalline lattice. The crystalline form of the pharmaceutical compound is usually harder and possesses higher elasticity and lower plasticity compared to the amorphous form. The crystal rigidity in the former is attributed to the three-dimensional ordered crystal structure involving tightly interacted molecular networks and sometimes physical interlocks. Whereas, the latter form exhibits a liquid-like structure which allows for molecular mobility. Therefore, the existence of amorphous compound in pharmaceutical formulation promotes plastic deformation, which facilitates the compressibility of tablets. For instance, lactose monohydrate is an excipient employed for tableting. Despite that crystalline lactose monohydrate is brittle in its nature, spray-dried lactose monohydrate is amorphous which makes it desirable for direct compressing due to its mechanical properties such as its high tensile strength (Storey and Ymen, 2011; Byrn, Zografi and Chen, 2017).

The effect of solid forms on the mechanical properties is not only manifested in the crystalline and the amorphous samples but, also in other crystalline forms (polymorphs) owed to the difference in their crystalline structure. For instance, Sulphamerazine is a pharmaceutical excipient which comprises of two polymorphs form I and form II. Form I polymorph displays high plasticity, which makes it commonly desirable in tablet compressing due to its high tensile strength. The mechanical behaviour differences in these two polymorphs are attributed to the difference in their inner crystalline structure. Since, form I, exhibits slip planes which favour compressibility and compatibility needed for tablet compression as opposed to form II (Sun and Kiang, 2008). Moreover, the presence of water molecules within the crystal structure has a variable impact on the pharmaceutical compound, for instance, Magnesium stearate exists in four hydration states; Magnesium stearate anhydrous, monohydrate, dihydrates, and trihydrate. The dihydrates form is chosen over other forms in a tablet formulation as a lubricant. Since, the dihydrates form contains water molecules that are situated between fatty acid layers (Figure 2-16) which are believed to promote shearing in the event of compression (Ertel and Carstensen, 1988).

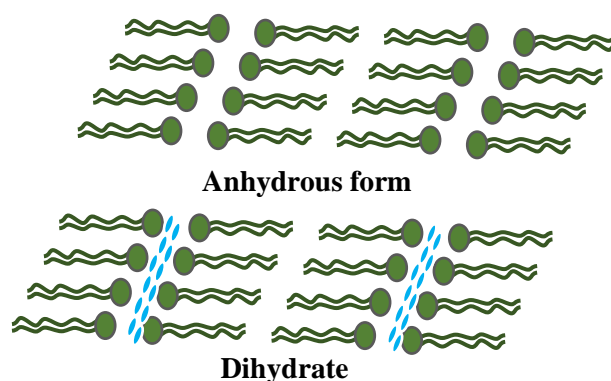


**Figure 2-16: Schematic shows crystalline packing of Magnesium steroid anhydrous and dihydrates form (modified from (Byrn, Zografis and Chen, 2017))**

The elastic properties of the organic crystal reflect the forces between the molecules in the crystal. For instance, the elastic properties represented by Young's modulus value were determined from the molecular modelling of the of primidone form A, form B and, aspirin. It was found that the Primidone has higher Young's modulus compared to Aspirin, which was attributed to variable hydrogen bonds motifs in the crystal structure of the two compounds. Whereby, Aspirin molecules encompass carboxylic group with one hydrogen bond donor and a nearby one hydrogen bond acceptor forming dimers (Figure 2-17), whereas, Primidone has two hydrogen bonds and two hydrogen bonds acceptors per molecule (Figure 2-18). Similarly, Primidone form B has a higher Young's modulus value compared to form A which is associated with the extended hydrogen bonds present in form B which contributes to a large resistance to the forces imposed on the extended hydrogen bonds motifs (Storey and Ymen, 2011).

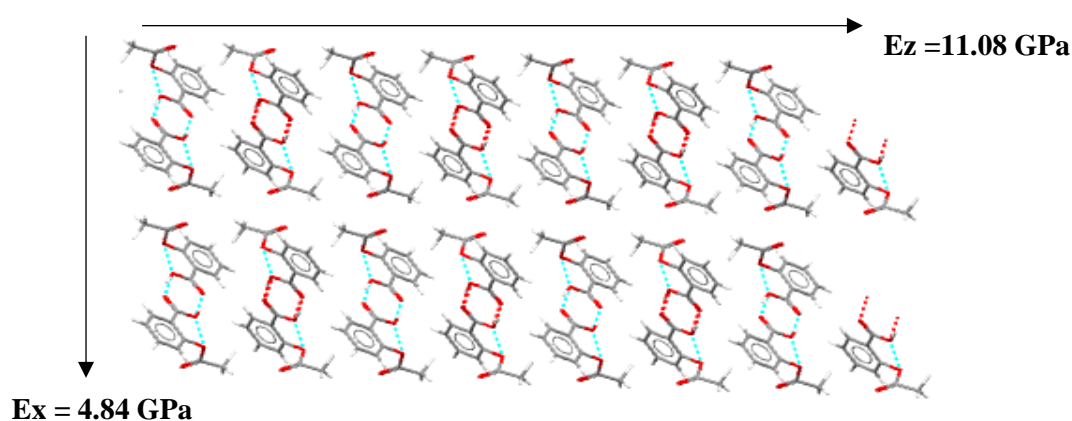


**Figure 2-17 The crystal structure of Aspirin along with the modelled Young's modulus in x and y directions, (modified from (Storey and Ymen, 2011))**

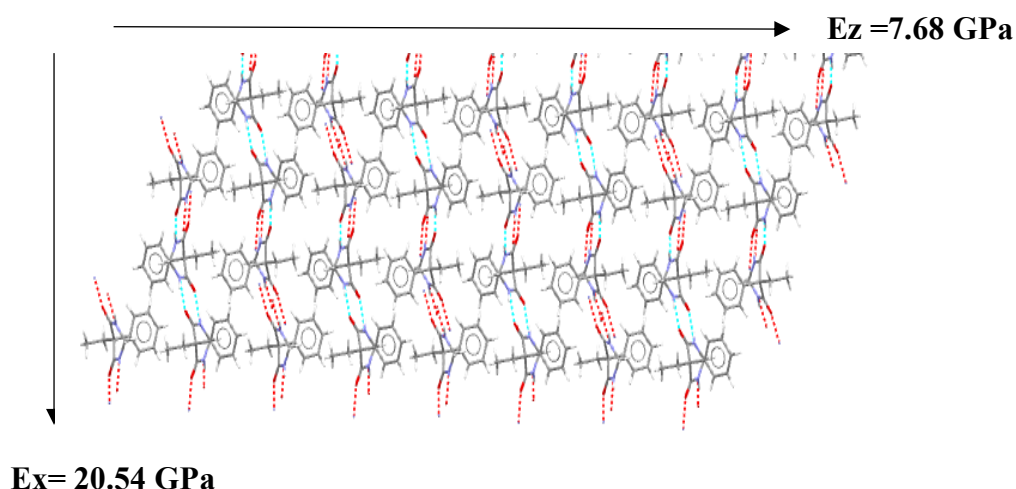


**Figure 2-18: The crystal structure of Primidone A along with the calculated Young's modulus in x and y directions, (modified from (Storey and Ymen, 2011))**

### 2.3.5. Particle Shape and Size

Particle size and shape of the solid pharmaceutical impact on the bulk performance of the powder (i.e. flowability) and influence the dissolution rate and the stability of suspensions. For instance, particles with greater circularity flow better than particles with needle shape (Hogan and Buckton, 2000), and particles of smaller sizes have a larger surface area available for dissolution. The particle size is related to the particle shape and the surface area (Bauer, 2009). According to the International Council for Harmonisation (ICH), the particle can be formed by six basic crystal shapes (habit) as shown in Figure 2-19 (Byrn, Zografis and Chen, 2017). The crystal habit is controlled by its internal crystal structure and the collective growth of specific faces. The habit of the crystals is strongly influenced by the crystallization conditions (Storey and Ymen, 2011). The crystallisation involves various underpinning processes that can be subdivided into two main stages, nucleation and growth. The first step is driven by the superstition process, where, stable clusters of crystallised material ( of size from 1 nm to 10 nm) are formed as a result of nucleation. The second stage involves a stable growth of the formed clusters which tend to develop into fully faceted 3D crystals (Docherty *et al.*, 1991). The mode of crystal growth occurs through the surface step motion, where, the surfaces of crystals tend to be adsorbed onto mono-molecular compound within the growth environment at the expense of a heteromolecular compound which is usually a solvent and/or impurities (Hammond, Pencheva and Roberts, 2012).

The crystal habit or morphology is controlled by the relative growth rate, and the deposition of each plane in the crystal. The slowest growing face is the most morphologically important face of the crystal, whereas, the smallest face is the one manifesting the fastest growing rate (Li *et al.*, 2013). The growth rate of the crystal is primarily dependent on the strength of the bonds of the faces deposited on various crystal surfaces which, in turn, depends on the internal structure

of the crystal. This implies that any factor influencing the growth rate can ultimately alter the crystal habit. The external factors include the type of solvent used, the degree of supersaturation, the temperature, the impurity, the concentration, and drying techniques employed during the crystallisation process (Berkovitch-Yellin, 1985). The relationship between the external morphology, the internal structure, and symmetry of the crystal has long been the interest of scientists (Berkovitch-Yellin, 1985). However, determining the crystal habit remains a problem in the theory of crystal growth due to the degree of complications associated with this process (Abramov, 2016). Chikhalia and co-workers stated that succinic acid crystals exhibiting a plate-like morphology are more prone to crystalline disorder during milling in corresponding to those exhibiting needle morphology (Chikhalia et al., 2006). Nevertheless, this varies dependent on the type of mill employed during the process of milling; since plate-like particles were more prone to breakage in a ball mill compared to the fluid jet mill. There is a lack in the literature about milling particles of different sizes and shapes.

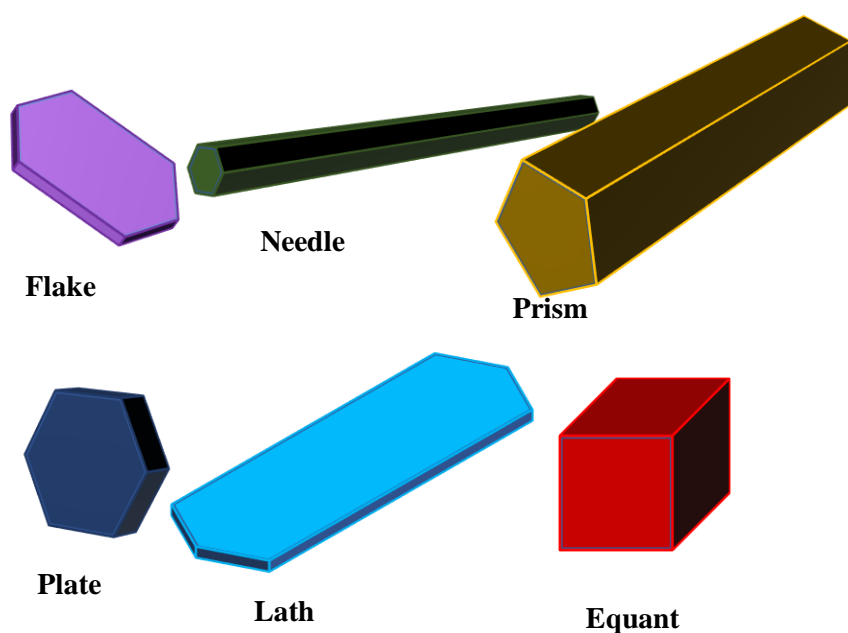


**Figure 2-19: The basic shapes of a crystal/particle (modified from (Storey and Ymen, 2011))**

## 2.4. Mechanochemistry

When a solid compound is introduced to high energy from the mill, its chemical, physical and crystalline structure may vary considerably as a result of compression, shear, or friction from the mill. As was mentioned earlier, any physicochemical changes arising from the excessive energy during milling are referred to as mechanochemistry (Snow, Richard H. Luckie, 1979; Chieng *et al.*, 2009; I. Colombo, Grassi and Grassi, 2009; Takacs, 2013; Descamps and Willart, 2016). Processes covered by mechanochemistry include accumulation of defects,

amorphisation, the formation of metastable polymorphs, and chemical reactions (Boldyrev and Tkáčová, 2000). Mechanochemistry can yield positive outcomes in the pharmaceutical industry, such as increasing the dissolution rate of the poorly soluble drug. Since the rate of dissolution of amorphous is much greater than its crystalline counterpart, however, this comes on the cost of the material stability.

Mechanochemistry can be considered as multiple steps process arising from different energetic parameters and different amount of energy accumulated in the activated solid in each step. Multiple milling parameters consider controlling, which can result in a variable impact on the milled product properties. Table 2-6, summarises the mechanical treatment of some pharmaceuticals, the produced mechanochemistry and, the potential impact on the product performances.

**Table 2-6: Table summarising the mechanical treatment, mechanochemistry and the influenced properties of some pharmaceuticals (modified from (Abouhakim, 2016))**

Material	Type of mechanochemistry	Mechanical treatment conditions	Influenced properties/performance	Ref
<b>Budesonide</b>	Phase transition from crystalline to amorphous	PBM; room temp; zirconium vessel = 45 cm <sup>3</sup> ; 7 balls, D =15mm; t = 15 hr	Enhanced solubility and bioavailability	(Descamps <i>et al.</i> , 2007)
<b>Indomethacin</b>	Amorphous formation increases with time of milling	Cryomilling in MM301 B.M., vessel = 25 ml; 6 balls-D = 9 mm; stainless-steel vessel; frequency = 30 Hz; t = 15, 30, 60, 120, 180 and 240 min; in immersed $N_{liquid}$ for 3 min.	Enhanced dissolution rate	(Karmwar <i>et al.</i> , 2012)
<b>Indomethacin</b>	Formed a stable amorphous at 4°C which converted to a metastable crystalline at 30°C	Agate centrifugal B.M. . 10 balls, D =10 mm, 20 balls-D=15 mm, 4 balls- D =20 mm; speed = 200 rpm; at 4 °C & 30°C ; t =10 hr. stored at -20°C	Enhanced dissolution rate	(Otsuka, Otsuka and Kaneniwa, 1994)
<b>Indomethacin</b>	100% amorphous formation within 60 min of milling	Cryogenic impact SPEX mill; stainless steel; 10 cycles per second; 2 min grinding 2 min cooling; stored at -20°C	Enhanced dissolution rate	(Crowley and Zografi, 2002)

<b>Griseofulvin</b>	Reduction in crystallinity as a result of defects, increase in surface energy	SPEX cryogenic mill; t = 1, 5, 10, 30 min; a pre-cooling cycle of 2 min and milling cycles of 5 min separated by cooling intervals of 2 min. stored over phosphorous pentoxide under $-30^{\circ}\text{C}$	Increase in surface cohesion	(Elamin <i>et al.</i> , 1994)
<b>Carbamazepine dihydrate</b>	The phase transition to the anhydrous alpha form	B.M. for 15 to 60 min. Compression, Single punch machine	Reduced compressibility	(Lefebvre <i>et al.</i> , 2008)
<b>Griseofulvin Felodipine</b>	Reduction in crystallinity as a result of defects, increase in surface energy	A SPEX cryogenic impact mill; t = 10 min; stainless steel; 2 min grinding/2 min interval; cooled in $N_{liquid}$ ; frequency = 10 Hz (20 impacts per second)		(Chamarthy and Pinal, 2008)
<b>Sulfathiazole</b>	Polymorphs transition III $\rightarrow$ I and I $\rightarrow$ III	PBM; BPR 20:1; D = 8 mm and d = 3-5 mm; t = 1, 40, 90, 180 min; Speed = 200 & 600 m/s <sup>2</sup>	Enhanced solubility. Solubility of form I is better than form III	(Shakhtshneider and Boldyrev, 1993)
<b>Carbamazepine</b>	Crystalline phase transition from beta to alpha the most stable form. Phase transition from dihydrate to the alpha form	B.M. for 15 to 60 min. Compression Single punch machine	Reduced compressibility/ enhanced stability	(Lefebvre <i>et al.</i> , 2008)
<b>Griseofulvin</b>	Continuous increase in crystalline disorder.	SPEX cryogenic impact mill, t = 1, 5, 10, or 30 min, with a pre-cooling cycle of 2 min; 5 min grinding/2 min cooling; cooled in $N_{liquid}$ . stored over phosphorous pentoxide under $-30^{\circ}\text{C}$		(Otte and Carvajal, 2011)
<b>Ketoconazole</b>	Reduction in crystallinity	SPEX cryogenic impact mill, t = 1, 5, 10, or 30 min; with a pre-cooling cycle of 2 min; 5 min grinding/2 min cooling stored over phosphorous pentoxide under $-30^{\circ}\text{C}$	Increase in surface cohesion	(Otte and Carvajal, 2011)

<b>Cephalexin CEX</b>	Transition from crystalline to non-stable amorphous at 20°C and to a stable amorphous at 35°C and humidity 66%).	BM; 350ml; 35°C and 20°C; D & N. balls= 10 mm*20, 15 mm*10, 20 mm*4; speed = 200 rpm).; stored at -20°C, milled at 35°C and 20°C		(Otsuka Makoto and Kaneniwa Nobuyoshi, 1983; Otsuka, Otsuka and Kaneniwa, 1994)
<b>Brivanib alaninate</b>	Large increase in surface energy as a result of amorphous formation.	A Retch Cryomill; 50 ml, D = 25 mm; N. balls =1; milling cycle n = 1, 3, 6, 9, 21 at 5 Hz; t = 40 s and milling for 25 Hz for 10 s; cooled in <i>N<sub>liquid</sub></i> -70 C	Enhanced dissolution rate	(Shah <i>et al.</i> , 2015)
<b>Ampicillin trihydrate</b>	Breakdown of crystal lattice rupture of sensitive $\beta$ - lactam as the water molecules freed	Automated mortar (15min to 3 h)	Reduced compressibility	(Takahashi <i>et al.</i> , 1984)
<b>Chloramphenicol palmitate CPP</b>	Metastable crystalline forms B and C converted to an unstable amorphous form which converted to a stable crystalline form A by nucleation at 20°C.	Agate BM; capacity 350; D &N. of balls (10 mm* 20,15 mm*10,20 mm*4); 200 rpm.; stored at -20°C); Milled at 20°C, t = 150min	Enhanced stability	(Otsuka, Otsuka and Kaneniwa, 1994)

### 2.4.1. Milling Conditions Related to Mechanochemistry

#### *Type of Mill*

Ball mills generate a larger amount of energy compared to other mills such as fluid jet mills. Hence, are responsible for most of the mechanical activation and mechanochemistry. Example of materials that experience phase transition during milling by mean of ball mill are Sulfathiazole (Shakhtshneider and Boldyrev, 1993) Cephalexin (OTSUKA and KANENIWA, 1983), Chloramphenicol palmitate CPP, Indomethacin (Otsuka, Otsuka and Kaneniwa, 1994), Carbamazepine (Lefebvre *et al.*, 2008), Caffeine (Mazel *et al.*, 2011), Fostedil (Takahashi *et al.*, 1985) and Budesonide (Yu, 2001; Dudognon *et al.*, 2006), etc.

### ***Milling Duration***

It is important to control the period of milling since, it can induce significant change on the milled product. For instance, Indomethacin, an anti-inflammatory drug, exhibits multiple polymorphs, including  $\gamma$ ,  $\alpha$ , and  $\delta$ . Milling of these polymorphs from 4 min to 60 min led to an increased amount of amorphous up to 100% observed at longer milling duration. This was confirmed by a single broad X Ray-Powder Diffraction (XRPD) peak (Crowley and Zografis, 2002), as shown in Figure 2-20. Another example is the milling of Budesonide (an anti-inflammatory drug) which took 15 hr of milling to show a complete transformation from crystalline to amorphous which was identified by a single broad XRPD peak and, by the emerging of the glass transition temperature peak which was detected by DSC Figure 2-20. The amorphisation of Budesonide was linked to the generation of a large number of defects with longer milling periods (Descamps *et al.*, 2015). Sulphathiazole is a microbial drug found in three polymorphs. This pharmaceutical manifest an exceptional mode of phase transition when milled at different times. In the first 10 min of milling, Sulphathiazole room temperature stable form III started to transform into a high temperature (at 103°C ) stable form I. Interestingly, milling for 90 min caused a reverse phase transition with the restoration of form III. Whereas, milling for 3 hours produced a repeated phase transition (III  $\rightarrow$  I and I  $\rightarrow$  III). The former phase transition was explained by the fact that the energy of the mill creates defects that act as nucleation sites to promote the growth of form I at a higher temperature. Whereas the latter phase transition caused some confusion which leads to the assumption of the presence of an intermediate amorphous (form I) which recrystallizes back to crystalline phase (form III). (Shakhtshneider and Boldyrev, 1993; Brittain, 2002; Descamps and Willart, 2016).

In addition to phase transformation such as polymorphism or amorphisation, milling can be associated with chemical transformation. For example, milling of Lactose monohydrate, Citric acid monohydrate (Zielke, 1985) and, Ampicillin trihydrate (Takahashi *et al.*, 1984) caused a partial dehydration and structure disordering. Milling can contribute to changes in the molecular structure of the drugs which alters the physicochemical properties of the substance. For example, Piroxicam is used as a non-steroid anti-inflammatory agent that is poorly soluble in water which implies that it has a lower bioavailability. Milling of this compound led to an increase in the drug solubility four times higher compares to the non-milled compound, as a consequence of the changes produced at the molecular level (Shakhtshneider, 1997).

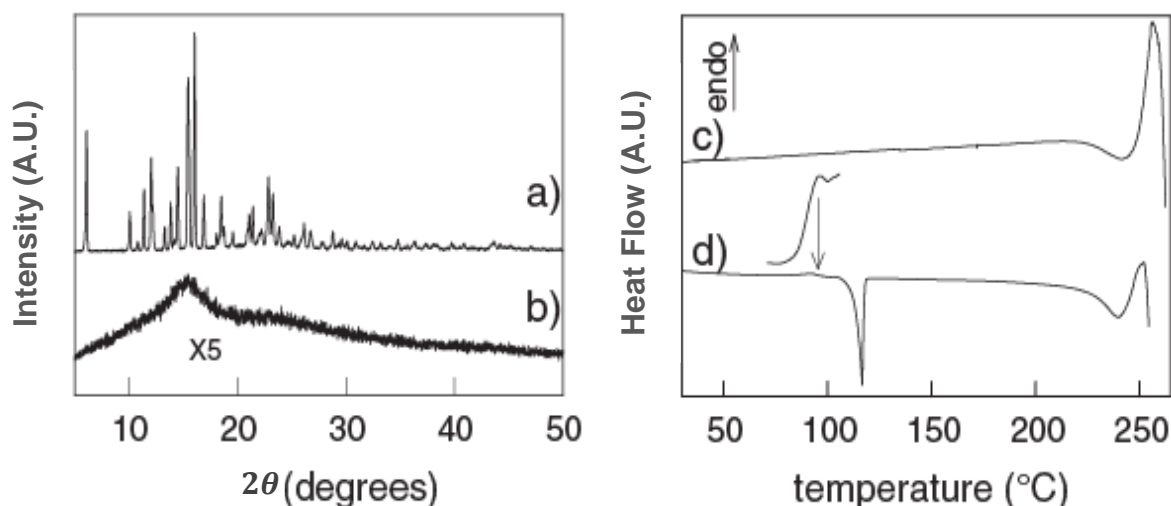


**Figure 2-20: X-ray powder diffraction patterns for budesonide rerecorded at room temperature before milling (a) and after 15 h milling process (b). DSC heating curves of crystalline budesonide before milling (c) and after 15 h milling process (d), the inset depicts a near view of the glass transition domain appearing in MDSC reversible heat flow (reprinted from (descamps et al. 2007))**

### *Temperature of Milling*

Milling temperature is considered one of the main thermodynamic properties that require considerable attention since it can impact the stability of the formed phase (Otsuka, Otsuka and Kaneniwa, 1994). For instance, milling of Cephalexin (antibiotic) at 20°C generated a non-stable amorphous which converts back to crystalline form. However, when Cephalexin was milled at 35°C and humidity below 66%, it forms a stable amorphous compound (Otsuka, Otsuka and Kaneniwa, 1994). Similarly, when Chloramphenicol Palmitate CPP metastable crystalline form B was milled at 20°C, CPP transformed to unstable amorphous form C which immediately crystallised to a stable crystalline form A. The stability of the formed amorphous is related to various factors including the glass transition temperature  $T_g$ , and crystallisation temperature  $T_c$  which are explained later (see section 3.2.2.). It was reported that the milling temperature impacted on the surface area, surface cohesion and on the surface energy of Brivanib alaninate. Milling of Brivanib alaninate in cryomill (milling at very low temperature) generated a product with higher surface area, higher surface energy, and higher cohesion compared to milling at ambient temperature. This was explained by the presence of the amorphous layer, which is thermodynamically stable at a lower temperature (Shah *et al.*, 2015). Another impact of the temperature of milling is reflected in the degradation of the product; hence it is important to monitor the milling temperature.

### ***The diameter of Milling Media***

The variation of the diameter of the milling media (i.e. ball of the mill) can contribute to a significant change in the intensity of milling. Milling media with larger diameter implies that the milled compounds have a larger area of contact with the balls, which allows more energy transfer. For example, when Sulphathiazole was milled with a larger diameter ball (8mm), the rate of phase transition increases as opposed to milling with a smaller diameter (3mm) (Shakhtshneider and Boldyrev, 1993).

### ***Milling Speed***

The speed of the mill has a direct impact on the produced energy. Milling at large speeds generates a larger amount of energy. Part of the energy is used for size reduction; however, a greater amount of energy can lead to lattice disruption, phase transition, and heat generation. For instance, milling Sulphathiazole at an acceleration of  $600 \text{ m/s}^2$  led to a rapid phase transition within a shorter time (40 – 50 min). However, milling at lower acceleration ( $200 \text{ m/s}^2$ ) results in a slower phase transition which takes approx. 180 min (Shakhtshneider and Boldyrev, 1993).

### ***The Energy of the Mill***

Different types of mills generate different amounts of energy due to the change in their material, number of balls, capacity, speed, etc. The impact of different mills energies was investigated by Chauruka, who reported that planetary ball mill generated larger microstructural disorder for Gamma Alumina as opposed to vibratory mill (Chauruka, 2015). For instance, Indomethacin was milled with vibratory Retsch mill (Karmwar *et al.*, 2012) and vibratory SPEX mill (Crowley and Zografi, 2002). Amorphous Indomethacin immersed at 180 min and 60 min when milled using Retsch and SPEX mills respectively. Despite that the principle of milling is similar in the two mills, SPEX mill introduces more energy through shear due to the curvature present in its vessel which allows the balls to move upwards and experience more contact with powders compared to Retsch mill (Chauruka, 2015). However, this cannot be taken as conclusive due to the lack of information about other parameters such as the speed of the mills and the number of milling media. There is insufficient work reported in the literature with regards to the impact of milling of materials at different energies, particularly pharmaceuticals.

## **2.4.2. Mechanism of Mechanochemistry**

The mechanism of mechanochemistry is not well understood due to the complication and diversity of the reaction types, reaction conditions, as well as the inhomogeneous nature of the solid-solid materials. This is attributed to the difficulty of the direct observation of the material encountering the mechanochemical process in microscopic and molecular levels (James *et al.*, 2012). Other constraints include the lack of studies and limited literature covering

mechanochemistry, particularly for organic materials and pharmaceuticals. Few models and theories were developed to describe the process of mechanochemistry but have limited application. Some of these models found applicability in areas such as inorganic materials including metals and metal oxide (I Colombo, Grassi and Grassi, 2009; Boldyreva, 2013; Tan and García, 2019). Among the earliest developed theories are the hot spot theory and the magma plasma theory. The hotspot theory is based on the friction between two surfaces sliding against each other. The surface friction contributes to plastic deformations and rises in local temperatures at the micro-region (within ca.  $1 \mu\text{m}^2$ ). The temperatures are believed to reach  $1000^\circ\text{C}$  for short periods ( $10^{-3} - 10^{-4}\text{s}$ ). For more brittle materials, Hot spot is suggested to occur at the tips of the propagating cracks causing few orders of magnitude temperature rise for a short time period, as was experimentally proven in inorganic compounds (for instance in metals) (James *et al.*, 2012). The magma plasma theory is related to the effects of the impact stress instead of lateral friction process. In this model, (Figure 2-21) it is assumed that a great amount of energy and energetic species including free electrons are ejected at the impact zones (magma sites) accompanied with an increase in local temperature which can exceed  $10^4 \text{ }^\circ\text{C}$  (Baláz, 2008).

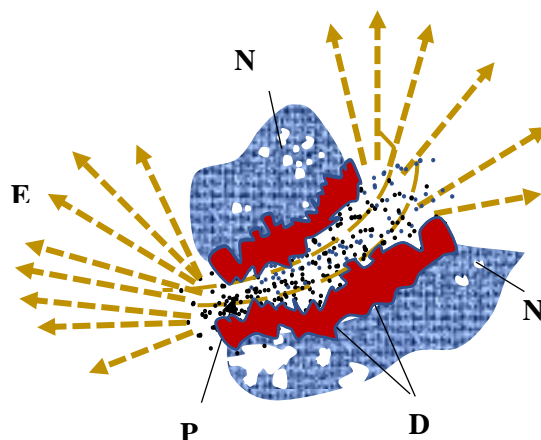


**Figure 2-21: Schematic shows the magma-plasma model, where; E – exo-electrons, N – undeformed solid, D – highly deformed surface layer, P – plasma (modified from (Baláz *et al.*, 2013))**

The hotspots and the magma zones are assumed to be the primary sites at which mechanochemical reactions are activated. However, these mechanisms do not seem practical for organic systems provided that the elevated temperatures can contribute to the decomposition of these types of materials. Nevertheless, the absence of the decomposition can suggest that these phenomena are occurring very shortly and/or at the too localised zone to be the primary site. Nevertheless, it was proposed that these zones can lead to the generation of frictional heating which dissipates in the form of energy (Boldyrev, 2006; James *et al.*, 2012; Boldyreva, 2013).

One of the most comprehensive models that describe the process of mechanochemistry of organic and inorganic compounds is the pulse model, in this model, when the solid is subjected to a successive series of mechanical forces (pulses), variable stress fields, and their relaxation form at regular intervals. The relaxation process involves variable physical or chemical changes to the solid manifested in the different relaxation channels including heat liberation, the formation of defects, formation of amorphous as shown in (Figure 2-23) (Boldyrev, 2006). The type of relaxation channel depends mainly on the type of mechanical loading (for instance, energy inputs and the loading rate) and the physical properties of the material.

In addition to the solid-solid system, the mechanism of mechanochemistry of solid-liquid and solid-gas systems was explained using mass transfer and molecular diffusion models. In these systems, the mechanochemistry is suggested to be driven by the surface migration of the solvent from the inner crystals or, the molecular diffusion of gas into the surface of the solid. Example of these systems include cocrystals, solvates, hydrates, and solid solutions which undergo mechanochemistry during the process of milling (Friščić and Jones, 2009).

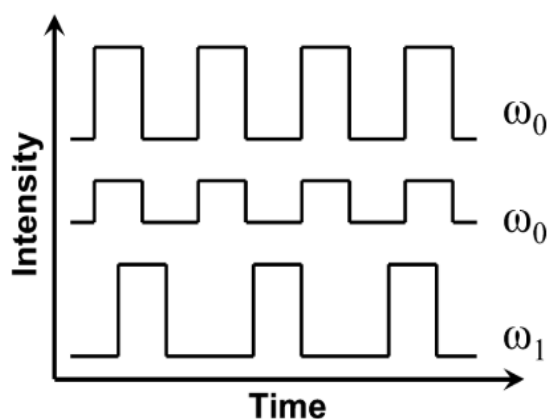


**Figure 2-22: Mechanical pulses varies by varying the intensity or frequency of the pulse (reprinted (Boldyreva, 2013))**

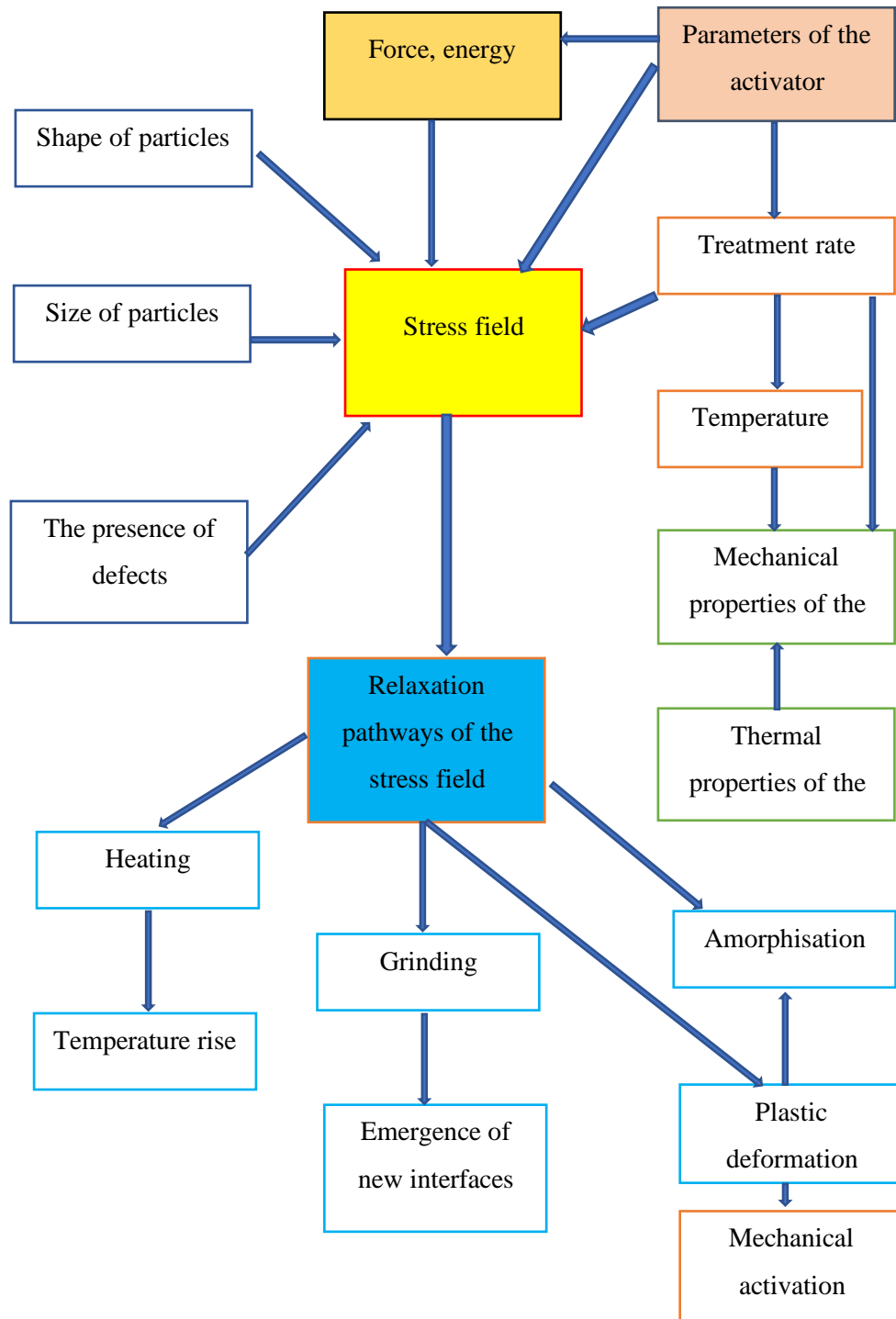


**Figure 2-23: Different relaxation channels of the stress field (modified from (Boldyrev, 2006))**

In 1979, the German mechanochemists established the concept of hierarchy to describes the duration (relaxation time) of each relaxation process (excitation state). The main relaxation processes such as fracture, defects, or dislocations exhibit longer relaxation times, as shown in

Table 2-7. These main excitation states might incorporate various temporary sub-states which occur at much shorter times.

**Table 2-7: Excitation processes and their relaxation times occurring in mechanically activated solids derived from the hierarchy model (Baláž, 2008)**

Excitation process	Relaxation time
Impact process	$> 10^{-6} s$
Triboplasma	$< 10^{-7} s$
Gaseous discharge	$\sim 10^{-7} s$
Hotspots	$10^{-3} - 10^{-4} s$
Electrostatic charging	$10^2 - 10^5 s$
Emissions of exoelectrons	$10^{-6} - 10^5 s$
Triboluminescence	$10^{-7} - 10^3 s$
Lattice defects	$10^{-7} - 10^6 s$
Dislocation motion	$10^5 cm^{-1}$
Lattice vibrations	$10^{-9} - 10^{-10} s$
Fracture formation	$10 - 10^3 cms^{-1}$
Fresh surface	At $1.3 \cdot 10^{-4} Pa$ : $1 - 10^2 s$
Lifetime of excited metastable states	At $10^5 Pa$ : $< 10^{-6} s$ $10^{-3} s$ $10^{-2} s$

The process of mechanochemistry manifested in the transition from crystalline to amorphous, was described by the mechanical and the thermodynamic destabilisation theories (I. Colombo, Grassi and Grassi, 2009). These theories were developed initially to express the transition from solid to liquid during the melting process, which shares similarities with crystalline, and amorphous system reflected in the transition from ordered to disordered phase. In the mechanical destabilisation theory, the phase transition from crystalline to amorphous occurs as a result of external pressure which causes the distortion of the hydrogen bonds and the vanish of the crystal lattice. Here, the crystals are rendered shear unstable due to the reduction in their harmonicity. This model was successfully implemented in the study of pressure-induced amorphisation of ice by (Tse, 1992). Where high pressure caused the softening of the crystalline lattice owed to the rapid drop in elastic moduli which makes the crystals shear unstable. This change was accompanied by the breakage of hydrogen bonds, dislocation of water molecules, and eventually loss of long-range order. Whereas in thermodynamic destabilisation theory, the transition from crystalline to amorphous is attributed to the accumulation of defects (which form as a result of mechanical energy) to a critical amount after which the amorphous form is thermodynamically more stable than crystalline counterpart (Chan and Doelker, 1985). In this case, the kinetic energy injected into the system can cause a

catastrophic increase in the density of dislocations and defects to the point where all the crystallinity is lost. The defects can be in the form of interstitial occupancies, line defects, and plane defects (e.g. grain boundaries and crystal surfaces) (I. Colombo, Grassi and Grassi, 2009). The defects can lower the temperature and activation energy of amorphisation by promoting nucleation and diffusion, which implies additional vacancies (Chan and Doelker, 1985). Eventually, an amorphous product emerges which has equal molar volume, enthalpy, and entropy to that of the liquid melt. There exists insufficient information in the literature that describes the mechanism of mechanochemistry of pharmaceutical solid during milling. However, it is established that process such as amorphisation is related to the accumulation of defects and plastic deformation due to mechanical energy.

## **2.5. Summary**

Milling is a vital process in solid pharmaceutical processing. However, the milling of each API requires designing a specific milling experiment based on extensive trial and error work. This chapter addresses the various aspects required to understand and anticipate the milling behaviour of pharmaceutical solid as follows:

The beginning of this chapter introduces the commonly employed mills in pharmaceutical powder processing, including planetary ball mill, vibration mill, and a jet mill and the type of stresses generated in each mill. This part covers the knowledge gap in the literature about the key milling parameters (critical process parameters) that can impact on the milled sample. The critical milling parameters include the time of milling, the speed of milling, the ball to power ratio, the number and sizes of the balls, and the temperature of milling. There is a gap in the literature with regards to the impact of different milling conditions on the milled powder, which requires paying attention, since, it will help to understand the milling behaviour of solid pharmaceutical. It is also important to address the amount of energy generated with each mill to enable establishing a relationship between the conditions of milling and the degree of the physicochemical change produced.

Subsequently, this chapter provides literature on the main material properties (critical attributes) which are responsible for the mechanistic behaviour of a solid when exposed to external stress, i.e. mechanical properties. It was identified that the literature lacks information on the material properties of the majority of pharmaceutical APIs due to complexities involved with the experimental work and limitation and cost of these APIs. Hence, the ultimate step is to anticipate/calculate these properties using computational chemistry. The prediction work requires understanding the underlying intrinsic properties that control the mechanistic properties (milling behaviour) of the sample. However, this is challenging due to insufficient work that links the underlying molecular structure accounting for the intrinsic properties to the behaviour of the material while experiencing an extrinsic impact. Finding the relation between the intrinsic and extrinsic properties of the pharmaceutical solid will enable addressing part of the knowledge gap in this field.

This chapter also highlighted the process of mechanochemistry arising from milling, which causes variable physicochemical changes to the milled product. The area of mechanochemistry of pharmaceuticals requires a lot of work due to the lack of understanding of this phenomenon. This section provided examples of pharmaceuticals experiencing mechanochemistry, their milling condition, and the produced physicochemical change. The comparison of these pharmaceuticals and the changes they experienced during milling enabled determining the milling parameters that are primarily associated with the mechanochemistry which addresses part of the knowledge gap in the literature and allows for designing a milling experiment for the rest of the thesis. It was found that amorphisation is the most commonly produced type of mechanochemistry; hence special attention is paid to this phenomenon.

An additional essential element that was touched upon in this chapter is the solid-state analytical methods required to examine the emergence of amorphous as a result of milling. Providing a complementary characterising method will contribute to understanding the milling behaviour of solid pharmaceuticals.

The conclusive summary that can be taken from this literature work is that ball mills are commonly associated with the mechanochemistry of pharmaceuticals, particularly their amorphisation due to the high energy generated from this type of mill. Hence, the experimental focus of this thesis will be mainly on the ball mills, including a planetary ball mill and vibratory mill (single ball mill). Moreover, the literature outcome indicates that mechanical properties are the fundamental properties that can influence the milling behaviour of the material. Hence, special attention will be paid in this thesis to predict these properties from the molecular level. Furthermore, the literature review also points out that amorphisation is the most common type of mechanochemistry associated with ball mills; hence special consideration is provided to this type of behaviour. The investigation of the literature points out that various aspects can lead to amorphisation, including generation of defects and plastic deformation. Hence, an additional goal is to predict the susceptibility of pharmaceutical to plastic deformation.

Finally, the aim is to find a correlation between the energy levels arising from planetary ball mill and single ball mill and the rate, extent, and kinetics of the processes of comminution and amorphisation of materials.

## **Chapter 3 Materials and Method**

### **3.1. Introduction**

### **3.2. Materials**

### **3.3. Material Properties Predicting Methods**

### **3.4. Milling Methods**

### **3.5. Characterisation Techniques**

### **3.6. Energy Calculation**

### **3.7. Conclusion**

**This chapter outlines the materials selected for the rest of the thesis. The chapter follows by highlighting the prediction approaches employed to determine the material properties responsible for the mechanistic behaviour. It also provides an introductory of the type of mills selected for the milling process and the analytical methods used to characterise the feed and the milled product.**

## 3.1. Introduction

The solid pharmaceutical desired for the investigation of the impact of milling needs to demonstrate specific characteristics, precisely, those related to stability and safety. This chapter starts by providing an introduction of the pharmaceuticals selected for the rest of the thesis work along with the rationale behind the selection process. This chapter follows by outlining the modelling approaches used to predict the critical material properties that influence the milling behaviour of the solid pharmaceuticals. These properties include the crystal habit, slip planes, and the mechanical properties which are predicted from modelling the intrinsic molecular properties via computational chemistry. The experimental part of this project involves milling of the solid pharmaceuticals using different mills; planetary ball mill and single ball mill; hence, an introductory to these mills is provided in this chapter. In order to assess for the effect of milling on the solid pharmaceutical, a full characterisation of the feed and milled product is required using multiple solid-state characterisation techniques. The characterised properties include size, morphology, crystalline, thermodynamic and intermolecular properties. Therefore, an overview is included in this chapter covering the analytical techniques employed in the experimental part, including SEM, laser diffraction, XRPD, TGA, DSC, and FTIR.

### 3.1.1. L- Glutamic Acid

To establish a safe and optimal experiment, preliminary milling work is preferably conducted on a pharmaceutical powder which is available in sufficient quantities at low cost and is safe to use under laboratory condition as opposed to pharmaceutical API's which are usually expensive and come in a limited quantity.

L- Glutamic acid (LGA) (chemical formula:  $C_5H_9NO_4$ , molecular weight: 147.13 g/mol) is an amino acid found in the bodies of mammals that is usually involved in neurotransmission proteins. LGA is an approved nutraceutical compound used commercially as a flavours enhancer (Luz-Lima *et al.*, 2016). For the pharmaceutical applications; LGA is employed in the treatment of breast cancer due to its capacity to inhibit cancer cells. It was also found that LGA manifests strong antibacterial effects (Aarthi *et al.*, 2018). LGA exists in two polymorphic forms; a metastable form ( $\alpha$ ) which has a prism shape and a stable form  $\beta$  which exhibits a needle-like morphology (Figure 3-1) (Khan *et al.*, 2011). This study focuses on  $\beta$ - (LGA) due to its higher stability as compared to  $\alpha$  form.  $\beta$ -(LGA) was supplied by VWR International (BDH) as powder with 99% purity, and have a crystal size of  $D_{50} = 132\mu m$  (Figure 3-2).

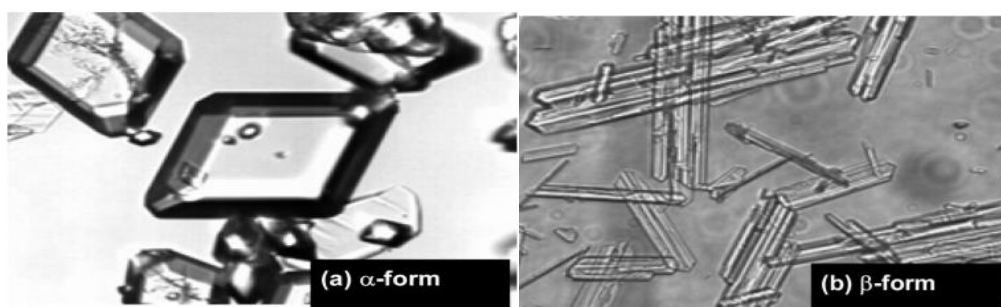


**Figure 3-1: Microscopic image of two polymorphic forms of glutamic acid; (a),  $\alpha$  form, (b)  $\beta$  form.(reprinted from (Borissova *et al.*, 2009))**

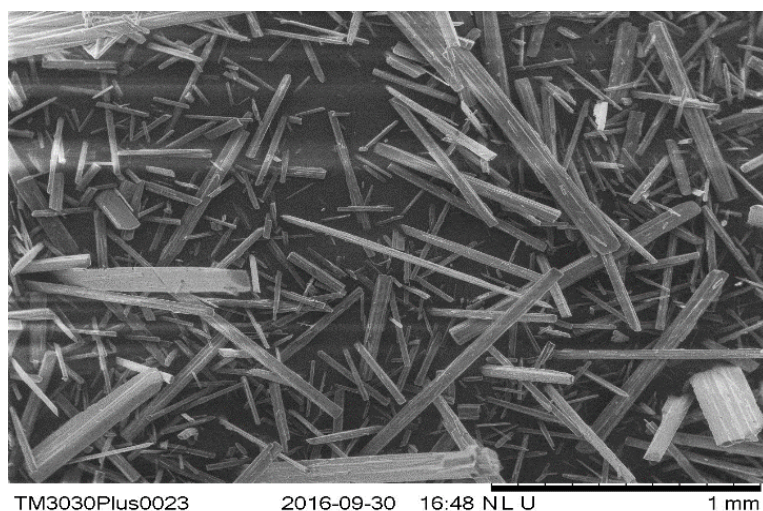


**Figure 3-2: SEM images of  $\beta$  glutamic acid**

### **3.1.1.1. Crystallisation of $\beta$ -(LGA)**

The crystallisation of  $\beta$ -(LGA) was conducted to produce a large amount of  $\beta$ -(LGA) at the University of Leeds as part of a group project during the master's term (Abouhakim *et al.*, 2016). The experimental crystallisation setup is shown in Figure 3-3. The crystallisation work was carried out in a 25- glass QVF unit vessel which consists of a 20-L jacketed stirred glass reactor, an associated feed vessel of 5-L, and a condenser. The reactor was set at 90°C, controlled through a Huber Unistat 510 circulation thermostat, and was monitored using a platinum-resistant thermometer. The temperature difference between the vessel and jacket oil was maintained at <50 C° to prevent thermal shock to the glass.

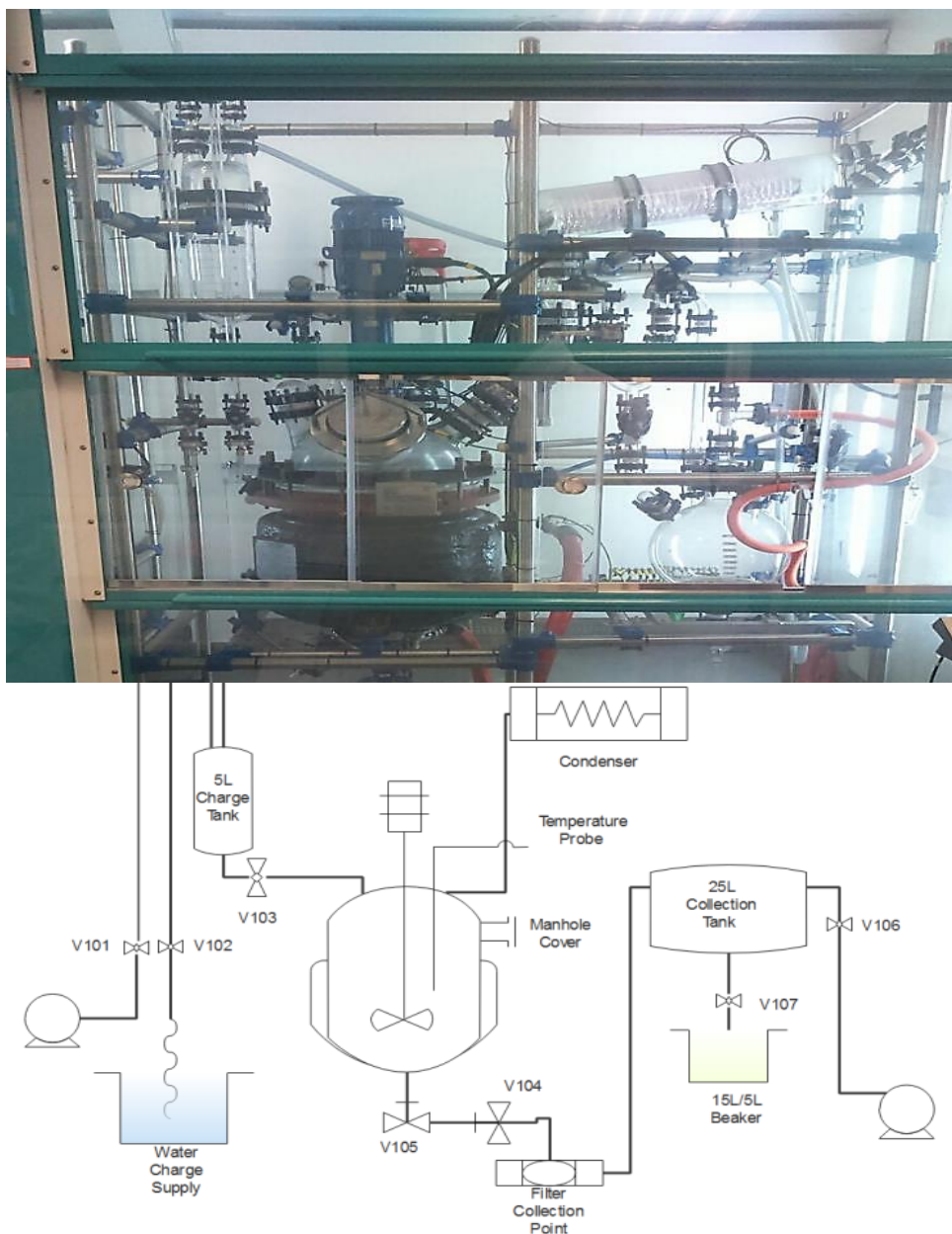


**Figure 3-3: Crystallisation of  $\beta$ -(LGA) experimental setup**

A PTFE retreat curve impeller was employed to stir the solution at a speed of 540 rpm. The reflux condenser was used to prevent solvent loss through evaporation and was programmed at a water flow rate of  $0.8 \text{ m}^3/\text{min}$ . A large Buckner filtration unit (30 cm diameter) operating under vacuum conditions was used to remove the mother lacquer from the crystals. 0.675 kg of LGA was added to 15 L of deionised water to make a concentration of  $45 \text{ gL}^{-1}$  of LGA. Once the dissolution is completed, 0.034 kg of  $\beta$ -(LGA) was added as a seed to promote the nucleation and the crystal growth at a temperature of  $68^\circ\text{C}$ . The vessel was refluxed for 1hr to

allow the crystallisation of  $\beta$ -(LGA) and, the solution was kept at room temperature overnight for further crystallisation. The crystals flow into the filter were dried under vacuum and washed twice using 300 ml of methanol.

### 3.1.2. Selection of a Material Candidate

This work aims to investigate the mechanochemistry of pharmaceutical API during milling, with specific attention to the amorphisation process. Therefore, it is critical to select at least one API which encompasses a stable amorphous to allow for a reliable analysis of any formed amorphous. The drug candidate needs to meet the following characteristics:

- The solid drug should demonstrate the ability to form a thermodynamically stable amorphous without the need for additives.
- The drug must be readily available and safe to use under the laboratory conditions

#### 3.1.2.1. Screening of a Stable Amorphous

To facilitate the screening process of a pharmaceutical compound incorporating a stable amorphous, it is vital to understand the factors contributing to the stability of amorphous. There is a lack in the literature on the list of drugs that possess a stable amorphous. Nonetheless, a model was created to predict the ability of solid pharmaceuticals to form a physically stable amorphous formed during spray drying and melt quench experiments. The model created was based on the investigation of numerous thermodynamic properties of 50 solid pharmaceuticals to establish the property with the most influential impact on the stability of the amorphous formed (Graeser *et al.*, 2009; Baird, Van Eerdenbrugh and Taylor, 2010; Mahlin and Bergström, 2013). The measured and investigated thermodynamic properties are listed in Table 3-1. The outcome of the screening work demonstrates that the glass transition temperature  $T_g$ , the molecular weight  $Mw$  and the crystallisation temperature  $T_{cr}$  are amongst the main thermodynamic properties that can dictate the formation of stable amorphous (Mahlin and Bergström, 2013). The combination of the glass transition temperature and molecular weight alone was able to predict for 75% of physically stable amorphous for approx. One month (Mahlin and Bergström, 2013). This model is adopted in this work to help with screening for stable amorphous.

##### 3.1.2.1.1. Glass Transition Temperature $T_g$

Glass transition temperature  $T_g$  is considered the most important property that characterises the stability of the amorphous compound (Birju, Kumar Kakumanu and Bansal, 2006). An amorphous material comprising a high glass transition temperature is usually stable compared to that with lower  $T_g$  (Alzghoul *et al.*, 2014).  $T_g$  can be measured experimentally using DSC technique, alternatively, it can be predicted based on mathematical models such as that developed by Alzghoul *et al.*, (Alzghoul *et al.*, 2014). For instance, Mahlin *et al.* predicted 65% of the stable amorphous based on the values of their glass transition temperature  $T_g$  (Mahlin and Bergström, 2013).

**Table 3-1: Example of thermodynamically stable amorphous (for 22 days and their properties (Graeser *et al.*, 2009; Baird, Van Eerdenbrugh and Taylor, 2010; Mahlin and Bergström, 2013)**

<b>Compounds</b>	<b><math>T_g</math></b> °C	<b><math>T_m</math></b> °C	<b><math>T_{cr}</math></b> °C	<b><math>\Delta H_m</math></b> J/g	<b><math>\Delta G_{cr}</math></b> J/g	<b><math>\Delta S_m</math></b> J/K/g	<b><math>M_w</math></b> g/mol
<b>Bicalutamide</b>	50	192	97	123	45	0.26	430.4
<b>Famotidine</b>	50	167	104	185	61	0.42	337.4
<b>Glafenine</b>	63	164	120	87	28	0.20	372.8
<b>Glibenclamide</b>	62	172	-	116	39	0.26	494.0
<b>Indomethacin</b>	44	159	104	122	39	0.28	357.8
<b>Linaprazan</b>	100	246	147	148	64	0.29	366.5
<b>Metolazone</b>	109	266	-	109	49	0.20	365.8
<b>Omeprazole</b>	51	155	90	145	45	0.34	345.4
<b>Pimozide</b>	57	216	106	100	40	0.2	461.5
<b>Spirolactone</b>	91	213	127	60	230	0.12	416.6
<b>Warfarine</b>	68	162	-	195	63	0.45	308.3

$T_g$  is the glass transition temperature,  $T_m$  temperature of melting,  $T_{cr}$  temperature of crystallisation,  $\Delta H_m$  is the enthalpy of melting,  $\Delta G_{cr}$  Gibbs free energy of crystallisation,  $\Delta S_m$  entropy of melting,  $M_w$  molecular weight.

### 3.1.2.1.2. Molecular Weight $M_w$

Molecular weight is an important factor to consider when screening for stable amorphous. Since, compounds with larger molecular weight are less prone to crystallise due to their complex molecular structure (Zhou *et al.*, 2002; Bhugra and Pikal, 2008; Graeser *et al.*, 2009). Compounds with  $M_w > 300$  g/mole were found to exhibit a stable amorphous (Zhou *et al.*, 2002; Bhugra and Pikal, 2008; Graeser *et al.*, 2009; Mahlin and Bergström, 2013). Mahlin *et al.*, model has accurately predicted 84% of solids with the ability to form amorphous, provided that the solid has a  $M_w$  greater than 300 g/mole and a melting temperature greater than 140°C. This was explained by the fact that materials with  $M_w > 300$  g/mole have bigger molecules manifesting large amount of conformation and configurations which can hardly return to an ordered crystalline packing after the amorphisation (Zhou *et al.*, 2002; Bhugra and Pikal, 2008; Graeser *et al.*, 2009).

### 3.1.2.1.3. Temperature of Crystallisation

Crystallisation temperature  $T_{cr}$  can influence the stability of amorphous since it is directly related to the nucleation process and growth rate (Mahlin and Bergström, 2013). According to Mahlin *et al.*, model, 95% of materials were accurately classified based on their  $T_{cr}$  which yield the best prediction outcome (Mahlin and Bergström, 2013).

#### 3.1.2.1.4. *Reported Prices and Safety of The Stable Material*

In addition to the stability of the amorphous drug, the API's safety and costs are crucial criteria in the process of screening of a solid pharmaceutical that can be employed in this project. For this purpose, a list of the predicted stable amorphous prices and hazards category is created in Table 3-2. The drug's safety is classified under a harmonised system from category 1 to category 5. Where, category 1 represents the drugs or chemicals with the highest toxicity level, whereas, category 5 represents those with the lowest level of toxicity.

**Table 3-2: List of drugs with predicted stable amorphous along with hazard category and cost**

<b>Compound</b>	<b>Price (Sigma Alrich) X£/Ymg</b>	<b>Hazard Category</b>
<b>Bicalutamide</b>	330£/200 mg	2
<b>Famotidine</b>	101£/1000 mg	2
<b>Glafenine Hydrochloride</b>	19.30£/1000 mg	4
<b>Glibenclamide</b>	42/1000 mg	4
<b>Indomethacin</b>	236£/10000 mg	1
<b>Linaprazan</b>	-	2
<b>Omeprazole</b>	58.20£/100 mg	4
<b>Metolazone</b>	370£/25 mg	-
<b>Pimozide</b>	-	4
<b>Spirolactone</b>	-	2
<b>Rabeprazole Sodium</b>	177.5£/50 mg	2
<b>Lansoprazole Salt</b>	52£/250 mg	2

#### 3.1.2.1.5. *Summary of Material Screening*

The results of screening show that Omeprazole is the most desirable system for this project since it is available free of charge in salt form (Omeprazole magnesium) from AstraZeneca. It is also considered safer to use in correspondence to the other materials under laboratory conditions using adequate personal protective equipment. However, Omeprazole magnesium crystal structure was never solved or reported since it was synthesized; also the milling of this pharmaceutical was never performed to the best of our knowledge. Hence conducting work on this substance will cover some of the knowledge gap in the literature about this material and can be a starting block in understanding the mechanochemistry of pharmaceuticals, particularly the amorphisation process. For the rest of the thesis, the name was given to the solved structure of Omeprazole magnesium (as will come later) is Diaqua-bis(Omeprazolate)-magnesium (II) dihydrate (DABOMD).

### 3.1.3. Diaqua-bis(Omeprazole)-magnesium(II) dihydrate (DABOMD)

DABOMD powder is used to investigate the impact of milling on its physicochemical characteristics. Omeprazole (IUPAC name; 6-methoxy-2-[(4-methoxy-3,5-dimethyl-2-pyridyl)methylsulfonyl]-1H-benzimidazole) is a pharmaceutical drug developed for the treatment of stomach reflux and gastric acid-related disorders (Gustavsson Anders, Kjellbom Kristina, 1997; Renata Toplak Casar, 2013). It is developed by AstraZeneca as racemate active enantiomers, (S)- and (R)-Omeprazole (Hultman, Stenhoff and Liljeblad, 2007; Mishra, Ramamurty and Desiraju, 2015; Bhatt, 2017). The API has also been presented in various salt forms as a means of increasing stability (Skieneh *et al.*, 2016). In this work, the studied salt is the racemic form of DABOMD since it has high thermodynamic stability which facilitates the analysis of any amorphous formed. The powder stability is predicted from Omeprazole's high glass transition temperature (51°C) (Mahlin and Bergström, 2013) and the large molecular volume of DABOMD (345 g/mol). DABOMD Crystallisation, as well as crystal structure, is solved in chapter 4. The as-received powder of DABOMD is shown in Figure 3-4.

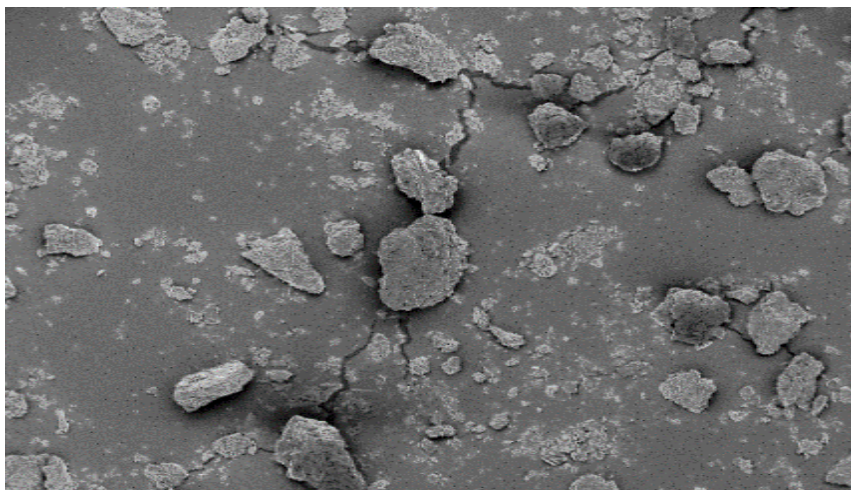


Figure 3-4: SEM images for the as-received powder of DABOMD

## 3.2. Material Properties Predicting Methods

### 3.2.1. Crystal Habit Prediction

The crystal habit can be simulated using in-silico tools. The derivation of the crystal morphology from the internal structure of the crystalline lattice through computer simulation has been successfully applied for various organic compounds (Bajcinca, Perl and Sundmacher, 2011). During the process of milling, it is assumed that the morphology of the crystal is a major factor impacting the fracture mechanism of the solid particle which can occur by geometric or thermodynamically driven mechanisms (Hossain Shariare *et al.*, 2012; Halme *et al.*, 2019). The geometric mechanism is obtained from BFDH morphology, whereas, the thermodynamic one can be predicted through the attachment energy calculation.

### 3.2.1.1. BFDH

The BFDH model is based on the lattice geometry and symmetry and was proposed by Bravais, Friedel, Donnay, and Harker (Docherty *et al.*, 1991). This model assumes that the energetically most stable and slowest growing faces are the ones with the highest density and largest spacing between adjacent layers, and the rate of growth of a particular surface is inversely proportional to the inter-planar d-spacing (Beyer, 2001). To quantify the structural agreement between crystal structures, a common method is to overlay a cluster of 15 molecules from each cluster and calculate the root-mean-square distance between heavy atoms (RMSD<sub>15</sub> value).

Mercury (Version 3.9; Macrae *et al.*, 2008) was used to visualize the crystal packing, to analyse the hydrogen bonding and to evaluate the d spacing.

### 3.2.1.2. Attachment Energy

The attachment energy,  $E_{att}$ , is defined as the energy released on the attachment of a growth-slice to a growing crystal face, and is calculated using Equation 3.1 (Bandyopadhyay and Grant, 2002).

$$E_{att} = E_{lattice} - E_{slice} \quad \text{Equation 3.1}$$

Where,  $E_{lattice}$  is the lattice energy of the crystal, and  $E_{slice}$  is the energy released on the formation of a growth-slice of a thickness which is equivalent to the interplanar d-spacing of the crystallographic plane representing a face attachment. This method is commonly employed to predict the crystal morphologies and is also employed in this work to characterise and identify the crystal planes that are the most weakly interacting which could serve as the slip planes (Sun, 2008).

For this work, the molecular modelling software Materials Studio (Biovia) was used to calculate the growth morphology using a suitable force field. To verify the accuracy of the force field (FF), an overlay of the FF-optimized crystal structure was made with a CASTEP optimized structure and to calculate the root-mean-square distance between heavy atoms (RMSD<sub>15</sub> value).

Prior to any calculation Material Studio was employed for geometry optimisation calculations. The generalized gradient approximation (GGA) Density Functional Theory (DFT) exchange-correlation (XC) functional of Perdew, Burke, and Ernzerhof (PBE) were used. Core electrons were modelled with ultrasoft pseudopotentials that were generated on the fly. Valence electrons were described using a plane-wave basis, with a kinetic energy cutoff of 620 eV. Reciprocal space sampling of the Brillouin zone used a fixed k-point spacing of 0.05 Å<sup>-1</sup>. Unit cells were fixed to the experimentally determined cell parameters, and the dispersion correction of Grimme (D2) was always applied. Self-consistent field (SCF) energy minimizations were performed until a threshold of  $1 \times 10^{-6}$  eV/atom was reached, and geometry optimizations continued until the total energy converged to  $1 \times 10^{-5}$  eV/atom with a maximum ionic force of  $3 \times 10^{-2}$  eV/Å. Lattice symmetry was used to increase calculation efficiency.

### 3.2.2. Slip Plane Prediction

Crystal slip planes depend on crystal packing and intermolecular interactions. Ionic interaction, hydrogen bonds, and Van der Waals force are primarily responsible for the crystal formation in an organic compound. Hydrogen bonds and Van der Waals forces have a major intermolecular force (Datta and David J.W. Grant, 2004; Storey and Ymen, 2011). It is proposed that hydrogen bonds have a significant impact on the breakage behaviour of the material (Datta and David J.W. Grant, 2004). The slip plane is suggested to be the easiest to displace. Slip planes can strongly dictate the material fracture mode during milling. A qualitative visualisation accompanied by the calculation of  $E_{att}$  where the planes with the lowest  $E_{att}$  are thought to be a slip plane was for long a commonly accepted technique for the identification of slip plane (Sun, 2008). Shariare et al (2012) concluded that generally, materials with the lowest d-spacing tend to exhibit a brittle failure, as these planes are more strongly interacting. Hence, d-spacing analyses could serve as a first indicator even in the absence of single-crystal structure data, given that d-spacing can be obtained from X-ray diffraction data (Hossain Shariare *et al.*, 2012) and other techniques. However, the d-spacing correlation is not expected to work for some materials due to other factors such as type hydrogen bonding framework (Hossain Shariare *et al.*, 2012; Halme *et al.*, 2019). Slip planes can be quantitatively determined from the attachment energy calculation. It is thought that surfaces with the least negative  $E_{att}$  are the most probable cleavage planes since they are the most weakly bound to the crystal face (Roberts, Rowe and York, 1994). Sun et.al examined slip plane of 14 crystals using the  $E_{att}$  model and concluded that this model yields only roughly a 50% success. The prediction of slip planes using  $E_{att}$  can produce inaccurate results for crystals that typically exhibit zig-zag or corrugated layer or slip plane (Sun, 2008).

More recently, it has been emphasized that more advanced sets of predictive tools such as energy frameworks and DFT calculations should be performed to get a more comprehensive view of the slip planes (Putra, 2016; Wang and Sun, 2018, 2019; Halme *et al.*, 2019). Crystal Interaction (CrysIn), an in-house developed tool (in AstraZeneca) was used to evaluate the static interactions between molecules present in a crystal based on the density functional theory (DFT). The intermolecular interaction energies in the first coordination cell of each molecule in the asymmetric unit of the crystal were calculated using B3LYP-D3/6-31G(d,p) as reported in Gaussian 16 (M. J. Frisch et al. 2016). This is a comparable method employed in, for instance, the energy framework calculations in CrystalExplorer (Turner *et al.*, 2015) or PIXEL (Gavezzotti, 2005). This approach enables the quantification of the intermolecular interactions present in a crystal and thus, can lead to the identification of slip planes with the weakest interactions.

### 3.2.3. Mechanical Properties Prediction

The impact of crystallographic structure on the mechanical properties of the crystal is a field that has received little attention so far (Datta and David J.W. Grant, 2004). The predicted mechanical properties include the elastic constants (Young's modulus) and the hardness. The elastic constants were calculated using CASTEP in Material Studio program, geometry optimisation is performed following the same setup as in the attachment energy calculations (Romain Gaillac, 2016). To enable visualisation of Young's modulus in X, Y, and Z, the elastic constant was calculated using (Gaillac, Pullumbi and Coudert, 2016).

The Hardness was determined using Equation 3.2 (Sun, Kothari and Sun, 2018).

$$H = 0.036 \times E \quad \text{Equation 3.2}$$

0.036 is the comparable value obtained from slop in (H/E) after testing brittle, plastic materials, and their binary mixture (Sun, Kothari and Sun, 2018). Whereby H is the indentation hardness, E is the Young's.

## 3.3. Milling Method

### 3.3.1. Planetary Ball Mill

Planetary ball mill is used in various industries for wet and dry grinding of particles down to manometer size due to its high-stress intensity which is achieved from high acceleration. It is classified as a high energy mill due to the movement of the grinding chamber with a large centrifugal force (Burmeister and Kwade, 2013). The high centrifugal force is generated from the rotation of the mill pot which is attached to a mill disc that rotates around the centre, while the pot consisting of the grinding balls and the material to be milled rotates simultaneously about its axis, hence, the name planetary (Neřkov, 2009) (Figure 3-5). The grinding process of the powder occurs as a result of impact and collision with the balls and the vessel wall (Fayed and Otten, 1997). Other applications next to comminution are mechanical alloying, where, two power components are milled to form homogenous alloy reducing the number of reagents and solvents needed in conventional reactions. Planetary ball mill is only available in pilot and laboratory scale up to 1-litre jar and is manufactured commonly by Fritsch GmbH and Retsch. This type of mill can introduce elevated temperatures to the material; it is thus essential to monitor the temperature by maintaining intervals during milling to allow the sample to cool. Thermally degradable materials can be milled using a cooling system such as flowing liquid nitrogen in different milling set up (RETSCH, 2019).



**Figure 3-5: Planetary ball mill PM100 ((RETSCH, 2019))**

### 3.3.2. Vibratory Mill

The vibratory mill is a high energy mill employed for various applications including pharmaceutical grinding; it is obtainable in a laboratory-scale (capacity of appx.10 ml) and industrial-scale (capacity from 50 to 250 ml) . The mill consists of a grinding ball sitting in a milling jar attached to a clamp that shakes several thousand times in a minute across the x-axis (Neikov, 2009). The shaking of the mill and the movement of the ball contributed to the size reduction of powder through impact and shear stresses (Chauruka *et al.*, 2015). Retsch MM200 vibratory mill is used in this work, as illustrated in Figure 3-6.

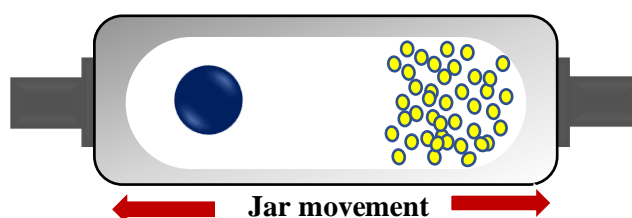


**Figure 3-6: Schematic shows ball and powder motion in the single ball mill ( modified from (Chauruka, 2015))**

## 3.4. Characterisation Techniques

### 3.4.1. X-Ray Powder Diffraction XRPD

XRPD is used to determine the crystal structure of the feed and product samples. As the X-ray beams strike the sample, the atoms cause the incident X-ray to radiate in different directions. The scattered X-ray provides information on the structure of the crystal. In a powder sample, particles are randomly orientated and exhibit different crystal faces. A proportion of planes are

oriented in the corrected position to allow diffraction for a set of faces as a function of angle. These angles and their relative intensities are converted to the d-spacing of the crystalline lattice (Byrn, Zografis and Chen, 2017). Bragg's law is used to derive the d-spacing between the crystals, as shown in Equation 3.3. According to Bragg's Law, constructive interference between X-rays occurs when the difference between their path length is an integer number wavelength. Where  $n$  is an integer representing the order of reflection,  $\lambda$  is the X-rays wavelength which depends on the X-ray source,  $d$  is the spacing between the crystals, and  $\theta$  is the angle between the X-ray incident beam which is normal to the reflecting lattice plane as shown in Figure 3-7.

In this work, XRPD patterns were recorded for the non-milled and milled samples using Phillips PW 1710 X-ray diffractometer using Cu K $\alpha$  radiation ( $\lambda=0.14406$  nm) at 40 kV and 30 mA setting. The XRPD S-scans were collected over a  $2\theta$  range of  $5^\circ$  - $55^\circ$  and an angular step of  $2\theta = 0.02^\circ$  using a fixed slit ( $3^\circ$ ) with 0.25 s per step. Diffract suite software is used for X-ray data analysis.

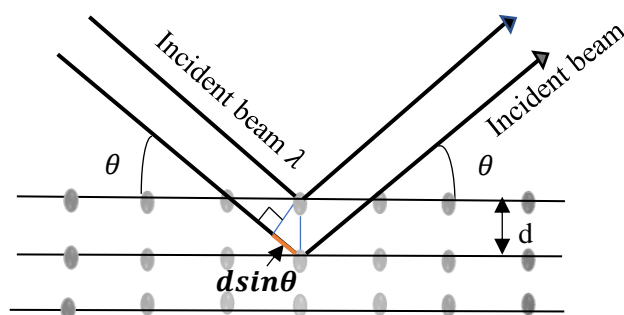


**Figure 3-7: Derivation of Bragg's Law ( amended from (Storey and Ymen, 2011)**

$$n\lambda = 2d\sin\theta$$

Equation 3.3

### 3.4.2. Single Crystal X-ray Diffraction

Single-crystal XRD is used to solve the crystal structure of an unknown compound from its single crystal. It enables the generation of detailed information about the crystal structure, molecular structure, bond length, and bonds angle. Single X-ray diffraction experiment is carried out in a diffractometer which consists of an X-Ray- beam monochromator impinging the single-crystal sample Figure 3-8. The single crystal is rotated to ensure that its planes are aligned to get diffraction accordingly with the Bragg's Law. The diffracted intensity is recorded with the aid of a two-dimensional X-ray detector. In this work, Single X-ray- diffraction was employed to solve the structure of DABOMD.

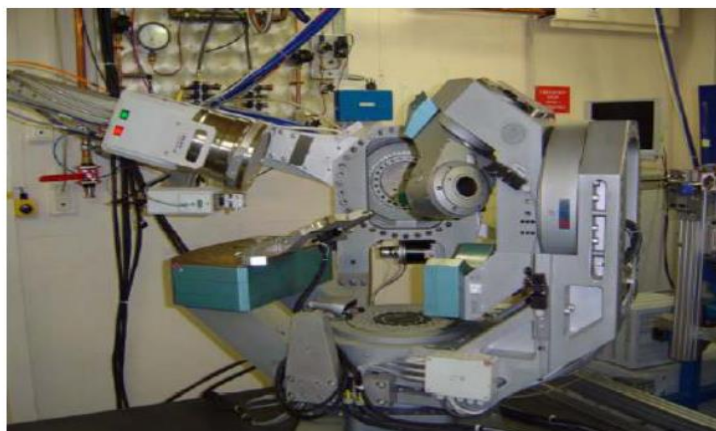


**Figure 3-8: Single-crystal X-ray diffractometer (reprinted from (Byrn, Zografí and Chen, 2017))**

### **3.4.3. Differential Scanning Calorimeter DSC**

Differential scanning calorimetry (DSC) is a thermo-analytical technique employed to evaluate the difference in the amount of heat flow to the sample to that of the inert reference as a function of temperature. The DSC cell comprises of a sample crucible and a reference crucible placed on a sensor that sits within the furnace (Figure 3-9 a). The sensors consist of a large number of thermocouples that provide high sensitivity and significant signals (Figure 3-9 b). The sample and reference are usually kept at the same temperature. When the sample undergoes a physical change such as phase transition, the heat subsequently flows in or out of the sample to maintain the same temperature as that of the reference. The nature of the heat flow is dependent on whether the sample is experiencing an endothermic or exothermic process. For instance, if the solid sample experiences an endothermic process (i.e. melt), the heat flows into the sample to maintain the same temperature as that of the reference. Similarly, if the sample experiences an exothermic process such as crystallisation, less amount of heat is required to increase the temperature. DSC displays a baseline background in the sample analysis. Any fluctuation from this baseline is attributed to a thermal event; the area under the peak is corresponding to the enthalpy change of that event (Instruments, 2020).

For this work, DSC analysis of the powder was carried out using a Mettler TC 3000 differential scanner calorimeter, with purged liquid nitrogen at a rate of 5 °C/min from 25 to 250 °C. TA instrument Universal analysis 2000 was used for the analysis.

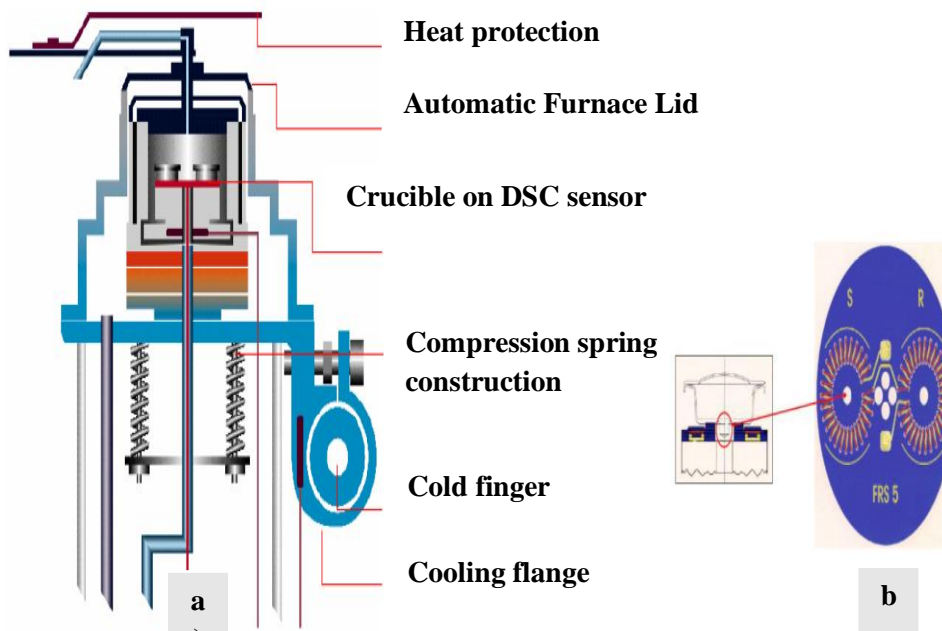
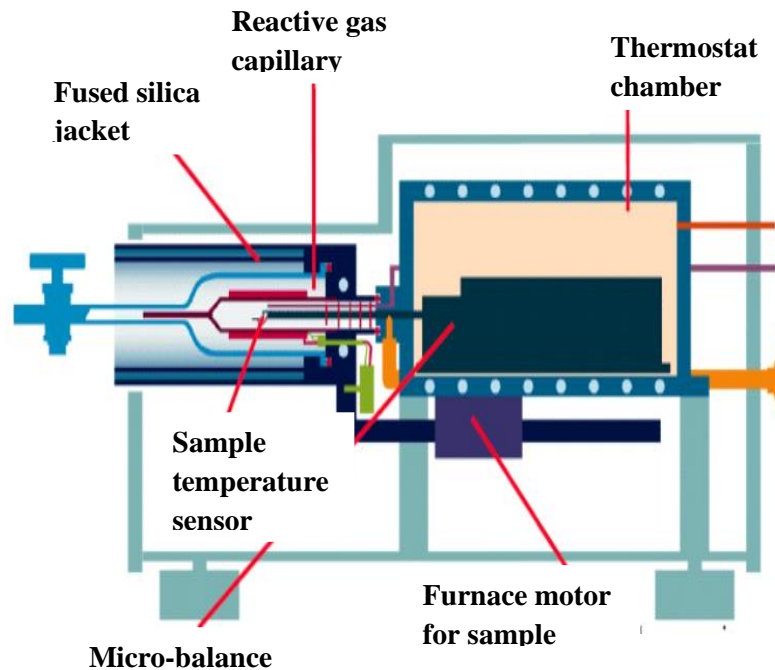


Figure 3-9: a) DSC cell, b) DSC sensor (reprinted from (Bibi et al., 2015))

#### 3.4.4. Thermal Gravimetric Analysis TGA

Thermogravimetric analysis (TGA) is a technique employed to measure the change in the sample mass as a function of temperature and or/time at a predetermined heating rate. The samples sit on a crucible attached to a microbalance which is then placed inside a furnace. The sample environment (conditions) can be controlled during measurement, including pressure, temperature, and humidity. This enables a wide range of investigations, including solvent adsorption/loss and decomposition. Such analysis requires a high degree of precision in weight, and temperature change. TGA instrument consists of thermocouples that enable temperature measurement within the furnace, a microbalance for the mass measurement, and a vacuum gas flow system which controls the atmosphere in the cell such as the humidity (Figure 3-10).

TGA was carried out with flowing gaseous nitrogen, and a rate of 5 °C/min from 25 to 250 °C. Approximately 5-6 mg of powder was placed in aluminium sealed pan with a hole on the top. TA instrument Universal analysis 2000 was used for the analysis.

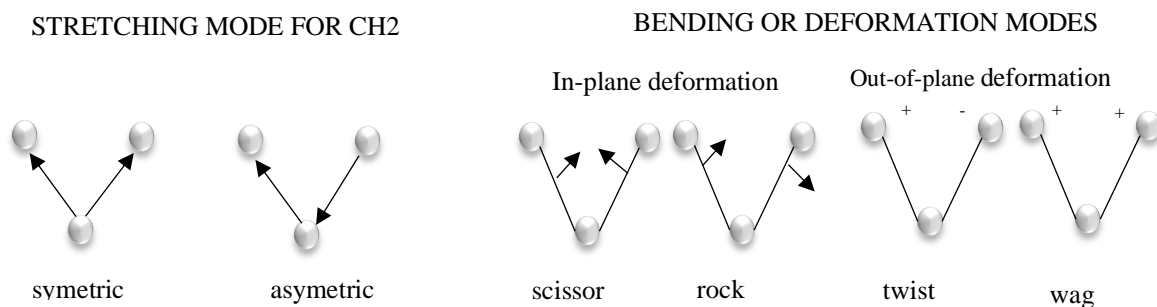


**Figure 3-10: Key Components of the TGA instrument (modified from (Roberts, 2016))**

### 3.4.5. Fourier Transform Infra-Red FTIR

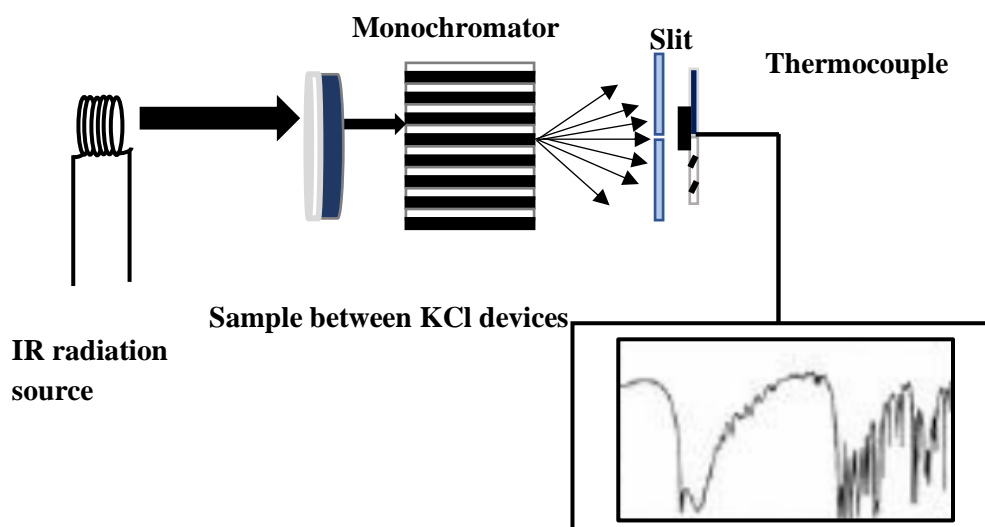
Infrared spectroscopy is a technique that can probe changes in molecular spectroscopy. It is sensitive to vibrational changes in the dipole as a result of unassociated or differently associated chemical conformation. The bonds in a molecule are continuously vibrating. When a molecule is exposed to infrared, the bonds can absorb electromagnetic radiations in the infrared region and vibrate at high amplitude. Each type of bond involves a resonant frequency which represents the strength of the bond and the mass (type) of atom at each end. The vibration of bonds can take two forms; stretching mode and bending or deformation mode. In the stretching mode, the bonds angle remains intact, whereas in the bending mode the bonds angle change.

Figure 3-11 shows the mode of vibration of the methylene group.



**Figure 3-11: Vibrational modes of a methylene group (modified from (El-Azazy, 2019))**

There are two types of an infrared spectrometer; dispersive and Fourier Transform. In a dispersive spectrometer, the sample transmitted radiation is divided by its component frequency and scanned using a grating or prism. Whereas in a Fourier instrument, all the frequency information is gathered using an interferometer. Fourier transform mathematic equation is then employed to extract the produced frequencies individually. The key components making dispersive infrared spectrometer are shown in Figure 3-12 and those making a Fourier transform infrared are shown in Figure 3-13.



**Figure 3-12: Schematic diagram of Infrared dispersive spectrometer (modified from (Barth, 2007))**

In this work, Attenuated Infrared Fourier FTIR-ATR transform technique was used. In the FTIR-ATR instrument, the sample is placed on a zinc selenide reflectance attenuated total (ATR) crystal instead of the KBR sample cell (Figure 3-14). As the beam hits the sample placed on the ATR surface, absorption takes place, and the spectra can be recorded. FTIR-ATR can be used for various forms of samples, including solids, liquids, or suspensions.

In this study, an infrared experiment was carried out on FTIR-ATR Thermo iS101 to analyse the milled, non-milled, and amorphous samples at a wavelength of 400 to 4000  $\text{cm}^{-1}$ . A background spectrum was conducted prior to any measurement, and 37 scans were taken for each sample.

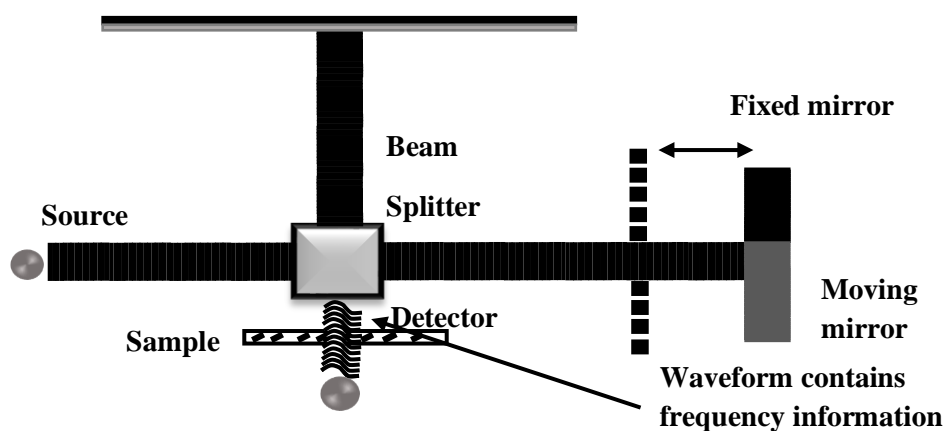


**Figure 3-13: Fourier transform infrared spectrometer ( modified from (Byrn, Zograf and Chen, 2017))**

Infrared can be employed to determine the functional groups and fingerprint for structure identification. In this work, FTIR was employed to identify the change in stretching and bending mode before and after milling as a tool of probing the intermolecular variation caused as a result of the milling, including amorphisation process. Figure 3-15 shows the Infrared spectroscopy correlation chart used to identify the change in absorption for specific functional groups of the materials.

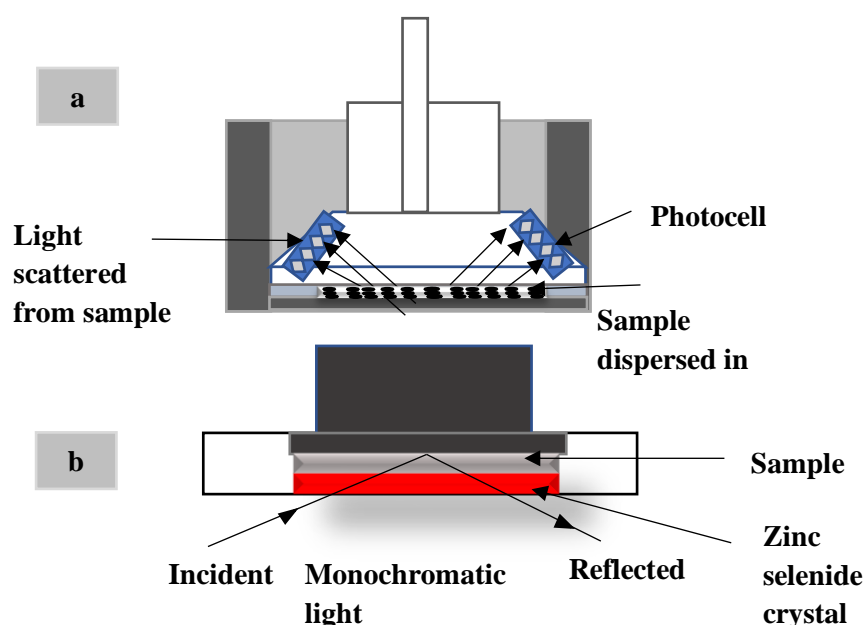


**Figure 3-14: a) Diffuse reflectance infrared instrument with Kbr sample cells and b) Attenuated total reflectance sample cell (modified from (Roberts, 2016))**

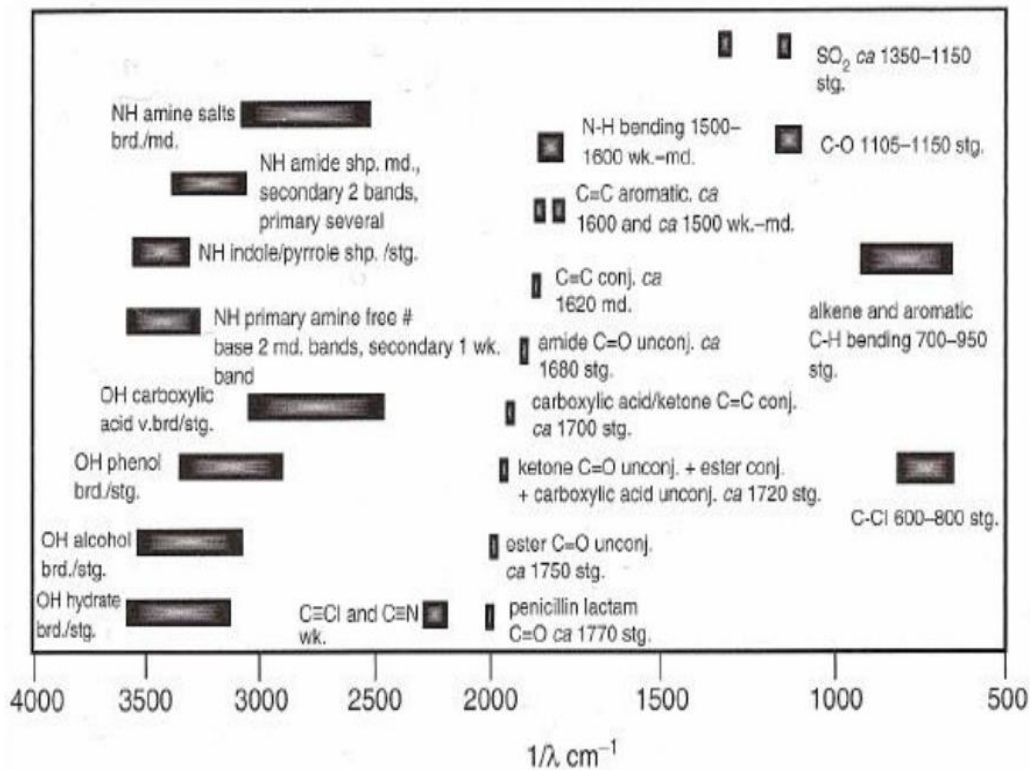


**Figure 3-15: Infrared spectroscopy correlation chart (reprinted from (Jakobs et al., 2000))**

### 3.4.6. Laser Diffraction

The laser diffraction technique is used to measure the particle size distribution of a dispersed particulate sample. The main components and setup of a typical laser diffraction instrument are shown in Figure 3-16, which involves laser light source, a focusing optic, and photodetectors. The particles pass through a focused laser beam and scatter light at an angle that is inversely proportional to their size generating particle size information. Where, smaller particles scatter light at low-intensity wide-angle, and larger particles scatter light at a higher intensity narrow-angle (Figure 3-17) (MalvernPanalytical, 2013).

The generated angular scattering intensity is then analysed to calculate the particle size distribution using Mie theory. Mie's theory assumes that particles are spherical, diffract light, and homogenous. Mie's theory predicts the intensity of scattered light based on the refractive index difference between the particles and the dispersing medium (Malvern Instruments Ltd, 2012). The data is presented as bimodal or gaussian normal distribution and is reported as a volume or equivalent area sphere diameter  $D_{10}$ ,  $D_{50}$  and  $D_{90}$  (Bauer Jhon, 2009).

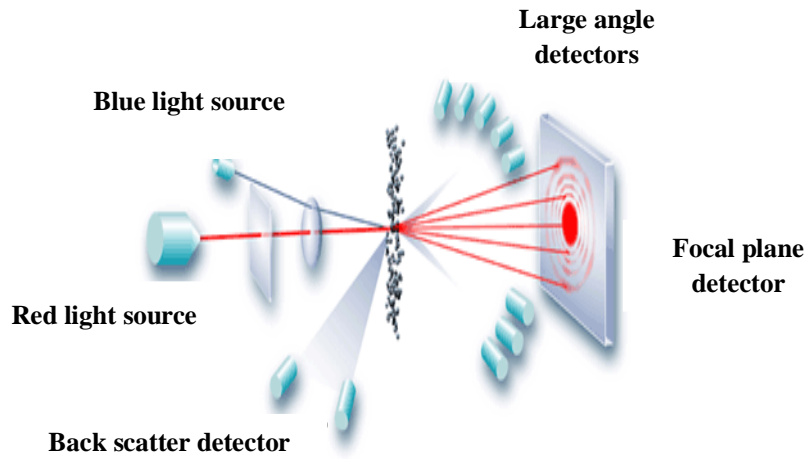


**Figure 3-16: Schematic diagram of the laser diffraction particle size apparatus (reprinted from (Malvern Instruments Ltd, 2012))**

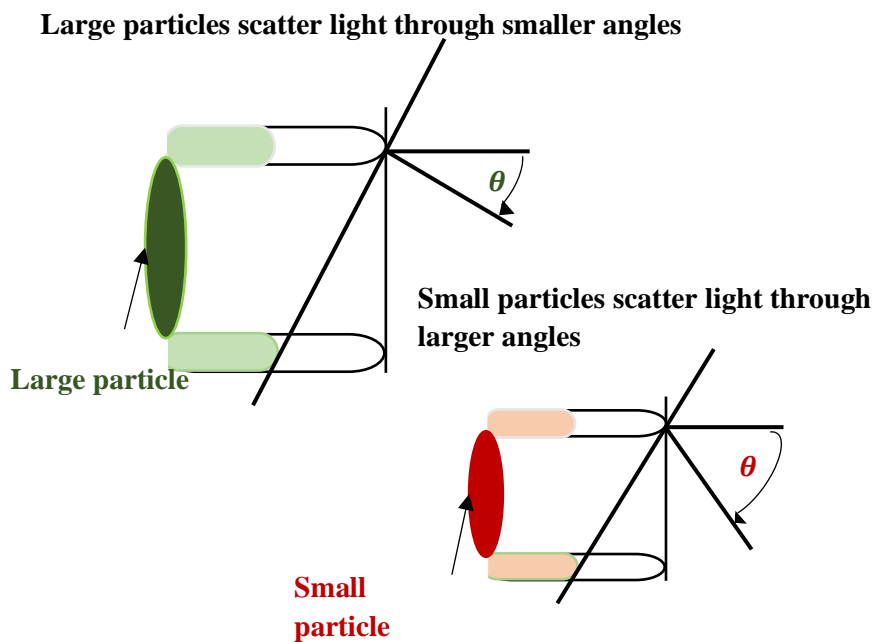


**Figure 3-17: Schematic shows light scattered from large and small particles (Malvern, 2015)**

### 3.4.7. Scanning Electron Microscope SEM

A scanning electron microscope (SEM) (Figure 3-18) is a type of microscope that uses electrons to produce a magnified image. An electron gun situated at the top of the microscope generates a beam of electrons. The produced electrons travel vertically in a path that is held in a vacuum. The electrons pass through an electromagnetic field and through lenses which enhances the beam focus. Once the beam strikes the sample, electrons and X-rays are ejected

from the sample. Emitted electrons and X-rays are collected by a detector in which are converted to an image displayed on a computer screen (Reimer, 1998).

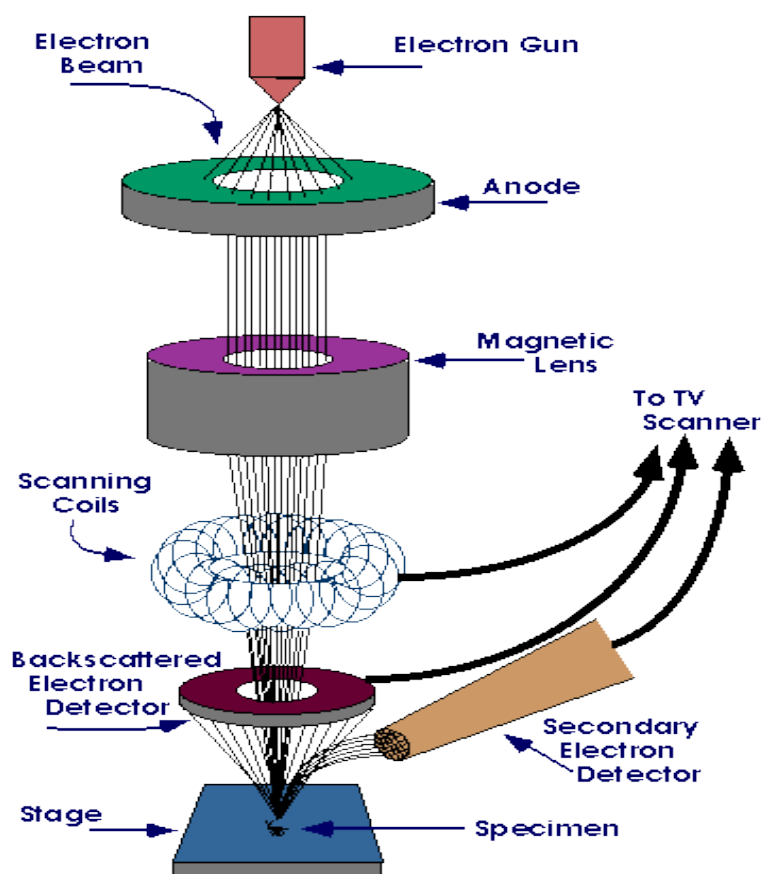


**Figure 3-18: Schematic diagram of SEM (reprinted from (Purdue University, 2010))**

### 3.5. Conclusion

This chapter outlined the materials selected for the rest of the thesis, the method employed for predicting the materials milling behaviour, and the experimental approaches that are followed to verify the prediction outcome and to investigate the process of mechanochemistry. The solid pharmaceuticals selected for the rest of the thesis are  $\beta$  L-Glutamic Acid ( $\beta$ -LGA) and Diaqua-bis(Omeprazole)-magnesium(II) dihydrate (DABOMD) which are used for the applications to treat cancer and stomach related issues. The methodology followed to predict the milling behaviour of the solid pharmaceuticals is based on computational chemistry, in which the single crystal is modelled to determine key properties including the crystal habit, mechanical properties, and the potential slip planes. For the experimental part, PM100 planetary ball mill and MM200 Retsch vibratory mill are used to mill the pharmaceutical solids. The impact of milling on the physicochemical properties of the feed and the product is assessed using laser diffraction, SEM, XRPD, DSC, TGA, and FTIR to determine the powder's morphological properties, crystal structure, thermodynamic properties, and intermolecular properties.

## **Chapter 4 Predicting the Material Properties of DABOMD by Modelling**

**4.1. Introduction**

**4.2. Crystal structure**

**4.3. Crystal Habit**

**4.4. Slip plane**

**4.5 Mechanical Properties**

**4.6. Conclusion**

**This chapter focuses on the prediction of the underlying key material properties influencing the milling behaviour of DABOMD which are determined from molecular level via computational chemistry**

## 4.1. Introduction

In order to predict the material properties of DABOMD, the information gathered from its crystal structure is required. Some literature has reported the crystal structure of Omeprazole (Ohishi *et al.*, 1989) itself and Magnesium Esomeprazole water/butanol solvate (Skieneh *et al.*, 2016), but no study exists which reports on the crystal structure of parent DABOMD since it was synthesised in the early 1990s. Thus, it is vital to solve its crystal structure by conducting some experimental and modelling work. Solving the crystal structure of DABOMD will enable determining the crystalline packings, molecular arrangements, and interactions. For this purpose, single X-ray diffraction as well as XRPD, DSC, and TGA are employed to evaluate the structure of DABOMD experimentally. Modelling approaches were coupled with the experimental outcome to produce the most reliable structure. The outcome of the crystal structure is used to identify the critical material properties that influence the mechanistic behaviour of the solid pharmaceutical during milling, including crystal habit, slip system, and mechanical properties using computational chemistry.

This chapter involves sections that were obtained from collaboration work; 1) Dr Christopher Pask from the University of Leeds conducted the single crystal diffraction measurements. 2) Dr Sten Nilsson from AstraZeneca conducted part of the computational work, including the validation of the hydrogen positions, the calculation of the attachment energy, the energy of the slip planes, and the mechanical properties. The author of this chapter conducted the rest of the work, including the analysis of the data provided by Dr Christopher Pask and Dr Sten Nilsson. The materials in this chapter were reproduced with the permission of the International Union of Crystallography (IUCr).

## 4.2. Crystal Structure

### 4.2.1. Crystallisation

The Racemic magnesium Omeprazole (R, S) crystalline powder (98% purity) was provided by AstraZeneca. Single crystals of DABOMD were obtained by vapour diffusion at room temperature from a saturated solution of DABOMD in ethanol (99% pure) using water as an anti-solvent. The solution was then filtered and stored at room temperature for 2 weeks. The crystallisation product is in the form of hexagonal platelet single crystals (Figure 4-1). The crystal dimensions were determined by the crystallographer from single XRD experiment of single crystal and were reported to be  $0.11 \times 0.03 \times 0.01$  mm.

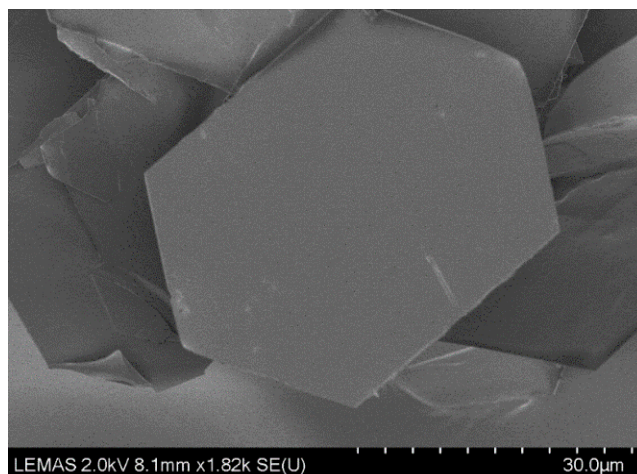


**Figure 4-1: Scanning Electron Microscopy image of a single crystal of DABOMD. (Reproduced with the permission of the International Union of Crystallography (IUCr) (Abouhakim *et al.*, 2020a)**

### 4.2.2. Solving Crystal Structure of DABOMD

Despite being developed in the early 1990s, no single-crystal structure determination has been published for DABOMD. This is potentially due to difficulties in growing single crystals of appropriate quality and size.

#### 4.2.2.1. Single Crystal Diffraction

The single-crystal diffraction of Diaqua-bis (Omeprazolate)-Magnesium Dihydrate was carried out at Leeds University, school of chemistry by Dr Christopher Pask. Measurements were conducted at 120K on an Agilent SuperNova diffractometer equipped with an Atlas CCD detector and connected to an Oxford Cryostream low-temperature device using mirror monochromated Cu K $\alpha$  radiation ( $\lambda = 1.54184$  Å) from a Microfocus X-ray source. The structure of DABOMD was solved using SHELXT intrinsic phasing method (George M Sheldrick, 2015) and was refined using SHELXL2014 full-matrix least-squares technique

based on  $F^2$  (George M. Sheldrick, 2015). The non-hydrogen atoms were added and refined anisotropically in the Fourier Map, whereas, the hydrogen atoms were positioned and refined isotropically using a riding model (a commonly followed approach by crystallographers to refine the molecular structure of a compound) (George M. Sheldrick, 2015). Anisotropic displacement parameters of the Omeprazolate anions were restrained using a rigid bond restraint. The crystal structure determined under the above conditions was deposited in the Cambridge Structural Database, reference: 1920020.

The molecular structure of DABOMD is shown in Figure 4-2. DABOMD crystallizes in monoclinic  $P21/c$  ( $Z = 2$ ,  $a = 17.475(9)$  Å,  $b = 8.051(2)$  Å,  $c = 14.190(5)$  Å;  $\beta = 109.91(5)^\circ$ ). The crystallographic data are summarised in Table 4-1, with selected bond lengths and bond angles shown in

Table 4-2 and Table 4-3. The independent asymmetric unit consists of one Omeprazolate anion, two water molecules, and 0.5 magnesium cation. The quality of the refinement is moderate ( $R_1 = 15.0\%$ ) caused by the thin platelet crystal. Applying the symmetry operations of  $P21/c$  gives DABOMD with two anions of Omeprazolate and two molecules of water (W1), positioned around a twofold axis, coordinated to one central magnesium cation which is located on an inversion centre (Figure 4-2). The magnesium shows a distorted octahedral geometry, with *cis* bond angles around the magnesium ranging from  $81.3(3)$  to  $98.7(3)^\circ$ . Mg-O and Mg-N bond lengths of  $2.086(7)$  and  $2.168(8)$  Å via bidentate coordination are consistent with the previously published structure of Esomeprazole magnesium water/butanol solvate (Skienh *et al.*, 2016). Mg-O(H<sub>2</sub>O) bond lengths of  $2.084(7)$  Å to W1 are also consistent with previously published bond lengths (Skienh *et al.*, 2016). The two additional molecules of water (W2) hydrogen bonds donate to the pyridyl nitrogen atom of each Omeprazolate, with O...N distances of  $2.833(13)$  Å. Each W1 water molecule also undergoes hydrogen bond donation to the benzimidazolate nitrogen atom of an adjacent omeprazolate anion (O...N distance of  $2.745(10)$  Å) leading to the formation of layers of molecules in the *bc* plane as shown in Figure 4-3. W1 also forms two separate hydrogen bonds to W2 (O...O distance of  $2.692$  Å and  $3.018$  Å). Thus, the magnesium bound water W1 is tetra-coordinated, while W2 is tri-coordinated.

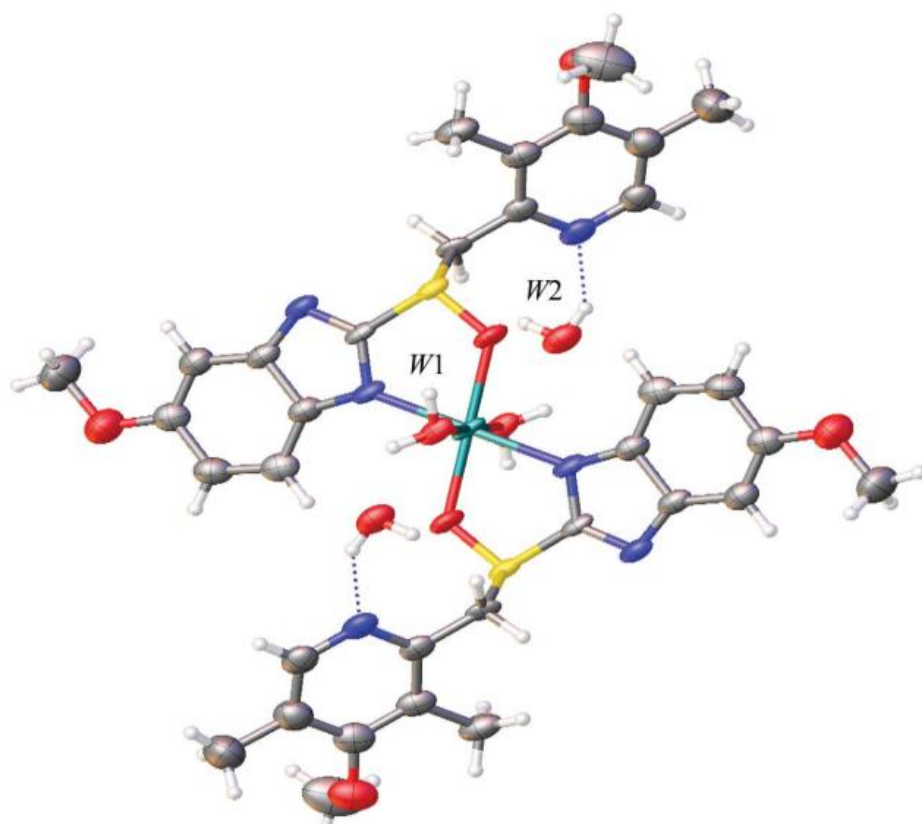


**Figure 4-2: Molecular structure of diaqua-bis(Omeprazole)-magnesium dihydrate (DABOMD). Thermal ellipsoids are shown at the 50% level with intermolecular hydrogen bonding between the molecules in the lattice shown in blue dotted lines Mg: green, S: yellow, N: blue, O: red, C: grey, H: white. (Reproduced with the permission of the International Union of Crystallography (IUCr) (Abouhakim *et al.*, 202a)**

**Table 4-1: DABOMD crystal data. (Reproduced with the permission of the International Union of Crystallography (IUCr) (Abouhakim *et al.*, 2020a)**

<b>Empirical formula</b>	<b>C<sub>34</sub>H<sub>40</sub>MgN<sub>6</sub>O<sub>8</sub>S<sub>2</sub>·2 H<sub>2</sub>O</b>
<b>Formula weight</b>	785.18
<b>Temperature/K</b>	120.0(2)
<b>Crystal system</b>	monoclinic
<b>Space group</b>	P2 <sub>1</sub> /c
<b>a/Å</b>	17.475(9)
<b>b/Å</b>	8.051(2)
<b>c/Å</b>	14.190(5)
<b>α/°</b>	90
<b>β/°</b>	109.91(5)
<b>γ/°</b>	90

<b>Volume/Å<sup>3</sup></b>	1877.1(14)
<b>Z</b>	2
<b><math>\rho_{\text{calc}}/\text{g}/\text{cm}^3</math></b>	1.389
<b><math>\mu/\text{mm}^{-1}</math></b>	1.994
<b>F(000)</b>	828.0
<b>Crystal size/mm<sup>3</sup></b>	0.11 × 0.03 × 0.01
<b>Radiation [Å]</b>	CuK $\alpha$ ( $\lambda = 1.54184$ )
<b>2<math>\theta</math> range for data collection/°</b>	10.768 to 147.15
<b>Index ranges</b>	-15 ≤ h ≤ 21, -9 ≤ k ≤ 9, -15 ≤ l ≤ 17
<b>Reflections collected</b>	8269
<b>Independent reflections</b>	3546 [R <sub>int</sub> = 0.1656, R <sub>sigma</sub> = 0.2009]
<b>Data/restraints/parameters</b>	3546/216/249
<b>Goodness-of-fit on F<sup>2</sup></b>	1.072
<b>Final R indexes [I &gt;= 2<math>\sigma</math> (I)]</b>	R <sub>1</sub> = 0.1496, wR <sub>2</sub> = 0.3519
<b>Final R indexes [all data]</b>	R <sub>1</sub> = 0.2299, wR <sub>2</sub> = 0.4164
<b>Largest diff. peak/hole / e Å<sup>-3</sup></b>	1.71/-0.66

**Table 4-2: Selected Bond Angles for DABOMD. (Reproduced with the permission of the International Union of Crystallography (IUCr) (Abouhakim *et al.*, 2020a)**

Atom	Atom	Length/Å
<b>Mg1</b>	O1	2.086(7)
<b>Mg1</b>	O4	2.084(7)
<b>Mg1</b>	N1	2.168(8)

**Table 4-3: Selected Bond Angles for DABOMD (IUCr) (Abouhakim *et al.*, 2020a)**

Atom	Atom	Atom	Angle/°
<b>O1</b>	Mg1	O1	180.0
<b>O1<sup>1</sup></b>	Mg1	N1	81.3(3)
<b>O1</b>	Mg1	N1	98.7(3)
<b>O1</b>	Mg1	N1	81.3(3)
<b>O4<sup>1</sup></b>	Mg1	O1	87.6(3)
<b>O4</b>	Mg1	O1	87.6(3)
<b>O4<sup>1</sup></b>	Mg1	O1	92.4(3)
<b>O4</b>	Mg1	O1	92.4(3)
<b>O4<sup>1</sup></b>	Mg1	O4	180.0(5)
<b>O4</b>	Mg1	N1	87.3(3)
<b>O4</b>	Mg1	N1	92.7(3)
<b>O4<sup>1</sup></b>	Mg1	N1	87.3(3)
<b>N1<sup>1</sup></b>	Mg1	N1	180.0

<b>S1</b>	O1	Mg1	120.6(4)
<b>C4</b>	O2	C7	117.9(11)
<b>C12</b>	O3	C16	115.1(12)
<b>C1</b>	N1	Mg1	140.6(6)
<b>C8</b>	N1	Mg1	116.1(7)
<b>C8</b>	N1	C1	103.3(8)
<b>C8</b>	N2	C6	103.3(8)
<b>C10</b>	N3	C14	117.3(10)
<b>N1</b>	C1	C2	131.9(10)
<b>N1</b>	C1	C6	107.1(9)

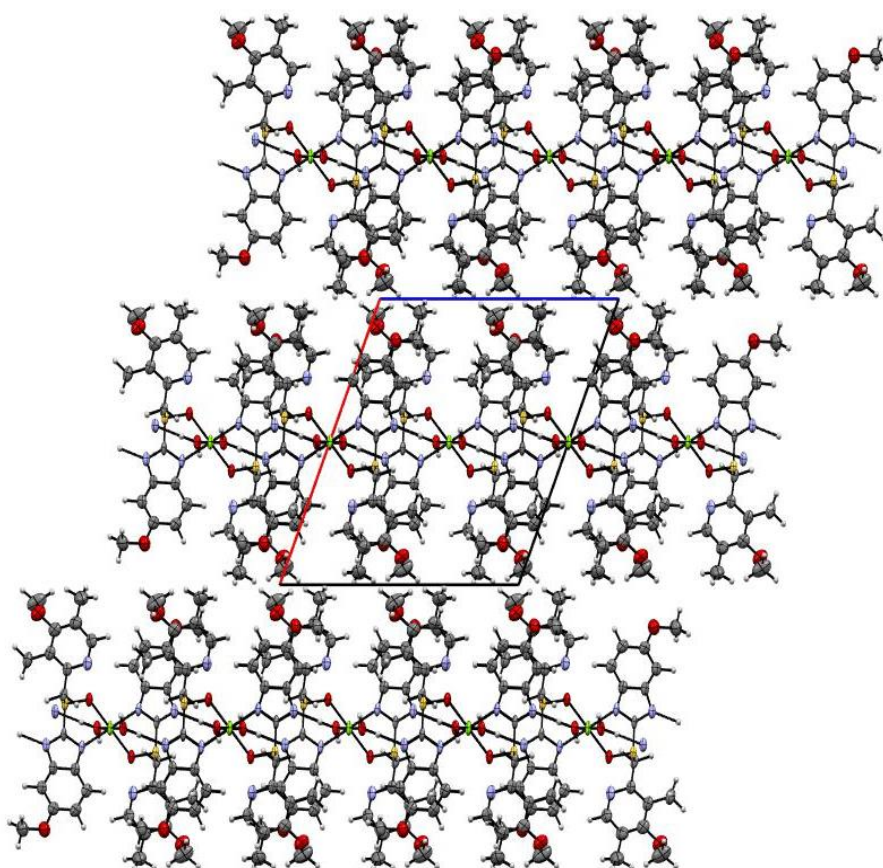


**Figure 4-3: Crystal packing arrangement of DABOMD viewed down the crystallographic b axis. Thermal ellipsoids are shown at the 50% level. Additional W2 water molecules are omitted for clarity. Intermolecular hydrogen bonding between the molecules in the lattice shown in dotted lines Mg: green, S: yellow, N: blue, O: red, C: grey, H: white. (Reproduced with the permission of the International Union of Crystallography (IUCr) (Abouhakim *et al.*, 2020a))**

#### 4.2.2.2. Validating Hydrogen Positions Computationally

The hydrogen positions on the water molecules were computationally varied to see if a slightly different h-bond network would generate a more stable structure. This part of the computational work was undertaken by Dr Sten Nilsson from AstraZeneca. To validate the hydrogen positions in the water molecules of DABOMD, two alternative structures with different hydrogen bonding patterns were constructed using Materials Studio (Dassault Systèmes) starting from the experimental crystal structure. Only the hydrogen's positions in the water were altered. These structures were further refined to find the optimal hydrogen bonding, and relative energies were calculated using dispersion corrected density functional theory (Clark *et al.*, 2005). Calculations under periodic boundary conditions were performed using version 17.1.0.48 of the Cambridge Serial Total Energy Package (CASTEP).

The two alternate structures were refined using CASTEP under the same symmetry constraints and their DFT-D energies compared. It was found that the structure where the O-H bonds of the Mg-bound W1 water are aligned roughly in parallel to the O(S)-Mg-O(S) bonds (Figure 4-4a) were about 3 kJ/mol more stable than when they are aligned roughly in parallel to the N-Mg-N bonds (Figure 4-4b). To quantify the water binding in the preferred CASTEP optimized crystal, their intermolecular interactions were calculated using B3LYP-D3/6-31G (d, p) by removing the water molecules pairwise from the crystal structures and further making individual energy calculations on the separated parts. Interestingly, the two pairs of waters bind with distinctly separated strengths, -26.8 and -35.5 kcal/mol, where the W1 waters binding to the magnesium cation are more strongly bound. This result will be further discussed in the TGA and DSC analysis below.

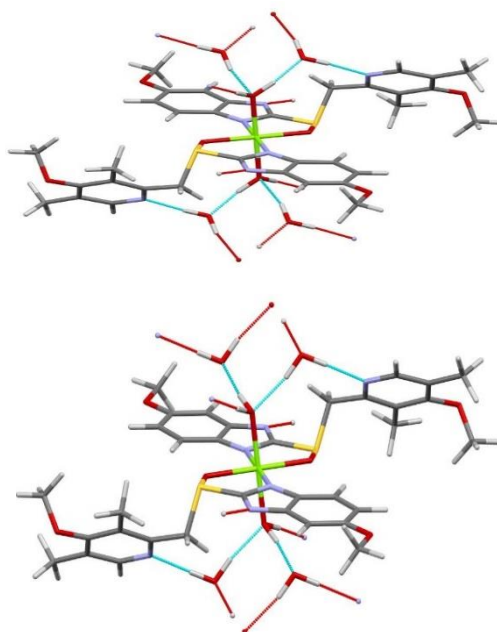


**Figure 4-4: CASTEP optimized DABOMD crystal structures with different hydrogen bond directions. (Reproduced with the permission of the International Union of Crystallography (IUCr) (Abouhakim *et al.*, 2020a)**

#### 4.2.2.3. Verifying Crystal Structure Using X-Ray Powder Diffraction

X-ray powder diffraction (XRPD) analysis was carried out to confirm the powders patterns corresponded to the correct structure prior to other bulk analytical techniques. The results were compared with the simulated XRPD patterns obtained from Single Crystal X-ray Diffraction.

Mercury (version 3.9) (CCDC, Cambridge, UK) was employed to generate simulated powder X-ray diffraction patterns for DABOMD using the single-crystal structure data acquired from solving the crystal structure.

Figure 4-5 shows XRD patterns of DABOMD simulated, experimental from single ground crystals, as well as experimental XRPD patterns of DABOMD powder. The powder and ground single-crystal XRPD patterns look similar and are in a close agreement to the simulated pattern from the single-crystal. A slight shift in  $2\theta$  for the calculated XRPD may be due to the difference in temperature since XRPD was run at room temperature, unlike single-crystal determination which was performed at 120K. The difference in temperatures is expected to give rise to an expansion in the unit cell dimension at room temperature.

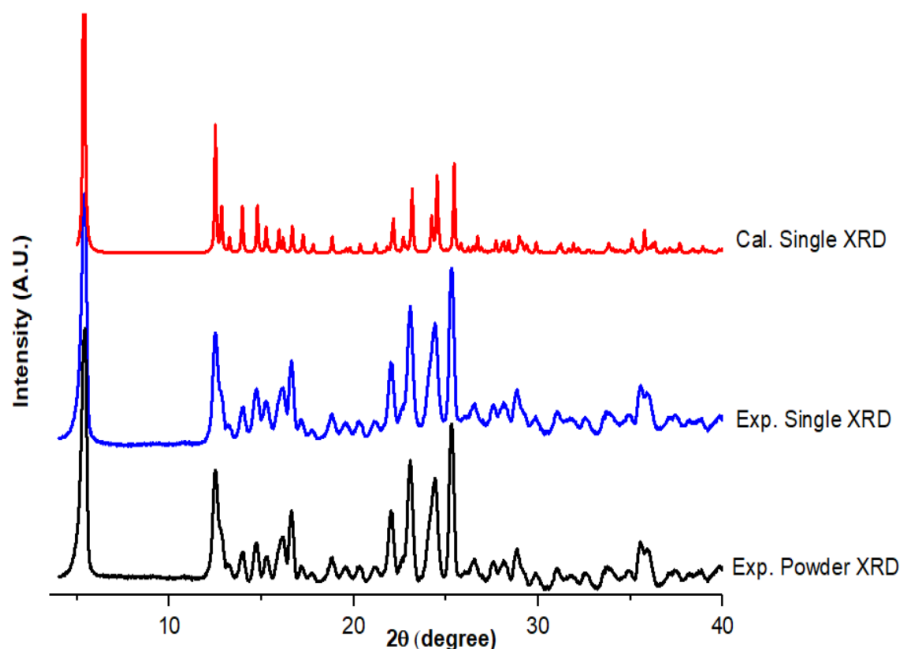


**Figure 4-5: XRD pattern of DABOMD, simulated from single crystal; experimental – single ground crystals, and experimental – bulk powder. (Reproduced with the permission of the International Union of Crystallography (IUCr) (Abouhakim *et al.*, 2020a))**

### 4.2.3. Crystal Solvent Contents

To confirm the total water content in the crystal lattice, thermogravimetric analysis (TGA) and Differential scanning calorimetry (DSC) analysis of the powder of DABOMD were performed.

The TGA results shown in Figure 4-6 revealed two different episodes for mass losses for DABOMD crystalline powder. The total amount of mass loss in both events is 8.6 %, which indicates two water molecules released at each event. These results are consistent with the single crystal XRD analysis and the intermolecular interaction analysis which indicate that the first two water molecules (W2) that are hydrogen-bonded only are lost at lower temperatures followed by the water molecules coordinated to the magnesium cation (W1). DSC analysis was performed on DABOMD crystalline powder (Figure 4-8). The DSC patterns display three distinct thermal events: an endothermic peak at  $109^\circ\text{C}$  followed by another endothermic at  $173^\circ\text{C}$ , and an exothermic peak at  $197.8^\circ\text{C}$ . The first endothermic peak corresponds to a water-loss event. A similar observation was reported for the dehydration of sodium Omeprazole (Murakami *et al.*, 2009) and the loss of water from the crystal structure for magnesium Esomeprazole water–butanol solvate (Skieneh *et al.*, 2016). The second endothermic event in Figure 4-7 corresponds to the loss of the more strongly bound water. The exothermic peak corresponds to a decomposition process of the crystalline form of DABOMD (Murakami *et al.*, 2009; Skieneh *et al.*, 2016), as confirmed by hot-stage microscopy visual analysis (Figure 4-8)

which shows that DABOMD does not undergo melting with high temperature. The hot stage microscope experiment was conducted using Leica DM2700 microscope, Linkham T95 hot stage, with a Nikon 3500 DSLR attached for taking photos. The experiment setup was as follows: approx. 0.1g of powder placed on a glass sheet was attached to the hot stage, which was set to heat up from 25°C to 180°C at a heat rate 10°C/min.

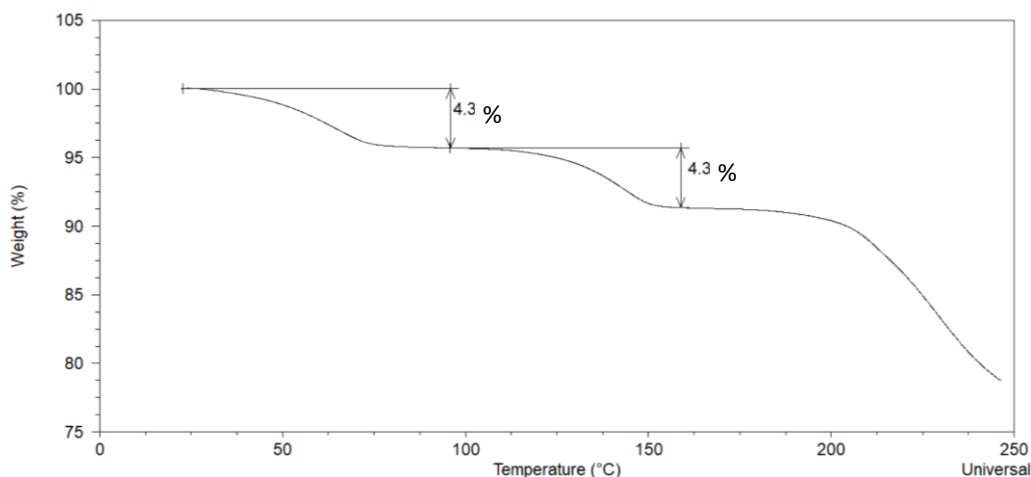


**Figure 4-6: Thermal Gravimetric Analysis plot of DABOMD crystalline powder heated from 25 to 250 °C at a rate 5°C/min. (Reproduced with the permission of the International Union of Crystallography (IUCr) (Abouhakim *et al.*, 2020a)**

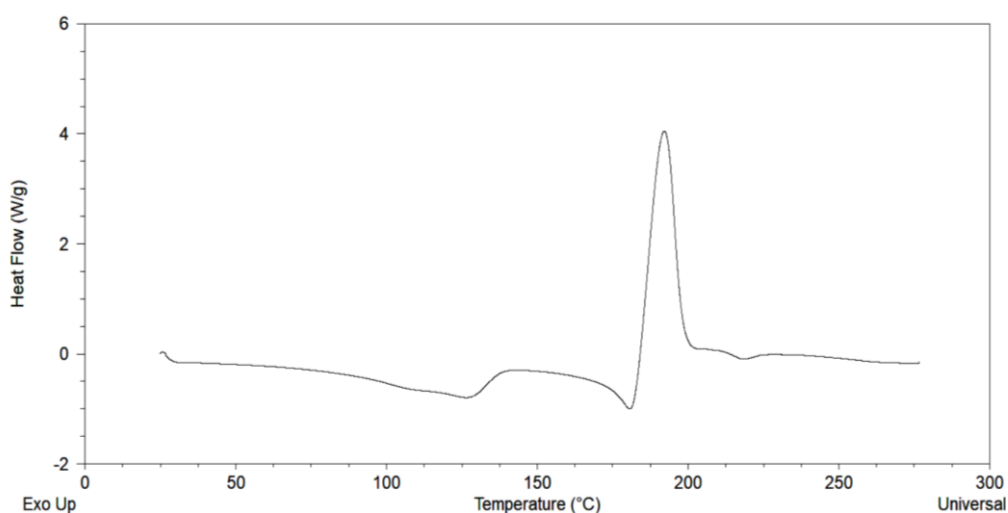


**Figure 4-7: Differential Scanning Calorimetry plot of DABOMD crystalline powder heated from 25 to 290 °C at a rate 5°C/min. (reproduced with the permission of the International Union of Crystallography (IUCr) (Abouhakim *et al.*, 2020a)**

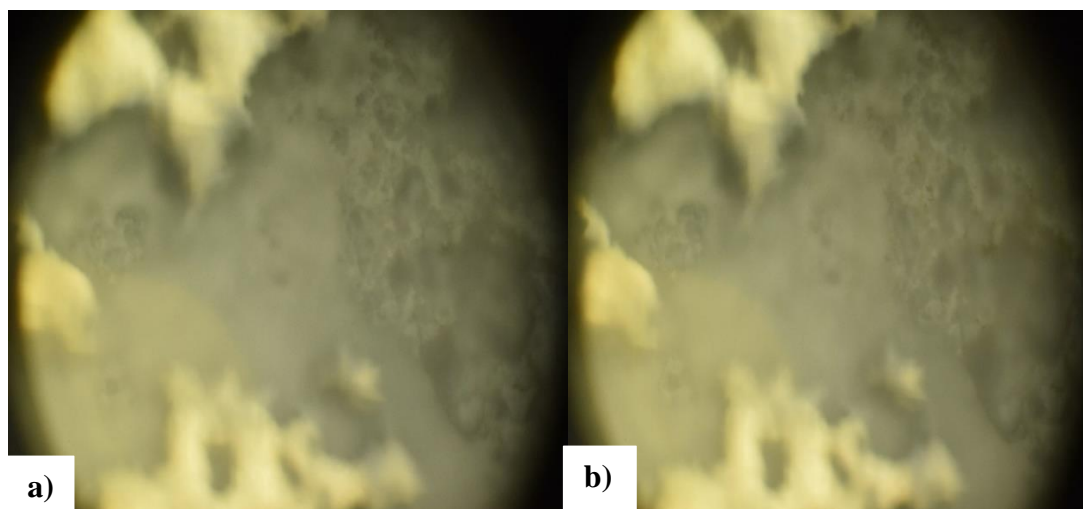


**Figure 4-8: Hot stage microscope image of DABOMD heated from 25°C to 190°C at a rate of 10°C/min. a) at 25°C, b) at 180 °C**

### 4.3. Crystal Habit

The crystal morphology can be obtained experimentally through the crystallisation of single crystals, or, can be simulated via Silico tools such as BFDH morphology and or attachment energy model.

#### 4.3.1. BFDH

The BFDH derived habit of DABOMD is shown in Figure 4-9. It can be seen that DABOMD exhibits a hexagonal plate morphology. The surfaces produced by BFDH model show that (100), (102), (011) and (1-10) are amongst the major surfaces with (100) being the most dominant face. This morphology agrees with the experimental morphology of DABOMD Figure 4-9c.

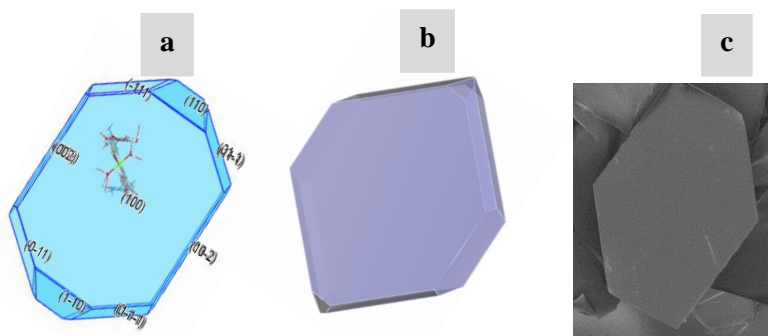


**Figure 4-9: DABOMD; a) Predicted morphology using BFDH Model, b) Predicted morphology using  $E_{att}$  growth morphology model c) Morphology from experimentally**

grown single crystal (Reproduced with the permission of the International Union of Crystallography (IUCr) (Abouhakim *et al.*, 2020a)

### 4.3.2. Attachment Energy

The molecular modelling software Materials Studio (Biovia) was used to calculate the growth morphology. Universal Forcefield was employed, other force-fields were tested but did not apply to magnesium salts. To validate the accuracy of the force field (FF), an overlay of the FF-optimized crystal structure was made with a CASTEP optimized structure and found an RMSD<sub>15</sub>-value of 0.4, thus a good agreement. Growth morphology calculations were based on the attachment energy model.

Figure 4-9b shows the morphology obtained with the attachment energy model. It can be seen that DABOMD exhibits a hexagonal platelet shape which is in a close match with the BFDH morphology as well as the experimental morphology of DABOMD. The attachment energy calculation shows that the face (100) is the major surface which coincides with BFDH major face. Where, (100) plane occupies more than 59% surface area (Table 4-4) and exhibits an  $E_{att}$  value of  $-25.8 \text{ kcal mol}^{-1}$  followed by (011) and (11-1) surfaces which possess  $E_{att}$  value equal to  $-75.9 \text{ kcal mol}^{-1}$ , and  $-78.8 \text{ kcal mol}^{-1}$  respectively. The face with the least negative  $E_{att}$  represents the slowest growing face and is the major habit face of crystal (Roberts, Rowe and York, 1994). Hence, it can be concluded that the face (100) is the major face of DABOMD.

**Table 4-4: DABOMD results from attachment energy(  $E_{att}$  ) calculations of growth morphology (Reproduced with the permission of the International Union of Crystallography (IUCr) (Abouhakim *et al.*, 2020a)**

$(hkl)$	Multiplicity	$d_{hkl}$ (Å)	Total $E_{att}$ ( $\text{kcal mol}^{-1}$ )	Area (%)
(1 0 0)	2	16.43	-25.8	59.4
(0 1 1)	4	6.89	-75.9	21.5
(1 1-1)	4	6.80	-78.8	9.0
(1 1 0)	4	7.23	-80.9	2.0
(1 0-2)	2	7.08	-101.7	8.1

The Zingg diagram characterization (using dimensions from SEM image, BFDH, and  $E_{att}$ ) for DABOMD further supports its platelet morphology (Figure 4-10). Chikhalia *et al.*, stated that crystals exhibiting plate-like morphology are more prone to crystalline disorder during milling compared to those exhibiting needle morphology (Chikhalia *et al.*, 2006). In general, it was suggested that particles exhibiting high elongation ratio (longest dimension over shortest dimension) reduce in size more rapidly (Hossain Shariare *et al.*, 2012; Halme *et al.*, 2019), for example, paracetamol and AZD5423 which have an elongation ratio of 2.1 and 3.4 respectively (Halme *et al.*, 2019). For DABOMD, the calculated elongation ratio from BFDH and 2-

dimension image is equal to 2.2, which is equivalent to a high elongation ratio according to (Halme *et al.*, 2019). Although the shape alone is not sufficient to predict the particle breakage behaviour (Vegt, 2007; Hossain Shariare *et al.*, 2012; Halme *et al.*, 2019).

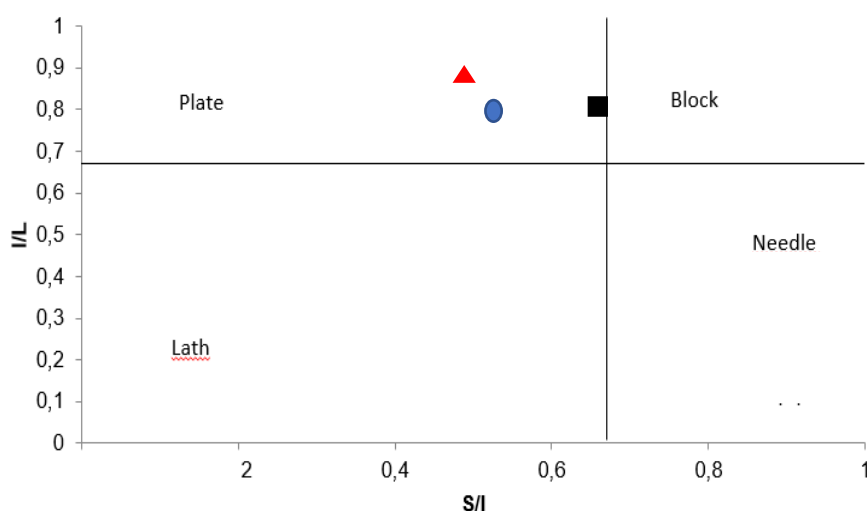
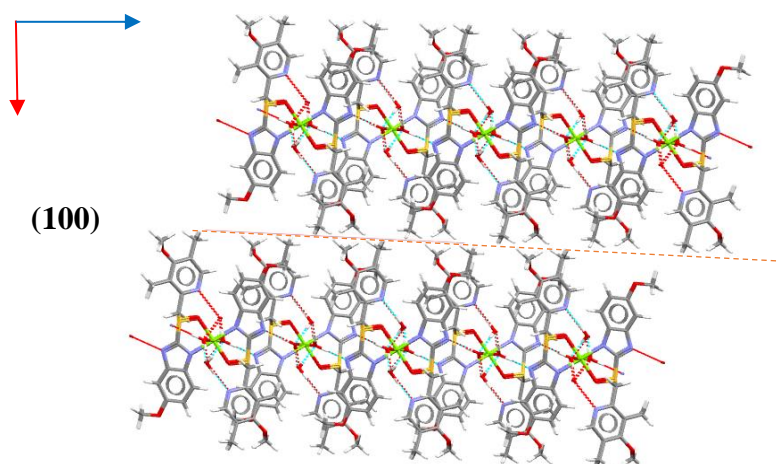


**Figure 4-10: DABOMD; Plot of Zingg diagram, where L is the longest dimension, I is the intermediate dimension, and S is the shortest dimension. Dimensions obtained from morphologies derived from BFDH (red triangle), attachment energy (blue circles), and experiment (back square) (Reproduced with the permission of the International Union of Crystallography (IUCr) (Abouhakim *et al.*, 2020a)**

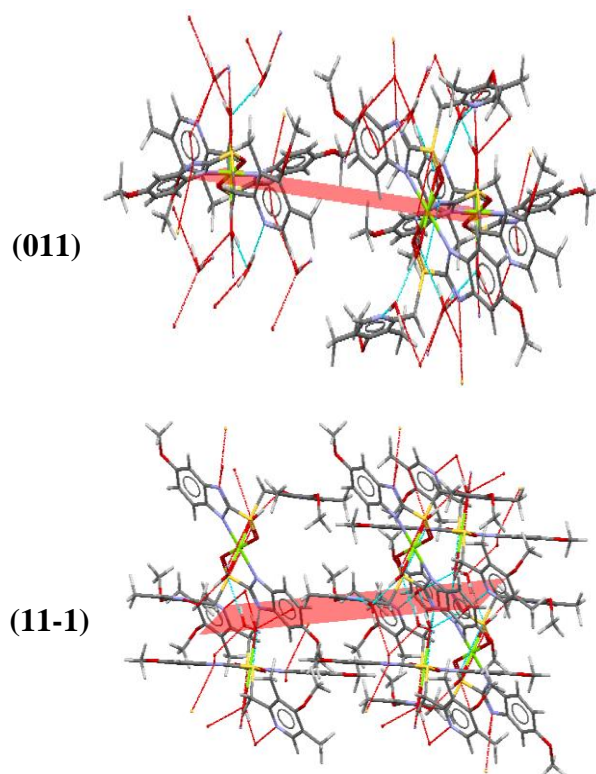
#### 4.4. Slip Plane

Table 4-4 shows that the plane (100) has the largest d-spacing with  $d_{hkl}$  equal to 16.43 Å which implies that it could serve as a candidate slip plane. Qualitative visualization of the plane (100) (Figure 4-11) indicates the presence of a slip plane between the methyl and methoxy groups present in DABOMD and no strong hydrogen bonding occurring crossing the plane. Thus, the crystal interaction is here controlled by weaker dispersion forces or only weak CH---O bonds. Other potential slip planes such as ((011), (11-1)) are controlled by classical hydrogen bonds or ionic interactions, thus more strongly interacting and held together (Figure 4-12).

Quantitative analysis from the attachment energy calculation (Table 4-4) indicates that (100) plane can serve as candidate slip plane since it clearly has the least negative  $E_{att}$ .



**Figure 4-11: Visualisation of the potential slip plane in DABOMD crystal (100) the major face of BFDH and the attachment energy (Reproduced with the permission of the International Union of Crystallography (IUCr) (Abouhakim *et al.*, 2020a)**



**Figure 4-12: Visualisation of (011) and (11-1) planes the second and third major face from attachment energy shows that slip is rather difficult in these planes since it requires breaking of the strongest hydrogen and ionic bonds in DABOMD (Reproduced**

with the permission of the International Union of Crystallography (IUCr) (Abouhakim *et al.*, 2020a)

The interaction energies along the (100) plane were computed using DFT energies via the CrysIn tool (built-in AstraZeneca). The interactions between methyl and methoxy groups result in a weak stabilization of only -1 to -4 kcal/mol as visualized in Figure 4-13. Other potential slip planes were also analysed and found to exhibit stronger interactions due to multiple hydrogen bonds. In summary, the qualitative observation of the BFDH morphology,  $E_{att}$  calculations and CrysIn analysis all indicate that the plane (100) is a candidate slip plane for DABOMD.

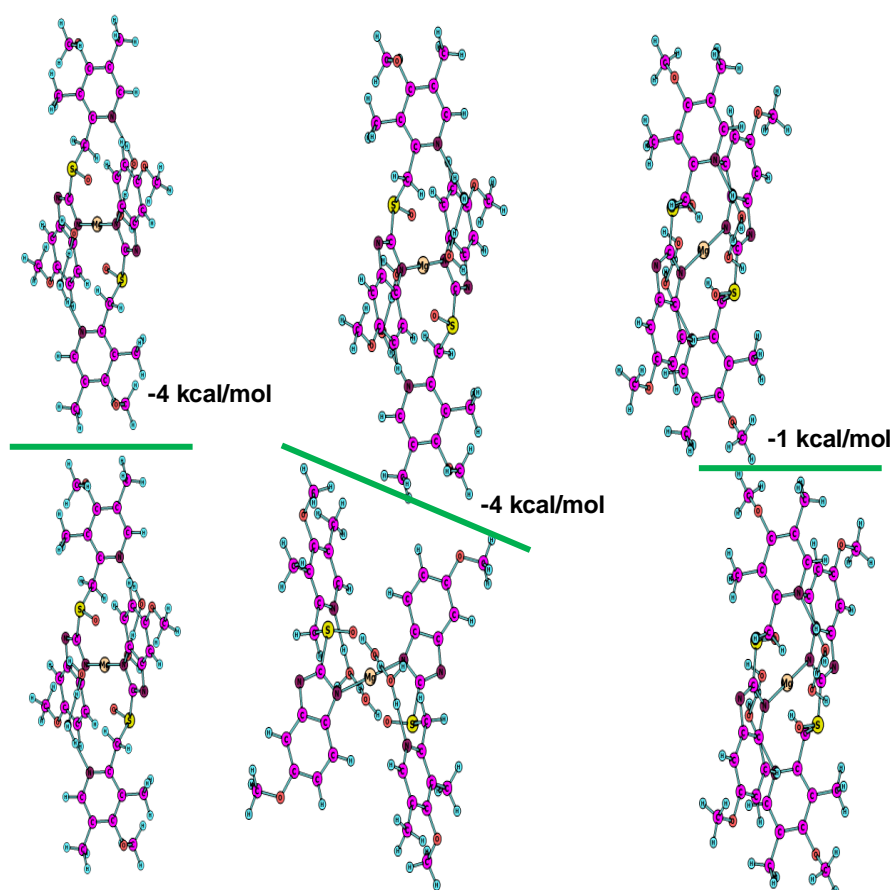


**Figure 4-13: Quantification of interactions along (100) plane visualized as green lines. (Reproduced with the permission of the International Union of Crystallography (IUCr) (Abouhakim *et al.*, 2020a)**

The visual examination of the crystal packing of DABOMD shows that the slip can occur through (100) face (Figure 4-11) is rather flat. Shariare *et al.*, and Halme *et al.* concluded that materials that show ductile behaviour tend to encompass flat slip planes due to the relatively lower force required to induce a displacement in flat slip planes compared with corrugated

ones. Also, materials exhibiting corrugated slip planes are more likely to glide in two directions upon stress, whereas, particles exhibiting a flat slip plane are more likely to slip in various directions (Hossain Shariare *et al.*, 2012; Halme *et al.*, 2019) This suggests that the slip of DABOMD is likely to glide in various directions (Figure 4-14).

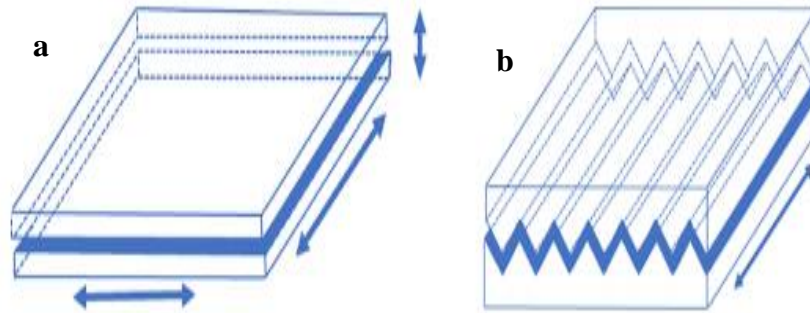


**Figure 4-14: Proposed slip direction in a crystal in a) a flat layer structure and b) corrugated structure (reprinted from (Halme *et al.*, 2019))**

In summary, the qualitative observation of the BFDH morphology,  $E_{att}$  calculations and CrysIn analysis all indicate that (100) is a candidate slip plane for DABOMD. In the event of external stress (i.e. from milling), the slip plane will facilitate the fracture and promote the plastic deformation of DABOMD.

#### 4.5. Mechanical Properties of DABOMD

The evaluation of elastic moduli values of DABOMD in the x, y, and z axis are illustrated in (Table 4-5), where the generated  $6 \times 6$  matrix of second order elastic constant obtained from the computational chemistry calculation is inserted in ELATE an online open source python model which allows a 3D visualisation of the Young's modulus (Gaillac, Pullumbi and Coudert, 2016). The calculated average Young's modulus is equal to 11.5 GPa and the calculated hardness is equal to 414 MPa which classifies DABOMD as moderately hard material according to Roberts *et al.* (1995) (Figure 4-15) (Roberts, Rowe and York, 1995). The results presented in (Table 4-5) show that DABOMD possesses variable Young's moduli across x-, y- and z-directions. Overall, the crystal system is rather isotropic (anisotropy value of 2.1, where, anisotropy is the difference in the Young's modulus in X a, Y and Z and is calculated from maximum Young's modulus value divided by the minimum one) (see Figure 4-16), but Young's moduli in different directions are in the borderlines according to the classification suggested by Roberts *et al.* (1995) (Figure 4-15).

**Table 4-5: Young's Modulus along different crystal axis for DABOMD (Reproduced with the permission of the International Union of Crystallography (IUCr) (Abouhakim *et al.*, 2020a)**

<b>Axis</b>	<b>Young's Modulus (GPa)</b>
<b>x</b>	10.38
<b>y</b>	9.12
<b>z</b>	15.09
<b>Min</b>	7.94
<b>Max</b>	16.45

It can be seen (Figure 4-16) that DABOMD has its lowest Young's modulus in x-(10.38 GPa) and y-directions (9.12 GPa), hence, according to the classification suggested by Roberts et al. (1995), it could potentially behave like a semi-brittle material with the tendency to plastic deformations when the crystal is stressed across x- and y-direction (Figure 4-17). Moreover, DABOMD exhibits its highest Young's modulus in the z-direction (15.1 GPa) which classify the crystal under a different category during the stressing events. It should be pointed that the z-direction is linked to the crystallographic dimension where the most hydrogen bonding are located (Figure 4-17), thus making this a more strongly bound crystalline direction, while the x-direction is linked to the dimension in which the (1 0 0) slip plane (Figure 4-11) is predicted.

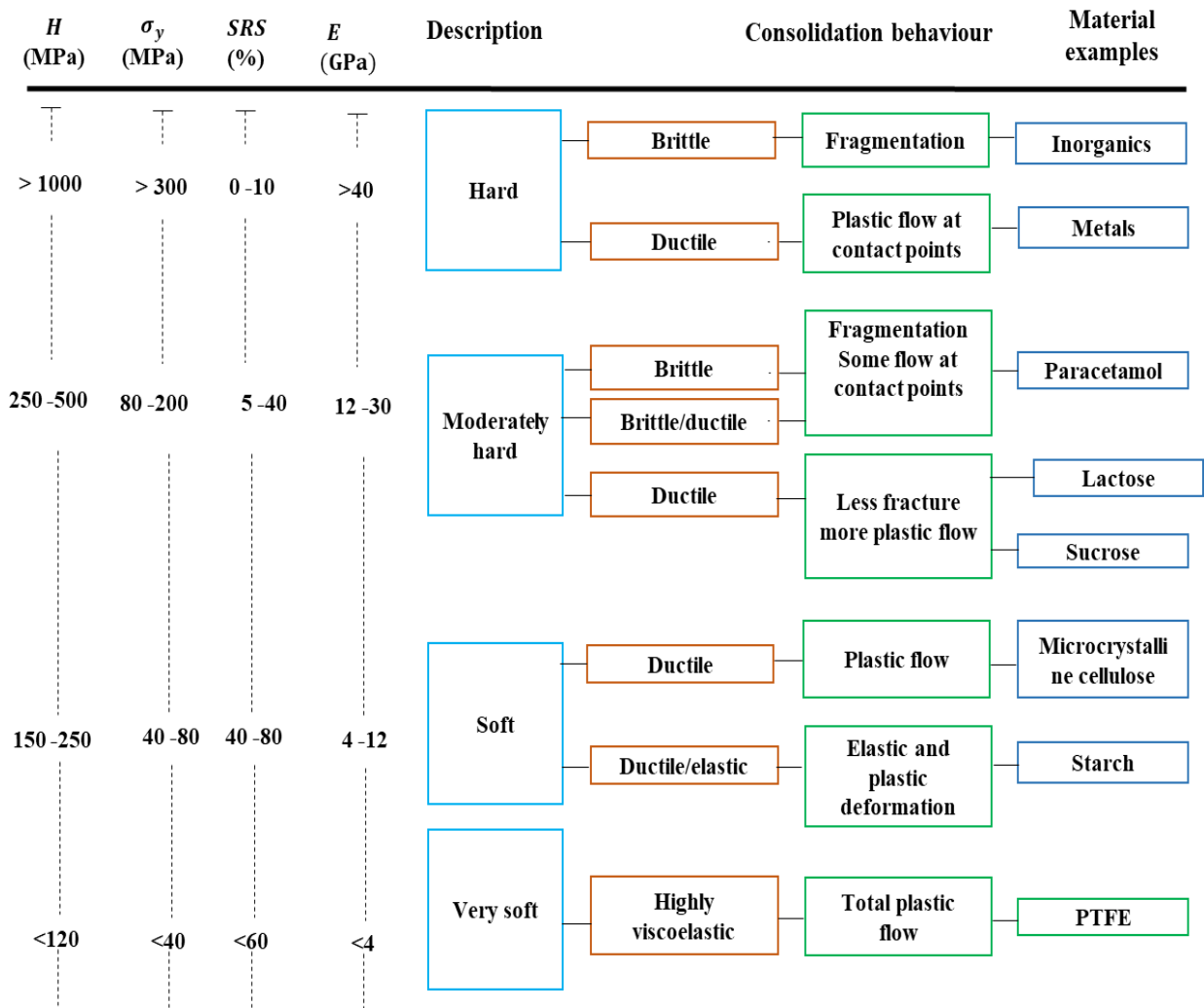
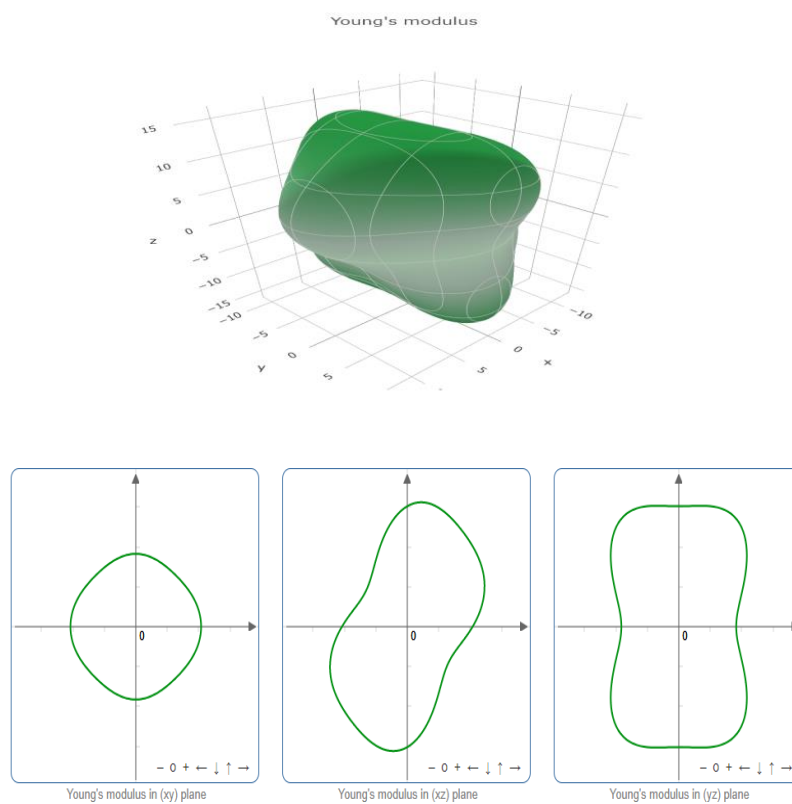
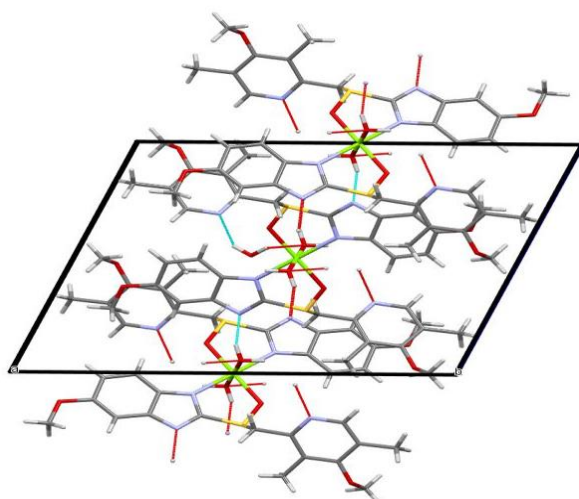


Figure 4-15: Classification of materials based on mechanical properties (adapted from Roberts et al. (1995)).



**Figure 4-16: Anisotropy of elastic moduli of DABOMD in different directions and planes. Highest Young's modulus is found along the z-axis. (Reproduced with the permission of the International Union of Crystallography (IUCr) (Abouhakim *et al.*, 2020a)**



**Figure 4-17: Hydrogen bonding in DABOMD crystal mainly along z-direction as visualized by red lines. (Reproduced with the permission of the International Union of Crystallography (IUCr) (Abouhakim *et al.*, 2020a)**

## 4.6. Conclusion

The first part of this chapter focuses on solving the single-crystal structure of diaqua-bis(Omeprazole)magnesium dihydrate (DABOMD), which encompasses four water molecules, two of which are directly coordinated to the magnesium cation while the other two are hydrogen-bonded to the pyridine functionality. DFT calculations show that the water molecules coordinated to magnesium are more strongly bonded in the crystal structure than the hydrogen-bonded water molecules. The expected difference in water mobility is qualitatively verified in TGA experiments, where two separate mass losses are observed at different temperatures. The second part of this chapter outlines the prediction of the crystal habit of DABOMD, the slip planes, and the mechanical properties. The qualitative and quantitative analysis of the crystal growth morphology shows that DABOMD displays a hexagonal plate with the most morphologically important face being (100). The visualisation of the crystal packing and quantitative assessment of the molecular interactions indicates that DABOMD encompasses a slip plane across (100). The calculation of the mechanical properties classifies DABOMD as moderately hard material. The conclusive remark is that DABOMD possesses a semi brittle nature and is likely to fracture particularly across the z-direction and is susceptible to amorphisation via plastic deformation. Hence, in the event of milling it is postulated that DABOMD would undergo extensive comminution and amorphisation.

## **Chapter 5 Predicting the Material Properties of $\beta$ -LGA by Modelling**

### **5.1. Introduction**

### **5.2. Crystal Structure**

### **5.3. Crystal Habit**

### **5.4. Slip plane**

### **5.5. Mechanical Properties**

### **5.6. Conclusion**

**This chapter focuses on the prediction of the underlying key material properties influencing the mechanistic behaviour of B-LGA during milling including crystal structure, crystal habit, and mechanical properties.**

## 5.1. Introduction

This chapter analyses the crystal structure of  $\beta$ -LGA. Experimental and modelling approaches are used to determine the crystal habit. The information from the crystal structure is employed to predict the mechanical properties and potential slip planes of  $\beta$ -LGA following the same methodology employed for DABOMD as in chapter 4. The computational work of this chapter was performed in AstraZeneca by Dr Sten Nilsson including the growth morphology by attachment energy model, the calculation of the mechanical properties, and the quantification of interactions for the slip plane assessment. The author of this chapter conducted the rest of the work, including the experimental part and data analysis.

## 5.2. Crystal Structure

### 5.2.1. Crystallisation

Single crystals of  $\beta$ -LGA are needed to identify the morphological properties.  $\beta$ -LGA single crystals were grown via cool crystallisation.  $\beta$ -LGA powder was dissolved in deionised water to form a saturated solution. Subsequently, the solution was filtered and stored at a temperature of 5°C for 10 weeks. Small crystals were formed and harvested from the solution. Figure 5-1 shows that  $\beta$ -LGA exhibits a needle shape of approx. 3mm in length.

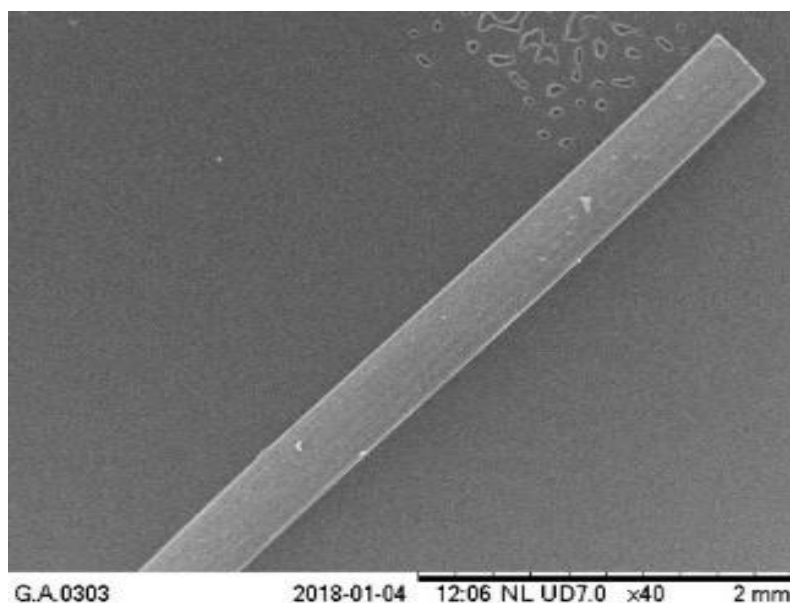


**Figure 5-1: SEM shows a grown single crystal of  $\beta$ -LGA**

### 5.2.2. Crystal Structure

The crystal structure of  $\beta$ -LGA molecule (Figure 5-2) was obtained from CCDC with the reference code LGLUAC01 and was optimised using Materials Studio (Biovia). The crystal is composed of molecules that are firmly held together with chains of hydrogen bonds. Where each molecule consists of four donors and four acceptors atoms forming the bonds  $\text{NH}_3\cdots\text{CO}$ , and  $\text{OH}\cdots\text{CO}$  (Hirayama *et al.*, 1980; Hammond, Pencheva and Roberts, 2012). The crystal packing arrangements in  $\beta$ -LGA can be viewed down the b axis in Figure 5-3 and the  $\beta$ -LGA crystal information is shown in Table 5-1. Both NH and OH are donors and participate in the hydrogen bonding. Strong  $\text{OH}\cdots\text{H}$  bonds form between the  $\alpha$  carboxylate (O1-C1-C2-C3) and the  $\delta$  carboxylate (O3-C5-C4) making hydrogen bond chains. Whereas,  $\text{NH}\cdots\text{H}$  bonds interlinks and form three-dimensional network. Where O1 accepts hydrogen bonds from two  $\text{NH}_3^+$ , O2 accepts hydrogen bonds from OH, and O3 accepts a hydrogen bond from  $\text{NH}_3$ . Information about the bonds and the angles involved in  $\beta$ -LGA can be found in (Hirokawa, 1955; Mogens S. Lehmann, Koetzle and Hamilton, 1972)

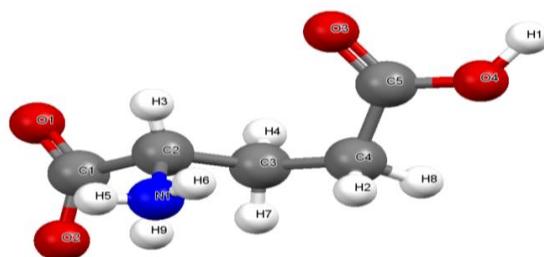


Figure 5-2:  $\beta$ -LGA molecular structure. N: blue, O: red, C: grey, H: white

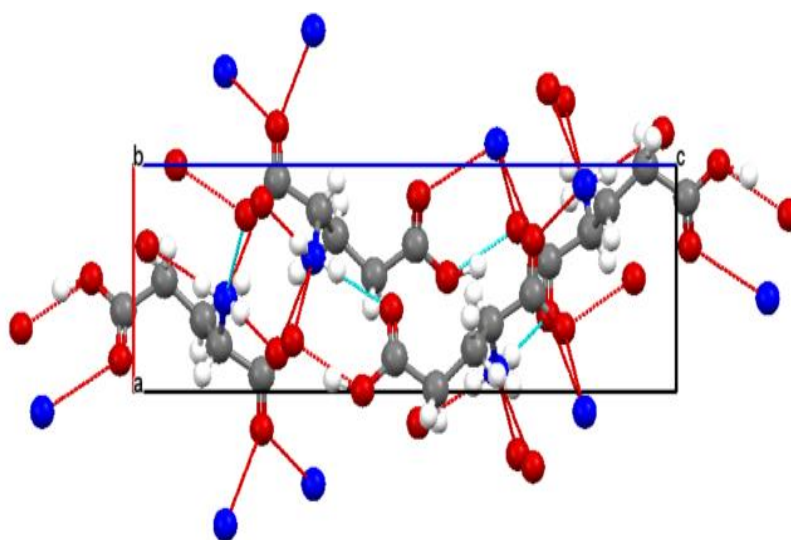


Figure 5-3: Crystal structure of  $\beta$ -LGA viewed from b axis. Where, N: blue, O: red, C: grey, H: white, and Hydrogen bonds in red

Table 5-1:  $\beta$ -LGA crystal data information (Hirokawa, 1955; M. S. Lehmann, Koetzle and Hamilton, 1972)

Empirical formula	$C_5H_9NO_4$
Formula weight	147.13
Temperature/K	0
Crystal system	Orthorhombic
Space group	$P2_1/c$
$a/\text{\AA}$	5.154
$b/\text{\AA}$	6.142
$c/\text{\AA}$	17.274
$\alpha/^\circ$	90
$\beta/^\circ$	90
$\gamma/^\circ$	90

<b>Volume/Å<sup>3</sup></b>	618.048
<b>Z</b>	4
<b>Z'</b>	4
<b>ρ<sub>calc</sub>/cm<sup>3</sup></b>	1.57
<b>μ/mm<sup>-1</sup></b>	0.129
<b>F(000)</b>	312
<b>R-Factor (%)</b>	2.6
<b>Polymorph</b>	Beta Polymorph

### 5.3. Crystal Habit

The crystal habit for  $\beta$ -LGA of the experimentally grown crystals has needle-like morphology with the dominant face being (002) (Figure 5-4a) which is in agreement with (Palanisamy and Karuppanan, 2016; Aarthi *et al.*, 2018; Turner *et al.*, 2020).

#### 5.3.1. BFDH

The BFDH morphology of  $\beta$ -LGA is displayed in Figure 5-4b. BFDH morphology shows that  $\beta$ -LGA crystal has an elongated rectangular shape with (002) being the most dominant, followed by (011) and (101) faces. The dominant face (002) of the BFDH morphology agrees with the experimentally grown crystals. However, the BFDH morphology has a much thicker habit compared to the experimentally grown crystals.

#### 5.3.2. Attachment Energy

The molecular modelling software Materials Studio (Biovia) was used to calculate the growth morphology of  $\beta$ -LGA using Compass II force field. Figure 5-4c shows the predicted morphology of  $\beta$ -LGA single crystal using the attachment energy models. The attachment energy calculation (Table 5-2) generates hexagonal-shaped crystals with the most dominant face being (110) which occupies an area of 41.7 % followed by the faces (002) and (011) which sit on an area of 35.2% and 21.5% respectively.

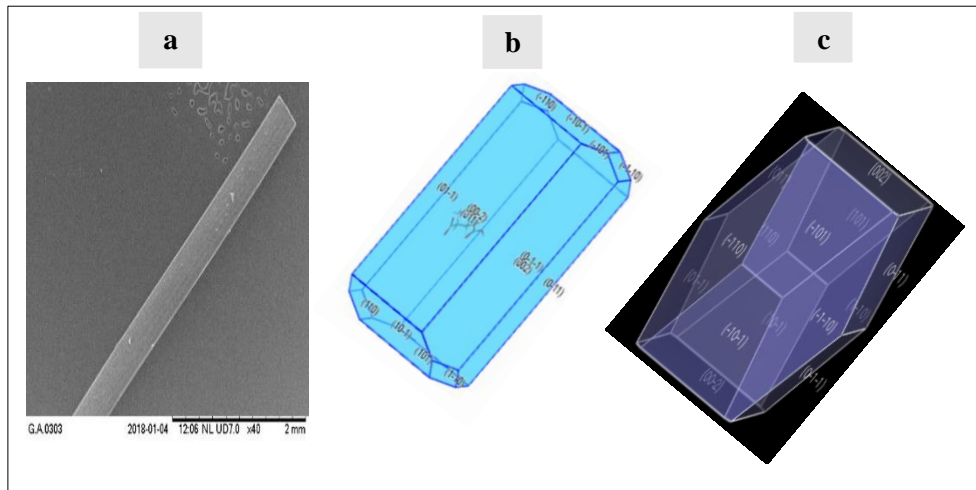


**Figure 5-4:  $\beta$  –LGA: a) Morphology from experimentally grown crystals, b) Predicted morphology using BFDH Model c) Predicted morphology using  $E_{att}$  growth morphology**

Overall, for  $\beta$  –LGA, none of the predicted models agrees with the experimental habit, nonetheless, (002) the major experimental face coincides with the BFDH major face and with the second major face in the  $E_{att}$  model which indicates that this face is the preferred orientation for crystals. The discrepancy between the predicted habits and the experimental habit is down to the fact that; the BFDH morphology is based on the lattice geometry, which does not account for the internal crystal forces. Also, the attachment energy model assumes that the  $E_{att}$  energy is proportional to the growth rate of the faces, which might not always be the case (Winn and Doherty, 2000; Sun and Kiang, 2008). Moreover, these models are designed to predict the habit of the crystals that are grown in vapour. Hence, they are not always accurate for predicting the habit of the crystals that are grown from solution; giving that they do not account for the external forces and the effect of the solvents which might impact on the habit (Winn and Doherty, 2000).

The Zingg diagram morphology characterization (using dimensions from SEM image, BFDH and  $E_{att}$ ) summarises the shape factors of the experimental and modelled habits (Figure 5-5).

**Table 5-2:  $\beta$  –LGA results from attachment energy ( $E_{att}$ ) calculations of growth morphology**

$(h k l)$	Total $E_{att}$ ( $kcal mol^{-1}$ )	Area (%)
(110)	-119.9	41.7
(002)	-93.3	35.2
(011)	-122.6	21.6
(101)	-156.9	1.4

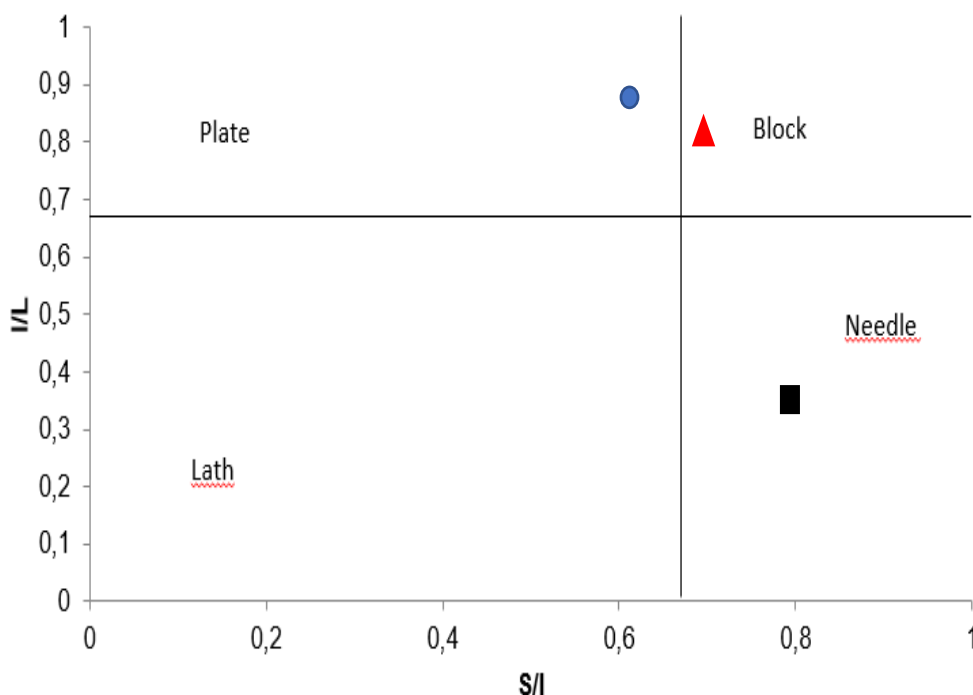


**Figure 5-5:  $\beta$  –LGA Zingg diagram, where L is the longest dimension, I is the intermediate dimension, and S is the shortest dimension. Dimensions obtained from morphologies derived from BFDH (red triangle), attachment energy (blue circles), experiment (back square)**

## 5.4. Slip Plane

To evaluate the slip plane of  $\beta$  –LGA, combined qualitative and quantitative assessments are employed. A holistic visualization of the crystal packing across the [100], [010] and [001] projection planes (Figure 5-6) shows that the crystal has an extensive network of hydrogen bonding with no observed possible slip plane. The different interactions can be easily visualised in Figure 5-7 where, the strongest, intermediate, and weaker interactions are represented by long yellow lines, long pink lines, and short pink lines respectively. These binding interactions were quantified using CrysTool as shown in Table 5-3. It can be seen that the charge assisted ionic bonding between  $NH^3+$  and  $COO^-$  groups has the strongest interaction of  $-35\text{ kcal/mol}$  and accounts for the majority of the interactions in  $\beta$  –LGA crystal which agrees with the qualitative analysis of the crystalline packing. The materials exhibiting large amounts of hydrogen bonds possess a brittle nature (Datta and David J.W. Grant, 2004). Hence, it is postulated that  $\beta$  –LGA is more prone to brittle deformation rather than plastic deformation.

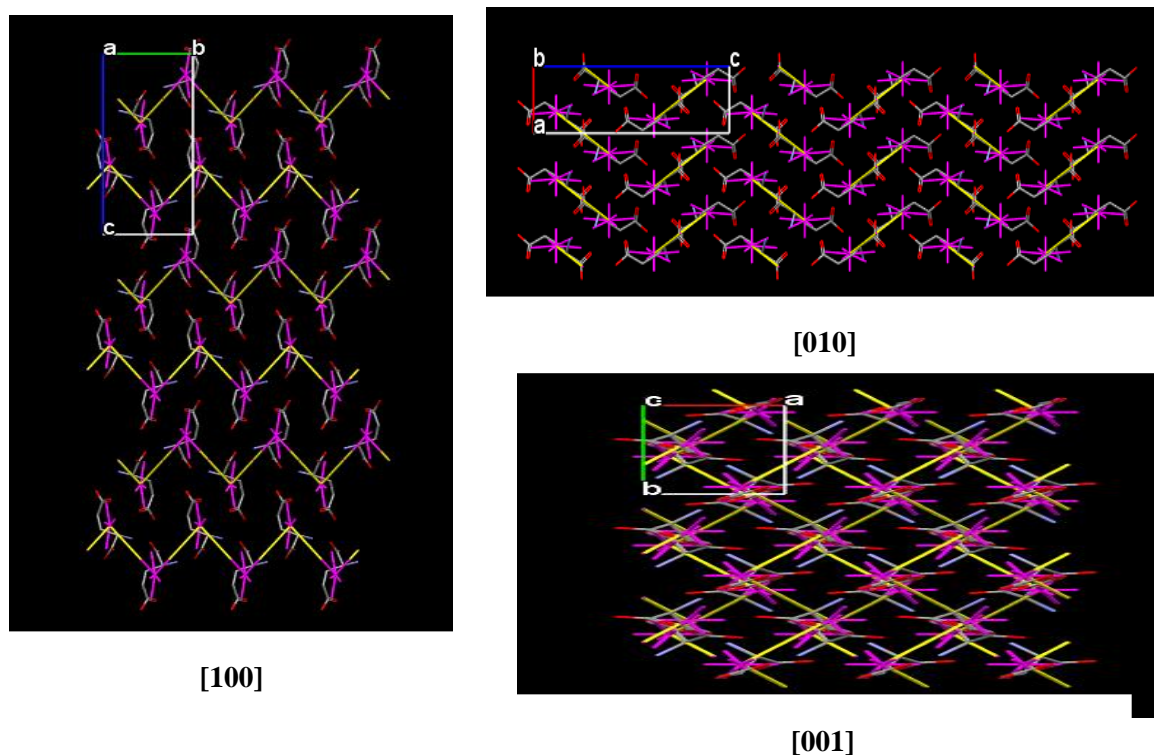


**Figure 5-6: (1) Visualisation of the crystal packing of  $\beta$  –LGA shows that no slip plane is present due to the extensive hydrogen bonds interactions including charged assisted hydrogen bonds shown in yellow**

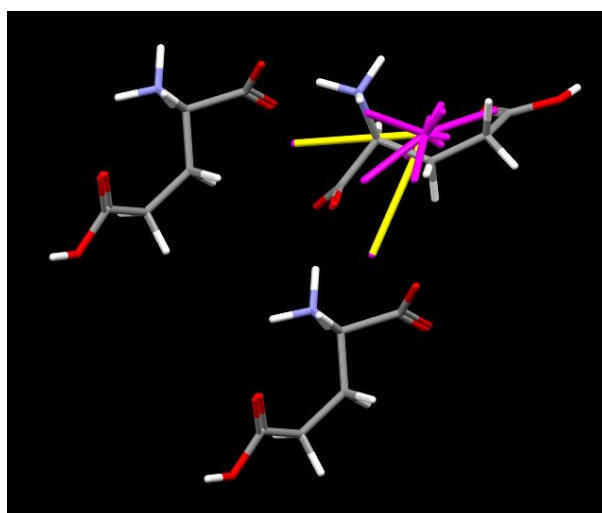


**Figure 5-7: Qualitative Visualisation of the different interacting forces in  $\beta$  –LGA. The longer the line the stronger the interaction. Where, long yellow represents the strongest interactions, and long pink represent the medium interactions, whereas, short pink represents weak interactions. N: blue, O: red, C: grey, H: white**

**Table 5-3: Table shows the calculated interactions in  $\beta$  –LGA crystal**

Type of Interaction	Qualitative Observation	Calculated Interaction Energy <i>kcal/mol</i>
$NH^{3+} + COO^{-}$	short-distance yellow line	-35
$NH^{3+} + COO^{-}$	long-distance	-21
H-bond between $COOH$ and $COO^{-}$	-	-18
$NH^{3+}$ and $COOH$	short-distance	-17
$NH^{3+}$ and $COOH$	long distance	-11
CH carbonyl Pi	-	-6

The crystal growth occurs typically in the direction of the strongest interactions (in this case the long yellow lines), the pattern of the strongest interactions can be visualised in a packed crystal as in Figure 5-8 which suggests that the crystal is growing in the b direction. An observation of the BFDH morphology shows that the growth direction is from left to right (Figure 5-9). Based on this growth direction, it is expected that BFDH morphology must be much thinner as is the case in the experimentally grown crystals. For a better prediction of the crystal growth morphology, a model is required that can predict the habit based on the strongest interactions in the crystal.

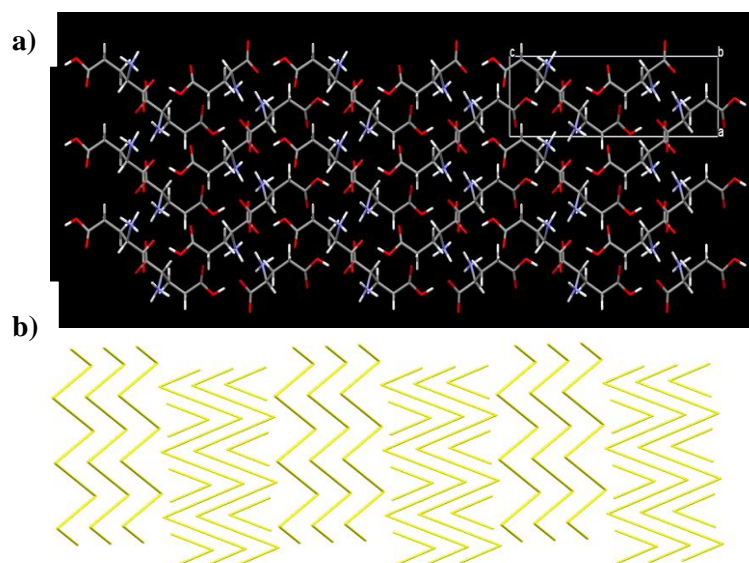


**Figure 5-8: Visualisation of the a) 3\*3 crystal packing of  $\beta$  –LGA and b) its corresponding pattern of the strongest hydrogen assisted interactions**

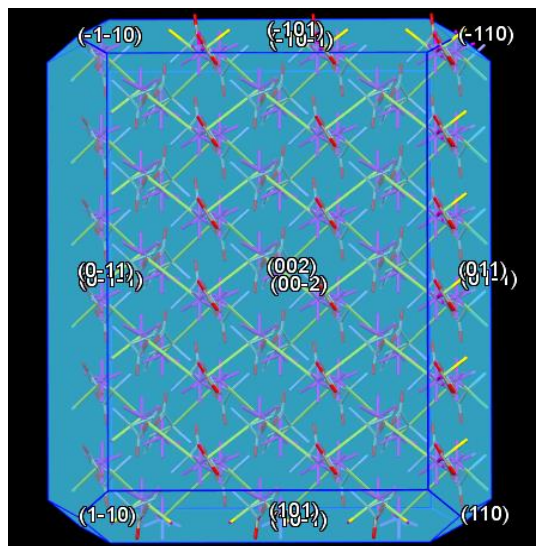


**Figure 5-9: Visualisation of the interactions within (002) face**

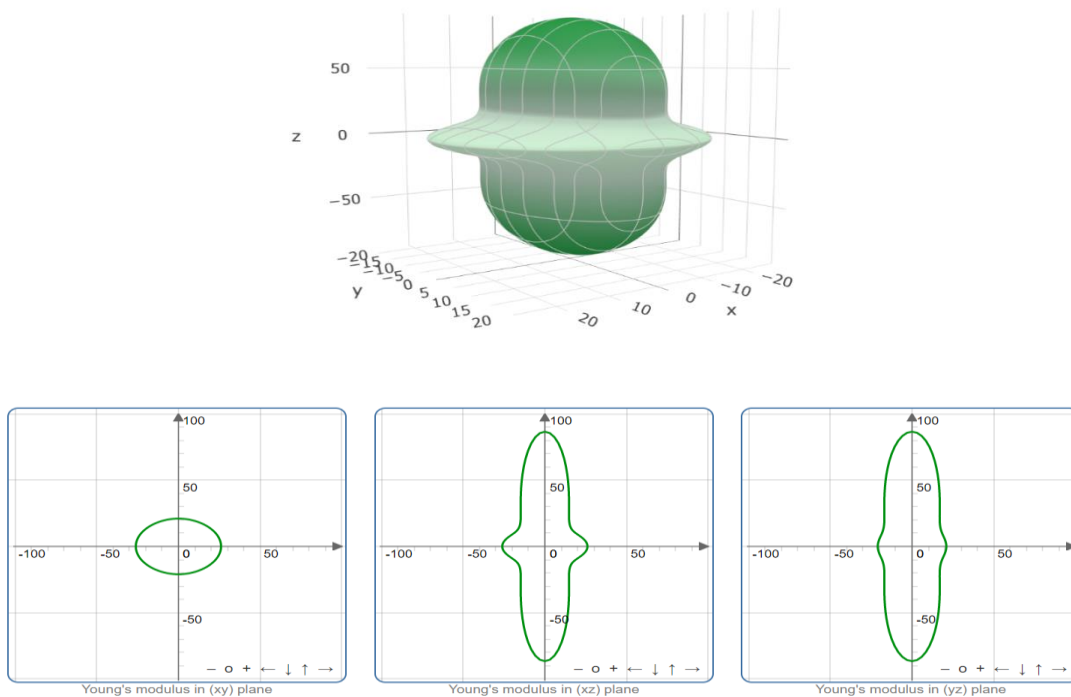
## 5.5. Mechanical Properties

The evaluation of elastic moduli values of  $\beta$ -LGA in the x, y, and z-axis are illustrated in (Table 5-4). The average calculated Young's modulus is equal to 32.9 GPa and the calculated hardness is equal to 1605 MPa which classifies  $\beta$ -LGA as hard material according to Roberts et al. (1995) (Figure 4-15). This outcome further stresses that  $\beta$ -LGA is would rather undergo a significant fracture. The elastic moduli in the directions x, y, and z show that  $\beta$ -LGA has a higher value in z axis since they are linked to crystallographic direction which associated with the most potent interaction as compared to the x and y-axis. This outcome is compatible with the interaction quantifications, which further supports that  $\beta$ -LGA could potentially experience significant fracture and lower plastic deformation in the event of milling. Also, it can be seen  $\beta$ -LGA exhibits a large anisotropy of value equals to 4.18 (calculated from maximum Young's modulus value divided by the minimum Young's modulus value) owed to the highest ionic interactions occurring in the z-direction (Figure 5-10) which suggests that  $\beta$ -LGA could fracture extensively in the z direction. in the z direction.

The predicted mechanical properties using computational chemistry provide a good approximation, however experimental approach is highly desirable i.e. using nanoindentation.

**Table 5-4: Young's Modulus along different crystal axis for  $\beta$  –LGA**

Axis	Young's Modulus (GPa)
<b>X</b>	26.1
<b>Y</b>	21.0
<b>Z</b>	86.6
<b>Min</b>	21
<b>Max</b>	87

**Figure 5-10: Anisotropy of elastic moduli of  $\beta$  –LGA in different directions and planes. Highest Young's modulus is found along X-axis (visualised in (Romain Gaillac, 2016))**

## 5.6. Conclusion

Modelling was conducted on  $\beta$  –LGA crystals to predict its crystal habit, mechanical properties, and identify any possible slip of the planes in the event of milling. The experimentally grown crystals have a needle-shaped morphology. Neither BFDH, nor  $E_{att}$  energy model predicted a crystal habit that agrees with the experimental habit, which has needle shape. However, the BFDH predicted that morphology shares the same morphologically important face (002) as that of the experimentally grown crystals, which also coincides with the second morphologically important face in the attachment energy model. The calculation and the visualisation of the bonding interactions reveal that  $\beta$  –LGA exhibits an extensive

network of hydrogen bonds with many ionic hydrogen interactions which indicates that  $\beta$ -LGA is likely to experience a significant fracture. The calculations of the mechanical properties show that  $\beta$ -LGA possesses high values of Young's modulus and hardness which classifies the material as hard and has no-slip planes which are mainly owed to the presence of a vast network of strong interactions including ionic hydrogen bond network within its crystal structure. This suggests that in the event of milling,  $\beta$ -LGA will show a high propensity to fracture (significant comminution) and a lower susceptibility to amorphisation through plastic deformation as energies from milling will be used in the process of fracture rather than wasted on plastic deformation.

## **Chapter 6 Milling of DABOMD**

### **6.1. Introduction**

### **6.2. Milling of DABOMD with planetary ball mill**

### **6.3. Milling of DABOMD with single ball mill**

### **6.4 Conclusion**

**This chapter outlines the process of milling DABOMD using planetary ball mill and single ball mill. The impact of these mills on the physical and chemical properties of the samples was assessed and compared. A relationship was established between the predicted material properties and the observed milling behaviour.**

## 6.1. Introduction

The impact of milling on the physical and chemical structure of DABOMD is investigated in this chapter. The aim is to verify the anticipated behaviour obtained from the modelling work conducted in Chapter 4 and to establish a relationship between the material properties, milling conditions, and the milling behaviour of the solid pharmaceutical. Ball mill is commonly used in the pharmaceutical industry for the size reduction of pharmaceutical solids. This type of mill was repeatedly reported for its association with the mechanical activation and amorphisation of pharmaceuticals including, Budesonide (Descamps *et al.*, 2007), Indomethacin (Otsuka, Otsuka and Kaneniwa, 1994), and Cefalexin (Otsuka Makoto and Kaneniwa Nobuyoshi, 1983; Otsuka, Otsuka and Kaneniwa, 1994). Two types of ball mills are employed in this section, including PM100 planetary ball mill (PBM) and MM200 single ball mill (SBM). The extent of size reduction (comminution) and mechanochemistry (amorphisation here) will be assessed and compared for the two mills. Since in theory, the two mills generate different amounts of energy which can ultimately lead to a variable impact on the milling behaviour of the material (Chauruka *et al.*, 2015). The evaluation of the impact of milling involves full characterisation of the feed and milled DABOMD to examine its morphology, size, crystalline structure, thermodynamic properties, and intermolecular structure. This is achieved through the implementation of solid-state analytical techniques such as SEM, laser diffraction, XRPD, TGA, DSC, and FTIR.

The first part of this chapter outlines the milling of DABOMD using a planetary ball mill. The materials in this part of the chapter were reproduced with the permission of American Chemical Society (ACS). The second part of this chapter addresses the milling experiments performed using a single ball mill. In this Chapter the amount of amorphous DABOMD formed with planetary ball mill was quantified using chemometric analysis of the FTIR which was performed by Dr Maryam Asachi. Also, the computational modelling of the FTIR spectra of DABOMD was conducted by Dr Sten Lill. All the rest of the work in this chapter including the analysis of the data obtained from collaborative efforts was conducted by the author of this chapter.

## 6.2. Milling DABOMD with Planetary Ball Mill

### 6.2.1. Experimental Setup

The planetary ball mill PM100 used in this work is shown in Figure 6-1. The powder samples of DABOMD were milled between 1 and 300 min at a speed of 650 rpm in 250 ml steel jar, using four balls with a diameter equal to 15 mm at a ball to powder ratio (BPR) of 10:1 by weight. The selected BPR allows for increased contacts and better particle breakage and size reduction (Chauruka, 2015). The milling jar was filled for up to two-thirds of its volume with the powder and the balls. The mill was set to run for 20 min with periodical breaks to prevent the temperature rise in the system. The media lid was sealed tightly with the aid of a safety clump. The mill was regularly monitored for safety and to prevent a temperature rise of the bulk.

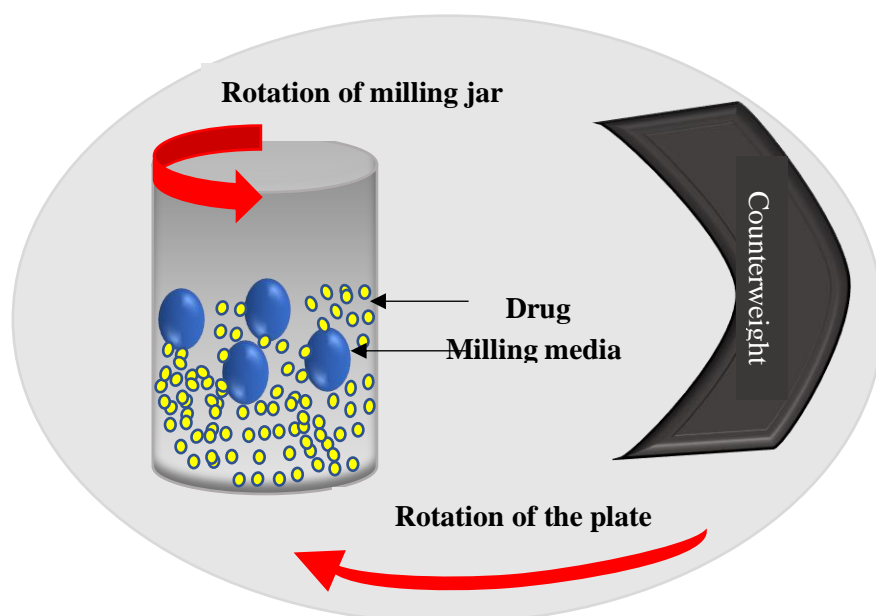


**Figure 6-1: Schematic of a planetary ball mill (Reproduced with the permission of American Chemical Society (ACS) (Abouhakim, et al., 2020b))**

### 6.2.2. Power Characterisation of DABOMD

#### 6.2.2.1. Particle Size Distribution

##### 6.2.2.1.1. Particle Size Distribution Using Laser Diffraction

The as-received non-milled powder of DABOMD was milled using a planetary ball mill at successive times from 1 min to 300 min. The particle size measurement of the feed and milled powders of DABOMD was performed in Malvern 3000 dry system. The powder was dispersed in the air at a pressure of 2 bars, a feed rate of 50%, and at an obscuration ranging from 2 to 10%. The average particle size distribution was obtained from a two replicates sample measurement for reliability. The standard deviation of the average diameter calculated from three replicates of the non-milled sample is 1.49, which is considered within the accepted range

(+2) according to (Horiba, 2019). The data obtained from laser diffraction measurement is presented in the form of particle size distribution PSD (Figure 6-2), and in the form of cumulative distribution (Figure 6-3). The particle size is reported according to particle size diameters  $D_{10}$ ,  $D_{50}$ , and  $D_{90}$  which represent 10%, 50% and, 90% of the total volume distribution in a measured sample respectively as shown in (Table 6-1).

It can be seen from Figure 6-2 that the process of milling caused a significant reduction in  $D_{50}$  and  $D_{90}$  over time. The particle size distribution of the feed sample has a trimodal profile owed to the presence of particles of various sizes and agglomerates which transformed into a narrower profile centred around  $10 \mu m$  with longer milling time. There was a significant size reduction between the non-milled samples and those milled for 300 min. Where the non-milled sample had a  $D_{90}$  of  $211 \mu m$  while, the 300 min milled sample had a  $D_{90}$  of  $35.3 \mu m$ . Interestingly, the cumulative size distribution depicted in (Figure 6-3) shows a significant size reduction between the non-milled and the 15 min milled samples which can be suggested to be related to comminution + deagglomeration process, followed by a steady size reduction between 15 min and 300 min of milling. Moreover, the PSD and cumulative data indicate that the agglomeration is taking place as a result of the adhesion of the produced fines to the larger particles which can be associated with a large amount of energy dissipated at the beginning of milling (first 1 min) which promotes cold welding of particles. Analysis of the concentration of the fine as a function of time showed negligible variation in  $D_{10}$  (diameter representing 10% of the distribution), which is likely to be due to the lack of impact of the planetary ball mill on the fines and might also be due to the resolution limit of the laser diffraction measurement method.

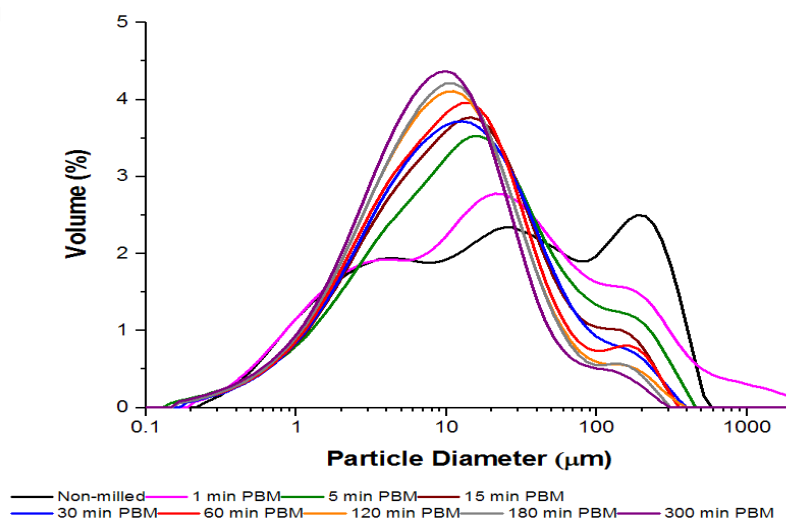


**Figure 6-2: Particle size distribution of non-milled and milled DABOMD in planetary ball mill from 1min to 300 min (Reproduced with the permission of American Chemical Society (ACS) (Abouhakim et al., 2020b))**

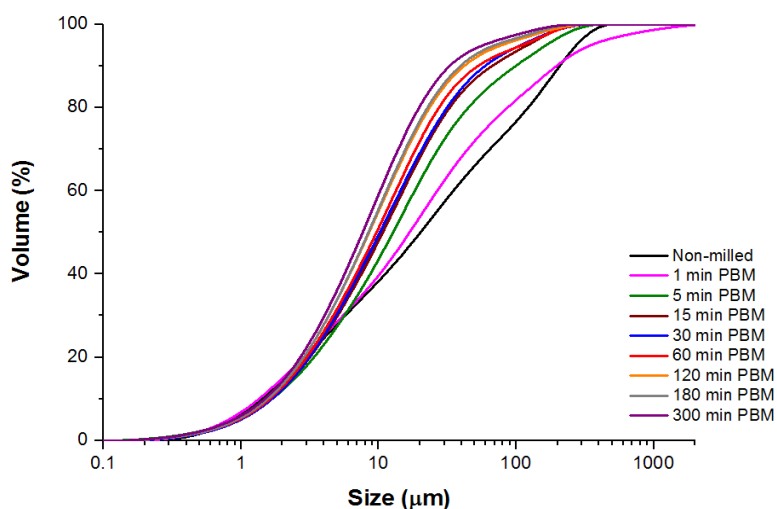


**Figure 6-3: Cumulative distribution of non-milled and planetary ball milled DABOMD from 1min to 300 min (Reproduced with the permission of American Chemical Society (ACS) (Abouhakim et al., 2020b))**

**Table 6-1: Characteristic sizes ( $D_{10}$ ,  $D_{50}$ , and,  $D_{90}$ ) of non-milled and milled DABOMD samples in planetary ball mill from 1min to 300 min (Reproduced with the permission of American Chemical Society (ACS) (Abouhakim et al., 2020b))**

Sample	Particle Size ( $\mu\text{m}$ )		
	$D_{10}$	$D_{50}$	$D_{90}$
<b>Non-milled</b>	1.5	21.2	211.0
<b>1 min PBM</b>	1.5	16.4	186.0
<b>5 min PBM</b>	1.7	12.7	98.1
<b>15 min PBM</b>	1.7	11.2	66.9
<b>30 min PBM</b>	1.7	9.9	58.9
<b>60 min PBM</b>	1.7	9.9	51.8
<b>120 min PBM</b>	1.6	8.7	45.6
<b>180 min PBM</b>	1.7	8.7	40.1
<b>300 min PBM</b>	1.5	7.5	35.3

#### 6.2.2.1.2. Particle Size Using Image Analysis

A scanning electron microscope (SEM) was used for quantifying the size of particles of the non-milled sample as a complementary technique for laser diffraction (Figure 6-4). ImageJ analysis software was employed to analyse more than 500 particles from multiple SEM images of each sample. The number-based measured the average diameter of the non-milled sample of DABOMD is equal to  $17.9 \mu\text{m}$  and has the standard deviation of 1.59. Particle quantification SEM is compared with the measured median diameter ( $D_{50}$ ) obtained by laser diffraction shows that the two are in the same range (Table 6-2). The coefficient of variation was obtained by

dividing the standard deviation by the average median diameter. The median diameter  $D_{50}$  of the sample milled in the planetary ball mill follows the same reduction pattern as that observed with the laser diffraction analysis, and the size is comparatively in the same range even that SEM is a different technique to laser diffraction. SEM size analysis might not be conclusive due to the limitation involved with presenting all the sample powder in a single SEM stub, in addition to the fact that it only shows two dimensional of the particles.

**Table 6-2: Measurement of the non-milled DABOMD powder using SEM and laser diffraction**

Measuring technique	Average/Median diameter ( $\mu m$ )	Standard deviation	Coefficient of variation	Small observe diameter ( $\mu m$ )
SEM	17.9	1.49	0.083	3.3
Laser diffraction	21.2	1.59	0.075	-

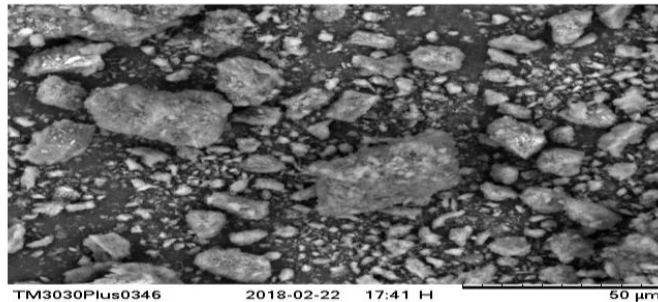


**Figure 6-4: SEM used for quantitative image analysis**

**Table 6-3: Median diameter of DABOMD non-milled and milled with planetary ball mill, measured using image analysis**

Sample	Number based average diameter ( $\mu m$ )
Non-milled	17.9
1 min PBM	12.1
5 min PBM	9.5
15 min PBM	9.1
30 min PBM	8.6
60 min PBM	7.4
120 min PBM	6.7
180 min PBM	5.5
240 min PBM	5.5
300 min PBM	5.2

### 6.2.2.2. Morphology

The surface and the morphological properties of DABOMD were examined using a Carl Zeiss EVO MA15 scanning electron microscope (SEM) at 20 kV in backscattered imaging mode. Carbon tabs were coated with powder samples and placed on the SEM metal stubs. Sample stubs were sputter-coated with a conductive layer of platinum before the analysis to prevent the charging of the samples.

Representative SEM images of the non-milled and milled powders of DABOMD from 1 min to 300 min are shown Figure 6-5 to allow a more straightforward observation of the feed and the milled product of DABOMD, further images of all the milled samples are shown in Figure 6-6 and Figure 6-7. It can be observed that the non-milled particles of DABOMD are irregular in shape and display a variable size distribution and some agglomerated crystals (which are low in number but high in volume) which agrees with the PSD analysis. As the milling proceeds, the particle shapes have not much changed, but a remarkable de-agglomeration process can be observed throughout the milled samples, yet some of the produced fine particles can be observed to adhere to the surface of larger ones see, for example in Figure 6-7j .

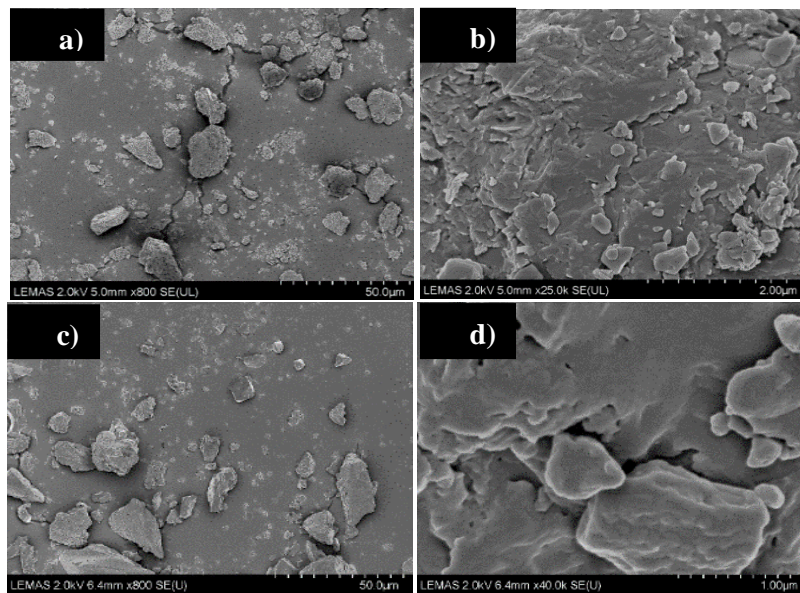


**Figure 6-5: SEM images show the morphology of DABOMD, a-Non-milled ( $\times 800$ ), b-Non-milled ( $\times 25000$ ), c-300 min milled ( $\times 800$ ), d-300 min milled ( $\times 25000$ ). Figures are shown for easier comparison of the feed and product DABOMD**

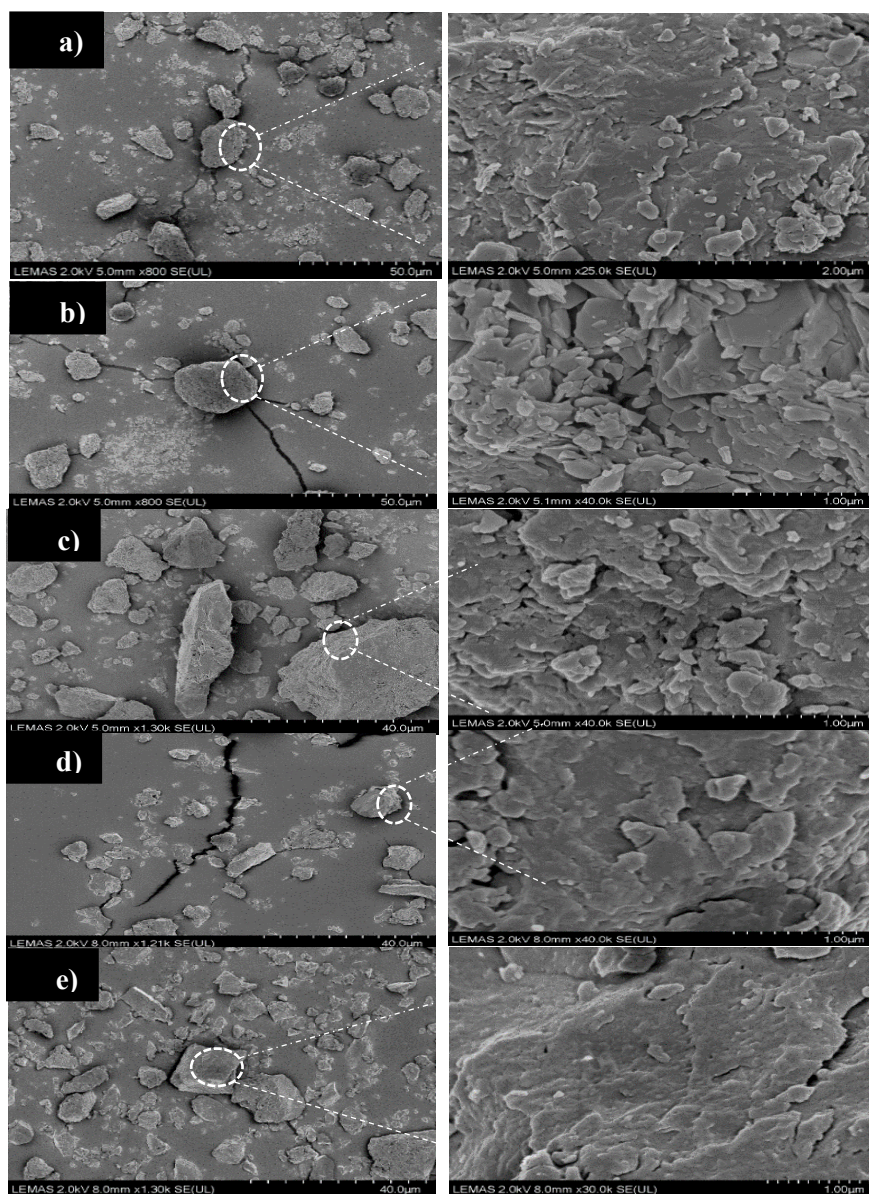


**Figure 6-6: SEM images show the morphology of DABOMD particles (left) and their surfaces (on the right), a-Non-milled, b- 1min milled, c-5min milled, d-15min milled, e- 30min planetary ball mill (Reproduced with the permission of American Chemical Society (ACS) (Abouhakim et al., 2020b))**

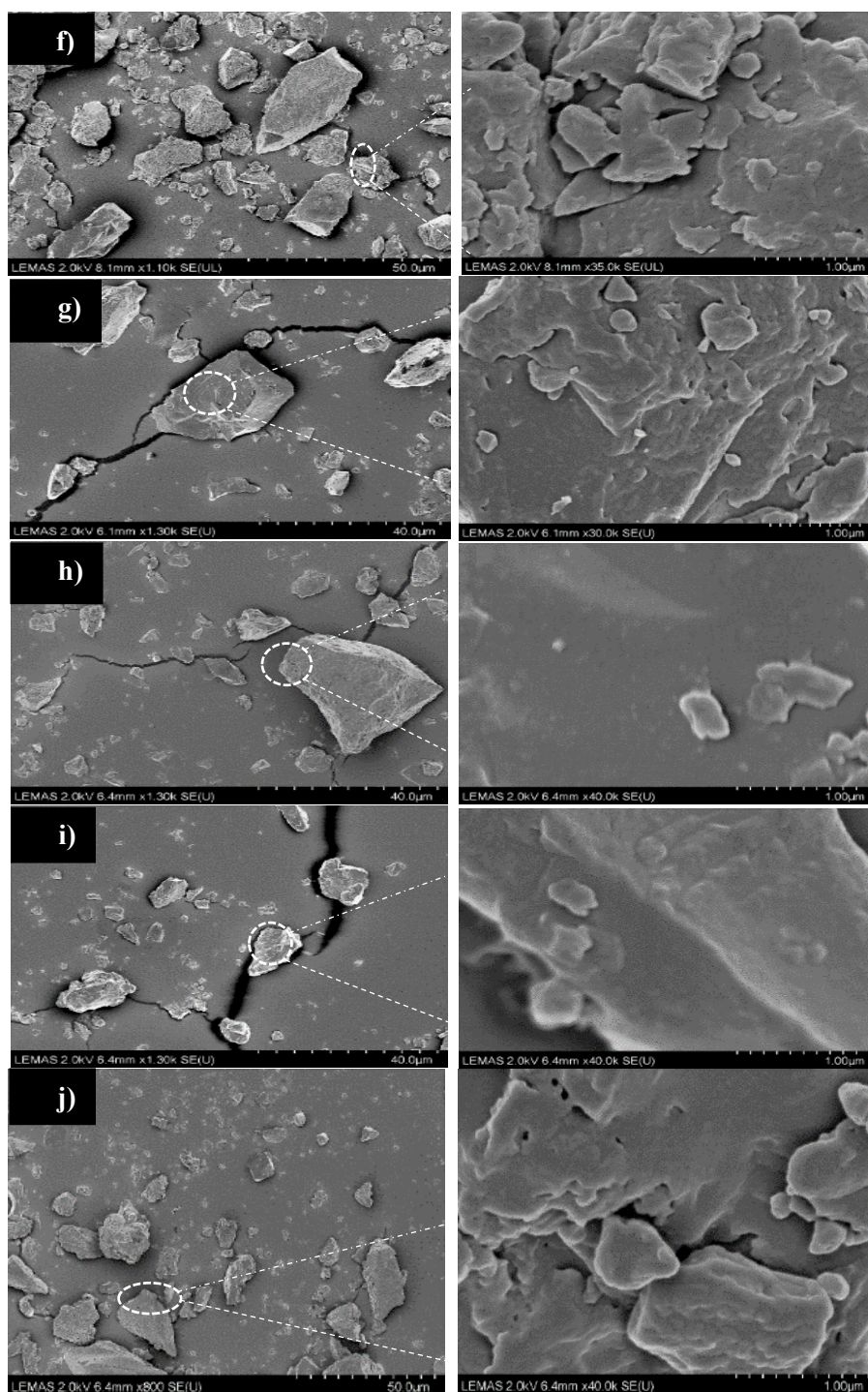


**Figure 6-7: SEM images show the morphology of DABOMD's particles (left) and their surfaces (on the right), f-60min milled, g- 120min milled, h-180min milled, i-240min milled, j-300min planetary ball mill (Reproduced with the permission of American Chemical Society (ACS) (Abouhakim et al., 2020b)**

### 6.2.2.3. Crystalline Properties

X Ray-Powder Diffraction (XRPD) analytical method is used to determine the effect of milling on the crystalline properties of DABOMD. To allow for a straightforward comparison, The XRPD of the milled samples are plotted along with standard crystalline and amorphous samples of DABOMD, as shown in Figure 6-8. XRPD of crystalline non-milled DABOMD exhibits a series of sharp peaks corresponding to the crystalline material, whereas, that of standard amorphous material possesses a typical halo peak with two broad maxima at  $17.5^\circ$  and  $24^\circ$  respectively as shown in Figure 6-8. As the milling progresses, the XRPD patterns change rapidly manifesting a reduction in intensity as well as broadening of the Bragg peaks evident, which indicates a phase transition from crystalline to amorphous. Beyond 60 min of milling, it appears that sharp Bragg peaks characteristics for a crystalline are absent, a typical scattering pattern for materials without long-range order is observed.

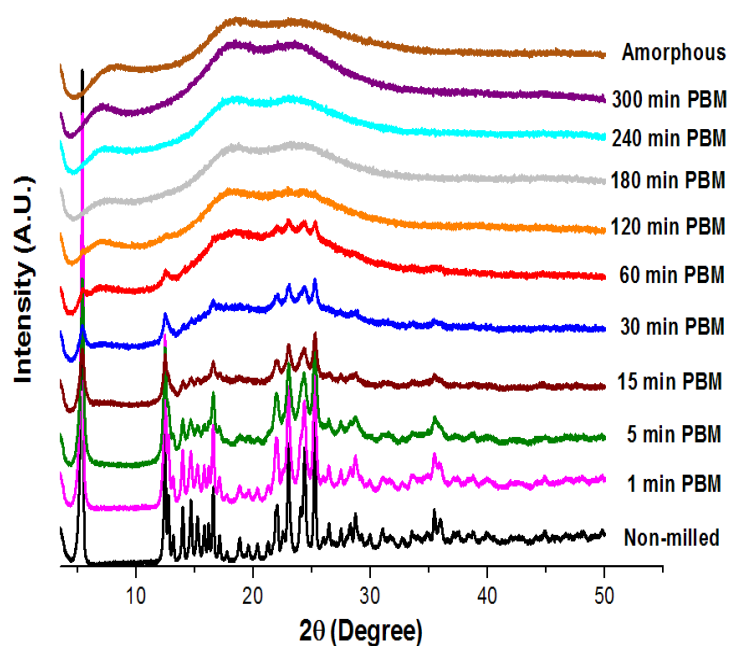


**Figure 6-8: XRPD of DABOMD before milling and after milling with planetary ball mill from 1 min to 300min (Reproduced with the permission of American Chemical Society (ACS) (Abouhakim et al., 2020b))**

### 6.2.2.4. Thermodynamic Properties

Since the study of the crystalline properties revealed that a phase transition from crystalline to amorphous is taking place, in theory, this transformation must be associated with thermodynamic/thermochemical change. Therefore, TGA and DSC are employed to evaluate the impact of milling on the thermochemical properties of DABOMD. TGA analysis of the crystalline non-milled DABOMD shows that two mass losses at two different temperatures corresponding to two different types of water interaction present in the crystalline lattice as

was revealed in Chapter 4. As the milling progresses, it appears that the amount of mass loss detected by TGA reduces significantly with milling time (Figure 6-9) which suggests that milling promotes dehydration, reflected in the release of water molecules from the crystalline lattice. This outcome agrees with the change in the crystalline properties detected by XRPD. The TGA pattern obtained for the milled samples (120 min and longer) of DABOMD is analogous to that reported for amorphous Esomeprazole magnesium (Reddy *et al.*, 2004) prepared by vacuum drying. Similarly, it has previously been suggested that Sodium omeprazole undergoes amorphization as a result of drying (Murakami *et al.*, 2009).

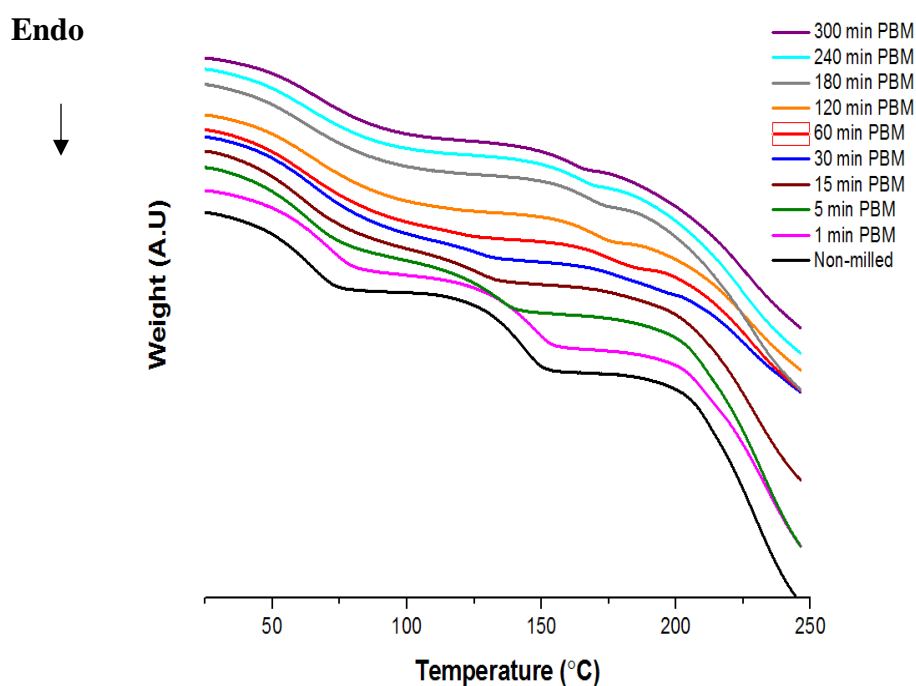


**Figure 6-9: TGA Profile of DABOMD for the non-milled and milled in planetary ball mill at a temperature 25 to 250 °C and a rate of 5°C/min (Reproduced with the permission of American Chemical Society (ACS) (Abouhakim *et al.*, 2020b))**

The DSC analysis of the crystalline non-milled DABOMD shows three distinct thermal events; two endothermic and one exothermic at 109 °C, 173 °C and, 197.8 °C respectively (Figure 6-10). The first endothermic peaks represent a water loss event of the weakly bonded water, whilst the second endothermic peak corresponds to the loss of the more strongly bonded water. The third exothermic peak represents the decomposition of DABOMD. As the milling progresses, the DSC profile for the milled sample (Figure 6-10) shows that the peak intensity continuously reduces with milling time and shifts to lower temperatures which is consistent with a loss of crystallinity. The thermal behaviour of the longer milled sample is analogous to that of amorphous Esomeprazole magnesium (Reddy *et al.*, 2004). Overall, thermochemical

analyses suggest that the amorphisation of DABOMD is driven by the sequential dehydration processes during milling.

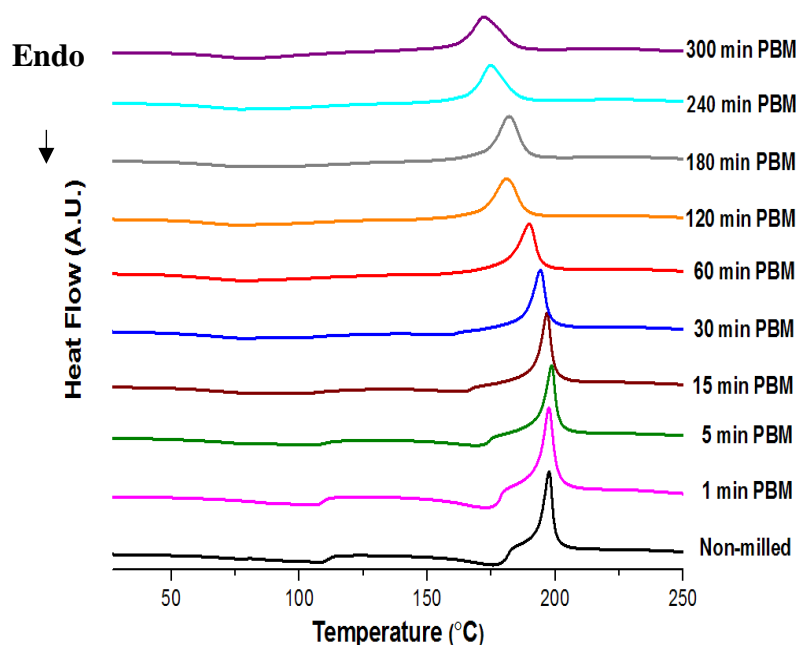


**Figure 6-10: DSC Profile of DABOMD for the non-milled and milled samples in a planetary ball mill at a temperature 25 to 250 °C and a rate 5°C/min. (Reproduced with the permission of American Chemical Society (ACS) (Abouhakim et al., 2020b))**

#### 6.2.2.5. Intermolecular Properties

The phase transformation from crystalline to amorphous occurs as a result of the change in the molecular interactions. The interactions can take form of hydrogen bonds which play an important role in the crystalline packing, in addition to weaker interactions such as van der Waals interactions or electrostatic interactions (Kaushal, Chakraborti and Bansal, 2008). Fourier Transform Infrared (FTIR) spectroscopy is sensitive to the level of order and disorder present in the crystal structure, including changes in hydrogen bonding (Stephenson, Forbes and Reutzel-Edens, 2001; Markovic *et al.*, 2006), thus, it was used to probe the impact of milling on the molecular structure together with computational studies. Figure 6-11 and Figure 6-12 show the FTIR spectra of the crystalline non-milled DABOMD, the amorphous standard, and the milled samples.

As the milling progresses, broadening and disappearance of the FTIR peaks are evident for the milled samples (relative to the spectra of crystalline samples). Samples milled for 300 min exhibit very similar FTIR spectra to the reference amorphous DABOMD. Marked changes in the spectral region's diagnostic for hydrogen bonding are also evident.

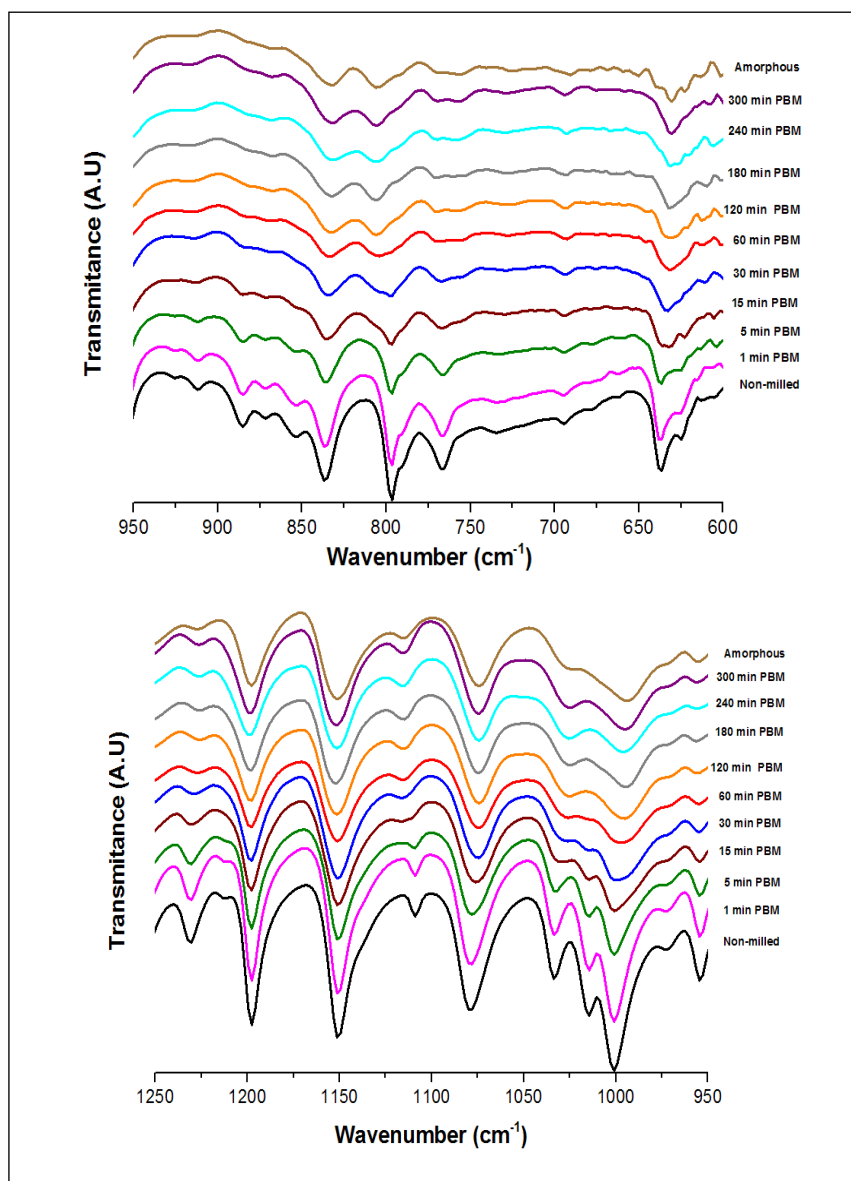


**Figure 6-11: FTIR-ATR of non-milled and milled DABOMD in planetary ball mill showing scan from a- 600 to 950 cm<sup>-1</sup>, b- from 950 to 1200 (Reproduced with the permission of American Chemical Society (ACS) (Abouhakim et al., 2020b))**

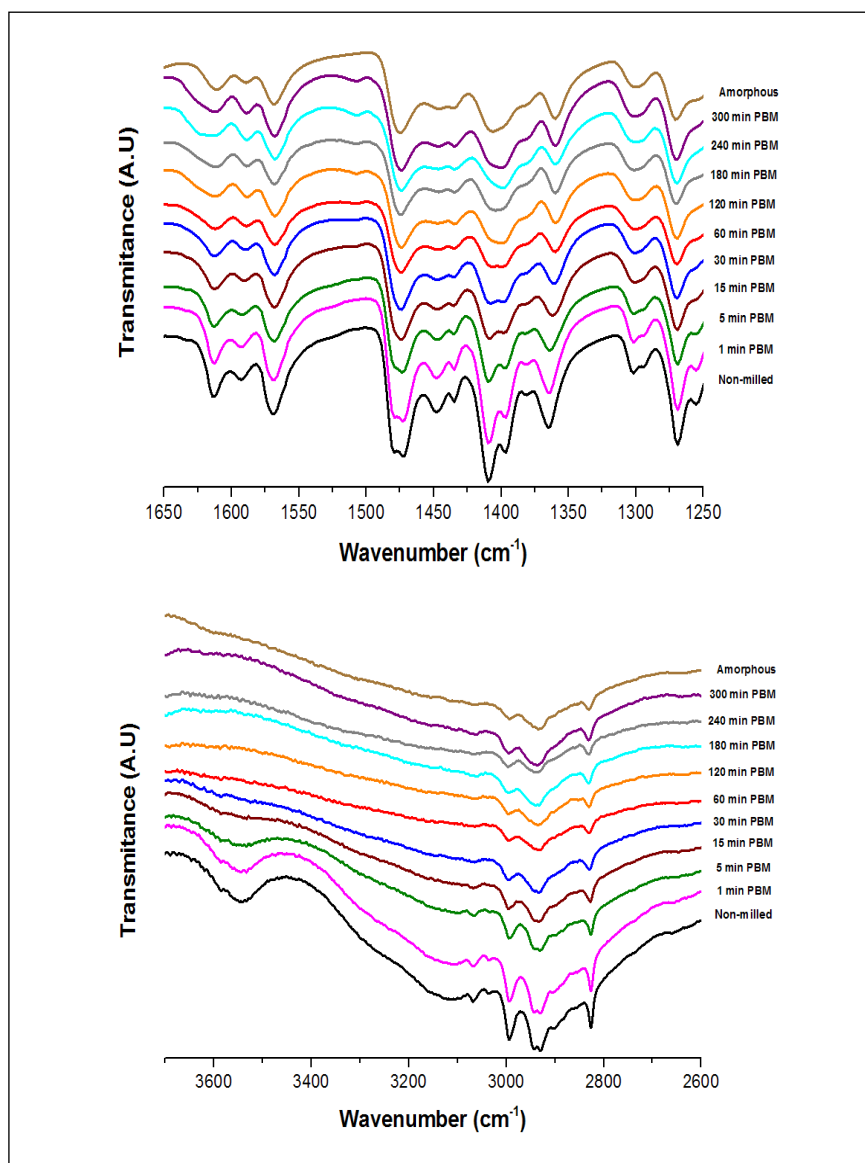


**Figure 6-12: FTIR-ATR of non-milled and milled DABOMD in planetary ball mill showing scan from c-1200 to 1600  $\text{cm}^{-1}$  and d from 2600 to 3700  $\text{cm}^{-1}$  (Reproduced with the permission of American Chemical Society (ACS) (Abouhakim et al., 2020b))**

To try to assist with the positioning of specific spectra, Dr Sten Lill conducted density functional theory (DFT) calculations on a molecular system mimicking the crystal structure (Figure 6-13). Computed IR-spectra was generated for a geometry optimized representative molecular model system using B3LYP-D3/6-31G(d,p) as implemented in Jaguar 10.7 (Bochevarov *et al.*, 2013). A few atomic positions were fixed in the optimization to keep the feature of the influence of the periodic crystal structure. This is a standard procedure for modelling, for example, enzymatic reactions (Lill and Siegbahn, 2009). These positions are marked in Figure 6-13 and Table 6-4.

The computed IR shows that the vibrations involving the two waters are strongly coupled making the assignment of the experimental spectra with broad peaks challenging. However, peaks in the region 3300-3600  $\text{cm}^{-1}$  can be easily assigned to O-H stretch modes, involving both W1 and W2. Also, the O-H stretch of W1 involving the hydrogen bonding to the benzimidazole nitrogen can be tentatively assigned to the broad peak at 3130  $\text{cm}^{-1}$ , but a more specific assignment of other peaks was not possible. However, the breaking of the hydrogen bonding pattern upon elongated milling time is evident from the marked changes in the FTIR spectral regions corresponding to these O-H bands, in line with earlier studies (Murakami *et al.*, 2009). The sharper peaks observed in the region 2800 to 3100  $\text{cm}^{-1}$ , is mainly assigned to C-H stretches of the methyl and methoxy groups on the aromatic systems. As shown below, these groups are located at likely crystal cleavage planes and hence are affected by the milling as shown by the peak broadening. These FTIR results suggest that hydrogen bond breaking is associated with the amorphisation of DABOMD in line with the TGA and DSC results of suggested hydrate water loss is taking place.

**Table 6-4: Table shows the mode of vibration for the main functional groups in DABOMD (Reproduced with the permission of American Chemical Society (ACS) (Abouhakim et al., 2020b)**

Functional group	Type of vibration mode	Crystalline vibration ( $\text{cm}^{-1}$ )	Amorphous vibration ( $\text{cm}^{-1}$ )	300 min milled vibration ( $\text{cm}^{-1}$ )
O-H	Stretch	3300-3600	3070-3660	3070-3660
S=O	Stretch	1001.2	993.9	994.9
C-H in CH <sub>3</sub> or O-CH <sub>3</sub>	Stretch	2929.5	2934.1	2935.7
Benzimidazole H3C-O	Bend	1197.7	1197.8	1198.1

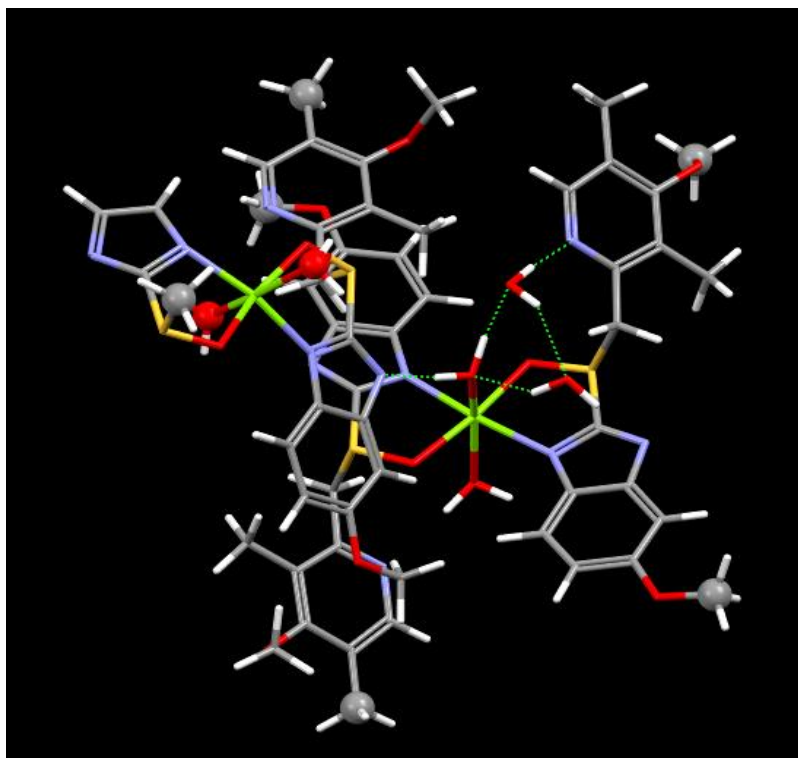


**Figure 6-13: A model system of DABOMD for calculation of molecular IR-spectra, especially highlighting the hydrogen bond network. Fixed atomic positions are marked with larger balls**

#### **6.2.2.6. Quantification of Amorphous**

##### **6.2.2.6.1. Quantification of Amorphous using XRPD**

A series of XRPD scans were carried out on the crystalline, and the standard amorphous samples of different ratios by weight of (0%, 20%, 40%, 60%, and 80%), and a calibrated curve was plotted from the derived data corresponding to the integrated areas under peaks at  $2\theta$  equal to  $5.3$  and  $25.2^\circ$ . The generated curve has an R-value equal to 0.9949 (Figure 6-14). The equation derived from the calibration curve is used to quantify the phases formed as a result of milling. This method of quantification was described by (Birju, Kumar Kakumanu and Bansal, 2006). The amount of amorphous samples formed during milling is shown in Figure 6-15 and Table 6-5. It can be observed that the first 5 min of milling about half of the crystalline sample (55%) have transformed into amorphous, the rest of the amorphisation occurs steadily with successive milling, where, approx. 98% of amorphous was formed after 300 min.

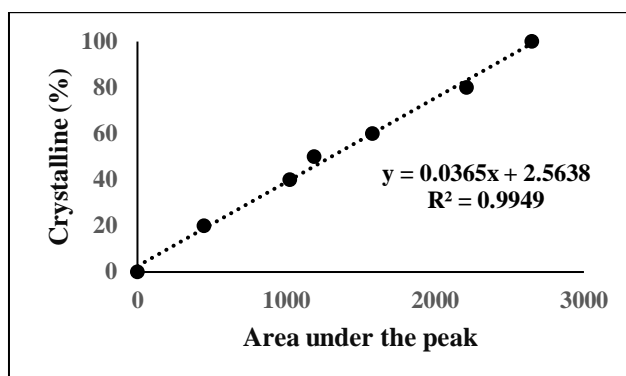


**Figure 6-14: Calibrated Curve of the area under the curve of different ratios of standard crystalline and amorphous DABOMD measured by XRPD**

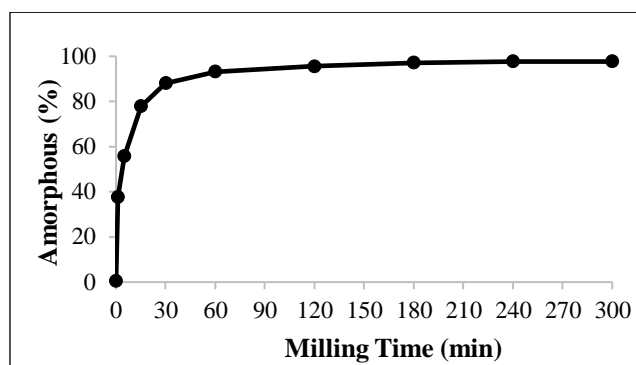


**Figure 6-15: Percentage amorphous of DABOMD forming during different milling time in the planetary ball mill by XRPD (Reproduced with the permission of American Chemical Society (ACS) (Abouhakim et al., 2020b))**

**Table 6-5: Percentage amorphous of DABOMD forming during different milling time in planetary ball mill measured by XRPD (Reproduced with the permission of American Chemical Society (ACS) (Abouhakim et al., 2020b))**

PBM Milling time (min)	Amount of Amorphous (%)
0	0
1	0.37
5	0.56
15	0.78
30	0.88
60	0.93
120	0.96
180	0.97
240	0.98
300	0.98

### 6.2.2.6.2. Quantification of Amorphous using Chemometrics Analysis of FTIR

The percentage amorphous of DABOMD formed during milling was quantified from the chemometric analysis of the FTIR data by Dr Maryam Asachi.

The mole fraction  $x_i$  of crystalline and amorphous DABOMD in samples taken before and after milling were quantified using a chemometric linear combination of FTIR spectra. All the quantifications were conducted in the MATLAB R201 software using a code that was previously established for the measurement of different components in detergent powder mixtures using Near Infrared (NIR) (Asachi *et al.*, 2017). A spectrum consists of  $N_k$  intensities ( $I$ ) measured at a specific wavenumber ( $\lambda_k$ ). Spectrum pre-treatment was carried out using 1<sup>st</sup> and 2<sup>nd</sup> ( $dI'$ ,  $dI''$ ) derivatives to remove the offset and base line shifts arising from differing particle sizes as shown in Equation 6-1 and Equation 6-2 (Vanarase *et al.*, 2013; Asachi *et al.*, 2017).

$$dI'(\lambda_k) = \frac{I(\lambda_{k+1}) - I(\lambda_k)}{\lambda_{k+1} - \lambda_k} \quad \text{Equation 6-1}$$

$$dI''(\lambda_k) = \frac{I(\lambda_{k+1}) - I(\lambda_k) + I(\lambda_{k-1})}{(\lambda_{k+1} - \lambda_k)^2} \quad \text{Equation 6-2}$$

Calculation of the solid phases using FTIR spectra was conducted according to Johanson (2014) approach as shown in Equation 6-3. This assumes that the surface consists of either crystalline or amorphous domains, and the intensity of reflected light is determined by the surface area fraction of those two respective domains:

$$dI_{mix.pred}(\lambda, f_{AAC}) = f_{AAC} dI_{amp}(\lambda) + (1 - f_{AAC}) dI_{cryst}(\lambda) \quad \text{Equation 6-3}$$

Here,  $f_{AAC}$  is the area fraction of the amorphous material on the surface of the particles. The predicted first or second-order derivative spectrum  $dI_{mix.pred}$  (Equation 6-1 or Equation 6-2) contains surface averaged contributions of the derivatives of the amorphous and crystalline reference spectra  $dI_{amp}$  and  $dI_{cryst}$ .

For a specific samples' spectrum, the amorphous content  $f_{AAC}$  is obtained by minimisation of the sum of residual differences squared (SOS) between the experimental FTIR intensity of mixture  $dI_{mix}(\lambda)$ , and the calculated value following Equation 6-4.

$$\min_{f_{AAC}} SOS = \min_{f_{AAC}} \left[ \sum_{k=1}^{N_k} (dI_{mix}(\lambda_k) - dI_{mix.pred}(\lambda_k, f_{AAC}))^2 \right] \quad \text{Equation 6-4}$$

The obtained results of the first and second derivatives are displayed in Table 6-6. It can be seen that the first derivative shows more amorphous content as opposed to the second

derivative, which could have underestimated the amount of amorphous. Moreover, comparing the chemometric data from FTIR to that obtained with XRPD shows that the first 15 min produced a larger amount of amorphous XRPD as opposed to the FTIR data. This difference is expected since the two analytical techniques possess different principles. Where XRPD shows the crystal content, FTIR is focused on the intermolecular differences that can emerge for instance as a result of the change in the water content which could be less detectable in the first few minutes of milling.

**Table 6-6: Percentage amorphous formed with planetary ball mill quantified using FTIR chemometric method of milled DABOMD and equivalent % water content from TGA**

Amorphous content based on Chemometric FTIR		
Milling time (min)	First derivative	Second derivative
0	0	0
1	0.10	0.12
5	0.35	0.22
15	0.71	0.63
30	0.83	0.71
60	0.91	0.71
120	0.93	0.82
180	0.99	0.98
240	0.99	0.94
300	1	0.96

#### 6.2.2.7. Mechanism of Amorphisation

The combined XRPD, DSC, TGA, and FTIR results revealed that DABOMD amorphisation during milling could be attributed to the progressive release of water molecules. The distortion/breakage of their hydrogen bonds eventually leads to the collapse of the crystal lattice of DABOMD. There is a near absence in the literature on studies probing the underlying mechanisms for amorphisation during milling of organic crystals. Understanding the mechanically induced amorphisation process requires (i) a thorough knowledge of the milling conditions and, (ii) knowledge of the underlying material properties of the feed, including its crystal structure and mechanical properties.

(i) In a planetary ball mill, the energy supplied to the particles gives rise to different forms of stress distribution including compression stress by impact and rolling, and shearing stress caused by sliding (Young *et al.*, 2007).

(ii) The crystal structure of DABOMD involves hydrogen bonds of different strength which hold the crystal lattice. Also, DABOMD incorporates two loosely bonded water molecules and

two strongly bonded water molecules, as was mentioned earlier. Therefore, it can be suggested that the impact and the shearing from the mill can cause distortion/breakage of the hydrogen bonds and the release of water molecules simultaneously, as was indicated previously from the thermal and intermolecular analyses. This can make the crystals shear unstable and lead to the emergence of amorphous DABOMD. Also, the kinetic energy and the heat generated from the mill can increase the vibration of the water molecules promoting dehydration, dislocation, and, accumulation of defects, hence, speeding up the phase transformation of DABOMD.

Moreover, as evaluated from the predictive calculations in Chapter 4, DABOMD exhibits a crystal slip plane through the (100) face with weak hydrogen bonding across the plane (Figure 4-11). Other candidate slip planes can be (011), (11-1) and (102) given that they hold secondary morphological importance as shown in Table 4-4. As was explained previously, slip planes are the planes incorporating the weakest interactions between neighbouring planes in the crystalline lattice making them the primary site for fracture in the event of stress such as milling. Also, the dislocations and defects such as a slip of the planes promote plastic deformation, which will ultimately lead to amorphisation (Baláž *et al.*, 2013). Analysis of the change in XRPD peaks upon milling shows that the most significant spectral change is evident at  $2\theta = 5.4$ , as illustrated in Figure 6-16 and (Table 6-7). This peak coincides with the major slip plane (100) to be mostly affected while the effect of other planes is less straightforward to interpret. Nevertheless, effects on (011), (11-1), and (102) are also observed. In addition to the XRPD, the effect of crystal cleavage at the plane (100) is reflected in the FTIR peak changes at 2800 – 3100, which represents the methoxy and methyl group respectively which are designated around (100) (Figure 5-6). Therefore, we postulate that the shear and impact from milling cause the crystal to be cleaved along the easiest slip planes, and it also affects the hydrogen bond breakage which leads to further crystalline disorder and amorphisation. Therefore, it can be observed that milling has not only led to the physical change of DABOMD but also caused a chemical change reflected in the dehydration process. Another example of where mechanical activation leads to a change in the chemistry of the molecule is Ampicillin trihydrate which transforms into the amorphous form upon grinding. Takahashi *et al.* (1984) suggested that the freed water molecules from dehydration caused by grinding leads to the collapse of the crystal lattice (Takahashi *et al.*, 1984).

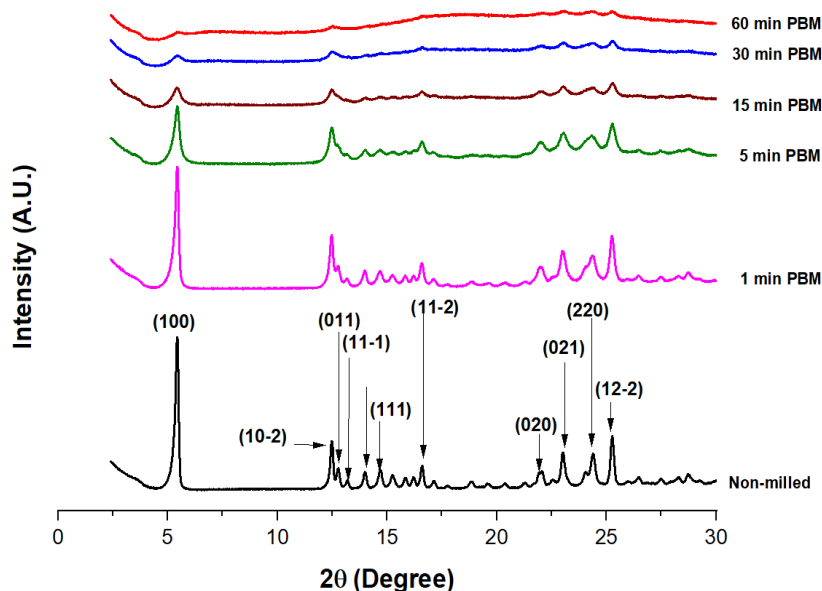


**Figure 6-16: Identification of planes involved in the crystalline disorder of DABOMD (Reproduced with the permission of American Chemical Society (ACS) (Abouhakim et al., 2020b))**

**Table 6-7: Planes of the significant XRPD peaks of DABOMD obtained from Mercury (Mercury User Guide and Tutorials 2018 CSD Release, 2017) (Reproduced with the permission of American Chemical Society (ACS) (Abouhakim et al., 2020b))**

Plane	2 $\theta$ (degree)
(100)	5.4
(1 0-2)	12.4
(011)	12.8
(1 1-1)	13.1
(20-2)	14.1
(111)	14.8
(210)	15.4
(012)	17.4
(021)	23.4
(12-2)	25.5

Various researchers have suggested amorphisation as a result of vitrification (melt quench) at the surface (Descamps *et al.*, 2015). To evaluate the impact of high temperature on DABOMD, hot stage microscope and thermal XRPD were both employed. Hot stage microscope was employed at a heating rate of 10°C from 25°C to 170°C to qualitatively visualise if DABOMD experiences melting as a result of a temperature increase. It was concluded that DABOMD

does not undergo melting with high temperature, as seen in (Figure 4-8). However, when heating DABOMD in a thermal XRPD (from 25°C to 170°C), it appears from Figure 6-17 that the crystallinity starts to effectively vanish above 120°C, which suggests that high temperature can be a contributing factor to the amorphisation of DABOMD. The temperature contribution is composed of the bulk temperature and the localised temperature. The bulk temperature is the temperature of the mill, which was measured by (Chauruka, 2015) and found that the highest temperature obtained is 80°C. The localised temperature is the temperature generated on the sub-micron regions on the impacting surfaces which might be much higher in correspondence to the bulk temperature, but it is challenging to measure (I. Colombo, Grassi and Grassi, 2009). It can be suggested that high temperature increases the level of dislocation, the slip of planes, and also increases the kinetics of water molecules promoting further dislocations.

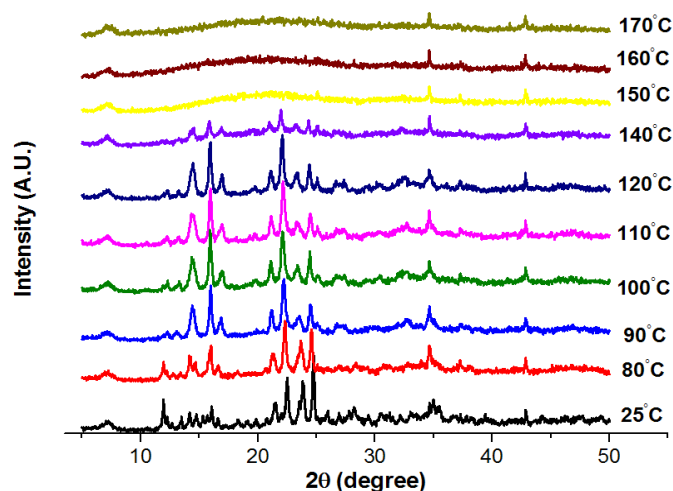


**Figure 6-17: Thermal Controlled XRPD of DABOMD from 25 to 170 °C (Reproduced with the permission of American Chemical Society (ACS) (Abouhakim et al., 2020b))**

In summary, the amorphisation of DABOMD is therefore associated with the following events; crystal cleavage via the slip of planes, water loss, accumulation of defects, and distortion of the hydrogen bonds holding the crystal backbone as a result of stresses and the temperature rise experienced during the process of milling. The order of these events is not known and can be further investigated with the study of kinetics. The slip of planes can promote particle fracture and the creation of new surfaces. The release of water molecules can create dislocation sites that further facilitate the slip and planar deformation, accumulation of defects, and eventually contribute to plastic deformation. Increased temperature can lead to dehydration, increase atomic mobility, and hence distortion of the crystalline lattice and may also lead to surface melt and formation of amorphous upon cooling, however, surface evident in this case (as was seen by hot stage).

### 6.2.2.8. The Kinetics of Comminution-Amorphisation

Prolonged milling of DABOMD resulted in (i) a significant comminution represented by a change in  $D_{50}$  and  $D_{90}$  (Table 6-1), (ii) contribute to a large amorphisation indicated by amorphous content (AAC) as was detected by XRPD (Table 6-5) and by FTIR chemometric analysis (Table 6-6), and (iii) leads to 50% water loss (WL), indicated by TGA quantification (Table 6-8).

**Table 6-8: The amount of water present in DABOMD detected by TGA (Reproduced with the permission of American Chemical Society (ACS) (Abouhakim et al., 2020b))**

Milling time (min)	Water content in DABOMD TGA (%)
0	8.7
1	8.3
5	7.7
15	7.2
30	6.5
60	5.9
120	5.3
180	4.7
240	4.3
300	4.2

The experimental changes in comminution, amorphisation and water loss of DABOMD follow an exponential pattern as shown in the experimental Figure 6-18, Figure 6-19, and Figure 6-20. It appears that the processes of comminution and amorphisation depict two sequential processes: a rapid event (approx. around the first 30 min of milling), and a slower event (after 30 min of milling) (Figure 6-18 and Figure 6-19). Interestingly the water loss process (Figure 6-20) also seems to occur in two sequential events; a rapid water loss and a slow water loss event. This further enhances that loss of water is associated with the comminution and amorphisation process of DABOMD.

To facilitate a quantitative description of the kinetics of comminution, amorphisation and water loss events. These mechanisms are presented by a parallel first-order process characterised by a time constant. This is first applied to the  $D_{90}$  ( $D_{50}$  can also be used); while defining the extent of comminution,  $x_{com}$ , as the fraction of change in  $D_{90}$  compared to the total change in its value. The extent that comminution reduces from 1 to zero in an exponential fashion that could be modelled as a two parallel rate process because their time constants vary by an order of magnitude as shown in Equation 6-5:

$$x_{com} = \frac{D(t) - D_{\infty}}{D_0 - D_{\infty}} = \alpha_{rpdc} e^{-t/\tau_{rpdc}} + (1 - \alpha_{rpdc}) e^{-t/\tau_{slwc}} \quad \text{Equation 6-5}$$

Here,  $D(t)$  is the  $D_{90}$  of the milled sample at time  $t$ , and  $D_0, D_{\infty}$  represent the  $D_{90}$  at the beginning and end of the milling process respectively. The time constants  $\tau_{rpdc}, \tau_{slwc}$  are the time scales for rapid comminution and slow comminution. It worth noting that the time scale  $\tau$  represents the inverse of the rate constant kinetic  $k$ . Since the time scale allows the visualisation of the sequence of events. The fitted model of kinetic is shown in Figure 6-18.

Similarly, to a model fit of the kinetic of the loss of crystallinity (amorphisation) is characterised here by the extend of crystallinity,  $x_{Cryst}$  ( Equation 6-6) which is obtained from the apparent amorphous content,  $f_{AAC}(t)$  as determined from the XRPD and chemometric analysis of the FTIR quantification of amorphous data as outlined in section (6.2.2.7.1 and 6.2.2.7.2).

$$x_{Cryst} = 1 - \frac{f_{AAC}(t) - AAC_0}{AAC_{\infty} - AAC_0} \quad \text{Equation 6-6}$$

$$= \alpha_{rpdam} e^{-t/\tau_{rpdam}} + (1 - \alpha_{rpdam}) e^{-t/\tau_{slwam}}$$

With,  $AAC_0, f_{AAC}(t)$  and  $AAC_{\infty}$  are the apparent amorphous content of the milled sample at time  $t = 0, t$ , and the end of the milling period respectively.

For completeness, the parameters  $\alpha_{rpdc}, \alpha_{rpdam}$  and time constants  $\tau_{rpdc}, \tau_{slwc}, \tau_{rpdam}$  in Equation 6-5 and Equation 6-6 were quantified by minimising the sum of squares between the measured and predicted extend of comminution and crystallinity according to Equation 6-7. Where  $\tau_{rpdam}$  is the time scale of rapid amorphisation.

$$SOS = \sum_{i=1}^9 [x_{com.meas}(t_i) - x_{com.calc}(t_i)]^2 \quad \text{Equation 6-7}$$

$$+ \sum_{i=1}^9 [x_{Cryst.meas}(t_i) - x_{Cryst.calc}(t_i)]^2$$

The water loss event can be modelled by fitting it to the extent of comminution, as shown in Equation 6-8.

$$\%water = 4.27 * \left( 1 + 0.74e^{-\frac{t}{\tau_{rpdam}}} + 0.26e^{-\frac{t}{\tau_{slwam}}} \right) \quad \text{Equation 6-8}$$

The outcome of fitting the data is provided in Table 6-9;

**Table 6-9: Table shows the outcome of the model fit of the kinetics of comminution amorphisation in the planetary ball mill and water loss in DABOMD**

	Comminution	Comminution	Amorphisation		Water loss	
	PBM, $D_{90}$	PBM, $D_{50}$	PBM (XRPD)	PBM (IR)	Fitted by XRPD	Fitted by FTIR
$k_1$	0.28	0.72	0.20	0.12	0.12	0.12
$k_2$	0.01	0.02	0.02	0.01	0.01	0.01
$\alpha$	81%	68%	81%	79%	101%	101%
$\tau_{\text{rpd}}$ (min)	3.6	1.4	5.6	8.3	5.3	8.3
$\tau_{\text{slw}}$ (min)	88.3	62.0	52.3	77.8	88.3	88.3

1) The model fitted to the comminution data from  $D_{90}$  (Figure 6-18, modelled) results in  $\alpha_{\text{rpd\_com}} = 81\%$ ,  $\tau_{\text{rpd\_com}} = 3.6 \text{ min}$  and  $\tau_{\text{slw\_com}} = 88.3 \text{ min}$ ; this confirms that rapid comminution accounts for 80% of the extend of comminution. The slower comminution occurs at a much slower time scale (88.3 min) which indicates that if comminution is considered complete when  $x_{\text{com}} < 1\%$ , then, the comminution is complete after approximately 300 min ( $x_{\text{com}} = 0.2 e^{-300/88}$ ). Similarly, the model fitted to  $D_{50}$  shows similar sequence of events with rapid comminution accounting for 80% of the extend of comminution occurring at approx. 1.4 min and a slower comminution event occurring at 62 min.

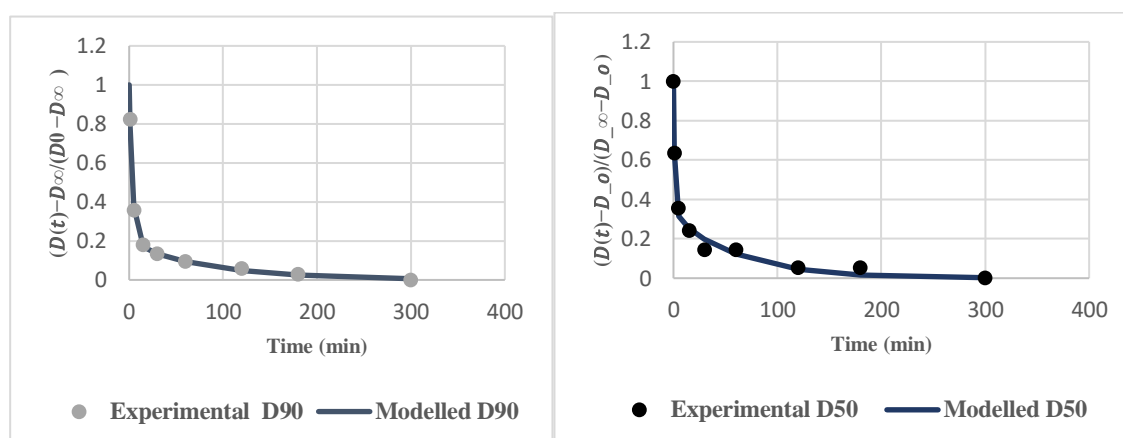


**Figure 6-18: The kinetic of comminution of DABOMD in planetary ball mill (Reproduced with the permission of American Chemical Society (ACS) (Abouhakim et al., 2020b))**

2) The model fitted to the amorphisation data (Figure 6-19, modelled) resulting in; a rapid amorphisation accounting for approx. 80% of amorphous which occurs in the first few minutes as follows;  $\tau_{rpd\_amp} = 5.6 \text{ min}$  obtained from XRPD data and  $\tau_{rpd\_amp} = 8 \text{ min}$  from the FTIR chemometric.

The final time constant represents the slower rate of amorphisation and occurs on a time scale of approx.  $\tau_{slw\_amp} = 52.3 \text{ min}$  according to the amorphous quantified by XRPD, and occurs in a time scale of  $\tau_{slw\_amp} = 77.8 \text{ min}$  according to the data gathered by the chemometric analysis. Although the kinetics of amorphous obtained from XRPD and FTIR are slightly different yet, they both agree about the sequence of events.

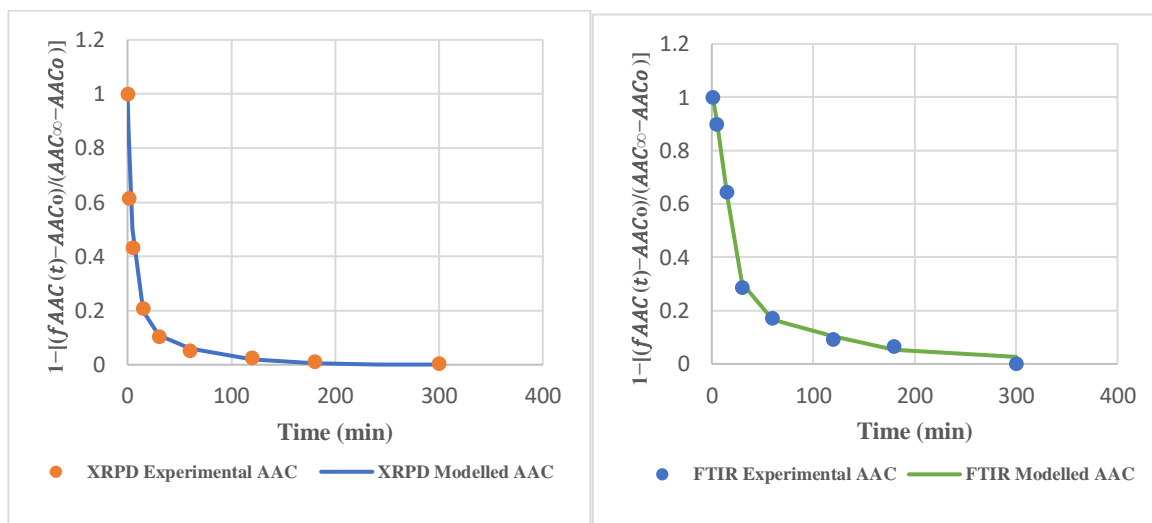


**Figure 6-19: The kinetic of amorphisation of DABOMD in planetary ball mill derived from; XRPD analysis and from FTIR Chemometric analysis (Reproduced with the permission of American Chemical Society (ACS) (Abouhakim et al., 2020b))**

3) The model fitted to the water content data (Figure 6-20, modelled) shows that the first rapid water loss occurs at a time scale  $\tau_{rpd\_amp} = \text{from } 5.3 \text{ to } 8 \text{ min}$ , which is equivalent to 25% water loss shown with TGA. This further enhances that the first rapid dehydration of water is associated with the rapid amorphisation since they both occur at the same time scale of approx. 6 and 8 min as was fitted using XRPD and FTIR. The second water loss occurs at a much slower rate around a time scale of 88 min.

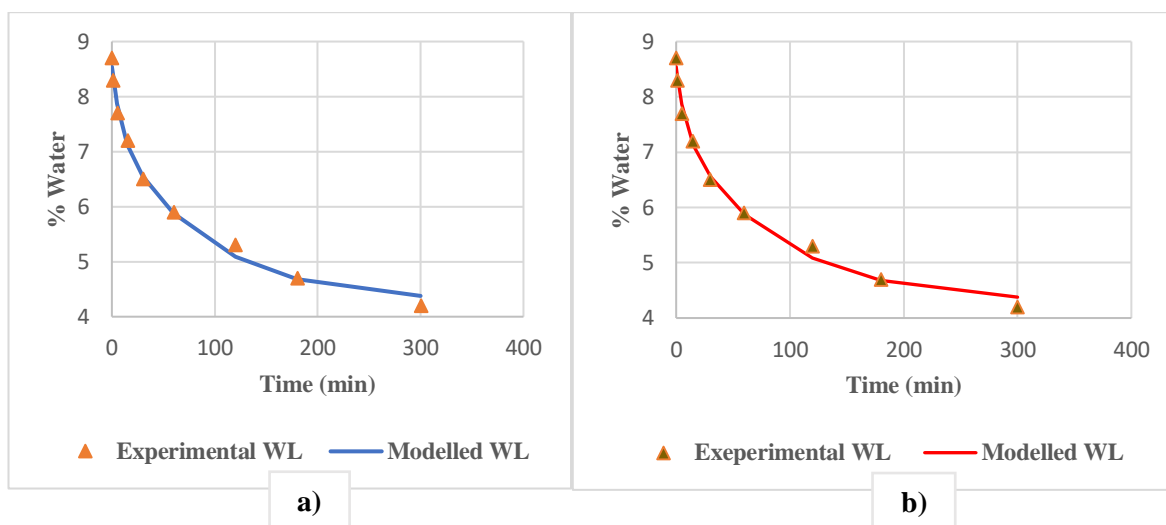


**Figure 6-20: The kinetic of the water present in DABOND during milling fitted model using XRPD and Chemometric FTIR**

#### 6.2.2.9. Derived Mechanism of Milling of DABOMD

We can finally propose a comprehensive mechanism that shows the sequential events occurring during the milling of DABOMD following the schematic illustrated in Figure 6-21. (1) It is believed that the first process corresponding to the shortest time scale of (i.e. 4 min) is attributed to the crystal cleavage via the slip of planes which accounts for the rapid comminution (size reduction + deagglomeration) process; this creates a large number of fresh surfaces and defects which agrees with the XRPD analysis of this plane shown in Figure 6-16. (2) The created surfaces allow for fast diffusion reflected in the rapid evaporation of water molecules from the crystalline lattice. Also, water was allocated near the slip plane (100) (Figure 4-11), which explains the rapid water loss immediately after the plane (100) deformation. The deformation of planes, dislocation, and mobility of the water molecules cause the breakage and the disruption of the hydrogen bonds in the lattice and eventually account for the rapid amorphisation observed in the subsequent time scale (i.e. at 8 min), the slip of planes also promotes plastic deformation. (3) The slower event of comminution is attributed to a decrease in the number of slip planes and the amount of generated defect. This implies that fewer surfaces are available for water diffusion, which explains the drop of water dehydration and hence slower amorphisation.

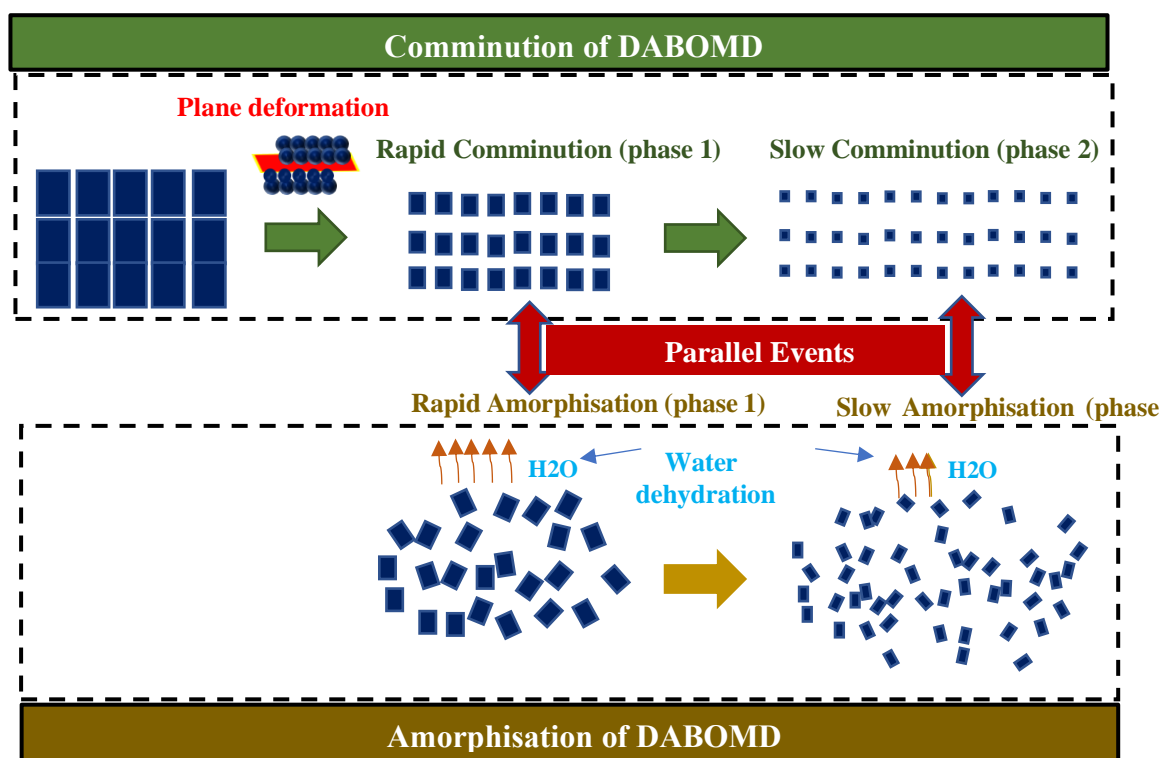


**Figure 6-21: A proposed mechanistic model for the milling process of DABOMD. Where the ordered particles represent the comminution, and the disordered particles represent the amorphisation (Reproduced with the permission of American Chemical Society (ACS) (Abouhakim et al., 2020b))**

## 6.3. Milling DABOMD with Single Ball Mill

### 6.3.1. Experimental Setup

Single ball mill MM200 Retsch (Figure 6-22) was used for the milling experiment. The powder samples of DABOMD were milled from 1 min to 300 min in a steel jar using a steel ball of a diameter equal to 10 mm. Approximately 1.3 g of powder was placed to fill the third of the jar's volume. The oscillation frequency and the time of milling can be varied depending on the desired experimental setup. The oscillation was set to 30HZ. The powder and the ball are added to the milling jar which is then securely tightened and attached to the clamp. Milling intervals of 10 min were regularly implemented to prevent the temperature rise of the system.

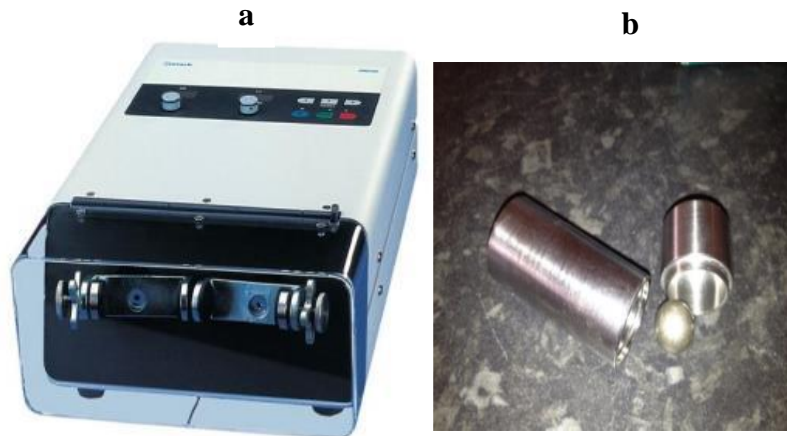


**Figure 6-22: Pictures illustrating a) Single ball mill MM200 and b) milling jar with milling media (Chauruka, 2015)**

### **6.3.2. Powder Characterisation of DABOMD**

#### **6.3.2.1.1. Particle Size Distribution**

#### **6.3.2.1.2. Particle Size Distribution Using Laser Diffraction**

The particle size measurement of the samples milled in a single ball mill was carried out using Malvern Mastersizer 3000 in a dry system set up following the same approach employed to measure the samples processed in the planetary ball mill. The particle size distribution, cumulative distribution, and size characteristics are displayed in Figure 6-23, Figure 6-24, and Table 6-10.

It can be seen that the particle size distribution profile of the single ball-milled is similar to that achieved in the planetary ball mill, i.e. PSD profile changes from a broad trimodal to a narrower profile (Figure 6-2 and Figure 6-23). This implies that the two mills generate sufficient energy to cause a significant fracture to DABOMD. When comparing the characteristic sizes of the two mills (Table 6-10), it is evident that the single ball mill generates smaller particles in the first 30 min of milling (with  $D_{90}$  equal to 171, 76.8, 51.1 and 52  $\mu\text{m}$ ) as opposed to the planetary ball mill of which ( $D_{90}$  equal to 180, 98.1, 66.9 and 58.9  $\mu\text{m}$ ). The mechanism of milling in a single ball mill is suggested to occur mainly by impact; whereas, that in planetary ball mill occurs by impact and shear. This indicates that the prevailing impact stress associated with single ball mill is an effective route for rapid particle fracture. However, milling for over 30 min shows that the process of particle size reduction declines in the single ball mill, which indicates that the agglomeration is taking over. Agglomeration is less apparent in the planetary ball mill compared to the single ball mill (observed at 30 min, 60 min, 180 min and 300 min). This can be explained by the fact that progressive milling leads to the formation of fines (not shown due to the low resolution of dry system in detecting fines) which tend to adhere to the surfaces and form large particles with the aid of Van der Waals forces. Apparently, the greater

energy dissipated in the planetary ball mill (probably from the aggressive shear stress) breaks the bonds of agglomerates and eventually leads to the formation of smaller particles. Thus, planetary ball mill yields smaller particles with longer milling time. This is seen for example, in the sample milled for 300 min in single ball mill which depicts a larger size ( $D_{90} = 48.2 \mu\text{m}$ ) compared to that milled with a planetary ball mill ( $D_{90} = 35.3 \mu\text{m}$ ). On the other hand, single ball mill impacted more on the fines as seen in  $D_{10}$ .

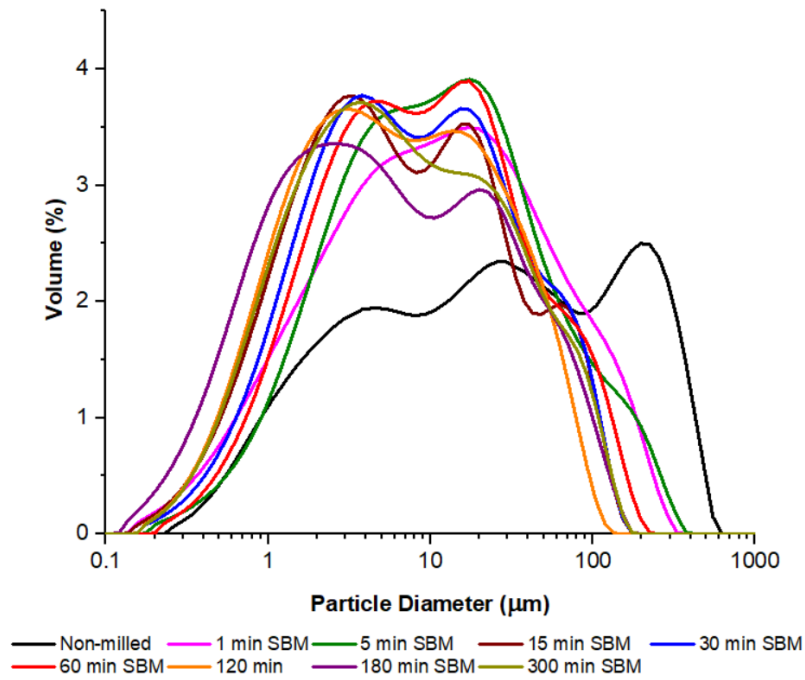


**Figure 6-23: Particle size distribution of non-milled and milled DABOMD in single ball mill from 1min to 300 min**

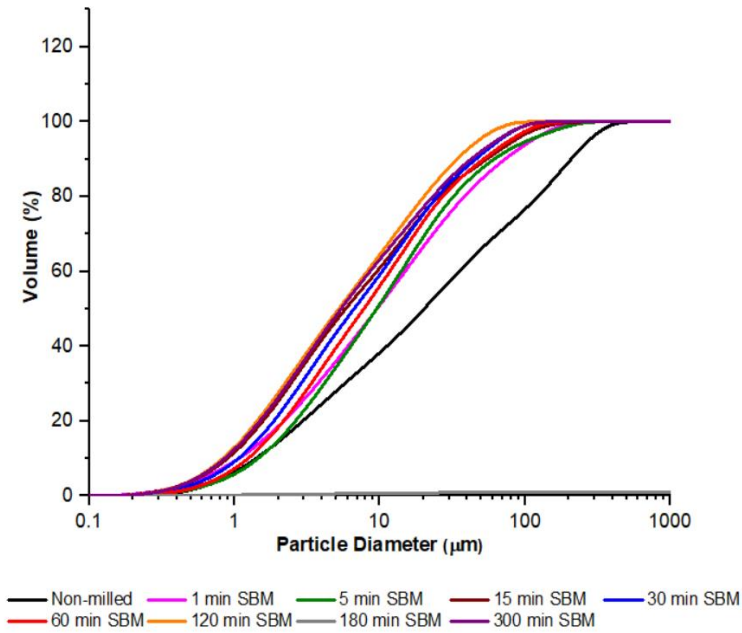


**Figure 6-24: Cumulative distribution of non-milled and single ball-milled DABOMD from 1min to 300 min.**

**Table 6-10: Characteristic sizes ( $D_{10}$ ,  $D_{50}$ , and,  $D_{90}$ ) of non-milled and milled DABOMD samples in planetary ball and single ball mill from 1min to 300 min**

Sample	Particle Size ( $\mu m$ )			Sample	Particle Size ( $\mu m$ )		
	$D_{10}$	$D_{50}$	$D_{90}$		$D_{10}$	$D_{50}$	$D_{90}$
<b>Non-milled</b>	1.5	21.2	211	Non-milled	1.5	21.2	211
<b>1 min PBM</b>	1.5	16.4	186	1 min SBM	1.4	13.7	171
<b>5 min PBM</b>	1.7	12.7	98.1	5 min SBM	1.7	11	76.8
<b>15 min PBM</b>	1.7	11.2	66.9	15 min SBM	1	6.1	51.1
<b>30 min PBM</b>	1.7	9.9	58.9	30 min SBM	1.2	7.6	52
<b>60 min PBM</b>	1.7	9.9	51.8	60 min SBM	1.4	8.4	58.9
<b>120 min PBM</b>	1.6	8.7	45.6	120 min SBM	1	6.8	45.6
<b>180 min PBM</b>	1.7	8.7	40.1	180 min SBM	0.7	5	45.7
<b>300 min PBM</b>	1.5	7.5	35.3	300 min SBM	1	6.1	48.2

### 6.3.2.1.3. Particle Size Distribution of DABOMD Using Image Analysis

SEM image analysis of the number based average diameter (Table 6-11) was performed following the same methodology employed for the planetary ball mill. It can be observed that the sizes of the average diameter obtained by image analysis are in the range of those produced by laser diffraction (Table 6-10). Furthermore, It can be seen that particle size reduction declines after 60 min of milling which can be associated with the dominance of the agglomeration process as was evident in the PSD analysis, i.e. samples milled for 240 min have larger mean diameter size than that milled for 180 min which equal to 7.8  $\mu\text{m}$  and 8.2  $\mu\text{m}$  respectively. However, the image analysis is not the best technique to probe agglomerates due to the challenging fluctuations with the threshold in the image analysis.

**Table 6-11: Median diameter of DABOMD non-milled and milled with single ball mill, measured using image analysis**

Sample	The number-based measured average diameter ( $\mu\text{m}$ )
Non-milled	17.9
1 min SBM	16.4
5 min SBM	12.0
15 min SBM	11.2
30 min SBM	10.7
60 min SBM	8.9
120 min SBM	8.2
180 min SBM	7.8
240 min SBM	8.1
300 min SBM	8.2

Overall, it can be suggested that the planetary ball mill is a good means for producing smaller particles with fewer agglomerates for longer milling times. On the other hand, a single ball mill causes rapid comminution for short milling periods.

### 6.3.2.2. Morphology

The powder morphology was analysed following the same setup applied in the planetary ball-milled samples. The morphology of the non-milled and the milled samples are shown in Figure 6-25 and Figure 6-26. In general, the morphology and the size distribution obtained with the single ball mill are similar to those observed in the planetary ball-milled samples. Where particles of DABOMD depict irregular sizes with agglomerated surfaces which tend to become smoother with milling. Yet agglomerates are more prevailing in the single ball-milled samples due to significant amounts of fines adhering to the surfaces, particularly at longer milling times as observed in Figure 6-26, which agrees with the PSD analysis.

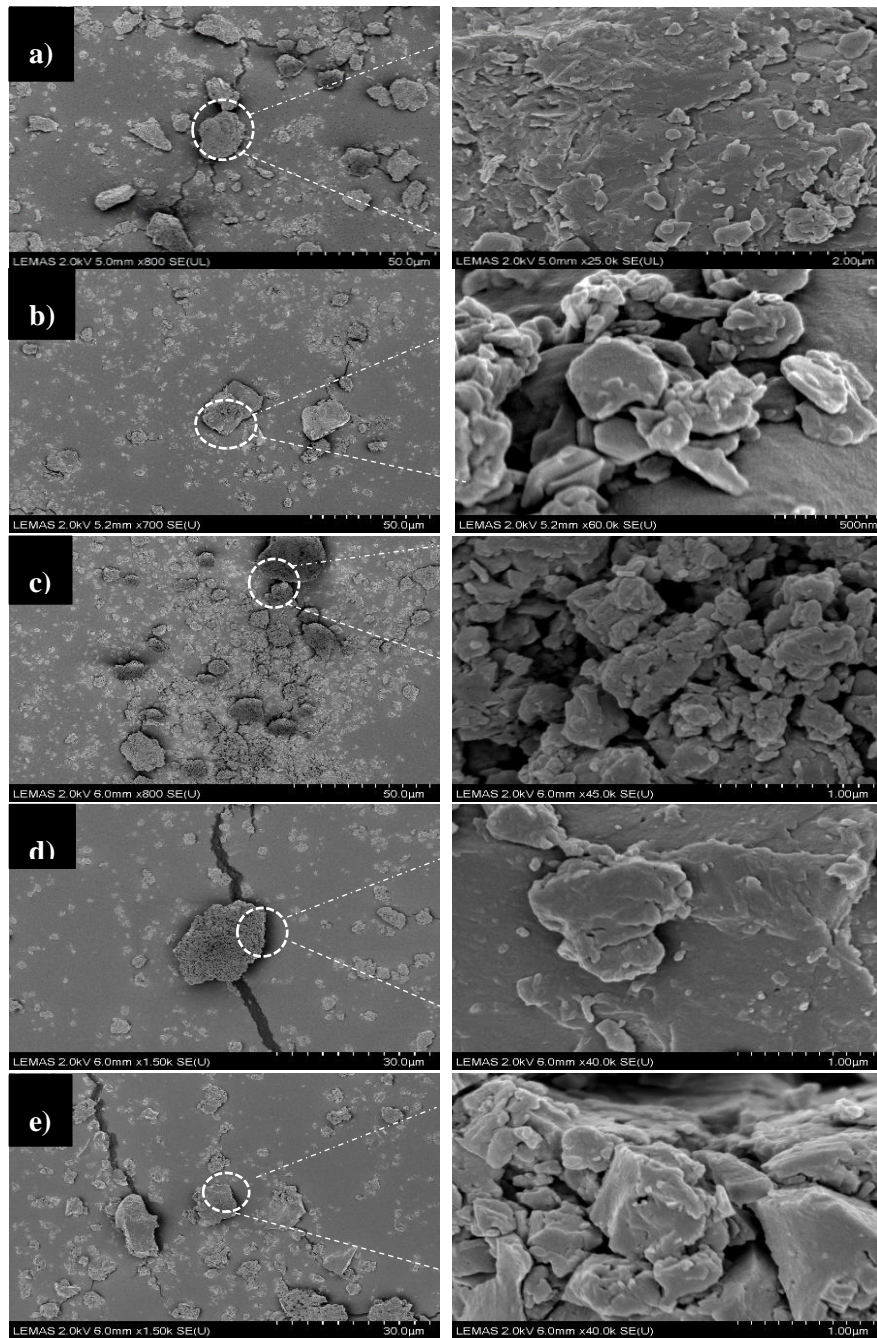


**Figure 6-25: SEM images show the Morphology of DABOMD particles (left) and their surfaces (on the right), a-Non-milled, b- 1min milled, c-5min milled, d-15min milled, e- 30min Single Ball Mill.**

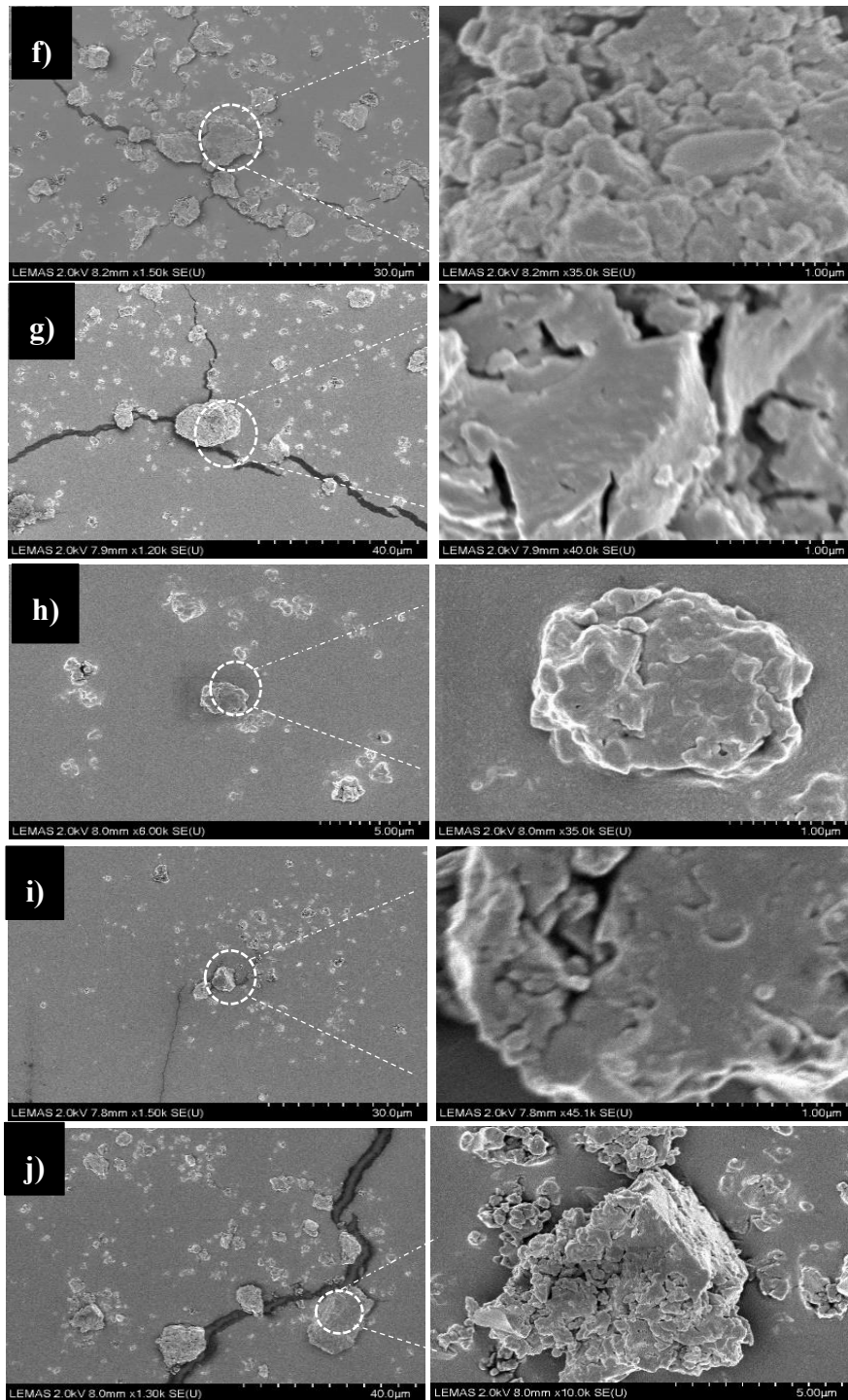


**Figure 6-26: SEM images show the morphology of DABOMD's particles (left) and their surfaces (on the right), f-60min milled, g- 120min milled, h-180min milled, i-240min milled, j-300min single ball mill**

### 6.3.2.3. Crystalline Properties of DABOMD

XRPD is used to determine the effect of the single ball mill on the crystalline properties of DABOMD following the same set-up used for the planetary ball mill. Milling of DABOMD leads to an apparent reduction of the Bragg's peaks within the first 15 min (Figure 6-27). Continuous milling resulted in an effective vanish of the crystalline sample within 120 minutes of milling. The XRPD patterns of the milled products from 240 min onwards are perfectly matching that of the standard amorphous which suggests that DABOMD underwent phase transformation from crystalline to amorphous as a result of milling in a single ball mill which is the same observed behaviour when milled in the planetary ball mill. However, the intensity of the peaks, particularly, between 1 min and 120 min seems slightly lower than those of the planetary ball-milled samples which suggest that single ball-milled samples have higher crystallinity. This further stress that single ball mill generates less energy compared to the planetary ball mill milling.

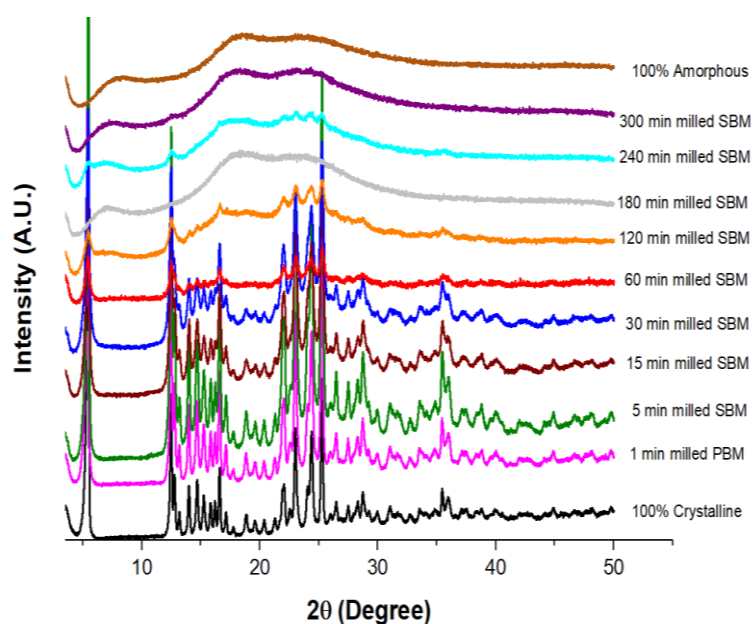


**Figure 6-27: XRPD of DABOMD before milling and after milling with single ball mill from 1 min to 300min**

### 6.3.2.4. Thermodynamic Properties

DSC setup in the single ball mill is similar to that in the planetary ball mill experiment. As the milling progresses, it can be seen that the intensity of the endothermic peaks reduces and that all the peaks tend to shift to a lower temperature which indicates the dehydration and the amorphisation of DABOMD (Figure 6-28) which was anticipated from the XRPD outcome. In general, the thermal behaviour of the single ball-milled samples of DABOMD is analogous to the patterns observed in the planetary ball mill.

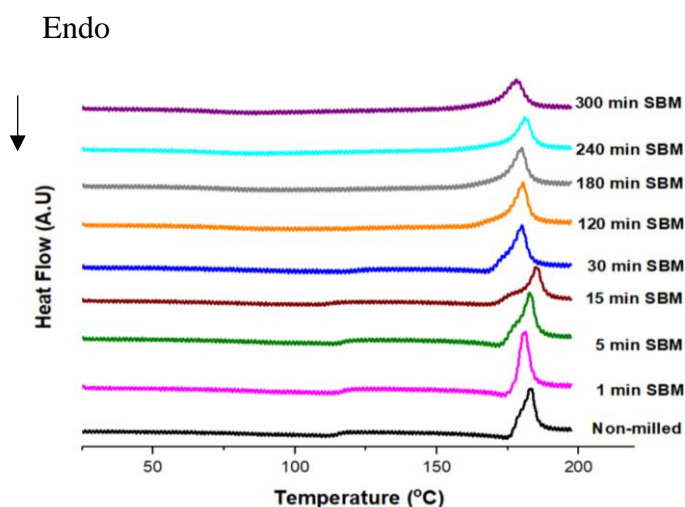


**Figure 6-28: DSC Profile of DABOMD for the non-milled and milled samples in a single ball mill at a temperature 25 to 250 °C and a rate 5°C/min**

#### 6.3.2.5. Intermolecular properties of DABOMD

In general, FTIR Spectra for samples milled with single ball mill exhibit very similar patterns as shown for samples milled in the planetary ball mill (Table 6-12, Figure 6-29 and Figure 6-30). For instance, the broadening of the O-H peak occurs at the same region 3070-3660  $\text{cm}^{-1}$  for a single ball milled sample as is the case from planetary ball milled and amorphous samples. The broadening of the major peaks in the single ball-milled follows the same pattern as that in the planetary ball-milled samples. This indicates that the mode of amorphisation of DABOMD in the single ball mill follows the same mechanism as in the planetary ball mill.

**Table 6-12: Vibrations of the main functional groups in non-milled crystalline and milled DABOMD in planetary and single ball mills**

Functional group	Type of vibration mode	Crystalline vibration ( $\text{cm}^{-1}$ )	Amorphous vibration ( $\text{cm}^{-1}$ )	300 min PBM vibration ( $\text{cm}^{-1}$ )	300 min SBM vibration ( $\text{cm}^{-1}$ )
O-H	Stretch	3300-3600	3070-3660	3070-3660	3070-3660
S=O	Stretch	1001.2	993.9	994.9	996.0
C-H in CH <sub>3</sub> or O-CH <sub>3</sub>	Stretch	2929.5	2934.1	2935.7	2939.7
Benzimidazole H <sub>3</sub> C-O	Bend	1197.7	1197.8	1198.1	1198.6

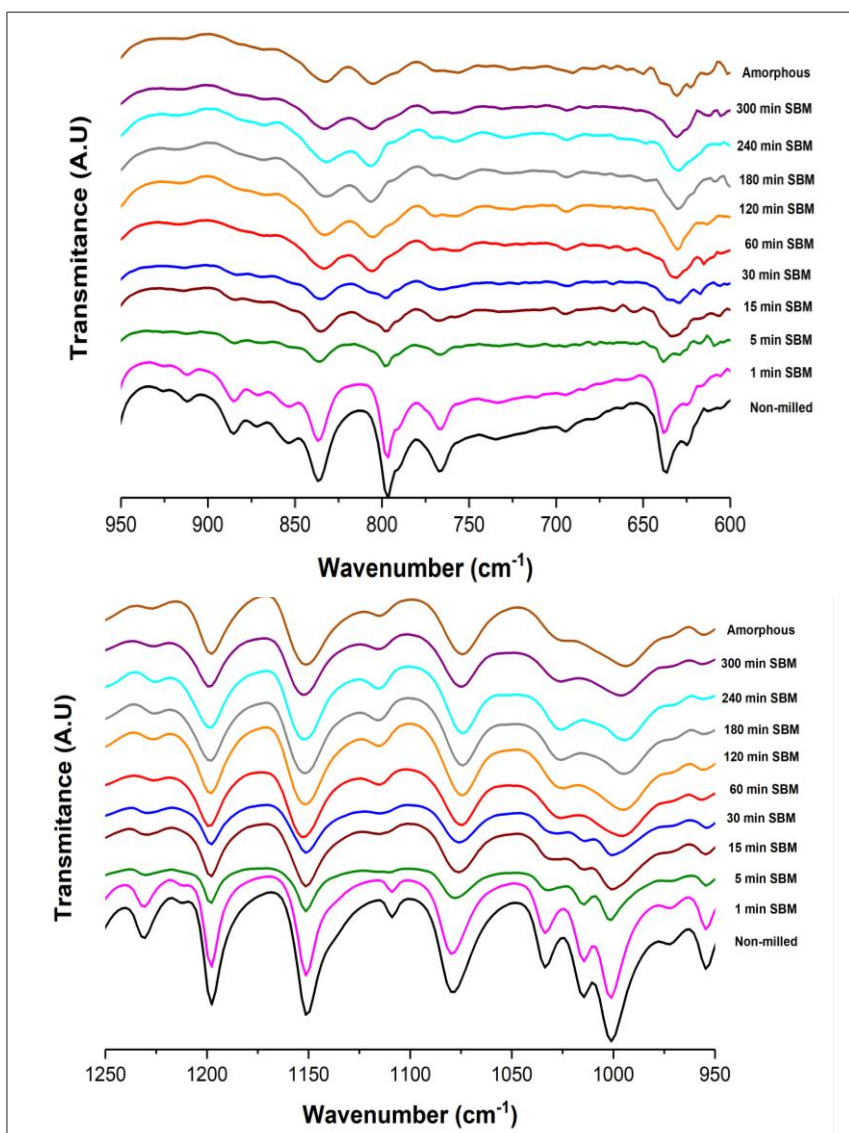


**Figure 6-29: FTIR-ATR of non-milled and milled DABOMD in single ball mill showing scan from a- 600 to 950 cm<sup>-1</sup>, b- from 950 to 1200**

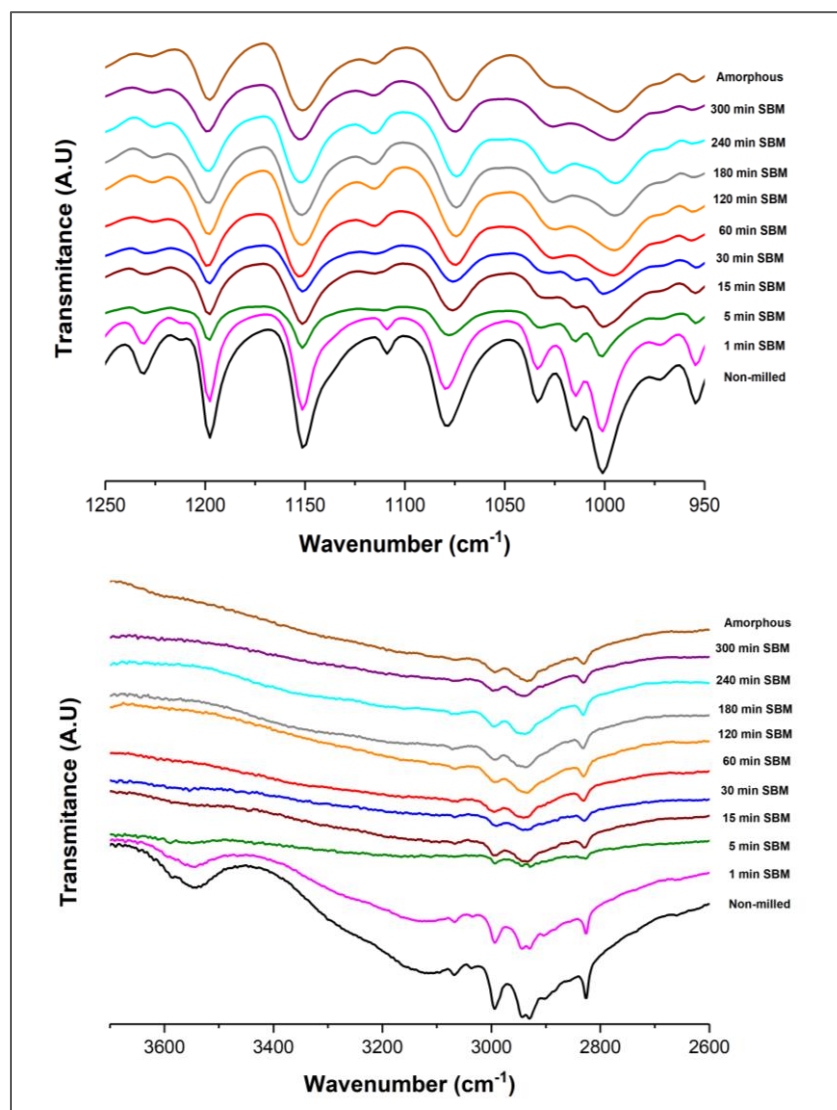


**Figure 6-30: FTIR-ATR of non-milled and milled DABOMD using single ball mill showing scan from c-1200 to 1600  $\text{cm}^{-1}$  and d from 2600 to 3700  $\text{cm}^{-1}$**

### 6.3.2.6. Quantification of Amorphous

#### 6.3.2.6.1. Quantification of Amorphous using XRPD Data

The amount of amorphous produced during the process of milling DABOMD in a single ball mill was quantified following the same method applied in the planetary ball mill. In general, it can be seen from Figure 6-31 and Table 6-13 that the single ball milling of DABOMD produced amorphous, which is slightly lower than that produced in the planetary ball mill. This suggests that lower energy is sufficient for the production of a large amount of amorphous DABOMD. It also suggests that the slip system (100) deforms under the impact stress and not only limited to the shear, but this will also be investigated further in later Chapter 8 see ( section 8.4.). Moreover, it is evident that in the first few minutes, a larger amount of amorphous is generated

in the planetary ball mill as opposed to a single ball mill which can be related to the higher shear stress associated with planetary ball mill that can accelerate the plane deformation. Higher energy can lead to a larger distortion of the crystalline lattice as a result of breakage/disruption of the hydrogen bonds. It can also increase the kinetic of water molecules and thus lead to rapid evaporation. The amount of energy produced in the two mills is yet to be calculated in Chapter 8.

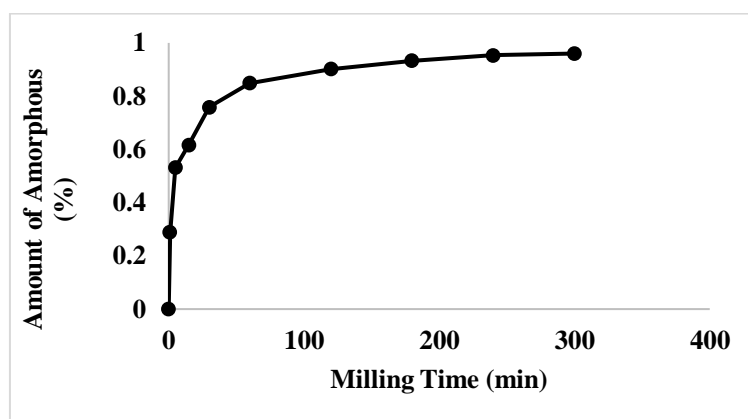


**Figure 6-31: Percentage amorphous of DABOMD forming during different milling time in single ball mill**

**Table 6-13: Percentage amorphous of DABOMD quantified from XRPD forming during different milling time in single ball mill**

Time (min)	Amorphous (%)
1	0.29
5	0.53
15	0.62
30	0.76
60	0.85
120	0.90
180	0.93
240	0.95
300	0.96

#### 6.3.2.6.2. Quantification of Amorphous Using FTIR Chemometric

The generated amorphous produced by the single ball mill (Table 6-14) was quantified using FTIR chemometric similar to that in planetary ball-milled samples. The data generated for instance from the first derivative does not seem to reflect the real scenario since it is expected to produce less amorphous in single ball mill as opposed to planetary ball mill as is indicated

by the XRPD Figure 6-27. Also, the second derivative of chemometric analysis seems to significantly underestimate the amount of the generated amorphous which could be associated with the curve smoothing to remove the impact of the noise. Therefore, the amorphous quantification by XRPD is employed for the rest of this thesis.

**Table 6-14: Percentage amorphous formed with single ball mill quantified using FTIR chemometric method of milled DABOMD and equivalent % water content from TGA**

Milling time (min)	Amorphous content based on Chemometric FTIR	
	First derivative	Second derivative
0	0	0
1	0.21	0.07
5	0.70	0.08
15	0.70	0.55
30	0.72	0.52
60	0.99	0.95
120	0.99	0.94
180	1	0.99
240	1	1
300	0.98	0.94

### 6.3.2.7. Kinetic of Comminution and Amorphisation in Single Ball Mill

Prolonged milling of DABOMD in the single ball mill follows an exponential pattern similar to that seen with planetary ball mill which reflects that the same mechanism is occurring in both mills and at the same sequence.

The outcome of the model fit of the kinetics of the comminution and amorphisation of DABOMD milled using a single ball mill is shown in Table 6-15.

**Table 6-15: Table shows the outcome of the model fit of the kinetics of comminution amorphisation in the single ball mill**

	Comminution		Amorphisation			
	SBM D90	SBM D50	PBM D90	PBM D50	SBM (XRPD)	PBM (XRPD)
$k_1$	0.4	0.65	0.28	0.72	0.17	0.20
$k_2$	0.04	0.035	0.01	0.02	0.01	0.02
$\alpha$	88%	81%	81%	68%	76%	81%
$\tau_{\text{rpd}}$	2.5	1.5	3.6	1.4	5.9	5.3
$\tau_{\text{slw}}$	25.0	28.6	88.3	62.0	100	52.3

1) The model fitted to the comminution data from  $D_{90}$  and  $D_{50}$  is shown in (Figure 6-32 modelled). It can be seen that the  $D_{90}$  depicts a better fit compared to  $D_{50}$ . The result shows that  $\alpha_{rpd\_com} = 88\%$ ,  $\tau_{rpd\_com} = 2.2\text{min}$  and  $\tau_{slw\_com} = 25\text{min}$ . This indicates that the comminution process is more rapid in the single ball mill and accounts for an additional 7% size reduction as opposed to the planetary ball-milled samples ( where,  $\alpha_{rpd\_com} = 81\%$ ). This is postulated to be associated with the prevailing impact stress mode in the single ball mill which promotes particle fracture. Interestingly, the rapid and the slow phases of comminution in the single ball-milled samples seem to occur at a faster rate (where  $\tau_{rpd\_com} = 3.6\text{min}$  and  $\tau_{slw\_com} = 88.3\text{min}$ ).

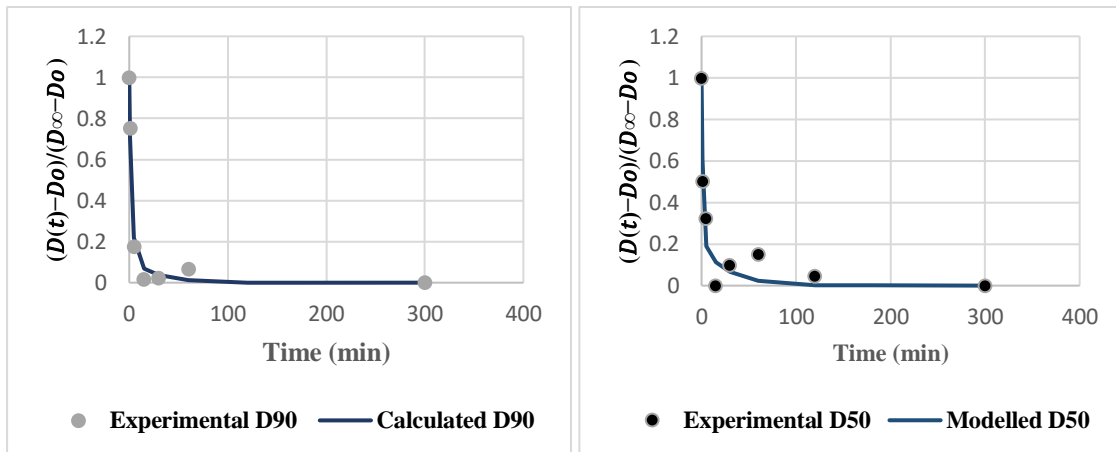


**Figure 6-32: The kinetic of comminution of DABOMD in single ball mill presented by  $D_{90}$  and  $D_{50}$**

2) The model fitted to the amorphisation data (Figure 6-33, modelled) shows; a rapid amorphisation accounting for approx. 80% of amorphous which occurs in the first few minutes as follows;  $\tau_{rpd\_amp} = 5.9$  which indicates that amorphisation occurs at a slower rate in single ball mill as opposed to planetary ball mill (where,  $\tau_{rpd\_amp} = 5.6$ ) which is associated with the larger energy available in the planetary ball mill that promotes amorphisation (including shear of planes, hydrogen bonds distortion and higher kinetics of water molecules). The second slower amorphisation phase occurs at  $\tau_{slw\_amp} = 100\text{min}$  which is slower compared to planetary ball mill (where,  $\tau_{slw\_amp} = 52.3\text{min}$ ). This is postulated to the prevailing shear mode in the planetary ball mill which promotes rapid amorphisation through extensive shearing of planes and plastic deformation.

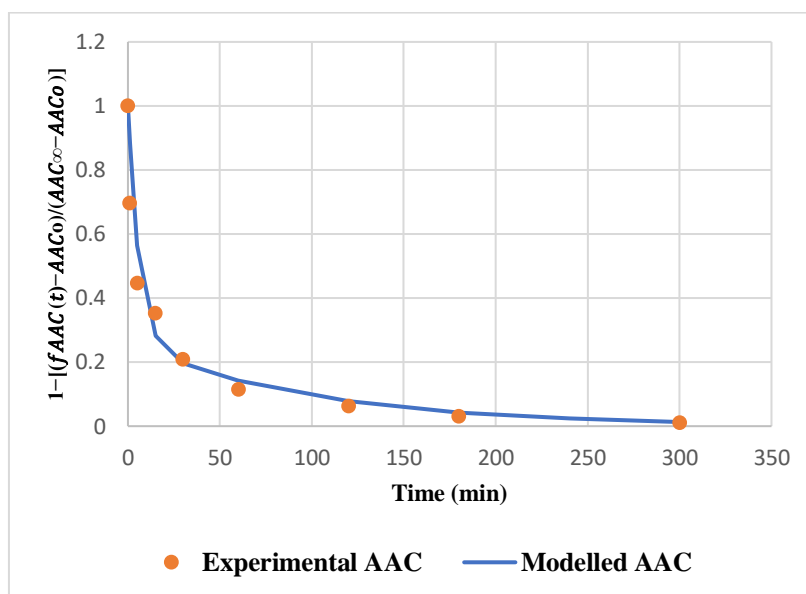


**Figure 6-33: The kinetic of amorphisation of DABOMD in single ball mill**

The summary to take is that DABOMD shows similar behaviour and deforms in the same manner in planetary ball mill and single ball mill. However, the single ball mill shows a rapid rate of comminution, particularly in the first 30min, while planetary ball mill exhibits a rapid rate of amorphisation. Also, planetary ball mill resulted in the formation of particles with smaller sizes as opposed to the single ball mill.

## 6.4. Conclusion

DABOMD was milled with a planetary and single ball mill at different times from 1min to 300 min. Special attention was paid to the comminution and amorphisation behaviour of DABOMD. It was found that the milling of DABOMD resulted in significant comminution and amorphisation with a slightly higher extent of comminution and amorphisation obtained with the planetary ball mill owed to the higher level of impact and shear stresses generated in this mill. The observed milling behaviour of DABOMD agrees with the predicted outcome from Chapter 4, which postulated that DABOMD is prone to fracture and plastic deformation. The comminution and amorphisation of DABOMD in the two mills occur parallel to each other's following an exponential pattern. The comminution process involves two phases; a rapid phase driven by the slip of planes ((100) system) which accounts for the majority of size reduction, and a slower steady-state phase which accounts for the remaining size reduction. The rate of comminution (kinetics) in the single ball mill is higher than that observed in the planetary ball mill, which was postulated to be linked to the prevailing impact stress in the single ball mill. Similarly, the amorphisation of DABOMD involves two phases a rapid phase

driven by the rapid water loss and plastic deformation and a slower phase driven by slower water loss. The rate of amorphisation in the planetary ball mill is higher than that in the single ball mill which is postulated to be linked to the prevailing shear in the planetary ball mill which promotes plastic deformation via shearing of planes. The formation of amorphous was demonstrated by investigating DABOMD's crystalline, thermodynamic and intermolecular properties using XRPD, TGA, DSC, and FTIR analysis, respectively. The amount of amorphous was quantified from XRPD data combined with FTIR chemometric analysis. The mechanism of milling of DABOMD was postulated to be driven by the deformation of the slip planes, which promotes fracture and plastic deformation and facilitate the loss of water molecules.

## **Chapter 7 Milling of $\beta$ –LGA**

### **7.1. Introduction**

### **7.2. Milling of $\beta$ –LGA with planetary ball mill**

### **7.3. Discussion**

### **7.4. Conclusion**

**This chapter outlines milling of  $\beta$  –LGA using planetary ball mill. The impact of this mill on the physical and chemical properties of  $\beta$  –LGA was assessed and compared to that of DABOMD. A relationship was established between the predicted material properties and the milling behaviour of  $\beta$  –LGA.**

## 7.1. Introduction

The impact of milling on the physical and chemical structure of Beta L-Glutamic Acid ( $\beta$ -LGA) is investigated in this chapter. The anticipated material properties suggest that  $\beta$ -LGA is more prone to fracture and less prone to plastic deformation, which suggested its susceptibility to significant comminution and lower amorphisation. Therefore, planetary ball mill is used to mill  $\beta$ -LGA due to its higher prevailing stress compared to the single ball mill to allow for maximum change. The impact of milling on the physical and chemical characteristics of  $\beta$ -LGA is assessed to evaluate changes in the morphology, crystalline thermodynamic/thermochemical and intermolecular properties. The relationship between the material properties, milling conditions and product characteristics of  $\beta$ -LGA is determined in this chapter and is compared to the outcome of milling of DABOMD.

## 7.2. Planetary Ball Mill

### 7.2.1. Experimental Setup

$\beta$ -LGA was milled using the planetary ball mill PM100 with the same set up followed for milling DABOMD. The milling was conducted at successive times from 5 min to 300 min.

### 7.2.2. Powder Characterisation

#### 7.2.2.1. Particle Size Distribution of $\beta$ -LGA

The particle size measurements of the feed and milled powders of DABOMD were obtained using laser diffraction wet system. Particle size analysis was undertaken in the Hydro unit of the Mastersizer 2000, where the sample is dispersed in a built-in tank in a suitable solvent. Approximately 0.5 g of  $\beta$ -LGA powder was dispersed in isopropyl at a speed of 1500 RPM and obscuration from 5 to 10%. The data is reported as equivalent volume diameters  $D(v, 90)$ ,  $D(v, 50)$  and  $D(v, 10)$ . The average particle size distribution was obtained from a three replicates sample measurement for reliability. The standard deviation of the medium diameter calculated from the size analysis of three replicates of non-milled sample of  $\beta$ -LGA is equal to 1.74. The statistical standard deviation of the average particle size distribution of  $\beta$ -LGA is shown in Figure 7-1. The generated data is displayed as particle size distribution PSD, cumulative distribution, and characteristic diameters are shown in Figure 7-2, Figure 7-3, and Table 7-1, respectively. The non-milled, as-received sample of  $\beta$ -LGA has bimodal distribution with median particle diameter equal to 96  $\mu\text{m}$ .

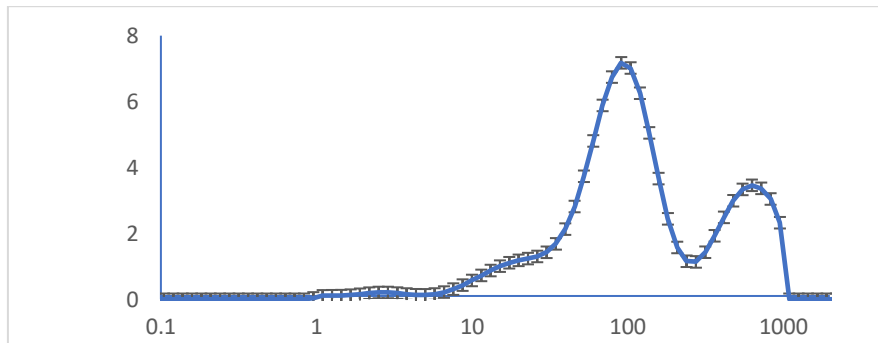


**Figure 7-1: Average particle size distribution of non-milled  $\beta$  –LGA with error bars**

Milling of  $\beta$  –LGA at different times leads to a prominent size reduction in  $\beta$  –LGA. For instance, the feed has a  $D_{90}$  equal to  $599.8 \mu\text{m}$  is reduced to  $148.5 \mu\text{m}$  with progressive milling from 5 min to 300 min. The cumulative distribution (Figure 7-3) shows that the highest rate of communication was received within the first 5 min of milling, with about 70% in size reduction. From 30 min onwards, the size of  $\beta$  –LGA shows replicated increasing and decreasing at irregular patterns. For instance,  $D_{90}$  increased from  $157.3 \mu\text{m}$  at 30 min to  $167.7 \mu\text{m}$  at 60 min and decreased back to  $138.8 \mu\text{m}$  at 120 min. This could be due to the agglomeration and the deagglomeration of the milled samples.

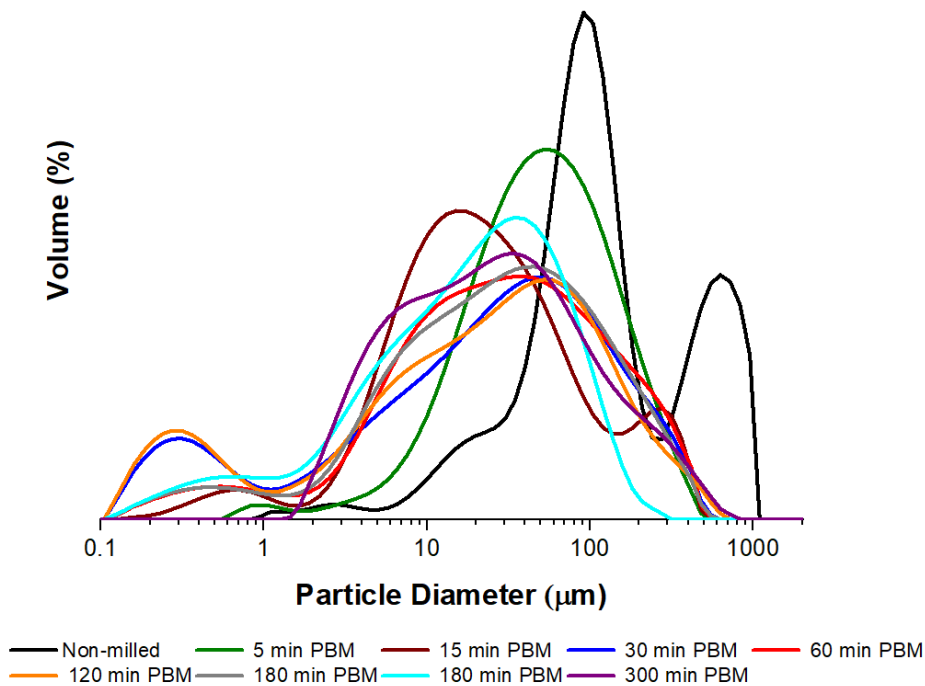


**Figure 7-2: Particle size distribution of non-milled and milled  $\beta$  –LGA in planetary ball mill from 15min to 300 min**

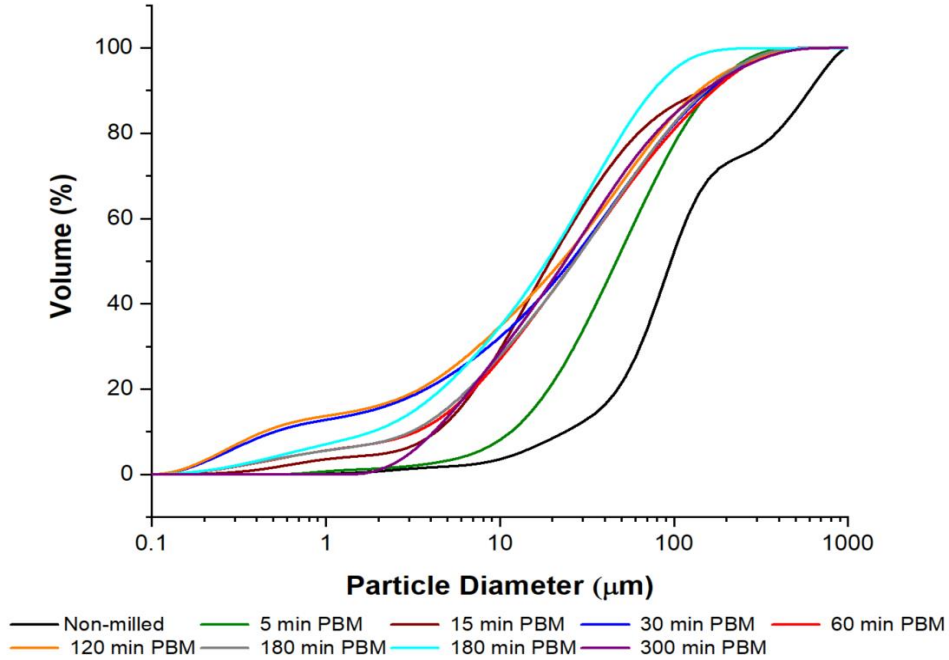


**Figure 7-3: Cumulative Distribution of non-milled and planetary ball milled  $\beta$  –LGA from 1min to 300 min**

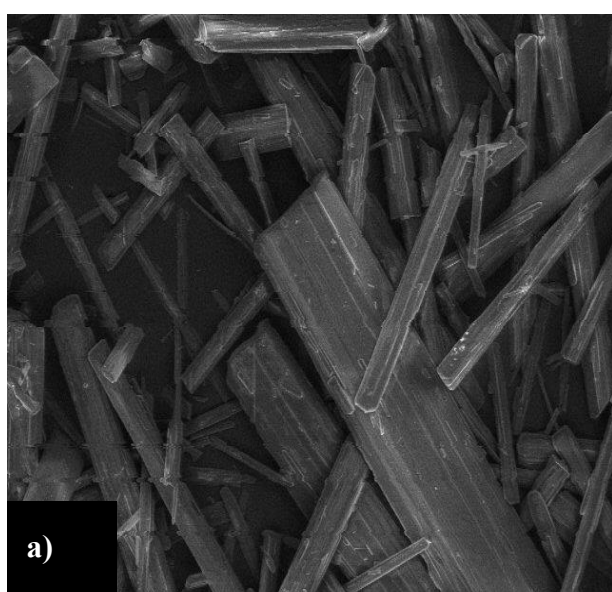
**Table 7-1: Characteristic sizes ( $D_{10}$ ,  $D_{50}$ , and,  $D_{90}$ ) of non-milled and milled  $\beta$  –LGA samples in planetary ball mill from 1min to 300 min**

Sample	$D_{10}$	$D_{50}$	$D_{90}$
Non-milled	23.7	96.0	599.8
5 min	11.6	46.7	161.3
15 min	4.3	19.5	146.1
30 min	0.5	25.6	157.3
60 min	3.3	26.7	167.7
120 min	0.4	22.6	138.8
180 min	3.1	26.9	152.0
240 min	1.8	18.6	75.9
300 min	4.2	23.7	148.5

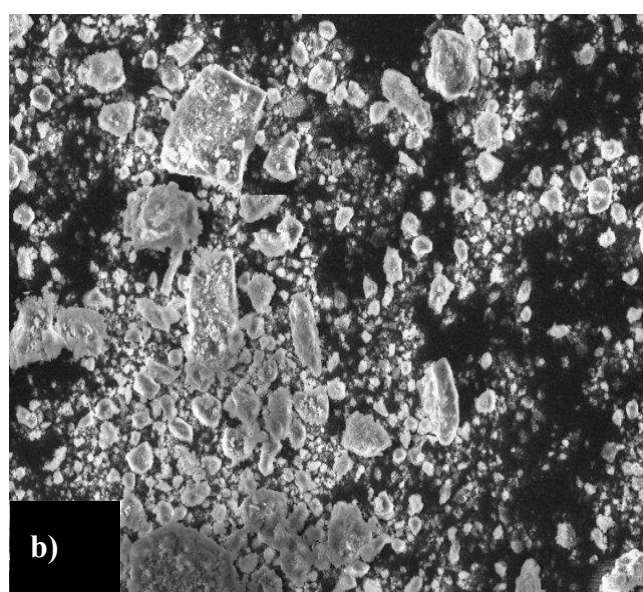
#### 7.2.2.2. Morphology $\beta$ –LGA

To examine the morphology of the non-milled and the milled  $\beta$  –LGA, SEM Hitachi TM3030Plus was used at 15kV. Samples were placed at a carbon tab which are positioned on metal stubs for analysis. The morphology of the non-milled and the milled samples of  $\beta$  –LGA

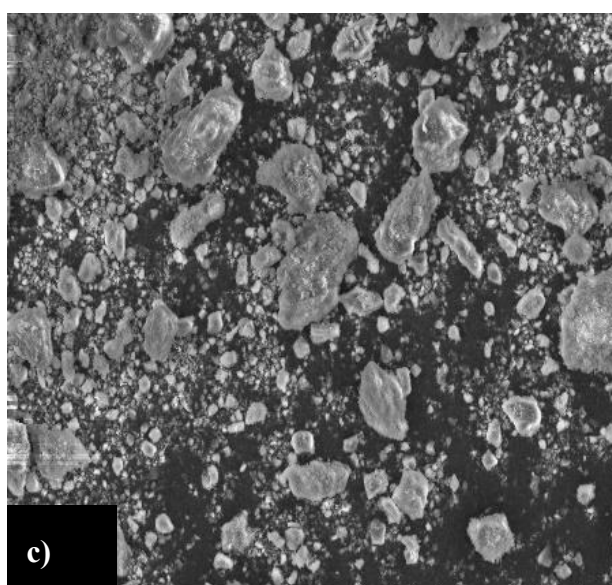
is shown in Figure 7-4 and Figure 7-5. The non-milled powder of  $\beta$ -LGA exhibits large particles of irregular sizes which have needle-like morphology (Figure 7-4a). As the milling progresses, the particles tend to lose their elongation and reduce in the size which agrees with the PSD analysis. Interestingly, It is evident that the milling increases the level of agglomeration after 60 min of milling which can be observed in Figure 7-4d. The number of fines seems to fluctuate at different times, for instance, the samples milled for 180 min (Figure 7-4f) appear to have more agglomerates than those milled for 120 min (Figure 7-4e). Similarly, the samples milled for 300 min (Figure 7-4h) appear to have fewer fines adhered on the surface compared those milled for 240 min (Figure 7-4g) which indicates that agglomeration and deagglomeration are taken place which is analogous to the PSD analysis.



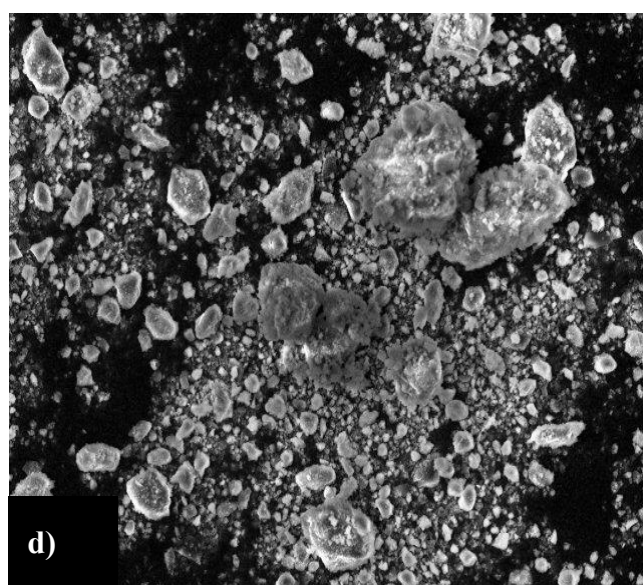
TM3030Plus0055 2018-02-09 14:20 HMM 300  $\mu$ m



TM3030Plus0041 2018-02-09 13:05 HMM 100  $\mu$ m



TM3030Plus0033 2018-02-09 12:34 HMM 100  $\mu$ m



TM3030Plus0069 2018-02-09 14:50 HMM 100  $\mu$ m

**Figure 7-4: SEM images of  $\beta$  -LGA, a) Non-milled, b) 15 min milled, c) 30 min, d) 60 min milled**

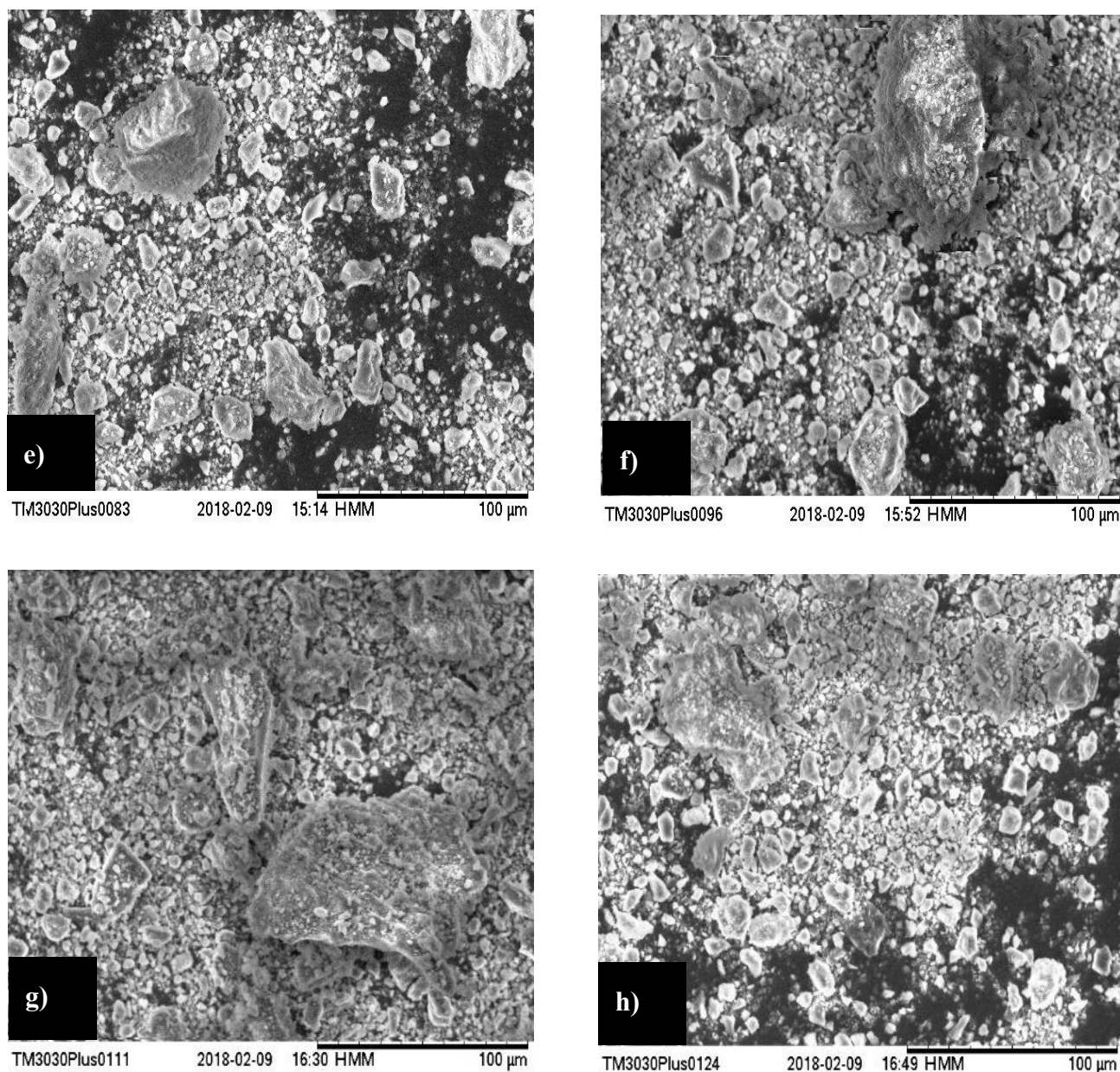


**Figure 7-5: SEM images of  $\beta$  -LGA, e) 120 min milled, f) 180 min milled, g) 240 min milled, h) 300 min milled**

### 7.2.3. Crystalline Properties

XRPD of the non-milled and milled  $\beta$  -LGA is shown in Figure 7-6. It can be seen that the non-milled  $\beta$  -LGA exhibits a sharp well defined Bragg peaks at  $10^\circ$ ,  $20^\circ$ ,  $26^\circ$ ,  $30^\circ$ ,  $34^\circ$ ,  $36^\circ$  and  $37^\circ$  which agrees with the reported literature (Wu *et al.*, 2010; Aarthi *et al.*, 2018). The XRPD comparison of the non-milled and the milled peaks of  $\beta$  -LGA reveal that they exhibit

variable peak intensities. This is associated with the fact that non-milled powders of  $\beta$ -LGA have a needle-like morphology and thus they tend to orientate with their flat faces parallel to the surfaces measured by XRPD (Cameron F. Holder and Raymond E. Schaak, 2019). According to the predicted work from Chapter 5,  $\beta$ -LGA most morphologically important face (following BFDH and experimentally grown crystals) is (002). To further assist with this, the experimental XRPD peaks of  $\beta$ -LGA were compared to the simulated peaks via assigning (hkl) planes as shown in Figure 7-7. The simulated XRPD along with the (h,k,l) of  $\beta$ -LGA were obtained from Mercury (Version 3.9) (CCDC, Cambridge, UK) following CCDC code LGLUAC01 as shown in Figure 7-7. This showed that the peak corresponding to face (002) at  $10^\circ$  exhibits a sharper and well-defined peak for the non-milled experimental powder as opposed to the simulated one. This further stresses that the variation in intensity is mainly due to the preferred orientations in the needle-like particles as opposed to the irregular shaped particles produced with milling which agrees with the SEM analysis (Figure 7-5). Moreover, it can be seen that as the milling progress, the XRPD peaks of the milled samples tend to become broader, which indicates some degree of amorphisation. Interestingly, it is also evident that the intensity of the XRPD peaks from 15 min onwards tends to fluctuate (decrease and increase) in an irregular manner. The decrease in the intensity indicates the formation of some amorphous, whereas, the increase of intensity suggests the recrystallisation of the formed amorphous. For example, sample milled for 60 min depicts a reduced XRPD intensity compared to that milled for 30 min due to the partial amorphisation. This is complementary to the observed size and morphological analysis of  $\beta$ -LGA, which explains the observed surface agglomeration, since the formed amorphous exhibits higher surface energy which favours agglomeration. However, the sample milled at 120 min has less crystallinity compared to that milled for 60 min, which suggests the recrystallisation of the formed amorphous. This pattern was repeated for the rest of the milling, which agrees with the obtained PSD analysis. Similar impact of milling of a pharmaceutical API was reported for indomethacin, Chloramphenicol palmitate CPP (Otsuka, Otsuka and Kaneniwa, 1994) and Sulphathiazole (Shakhtshneider and Boldyrev, 1993).

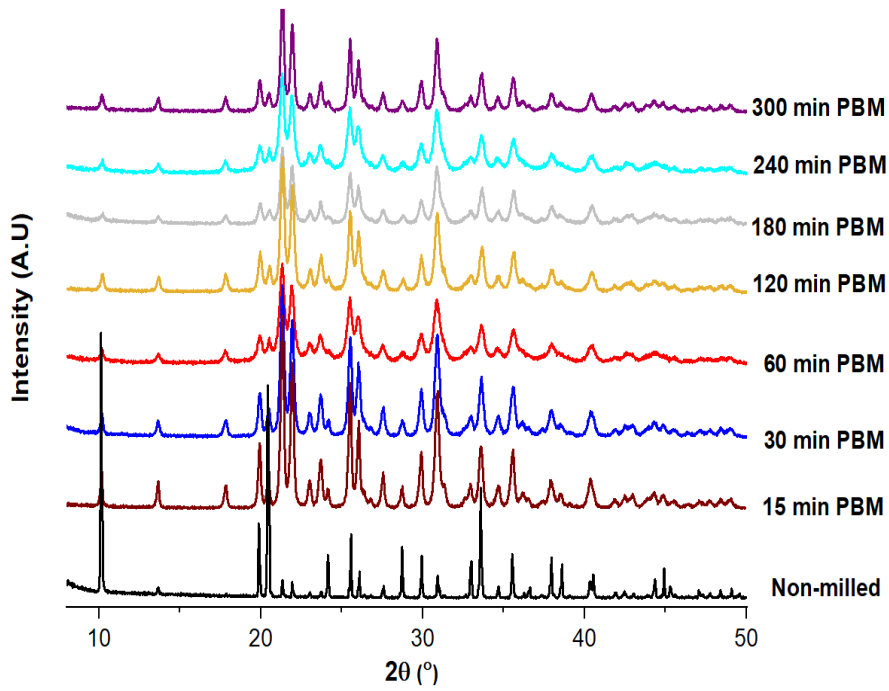


Figure 7-6: XRPD of  $\beta$ -LGA before milling and after milling from 1 min to 300min

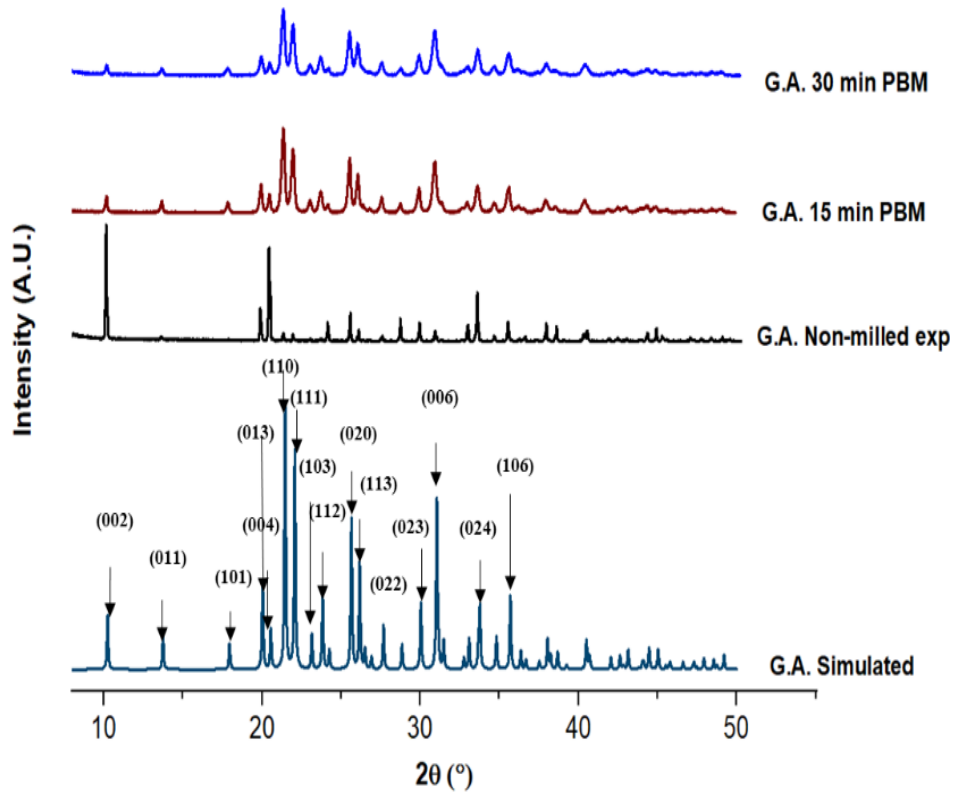
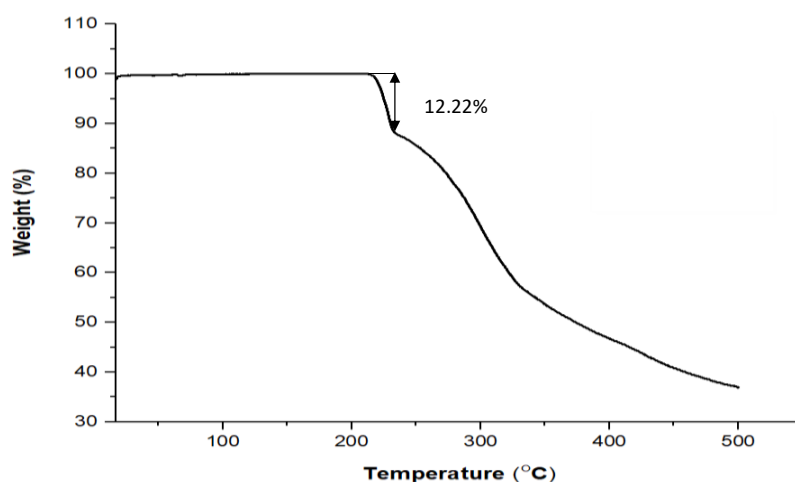


Figure 7-7: Assigning the planes to the peaks of  $\beta$ -LGA

### 7.2.4. Thermodynamic Properties

TGA profile for non-milled  $\beta$ -LGA is shown in Figure 7-8; it can be seen that  $\beta$ -LGA involves two mass losses. The first mass loss at 220°C is attributed to the water loss which was calculated to be 12.22% of the total mass; this is equivalent to one water molecule (12.24%) in  $\beta$ -LGA which agrees with the reported results in (Wu *et al.*, 2010). The second mass loss is postulated to be associated with the decomposition process. No further TGA analysis was conducted on the milled samples since it is believed that the temperature of  $\beta$ -LGA is not reaching 220°C due to the strict temperature monitoring process in the experiment. Having said that, the controlled temperature accounts for the bulk temperature of the milled samples and does not represent the temperature of the surface of the powder (impossible to measure) which can be higher than the bulk one. Further details regarding the impact of the temperature will be discussed later.



**Figure 7-8: TGA of non-milled  $\beta$ -LGA at 10°C/min**

The DSC analysis of  $\beta$ -LGA is shown in Figure 7-9; the non-milled  $\beta$ -LGA exhibits a sharp well-defined endotherm at 205.5°C which accounts for the melting and dehydration events (Wu *et al.*, 2010) which agrees with TGA. As the milling progresses, the endotherm tends to decrease in intensity and shifts to a lower temperature (i.e. the melting temperature of 300 min milled sample appears at 195 °C) which indicates the formation of the sample with lower stability, i.e. amorphous. Moreover, milling for 120 min led to the appearance of the glass transition temperature at 28°C (Figure 7-10), which is a clear indication of the presence of an amorphous sample. The glass transition temperature agrees with the reported value for the amorphous  $\beta$ -LGA prepared by melt-quench (Wu *et al.*, 2010). The absence of the glass transition temperature at shorter milling times might suggest that the amorphous is present at smaller quantities which could be lower than the detecting resolution of the DSC.

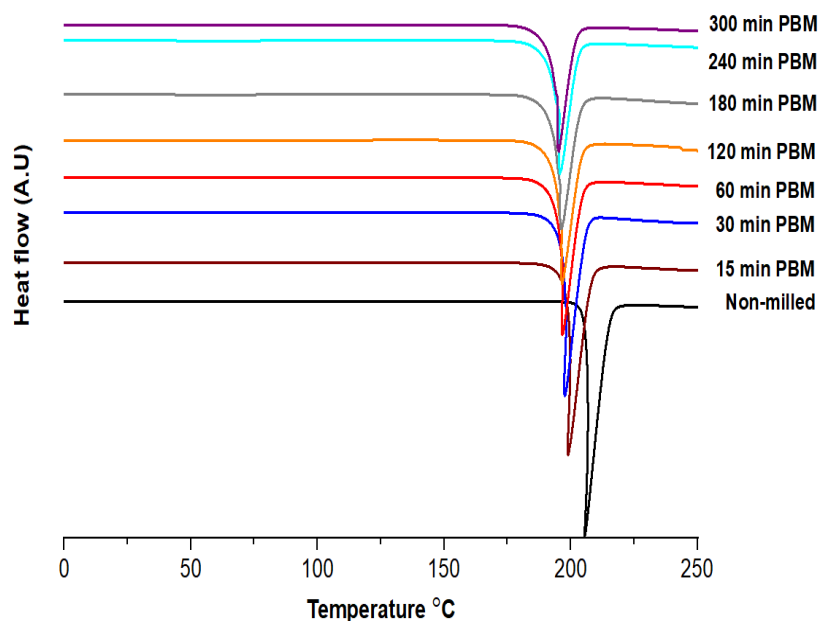


**Figure 7-9: DSC Profile of  $\beta$  –LGA for the non-milled and milled samples from 25 to 250 °C and 10°C/min**

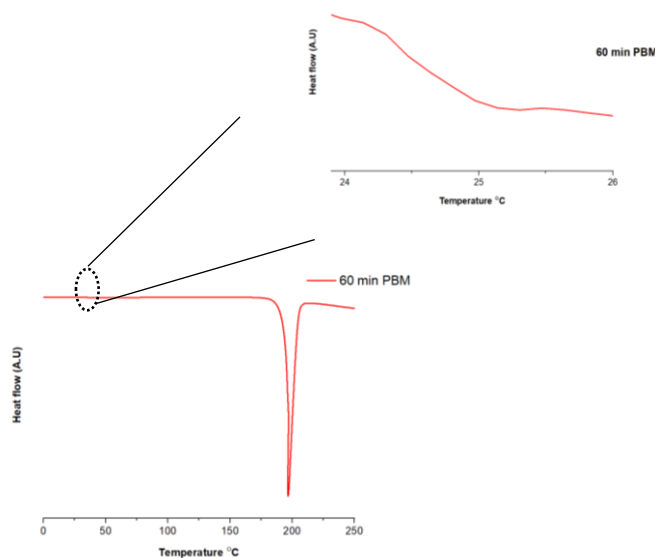


**Figure 7-10: Glass transition temperature the 60 min milled  $\beta$  –LGA**

### 7.2.5. Intermolecular Properties

In general, FTIR patterns for  $\beta$  –LGA show an some level of reduction and broadening in the intensity of the spectra (Figure 7-11 ). Almost all the peaks show a reduction owed to their involvement with the hydrogen bonding in  $\beta$  –LGA as shown in Table 7-2. The change in intensity is also an indication for the crystalline disordering and amorphisation as was

suggested by previous techniques. Hence, it can be postulated that the breakage/distortion of the hydrogen bonds is associated with the comminution of  $\beta$ -LGA.

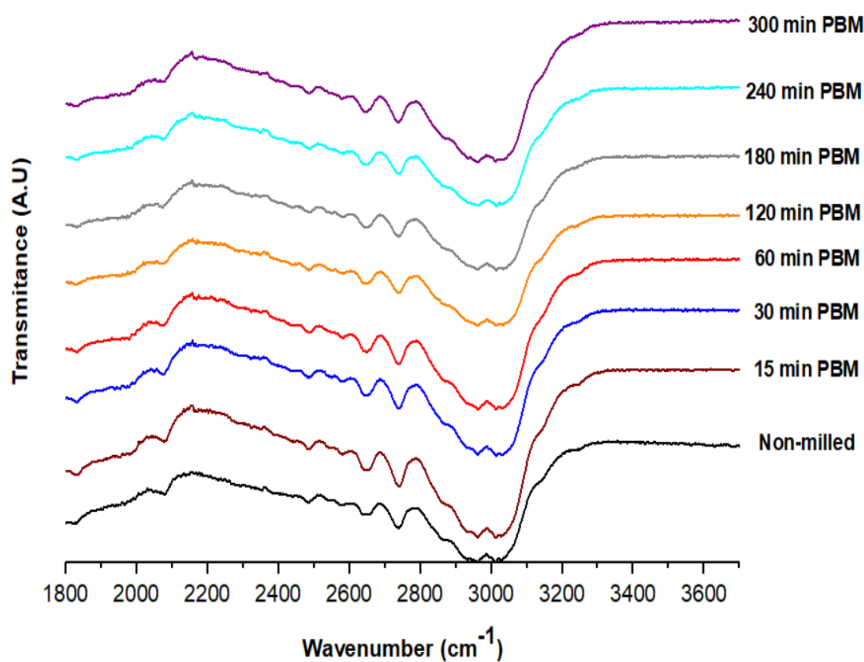


**Figure 7-11: FTIR-ATR of non-milled and milled  $\beta$ -LGA in planetary ball mill showing scan from 1600  $\text{cm}^{-1}$  to 3700  $\text{cm}^{-1}$**

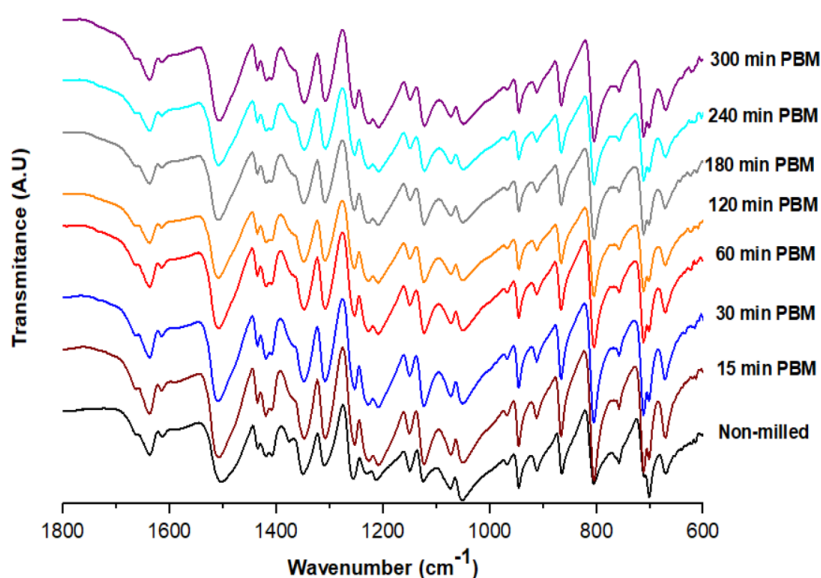


**Figure 7-12: FTIR-ATR of non-milled and milled  $\beta$ -LGA in planetary ball mill showing scan from 600  $\text{cm}^{-1}$  to 1800  $\text{cm}^{-1}$**

**Table 7-2: FTIR-ATR of non-milled and milled  $\beta$  –LGA in planetary ball mill**

Functional group	Type of vibration mode	Crystalline vibration ( $cm^{-1}$ )	300 min milled vibration PBM ( $cm^{-1}$ )	Reference
<b>N-H</b>	Stretching	3013.53	3013.12	FTIR in (Fouad <i>et al.</i> , 2009)
<b>O-H</b>	Stretching	2505.18-2798.32	2503.25-2804.11	(Wu <i>et al.</i> , 2013; Aarthi <i>et al.</i> , 2018)
<b>C=C</b>	stretching	2738.19	2739.02	(Wu <i>et al.</i> , 2013; Aarthi <i>et al.</i> , 2018)
<b>COO</b>	Stretching	1503.94	1503.09	( <i>Chemistry: IR of amino acids</i> , 2016)
<b>C-N</b>	Stretching	1348.14	1347.95	(Mohamed and Mohammed, 2013)
<b>C=O</b>	Stretching	1636.71		1637.40
<b>O-H</b>	bending	1123.03	1122.75	(Mohamed and Mohammed, 2013)

### 7.2.6. Quantification of Amorphous

The amorphous quantification is achieved through measuring the area under the XRPD peaks of the standard crystalline, and milled samples of  $\beta$  –LGA following the same methodology applied for DABOMD. The amount of amorphous formed with milling  $\beta$  –LGA is shown in Table 7-3.

**Table 7-3: The amount of amorphous  $\beta$  –LGA quantified from XRPD**

Time (min)	Amorphous from XRPD (%)
<b>0</b>	0
<b>15</b>	13.5
<b>30</b>	18.3
<b>60</b>	37.8
<b>120</b>	30.0
<b>180</b>	48.9
<b>240</b>	37.8
<b>300</b>	42.4

Overall, the solid-state characterisation of  $\beta$ -LGA indicates that significant comminution occurs as a result of the breakage of hydrogen bonds network. Furthermore, XRPD peaks broadening, thermal analysis from DSC, and TGA all indicate that the partial amorphisation of  $\beta$ -LGA.

## 7.3. Discussion

### 7.3.1. Comminution Amorphisation Relation

The comminution and amorphisation profiles of  $\beta$ -LGA are shown in Figure 7-13 and Figure 7-14. The profiles were model fitted following the same equations ( 6.5, 6.6, and 6.7) employed for the model fitting of the comminution and amorphisation profiles of DABOMD.

1) The comminution of  $\beta$ -LGA does not follow a perfect exponential pattern as was the case of DABOMD since it consists of many fluctuations corresponding to numerous events including size reduction, agglomeration, and deagglomeration processes. Yet, the model fit can still provide an insight into the kinetics of the comminution process of  $\beta$ -LGA. The first stage of comminution (rapid comminution) (Figure 7-13) occurs in the first 15 min and accounts for the size reduction process, followed by the slower comminution phase (which accounts for the variable agglomeration, deagglomeration and some size reduction taking place). The model fit outcome for the kinetic of comminution is shown in Table 7-4. It can be seen that the first phase of comminution results in approximately 90% of the comminution process and occurs at a time scale of 2.5 min. This result enhances the great breakage propensity of  $\beta$ -LGA which agrees with the predicted work suggesting its higher susceptibility to fracture. The slower comminution phase occurs in a time scale of 50 min, which accounts for a lower size-reduction  $\sim$  5%, which suggests that particles reached their critical sizes. As the particles achieve their critical size, any additional energy is dissipating in the form of defects which accumulates and causes the emergence of amorphous and ultimately the formation of agglomerates as a result of the higher surface energy. It can be seen that the rate of comminution of  $\beta$ -LGA is larger than that observed in DABOMD (equals 80%), although they both receive the same level of milling energy and experience the same stress conditions. The difference between their behaviour is suggested to be mainly related to their different intrinsic molecular properties including crystal structure, slip planes, and mechanical properties as predicted by the simulations in Chapters 4 and 5.

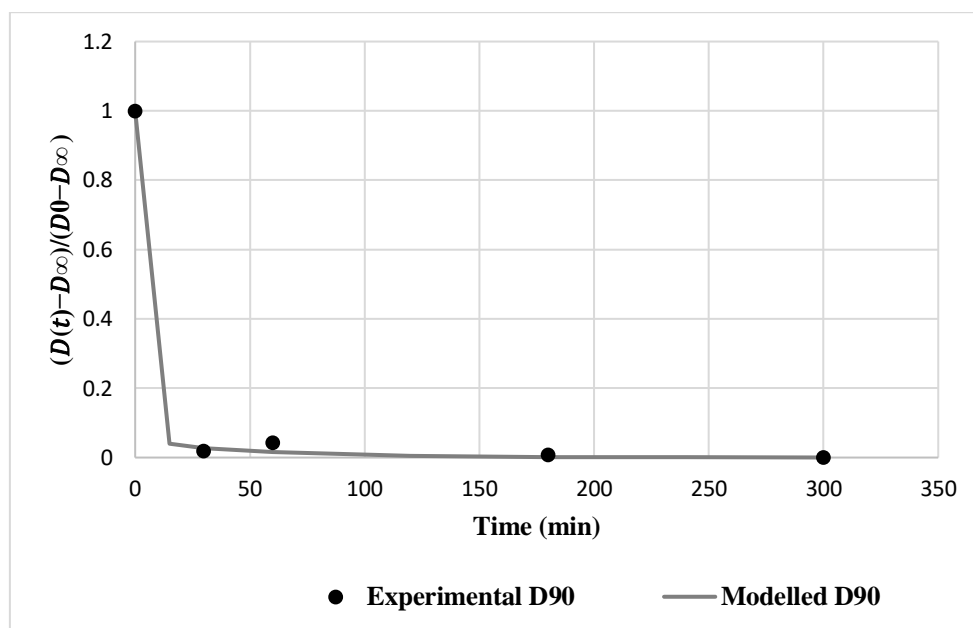


Figure 7-13: The kinetic of comminution of  $\beta$  –LGA presented by  $D_{90}$

Table 7-4: Table shows the outcome of the model fit of the kinetics of comminution and amorphisation of  $\beta$  –LGA

	Comminution	Amorphisation
	D90	XRPD
$k_1$	0.4	0.03
$k_2$	0.02	0.01
$\alpha$	95%	75%
$\tau_{\text{rpd}}$ (min)	2.5	58.8
$\tau_{\text{slw}}$ (min)	50	100

2) The partial amorphisation of  $\beta$  –LGA was model fitted using data from XRPD. It can be seen that the experimental amorphisation pattern depicts the same pattern observed in the comminution process. This implies that the amorphisation can be generally fitted into two main stages; the first amorphisation occurs at a time scale of approx. 58 min and accounts for approx. 80 % of the generated amorphous, which is analogous to the experimental data. The second amorphisation stage occurs at a time scale of 100 min.

Interestingly, the amorphisation of  $\beta$  –LGA occurs at a much lower rate compared to that of the comminution. For instance, the first phase of amorphisation exhibits a rate which is one order of magnitude larger ( $k_1$  of amorphisation is equal to approx.  $0.03 \text{ min}^{-1}$  compared to  $0.4 \text{ min}^{-1}$  in comminution) (Table 7-4). On the other hand, the amorphisation of  $\beta$  –LGA is

significantly lower than that obtained with the milling of DABOMD (i.e.  $\beta$ -LGA has rate constant of amorphisation first stage equal to  $0.03 \text{ min}^{-1}$  as opposed to DABOMD which has a rate constant of amorphisation equal to  $0.2 \text{ min}^{-1}$ ). The larger degree and rate of amorphisation of DABOMD is associated with the presence of slip planes that facilitated the plastic deformation as opposed to LGA which has no slip planes, in addition to the other differences such as mechanical properties and crystal structure between the two samples.

The slower rate of amorphisation for LGA implies that it is driven mainly by comminution, leading to the formation of defects which become nucleation and growth sites for amorphous.

It is evident that the comminution is dominating over the amorphisation of  $\beta$ -LGA throughout the entire milling, unlike DABOMD, which exhibits parallel comminution and amorphisation processes.

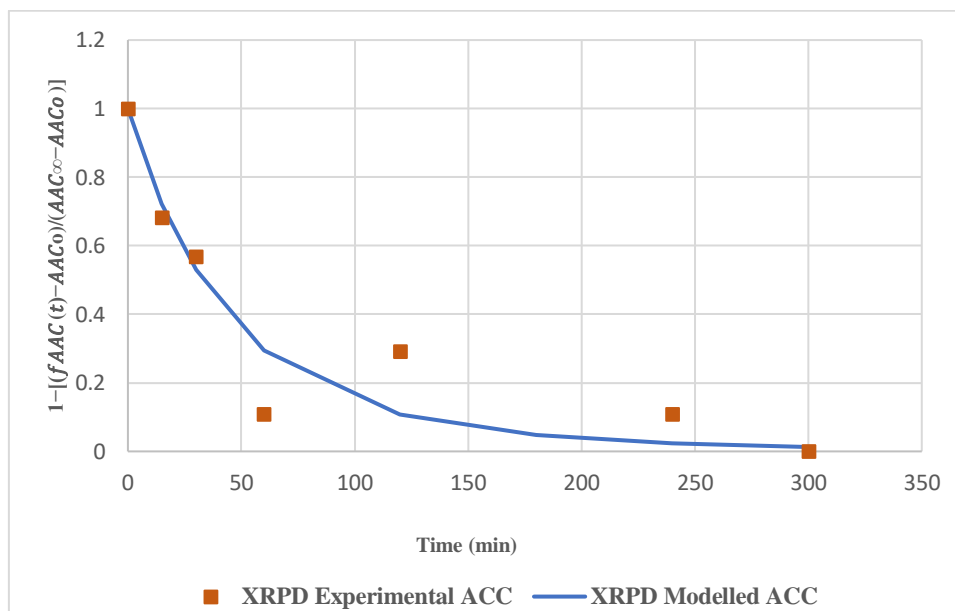


**Figure 7-14: The kinetic of amorphisation of  $\beta$ -LGA in planetary ball mill derived from; XRPD analysis**

### 7.3.2. Mechanism of Milling of $\beta$ -LGA

The proposed mechanism of milling of  $\beta$ -LGA is schematically shown in Figure 7-15. Milling of  $\beta$ -LGA results in a comminution that was dominating throughout the entire milling time followed by partial amorphisation.

The comminution can be subdivided to a rapid comminution process, followed by a series of replicating agglomeration and deagglomeration processes brought by the amorphisation and recrystallisation of  $\beta$ -LGA. The rapid and prominent comminution of  $\beta$ -LGA agrees with the predicted results from Chapter 4 which depicted that of  $\beta$ -LGA consists of an extensive network of ionic hydrogen bonds, which ultimately contribute to its prevailing brittle

deformation mode. The recrystallisation of  $\beta$ -LGA occurs mainly due to the unstable form of the amorphous produced with milling since  $\beta$ -LGA possesses a lower glass transition temperature which is closer to the room temperature, and a smaller molecular weight (the disordered crystals can reorder faster). Therefore, it can be postulated that the partial amorphisation of  $\beta$ -LGA is mainly driven by the defects generated during the process of milling. The generated defects accumulate and make nucleation and growth sites for the amorphous. Furthermore,  $\beta$ -LGA does not possess any slip plane which limits the process of plastic deformation a major contributor to effective amorphisation as was seen with DABOMD. The shear and impact stress arising from planetary ball mill resulted in a significant breakage of the hydrogen bonds network and ultimately led to a dramatic size reduction of  $\beta$ -LGA, seen particularly in the first phase of comminution (approx. 15 min).

Secondly, the temperature generated with milling is postulated to facilitate the nucleation and growth of amorphous. The high temperature from shear and impact is also suggested to promote surface melt and generates amorphous via the melt-quench process. The effect of increased temperature on  $\beta$ -LGA was investigated by (Wu *et al.*, 2010; Baláž *et al.*, 2013) who found that amorphous  $\beta$ -LGA (pyro-glutamic acid) was formed when  $\beta$ -LGA was heated from 140°C to 170 °C for multiple hours. In order to qualitatively assess the melting process, hot stage microscope was employed for  $\beta$ -LGA with similar settings used for DABOMD. Where,  $\beta$ -LGA powder was heated up to 210°C. Figure 7-16 shows the hot stage microscopic images of  $\beta$ -LGA at 25°C and at 210 °C. Despite that microscope does not have a high resolution to allow for the observation of the micro regions on the surface of powders, the melting event of  $\beta$ -LGA can be clearly observed at higher temperature as opposed to DABOMD (seen in Chapter 4). Although, the measured bulk temperature of the mill is monitored to prevent the rise in temperatures, the micro-regions particularly on the surface can still experience melting (I Colombo, Grassi and Grassi, 2009; Descamps and Willart, 2016). Furthermore, the generation of defects on the surface can promote surface-melt by lowering the melting temperature. Hence, it can be postulated that the breakage of hydrogen bonds is the main driver for the comminution of  $\beta$ -LGA, whereas, the generation of surface defects and surface melt are the main driver to the partial amorphisation of  $\beta$ -LGA.

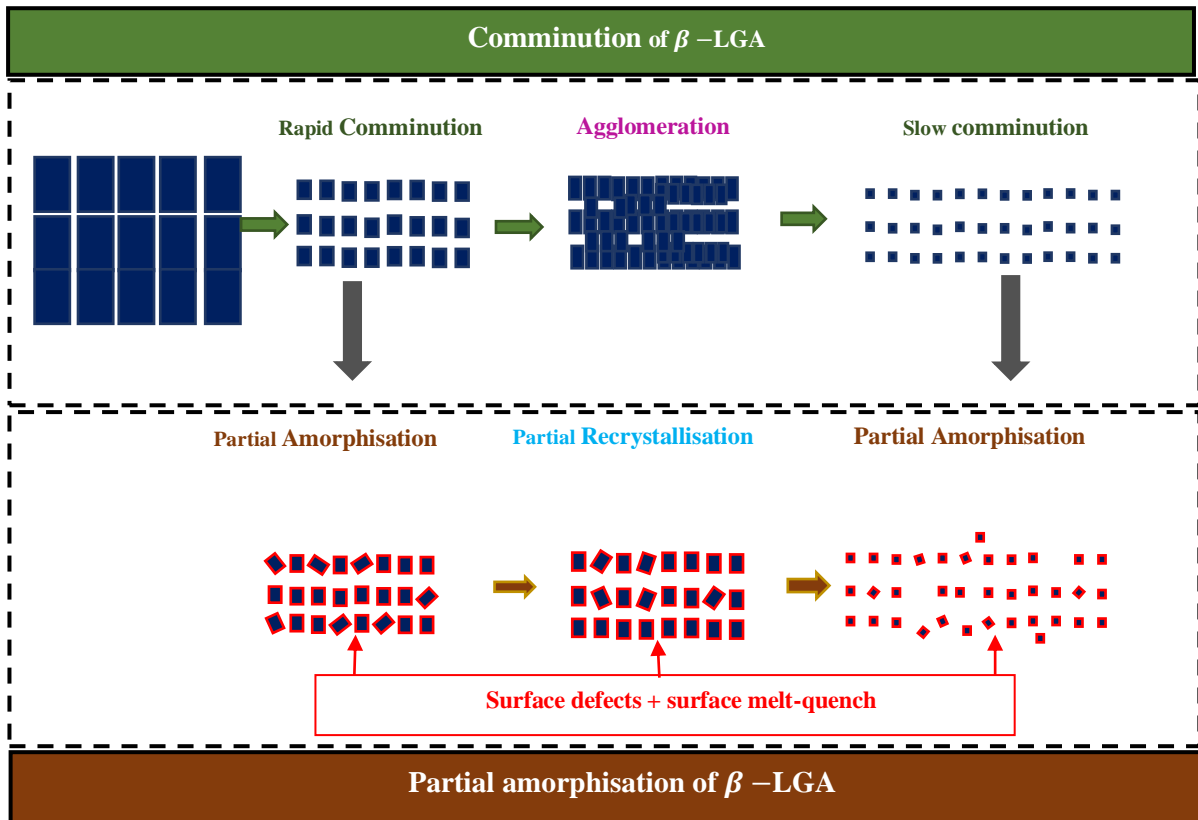


**Figure 7-15: Proposed mechanistic model for the milling process of  $\beta$ -LGA, ordered blue particle represents comminution partially disordered particles represents partial amorphisation**

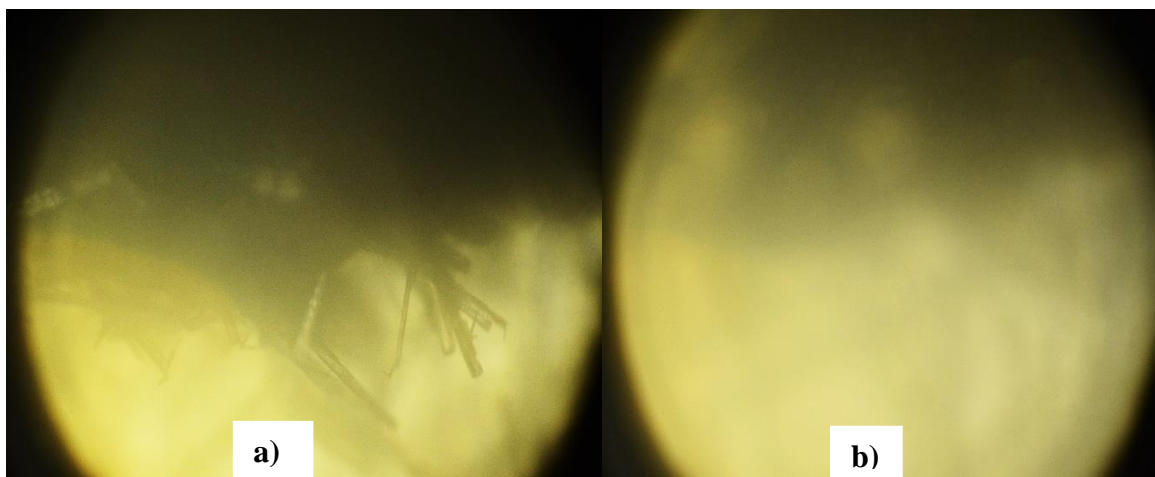


**Figure 7-16: Hot stage microscope image of  $\beta$ -LGA heated from at a rate of 10°C/min. a) at 25°C, b) at 210 °C**

## 7.4 Conclusion

$\beta$ -LGA was milled in planetary ball mill following the same settings employed for DABOMD.  $\beta$ -LGA experiences a significant degree of comminution and a partial amorphisation. The comminution and amorphisation occur successively, with comminution being the dominant process throughout the entire milling time. The initial rate of comminution of  $\beta$ -LGA is higher than that observed in DABOMD, which is followed by repeated agglomeration and deagglomeration events which are attributed to the amorphisation and recrystallisation of  $\beta$ -LGA. The amorphisation process is postulated to be driven by the generation of surface defects which promotes nucleation and growth of amorphous and also by the process surface melt-quench. The recrystallisation process occurs due to the unstable nature of the amorphous formed.

The outcome of milling agrees with the anticipated behaviour of  $\beta$ -LGA from the modelling work. The higher rate of comminution is related to the brittle nature of  $\beta$ -LGA brought by breaking the hydrogen bonding network. The lower/partial amorphisation of  $\beta$ -LGA during milling is related to the absence of a slip system that can promote plastic deformation.

## **Chapter 8 Quantification of the Energy of the Mills**

### **8.1. Introduction**

### **8.2. Calculating the Energy in planetary ball mill**

### **8.3. Calculating the Energy in single ball mill**

### **8.4. Compression test**

### **8.5. Verification of the Energies of using DEM Simulation**

### **8.6. DEM Simulation of the Planetary Ball Mill**

### **8.7. DEM Simulation of the Single Ball Mill**

### **8.8. Summary**

### **8.9. Conclusion**

**This chapter involves quantification of the energy of the milling DABOMD in planetary ball mill and in single ball mill using literature method and DEM simulation. A relationship was established between the energy of milling and the material behaviour.**

## 8.1. Introduction

The experimental work in Chapter 6 indicates that milling of DABOMD with planetary ball mill and single ball mill show a variation in the extent of comminution and amorphisation. It is believed that the level of energy in these two types of mills is different (Chauruka *et al.*, 2015) and this could be the main reason behind the difference observed in the milling behaviour of DABOMD in the two mills. Hence, this chapter focuses on calculating the energy employed in the milling of DABOMD in the planetary ball mill and the single ball mill. The relationship between the milling energy and the produced physicochemical changes lacks in the literature, particularly; the relationship between the mill energy and the mechanochemistry (i.e. amorphisation) which has not been widely investigated. The first part of this chapter provides a literature methodology to calculate the energy of the mills. A compression test was also conducted in this part to evaluate the effect of the impact stress arising in the two mills on the amorphisation of DABOMD.

In an attempt to validate the energy calculated, Discreet Elemental Method (DEM) is employed in the second part of this chapter to quantify the produced energy via simulating the planetary ball mill and the single ball mill. The DEM simulation work outlined in this chapter was carried out by Dr Mohammadreza Alizadeh Behjani, while the author of this chapter provided the interpretation of the analysis.

## 8.2. Calculating the Energy in Planetary Ball Mill

The energy transferred during the process of milling of DABOMD is produced as a result of balls-balls and ball-wall collisions and is calculated following the collision model (Avolio *et al.*, 2012; Bae *et al.*, 2014). The collision theory suggests that the energy generated inside the ball mill is a function of the mill variables and the mill geometry, as shown in Table 8-1 and Table 8-2.

**Table 8-1: Planetary ball mill variables**

Milling Variables	Symbol	Value
Number of balls	$N_b$	4
Powder weight (kg)	PW	0.0125
Angular velocity of the plate = 650 rpm = 68.07 rad s <sup>-1</sup>	$W_p$	68.07
Milling time (s)	t	60-1800

**Table 8-2: Planetary ball mill geometrical parameters**

Geometrical variable	Symbol	Value
Diameter of the ball (m)	$d_b$	0.02
Weight of the ball (kg)	$m_b$	0.04
Diameter of the pot (m)	$D_v$	0.12
Height of the pot (m)	$H_v$	0.106
Distances from the centre of the mill to the centre of the vial (m)	$R_p$	0.12
Distances from centre of the vial and the centre of the vial to its periphery (m)	$R_v$	0.06
Absolute angular velocity of the vial rad s <sup>-1</sup>	$W_v$	136.1

To simplify the calculations, the following assumptions are made;

The balls and the interval wall of the vial are covered with a thin layer of powder, as this allows all the kinetic energy to be transferred to the powder particles from the ball impact.

The energy is only generated from the collisions between balls and the wall

the balls move against the opposite wall without rolling and sliding

To investigate the impact of milling parameters on DABOMD. Two energy parameters should be considered, the total energy transferred to the mill  $P$  and the impact energy which cause deformation to the powder  $\Delta E_b$ .

Firstly, the total energy transferred to the planetary ball mill  $P^*$  normalised to the powder weight ( $PW$ ) as a function of time  $t$  is shown in Equation 8-1 ;

$$P^* = \frac{Pt}{KPW} = -\varphi_b N b m b t (Wp - Wv) \left[ W_v^3 \frac{(Rv - \frac{db}{2})}{Wp} + \right. \text{Equation 8-1}$$

$$\left. Wp Wv R p \right] \frac{(Rv - \frac{db}{2})}{2\pi PW}$$

Where  $P$  is the total energy transferred to the system,  $\varphi_b$ ,  $\varepsilon$  and  $\eta_v$  correspond to the geometrical parameters related to the number of the balls, and the vial's dimensions.

$$\varphi_b = (1 - \eta_v^\varepsilon) \text{Equation 8-2}$$

Where,  $\varphi_b$  can be derived using Equation 8-2, and  $\varepsilon$  can be calculated using Equation 8-3 with  $N_{b,v}$  and  $N_{b,s}$  and expressed according to Equation 8-4 and Equation 8-5 respectively.  $\varphi_b = (1 - \eta_v^\varepsilon)$  are geometrical parameters associated with the number of balls in the vial which depict the degree of filling of the vial.

$$\varepsilon = \log(0.05) / \log \left( \frac{N_{b,v}}{N_{b,s}} \right) \text{Equation 8-3}$$

Where,  $N_{b,v}$  represents the number of balls that can arrange in a simple cubic manner to fill the vial as shown in Equation 8-4 (MASROOR, SHEIBANI and ATAIE, 2016).

$$N_{b,v} = \pi D_v^2 H v / 4 d_b^3 \text{Equation 8-4}$$

Where,  $N_{b,s}$  represents the number of balls that can arrange in a simple cubic manner to cover one-third of the inner surface of the wall which is calculated according to Equation 8-5 (MASROOR, SHEIBANI and ATAIE, 2016).

$$N_{b,s} = \pi (Dv - d_b) H v / 3 d_b^2 \text{Equation 8-5}$$

Secondly, the impact energy,  $\Delta E_b$ , responsible for the deformation of the powder entrapped between the ball and the wall which is also responsible for the temperature rise within the mill can be derived from the expression following Equation 8-6

$$P = \varphi_b \Delta E_b N_b f_b \quad \text{Equation 8-6}$$

Where,  $f_b$  is the frequency of collisions which can be derived using Equation 8-7.

$$f_b = K \times \frac{w_p - w_v}{2} \times \pi \quad \text{Equation 8-7}$$

$K$  is a constant representing the time required to dissipate the energy which is equal to 1 (MASROOR, SHEIBANI and ATAIE, 2016).

$\Delta E_b$  is the difference between the kinetic energy  $E_b$  and the residual energy within the balls after the hit  $E_s$ .  $E_b$  and  $E_s$  are expressed in Equation 8-8 and Equation 8-9.

$$\Delta E_b = E_b - E_s \quad \text{Equation 8-8}$$

$$E_b = \frac{1}{2} m_b v_b^2 \quad \text{Equation 8-9}$$

Where,  $v_b$  is the absolute velocity of the ball.

$$E_s = \frac{1}{2} m_b v_s^2 \quad \text{Equation 8-10}$$

Where,  $v_s$  is the velocity of the ball after succession collision.

The total power transferred to the mill during milling at different times is shown in Table 8-3, and Figure 8-1, the energy transferred to mill DABOMD in 2 min is equal to 4.22 kJ/g which is in the range of the power needed to mill cellulose for 2 min (6.29 kJ/g) in (Avolio *et al.*, 2012). Also, the energy transferred to the system is equal to 20.2 J/g.s. The value of impact energy is analogous to that reported in (Bai *et al.*, 2014) for the given parameters.

**Table 8-3: Values of calculated energies in planetary ball mill**

<b>The energy input to the PBM P (J/s)</b>	253.2
<b>The energy input to the PBM P* (J/g.s)</b>	20.2
<b>Impact energy in the PBM (J/g.s)</b>	0.19

From Figure 8-1, it can be seen that approximately 93% of amorphous was formed at an energy input of 48.6 kJ/g which is about 20% of the total energy input to the system and, 97% of amorphous was generated at 60% of the total energy input to the system. This implies that large energy is required to distort the remaining crystalline lattice. It also provides guidance on the most cost-effective route that can be followed to generate amorphous.

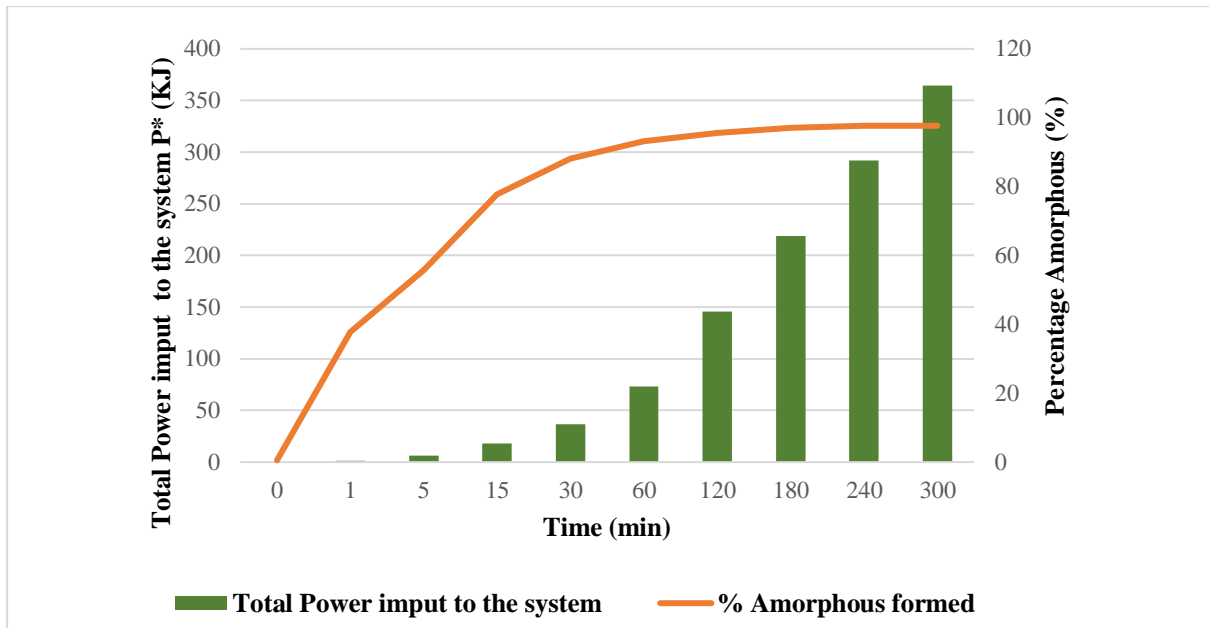


**Figure 8-1: Total energy transferred to the system in a planetary ball mill and the amount of generated amorphous**

### 8.3. Calculating the Energy Transferred to the Single Ball Mill

High-speed Camera (Imacon 790, Hadlands Photonics) was used to identify the velocity and aptitude of the milling jars in a single ball mill. The high-speed camera allows recording the moving part (milling jar) on a computer at a faster rate (250 frames per second). The experimental setup is shown in Figure 8-2.

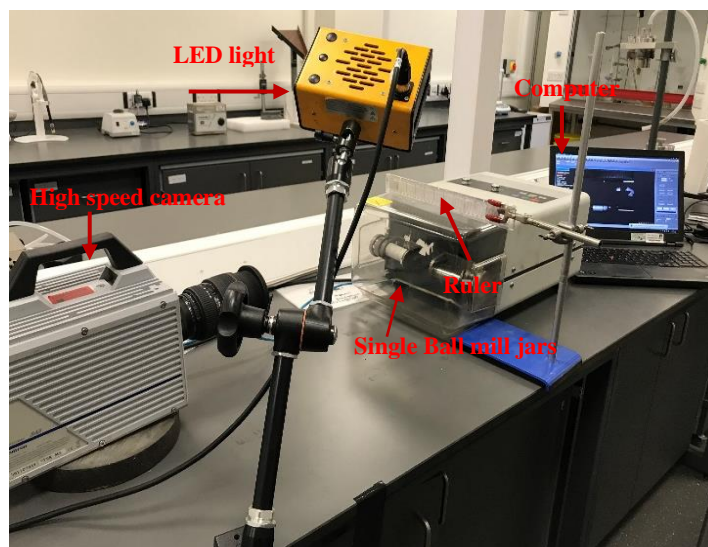


**Figure 8-2: Experimental setup for measuring the speed of the milling jar in the single ball mill using high-speed Camera**

The images from the high-speed camera were processed using TrackMate plugged in ImageJ software. The generated trajectory of the moving jar with respect to time is displayed in Figure 8-3. The mill variables are illustrated in Table 8-4.

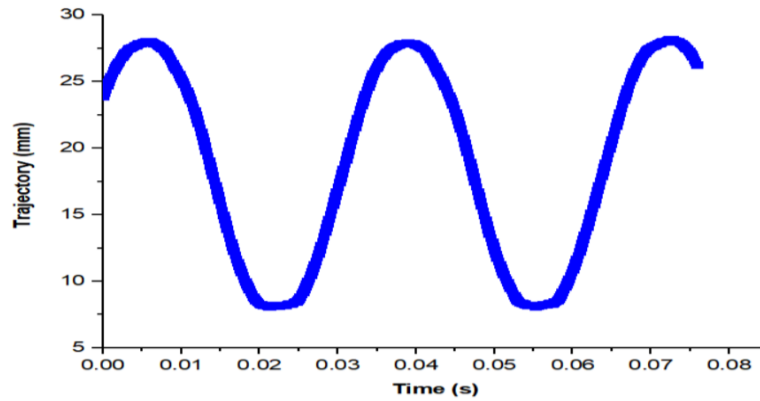


**Figure 8-3: Trajectory of the vibratory mill jar**

**Table 8-4: Single ball mill variables**

Milling Variables	Symbol	Value
Diameter of the ball (m)	$d_b$	0.01
Weight of the ball (kg)	$m_b$	0.004
Powder weight (g)	$PW$	1.3
Coefficient of restitution	$CoR$	0.16

The impact energy  $\Delta E_b$ , the kinetic energy  $E_b$ , and the residual energy in the balls after the hit  $E_s$  in the single ball mill is calculated using Equation 8-8, Equation 8-9, Equation 8-10. The absolute velocity  $v_b$  can be derived from tracking the ball as shown in Figure 8-2 and Figure 8-3. The residual velocity  $v_s$  is calculated following Equation 8-11 (Behjani, 2018). This implies that  $CoR$  can be derived from  $E_s$  and  $E_b$ .

$$\frac{v_s}{v_b} = CoR \quad \text{Equation 8-11}$$

Where  $CoR$  is the ratio of the residual velocity relative to the absolute velocity which can be measured using a high-speed camera and image analytical technique ( see later in section 8.5.1.1). To account for the powder weight,  $\Delta E_b$  is divided by the powder weight. Hence, the deduced impact energy is equal to 0.046 J/g.s. The energy produced seems realistic due to the lower mechanical energy produced from a single ball with smaller diameter vibrating in the axial direction as opposed to four larger balls moving in the radial direction with additional centrifugal forces in the planetary ball mill.

**Table 8-5: Energies from single ball mill compared to planetary ball mill**

Impact energy SBM $\Delta E_b$ J/g.s	0.046
Impact energy PBM $\Delta E_b$ J/g.s	0.19

#### 8.4. Compression Test

In order to investigate the type of stress that leads to the amorphisation of DABOMD, compression test was conducted at 250 KN using Instron compression test 5566, where approximately 0.4 g placed in a 10 mm die was compressed up to 10 KN as shown in Figure 8-4.

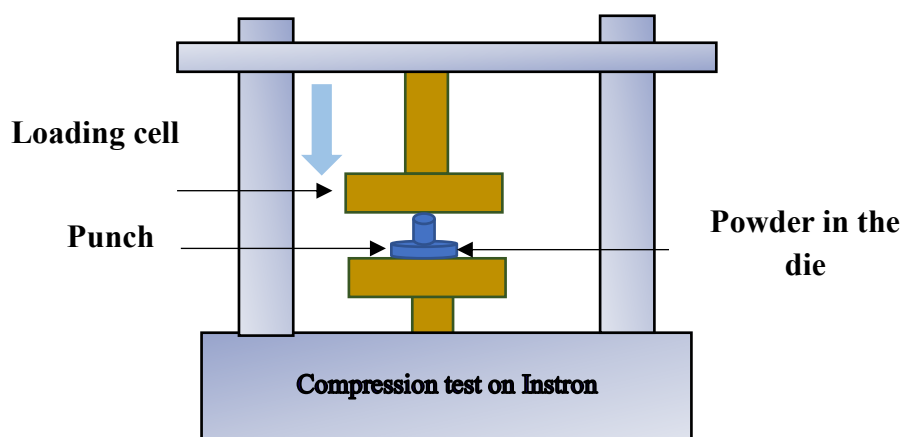


**Figure 8-4: Schematic shows the compression of DABOMD**

The load versus displacement curve produced from the compression test is illustrated in Figure 8-5. The generated energy from the compression test can be calculated using the trapezoid rule of the area under the curve. The calculated energy is equal to 2.21 J, which is equivalent to 5.52 J/g (Table 8-6).

**Table 8-6: Calculated energy from compression test compared to a single ball mill and planetary ball mill**

Compression energy (J/g)	5.52
Impact energy $\Delta E_b$ in PBM (J/g.s)	0.19
Impact energy in SBM $\Delta E_b$ (J/g.s)	0.046

The derived energy of compression is analogous to milling for approximately 0.5 min in planetary ball mill and is equivalent to 2min milling of DABOMD in a single ball.

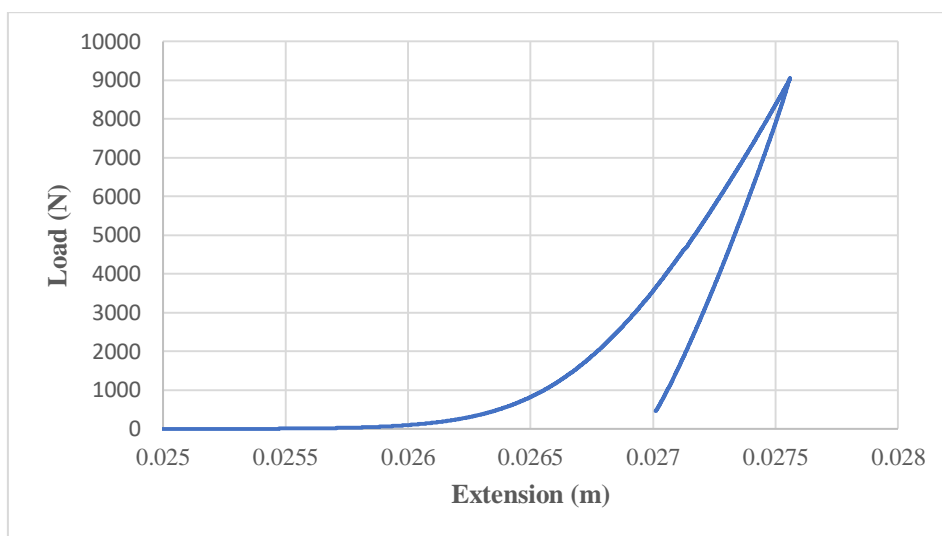


**Figure 8-5: Load versus extension graph for compression test**

The XRPD analysis shows that the compression of DABOMD leads to a reduction in its crystallinity which is indicated by its lower peaks intensity as compared to the non-milled sample (Figure 8-6). Interestingly, the XRPD profile of the compressed DABOMD appears intermediating between the samples milled for 1 min using a planetary ball mill and those milled for 1 min of sample milled in the single ball mill which agrees with our calculations.

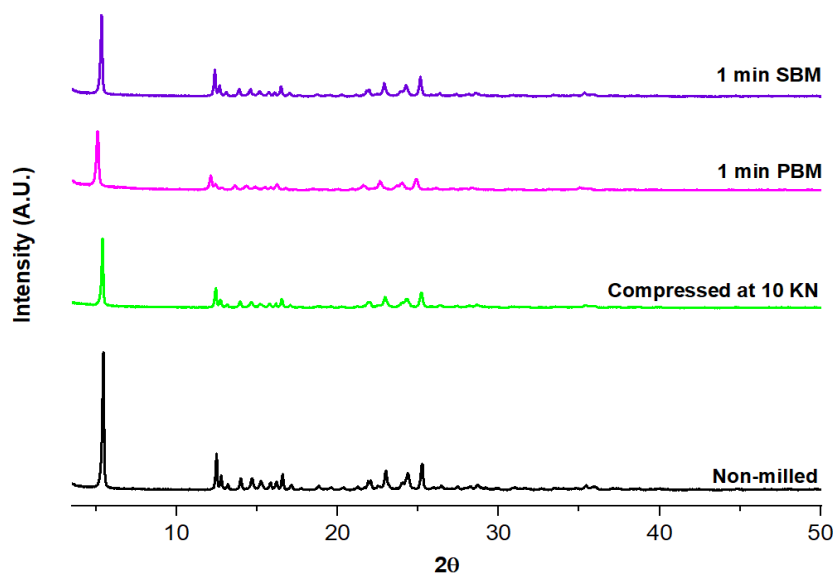


**Figure 8-6: XRPD profile of DABOMD after compression**

## 8.5. Verification of Energy Using DEM Simulation

DEM is a powerful tool employed to model the particle interaction; hence it is employed as a validation method for the energy calculations (EDEM, 2020). In principles, particles are tracked based on their conditions, including positions, velocity and external forces. In the present study, EDEM 2.7.1 software, provided by DEM Solutions, Edinburgh, UK, is used. The model employed for the calculations is Hertz-Mindlin no-slip (Behjani, 2018).

The general governing equations in DEM consider the translational and the rotational motion of particles as expressed in Figure 8-7 according to Equation 8.12 and Equation 8.13.

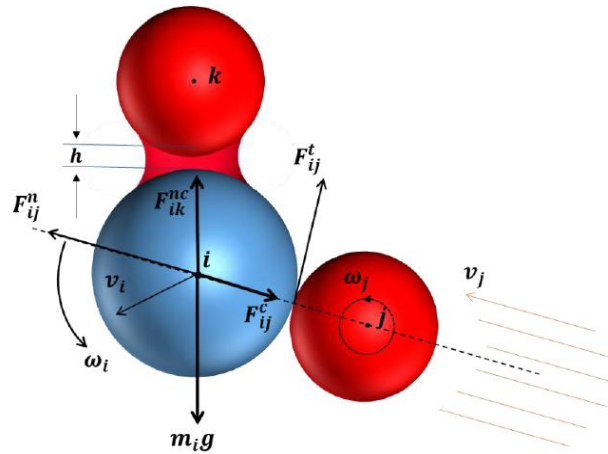


**Figure 8-7: Schematic shows forces applied to three arbitrarily interacting particles (reprinted from (Behjani, 2018))**

$$m_i \frac{dV_i}{dt} = \sum_j F_{ij}^c + \sum_k F_{ik}^{nc} + F_i^f + F_i^g \quad \text{Equation 8.12}$$

Equation 8.12 represents the translational motion of particle  $i$  in three dimensions, where,  $m_i$  and,  $V_i$  represent the particle mass and the particle velocity, respectively.  $F_{ij}^c$  is the contact force exerted on particle  $i$  from particle  $j$  or other bodies.  $F_{ij}^{nc}$  symbolises the non-direct forces such as Van Der Walls and electrostatic imposed on particles  $i$  and  $j$  by particle  $k$  or other forces. Other forces include  $F_{ij}^f$  and  $F_i^g$  which represent the particle fluid interaction force and the gravity force, respectively.

$$I_i \frac{dw_i}{dt} = \sum_j M_{ij} \quad \text{Equation 8.13}$$

Equation 8.13 displays the rotational motion of the particle  $i$  with  $I_i$  and  $w_i$  representing the motion of inertia and the angular velocity, respectively. These equations are solved according to a suitable contact model and at small time steps (Behjani, 2018).

### 8.5.1. Simulation Parameters

In addition to the mill's variables (i.e. speed, number and size of balls) and geometrical parameters, other parameters used in the simulation include the cohesion number, coefficient of restitution and the sliding friction as follows;

#### 8.5.1.1. Coefficient of Restitution

The coefficient of restitution (CoR) is employed in the DEM simulation to account for the presence of the powder within the mills. CoR depicts the ratio of the rebound velocity to the impact velocity. CoR depends on various factors, including the speed of the collision, material type. In this work, CoR was measured using a high-speed camera and image analytical technique. In this process, a random particle is chosen and released from a height proportional to  $h$  displayed in Figure 8-7. In this work the ball was released from a height (approx.20 cm) and impacted with a surface covered with a layer of DABOMD's powder, the obtained value CoR is 0.16. The coefficient of restitution for the ball-ball impact can also be measured. However, it is believed that balls will always be covered in a layer of powder; hence ball-powder CoR is implemented in the calculation. The coefficient of restitution is assumed to have an equal value for the two mills since the balls are made out of the same material (steel), same density, and have the same geometry.

#### 8.5.1.2. Sliding friction

The effect of the surface conditions is manifested in the surface properties, namely sliding friction and surface adhesion/cohesion. Sliding friction can be obtained by sliding two layers of particles as shown in Figure 8-8. Simply two flat surfaces are covered by a monolayer of particles that are tilted together until the upper surface slides (Behjani, 2018). This experiment is conducted for particle-particle and particle wall friction. The angle corresponds to the event of sliding is measured from the record taken by a high-speed camera. The obtained sliding friction is equal to 1.45 and 0.73 for powder-powder and powder-steel, respectively. The steel-steel is not applicable since balls are assumed to be covered with powder.

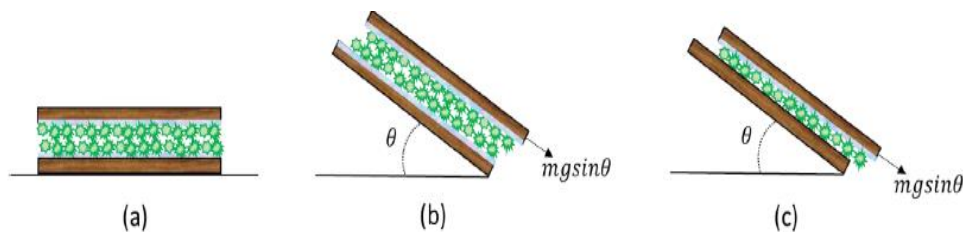


**Figure 8-8: Schematic diagram representing the coefficient of sliding friction, with (a) is the surface at rest, (b) particle-particle sliding friction and (c) particle-wall sliding friction (reprinted from (Behjani, 2018))**

### 8.5.1.3. Rolling friction

The rolling friction is used for DEM simulation to account for the effect of the shape of particles. The default value of a complete sphere is 0; however, it is a common practice to use a value of 0.01 to account for some irregularity in shape (Behjani, 2018).

## 8.6. DEM Simulation of the Planetary Ball Mill

In a planetary ball mill kinetic energy  $K.E.$  is calculated from the related velocity  $v$  of the ball-ball and ball-wall after collisions according to Equation 8.14. Where  $m$  represents the mass of the ball,  $n$  is the number of ball and ball-wall collisions occurring in one second. The simulation parameters employed from the experimental setup of the planetary ball mill are shown in Table 8-1 and Table 8-2 and Table 8-7.

$$K.E. = \sum_{j=1}^n = \frac{1}{2}mv_s^2 \quad \text{Equation 8.14}$$

The kinetic energy simulated using DEM is equivalent to the impact energy  $\Delta E_b$  derived from the literature. To account for the powder weight, the impact energy is divided by the powder weight PW.

DEM simulation of the planetary ball mill is shown in Figure 8-9. The kinetic energy after the impact is shown in Figure 8-10. It can be seen that the energy rises initially then drops after one second of simulation, this represents the increase in the kinetics of the ball as they are pushed hard at the start of milling then they stabilise shortly. The calculated impact energy normalised to the powder weight is shown in Table 8-8. The impact energy obtained from DEM simulation is equal to 0.22 J/g.s which is analogous to that calculated using the collision model from the literature which is equal to 0.19 J/g.s which further provides confidence in the calculation.

**Table 8-7: DEM simulation parameters for PBM**

<b>Planetary ball mill</b>	PM100
<b>Pot material</b>	Steel
<b>Pot material density <math>\rho</math> (gcm<sup>-3</sup>)</b>	7.8
<b>Shear modulus (GPa)</b>	210
<b>Poisson's Ratio</b>	0.25
<b>Coefficient of restitution of the powder-steel</b>	0.16
<b>Powder-powder sliding friction coefficient</b>	1.53
<b>Powder-Steel sliding friction</b>	0.73
<b>Rolling friction</b>	0.01
<b>Simulation time t (sec)</b>	6

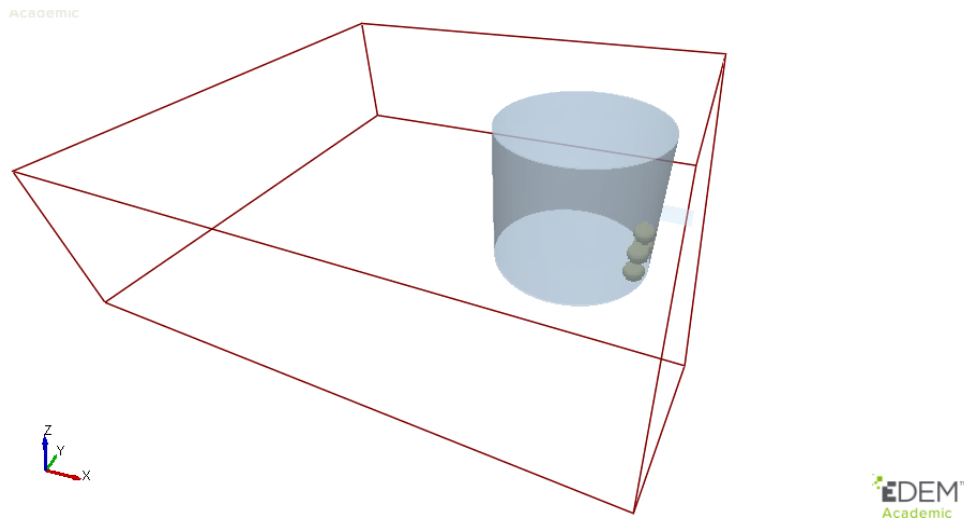


**Figure 8-9: DEM simulation of planetary ball mill**

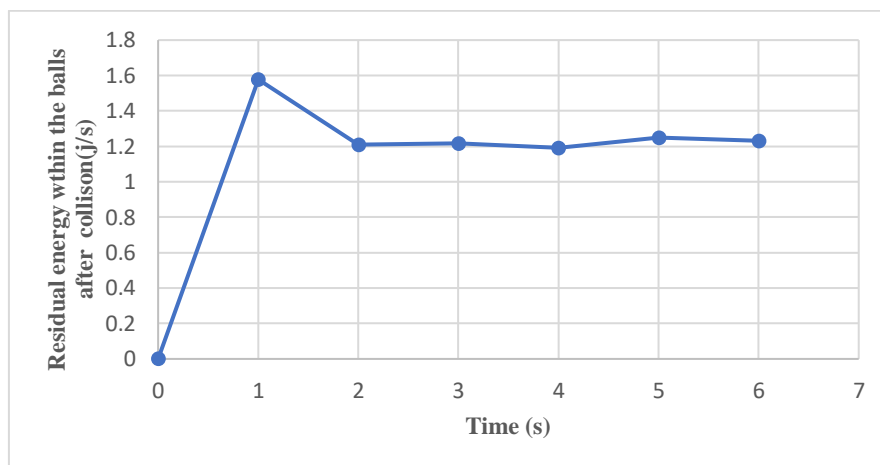


**Figure 8-10: Kinetic energy after the Collision of the balls in planetary ball mill**

**Table 8-8: Impact energy of the planetary ball mill simulated using DEM and literature**

<b>Impact Energy in PBM simulated using DEM (J/g.s)</b>	<b>0.22</b>
<b>Impact energy calculated from the collision model in the literature PBM (J/g.s)</b>	<b>0.19</b>

## 8.7. DEM Single ball mill

The single ball mill was simulated following the same setup used in the planetary ball mill while applying the parameters in Table 8-4 and Table 8-9. Since powder was simulated in the single ball mill, a scale-up particle diameter is required as the original power diameter would take huge computational time which was determined following (Behjani *et al.*, 2017) as seen in Equation 8.15.

$$\frac{\Gamma_1^5}{E_1^2 D_1^3} = \frac{\Gamma_2^5}{E_2^2 D_2^3} \quad \text{Equation 8.15}$$

Where,  $\Gamma_1$  and  $\Gamma_2$  are the interfacial energy of DABOMD which equivalent to the surface energy) can be obtained from Mercury (version 3.9) (CCDC, Cambridge, UK) which assumed to have a similar value of  $0.1 \text{ J/m}^2$ .  $E_1$  is the Young's modulus of the DABOMD taken from the previously calculated average Young's modulus.  $E_2$  is the scale-up modulus which is equal to  $2.5 \times 10^8$ , this is a lower Young's modulus value taken practically to reduce the computational time (Behjani, 2018).  $D_1$  is the original particle diameter which is equivalent to the  $D_{50}$  of non-milled DABOMD and  $D_2$  is the scale-up diameter respectively.

The impact energy was calculated following Equation 8.14. DEM simulation of the single ball mill at different times is shown in Figure 8-11. It takes about 0.3 s for the system to reach steady-state with a single ball mill as shown in Figure 8-12, unlike planetary ball mill which takes 2 s to reach steady state (Figure 8-10).

The calculated impact energy of DABOMD using DEM simulation of the single ball mill is equal to  $0.024 \text{ j/g.s}$  (Table 8-10) which underestimates the calculated energy from the trajectory of the milling jar recorded by the high-speed camera which was equal to  $0.046 \text{ j/g.s}$ . The difference between the calculated and the simulated energies of the single ball mill can be attributed to the fact that the high-speed camera tracks the movement of the milling jar contrary to the DEM which simulates the movement of the ball and the powder. The ball and powder might lag behind, which implies that it has a lower velocity compared to that recorded for the jar, which would ultimately account for less energy.

**Table 8-9: DEM simulation parameters for SBM**

<b>Single ball mill</b>	MM200
<b>Pot Material</b>	Steel
<b>Shear Modulus (GPa)</b>	210
<b>Poisson's Ratio</b>	0.25
<b>Density (gcm-3)</b>	7.8
<b>Particle original diameter (um)</b>	21.2
<b>Scale-up particle diameter (um)</b>	232.3
<b>Young modulus of large particles of powder (Pa)</b>	$2.5 \times 10^8$
<b>Shear modulus of powder (Pa)</b>	$10^8$
<b>Density of the particle (Kg/m<sup>3</sup>)</b>	1500
<b>Coefficient of restitution of the powder-steel</b>	0.16
<b>Powder-powder sliding friction coefficient</b>	1.53
<b>Powder-Steel sliding friction</b>	0.73
<b>Rolling friction</b>	0.01

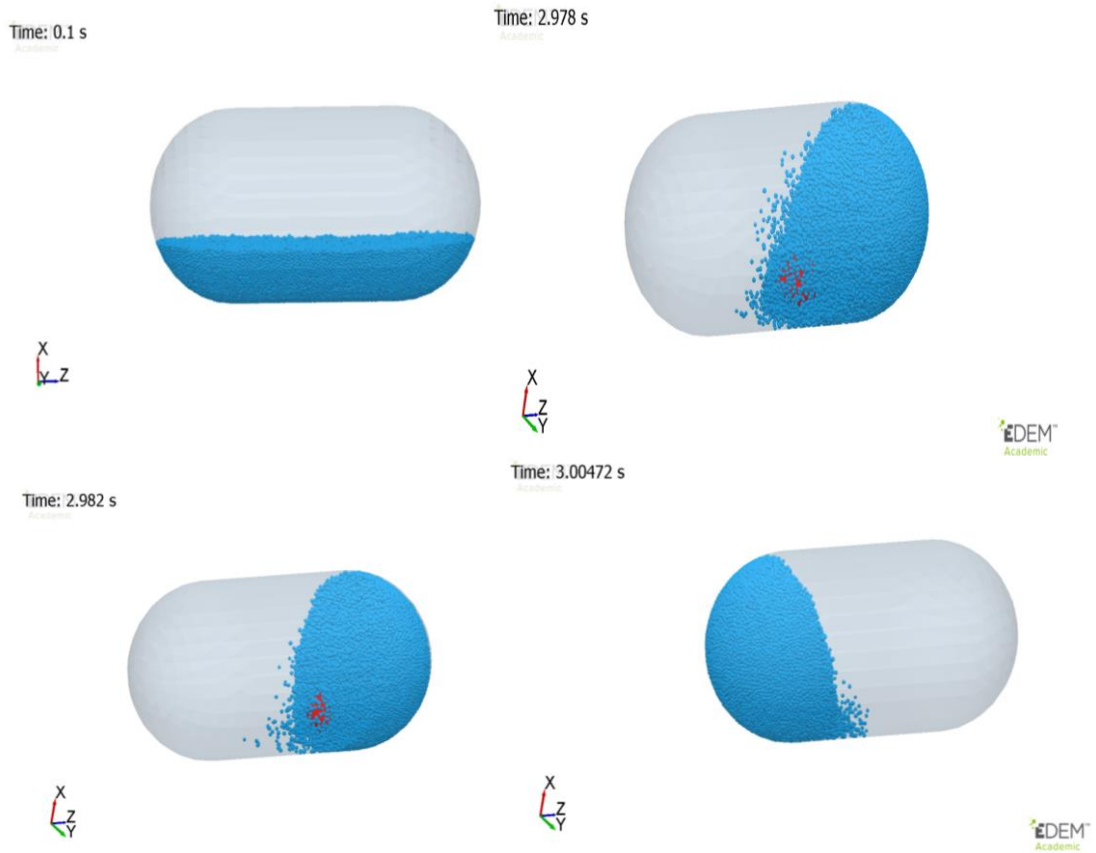


**Figure 8-11: DEM simulation of single ball mill**

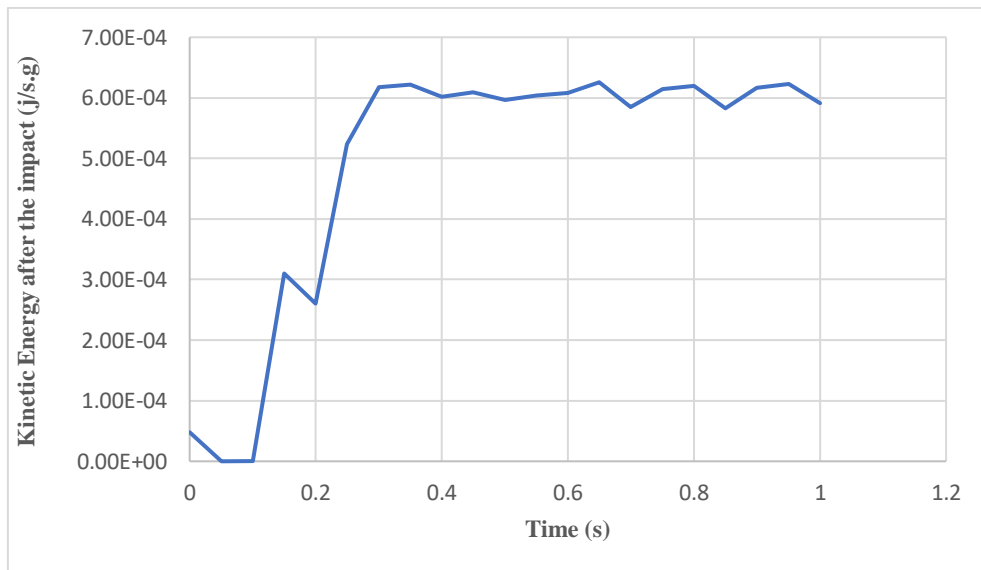


**Figure 8-12: Kinetic energy after the collision in single ball mill**

**Table 8-10: Impact energy of the single ball mill simulated using DEM and literature**

<b>Impact Energy in SBM simulated using DEM (J/g.s)</b>	0.024
<b>Impact energy calculated from high-speed camera SBM (J/g.s)</b>	0.046

## 8.8. Summary

The aim of this thesis was to understand the material behaviour during milling via establishing a relationship between the milling energy generated from certain milling conditions, the material properties of the feed, and the produced changes in the milled product. In this case, a relationship can be established between the comminution and amorphisation of DABOMD, and the energy associated with these two processes during milling. It became prevalent in Chapter 6 that DABOMD experienced significant comminution and amorphisation as a result of its sensitive nature to fracture and plastic deformation when milled in planetary ball mill and a single ball. The hypothesis was that the two mills generate different level of energies; with the planetary ball anticipated to produce more substantial energy due to the multiple wall/media impacts and collisions compared to the single ball mill, which was supported by the experimental outcome as seen in Chapter 6. This chapter allows a straightforward quantitative comparison of the processes of comminution, amorphisation and the amount of energy generated with different mills as shown in Table 8-11 which can help to address the questions what, when, and how much change occurs with milling. It is evident that the planetary ball mill produces a larger amount of energy compared to single ball mill with prolonged milling (5 to 9 times higher than SBM ) and thus promoting fracture, dehydration, dislocation, and, accumulation of defects. It is also evident that a lower amount of energy is sufficient to induce a remarkable change in DABOMD, which is mainly associated with its material properties. For instance, DABOMD experienced 20% size reduction and lost 30% of its crystallinity with energy as low as (1.5 to 2.8 J/g in SBM). Similarly, DABOMD underwent about 70% size reduction and approx. 50% amorphisation with energy starting from (21 to 41 J/g in SBM). This is attributed to the crystal structure of DABOMD, particularly, the presence of slip planes which tend to shear and deform under the presence of impact as was confirmed by the compression test. Higher energy supply to the crystals from planetary ball mill leads to a rapid phase transformation due to increased slip and shearing of planes caused by the prevailing stress, for instance, seen in planetary ball mill at 15 min with (AAC = 78 % at an energy = 171 J/g in PBM), and with (AAC= 62.4% at an energy = 21.6 - 41.4 in SBM ). The importance of the role the presence slip plane is further stressed when a more considerable amount of energy was required to cause a minimum crystalline disorder. For example, when milling from 60 min to 120 min double amount of energy was required to distort 2% of the crystal of the crystalline lattice ( i.e. AAC = 93% at energy = 684 J/g, and AAC = 95% at energy = 1368 in PBM). This comparison also provides a route for green mechanochemistry; if for instance, one wants to form an amorphous sample, a quick observation of the amount of energy required to distort the

remaining crystalline structure can help save energy, cost and optimise the process of milling. The outcome of DEM can be validated in the future by conducting repeated simulations. Also key energies such as impact and shear energies requires calculating from future simulation as this will provide an indication on the energies released from shear and impact stresses inside the mills.

**Table 8-11: The amount of energies used to generate different size, and amount of amorphous in planetary ball mill and single ball mill**

DABOMD		PBM Energy			SBM Energy			
Time (min)	D90 ( $\mu\text{m}$ )	AAC (%)	Collison Model calculation (J/g)	DEM simulation (J/g)	D90 ( $\mu\text{m}$ )	AAC (%)	High-speed camera tracking (J/g)	DEM Simulation (J/g)
0	211	0	0	0	211	0	0	0
1	186	37.8	11.4	13.2	171	29.1	2.76	1.44
5	98.1	55.7	57	66	76.8	53	13.8	7.2
15	66.9	77.8	171	198	51.1	62.4	41.4	21.6
30	58.9	88.1	342	396	52	76.7	82.8	43.2
60	51.8	93.1	684	792	58.9	85.2	165.6	86.4
120	45.6	95.6	1368	1584	45.6	93	331.2	172.8
180	40.1	97	2052	2376	45.7	93.1	496.8	259.2
240	–	97.7	2736	3168	0	95.3	662.4	345.6
300	35.3	98.2	3420	3960	48.2	96	828	432

## 8.9. Conclusion

The energies of the planetary ball mill and the single ball mill were quantified and validated following two steps. In the first part, the collision model was employed for the energy quantification in the planetary ball mill, whereas, a high-speed camera was employed to track the trajectory of the milling jar in the single ball mill. The quantified energy in the planetary ball mill is higher than that generated in the single ball mill which agrees with the experimental work in Chapter 6; where smaller particles and a larger amount of amorphous were obtained during milling in the planetary ball mill as opposed to single all mill.

A compression test was conducted on DABOMD powder to investigate its susceptibility to amorphisation under impact stress. It was found that DABOMD experienced some degree of crystalline disorder with compression, which suggests that the slip of the plane (100) is sensitive to the impact of stress.

In an attempt for a rough validation of the energy calculation, DEM simulation was used to calculate the energy of milling DABOMD in the planetary ball mill and the single ball mill. The energy obtained from DEM for the planetary ball mill is analogous to that calculated following the collision model. However, the energy calculated from the DEM simulation of the single ball mill is approximately half of that calculated from tracking the milling jar using the high-speed camera which is anticipated to be related to the fact that; DEM is simulating the movement of the ball and the powder which can lag in the milling jar as opposed to the high-speed camera which tracks the trajectory of the jar.

Overall, the energy quantification from; the collision model for the planetary ball mill, high-speed-camera for single ball mill, and from DEM simulation provide satisfactory results which agree with the experimental outcome.

Finally, a table summary was constructed to enable a quantitative determination of the amount of energy, the produced size and the amount of amorphous of DABOMD generate at different milling times in the planetary ball mill and single ball mill.

## Chapter 9 Conclusion and Future Recommendation

### 9.1. Conclusion

The impact of milling on the behaviour of solid pharmaceuticals DABOMD and  $\beta$ -LGA has been thoroughly investigated in this thesis. The aim was to predict how a pharmaceutical API would behave when it is exposed to different stresses, with particular attention to the degree of comminution and the potential amorphisation of the milled product. The second goal was to link between the generated energy and the degree of comminution and amorphisation while evaluating the mechanism of amorphisation in each case. The mode of failure and any potential amorphisation of the milled product was successfully predicted using computational chemistry and was empirically validated using a planetary ball mill and single ball mill. Also, the mechanism of amorphisation was proposed for each pharmaceutical. Moreover, the relationship between the energy of the mill and the degree of comminution and amorphisation was determined.

The predicted material properties include the crystal morphology, mechanical properties, and any potential existence of slip planes which can promote plastic deformation and amorphisation. These properties were predicted from the crystal structure, crystal and molecular arrangement, and interactions at the molecular level.

For DABOMD, the crystal structure was solved for the first time since it was synthesised 30 years ago. The outcome of the molecular modelling shows that DABOMD encompasses four water molecules with two different interacting forces. The predicted crystal habit shows that DABOMD possesses a hexagonal habit with (100) being the major face which agrees with the experimentally grown crystals which anticipate its susceptibility to disorder on its major face. Moreover, the calculation of the mechanical properties indicates that DABOMD is semi-brittle material with a propensity to fracture on the Z direction and higher propensity to plastic flow in the x and y directions. The third predicted property is the slip system which reveals that DABOMD contains a flat slip plane that is easy to deform which suggests that the deformation of this plane will promote the comminution and induce plastic deformation and amorphisation. The predicted work at the molecular level was verified experimentally, where, DABOMD was milled at different times with planetary ball mill and single ball mill. It was found that the two mills induce significant comminution and amorphisation of DABOMD, which agrees with the predicted outcome. It was also found that slightly higher comminution and amorphisation were generated in the planetary ball mill as compared to the single ball mill. The kinetic study of the milling of DABOMD revealed that the process of comminution and amorphisation occur parallel to each other in two phases following an exponential pattern; a rapid phase and a slower phase. The rapid comminution was driven by the breakage of (100) face and also the slip of its planes. The investigation of the amorphisation mechanism indicates that water loss was a major

factor for the amorphisation, which leaves the crystals by the process of mass transfer promoted by the availability of fresh surfaces. This was explained based on the crystal structure of DABOMD since two water molecules are present on the slip plane. The mechanism of milling of DABOMD unfolds rapid events starting by the slip of planes mainly (100) allocated on the major face which initiate and promote the breakage of hydrogen bonds, loss of water molecules and results in remarkable comminution and amorphisation in short milling time. The temperature from the impact and shear is a factor that can induce the process of amorphisation by promoting the dehydration process.

On the other hand, the prediction work undertaken on the molecular structure of  $\beta$ -LGA suggests that it is likely to experience a significant fracture due to and the presence of extensive charge assisted hydrogen interactions accountable for the higher value of its Young's modulus and hardness and for the absence of slip plane within its crystal structure. The absence of a slip plane suggests that amorphisation by plastic deformation is not possible for  $\beta$ -LGA. Hence, the experimental validation was based mainly on the application of planetary ball mill to allow for the maximum detection of the amorphisation process. The outcome of the experimental work shows that  $\beta$ -LGA undergoes a higher degree of comminution compared to DABOMD, which agrees with the predicted results. Also,  $\beta$ -LGA shows limited amorphisation, which occurs at lower kinetics compared to DABOMD due to the absence of slip planes. The mechanism of amorphisation of  $\beta$ -LGA was postulated to be associated with the nucleation and growth of amorphous on the defects generated on the surface, and with possible surface melt. It was also evident that processes of partial amorphisation and recrystallization repeatedly occurred during the milling of  $\beta$ -LGA which is postulated to occur due to the lower stability of the amorphous formed owed to the lower glass transition and molecular weight of  $\beta$ -LGA as opposed to DABOMD.

To establish a quantitative comparison between the change produced and energy usage. The energies generated during milling DABOMD were calculated following a collision model from the literature for the planetary ball mill and high-speed camera tracking in the single ball mill and was validated using DEM simulation. It was found that the planetary ball mill provides a significantly larger amount of energy in corresponds to the single ball mill which explains the variation in the level and the kinetics of comminution and amorphisation produced in the two mills. The calculations from the literature and the DEM simulation were analogous to each other in the planetary ball mill. However, the value of the energy produced with DEM simulation is lower compared to that calculated for the single ball mill, since DEM tracks the motion of the ball and the powder as opposed to the high-speed camera which tracks the movement of the jar in the single ball mill. A compression test was also conducted on DABOMD to investigate its susceptibility to amorphisation under impact stress. It was found that the amorphisation of DABOMD is possible to occur with the impact stress and not only limited to the shear stress.

Finally, a relationship was established between the amount of energy, the level of comminution and amorphisation of DABOMD when milled at different times in the planetary ball mill and single ball mill.

This thesis provides an efficient methodology that allows the anticipation and the verification of the milling behaviour of different pharmaceuticals. This approach is not only limiting to the process of milling, but it can also be implemented to understand the behaviour of the materials in other processes, including crystallisation, granulation, and tableting. The implementation of this approach in the pharmaceutical industry will optimise the control process, reduces the amount of time and costs associated with the trial and error empirical work required for each API and enables the formulation of a drug product with desired characteristics and performances. Moreover, the implementation of this methodology will prevent the loss and market withdrawal of various batches of medicines due to many unanticipated changes encountered by drugs. It is also considered as a safer route when dealing with the hazardous or limited amount of drugs. This thesis also provides a thorough study of the amorphisation in ball mills which will help the development of the field of mechanochemistry.

## **9.2. Future Work Recommendations**

During the modelling and experimental work of this project, multiple aspects have arisen that require addressing, which was challenging due to time constraints, limited resources, and sometimes misalignment with the project objectives. Covering all the aspects will provide a holistic understanding of the impact of milling on solid materials with different properties. A list of recommendations is provided for future work to cover some of these aspects as follows;

The determination of the mechanical properties and potential slip planes from experiments such as single crystal nanoindentation can further contribute to a more in-depth analysis of the material properties such as the mechanical properties and slip planes. However, this can be challenging due to the difficulty to grow a single crystal of the required size for nanoindentation (100  $\mu\text{m}$ ).

The investigation of the impact of milling on solid pharmaceuticals can be expanded to include other conditions/parameters, such as a different number of balls, ball diameters, and material of the milling vessels to allow for a comparison of different energies. The study of different type of stress, i.e. collisional stress, can also be carried out using a fluid jet mill. Another aspect that can be covered is the impact of cyclic compression tests as this embodies the repeated impacts of the balls inside the mills. Another interesting milling condition that requires looking at is wet milling experiment to provide an insight into how the presence of a solvent impact on the mechanochemistry.

The study of different types of mechanochemistry that can arise with milling, for example, the formation of new polymorph can contribute to an understanding of other microstructure impacts associated with mechanical treatment.

The investigation of mechanochemistry can be applied to a single crystal that is subjected to scratch or indentation in in-situ experiments which can be carried out in synchrotron radiation facilities. Work of this nature requires a significant amount of planning, commuting, and collaboration with the beam scientists.

The DEM simulation of the mills using powders of the original size can provide a holistic understanding of the milling dynamics and milling energies. However, this needs a superpower computer and a significant computational time. DEM simulations can be conducted on variable milling parameters, i.e. different numbers of balls, BPR as a tool to reduce the number of experiments. Another aspect that has not been addressed is the simulation of  $\beta$ -LGA to account for its specific powder properties. DEM simulation can also be carried out to model other mills such as fluid jet mill.

An additional interesting point to investigate, is the study of the surface chemistry, i.e. surface interaction, and surface energy of the milled samples, particularly, that milling leads to the formation of new surfaces which might impact on the exposed functional groups.

The assessment of the type of deformation/defect that arise with milling is another interesting area of work which will help identify the specific forms of defects that arise with milling, i.e. edge or screw dislocations. This can be addressed using AFM experiments which requires single crystals of quality surfaces.

The simulation of the amorphous formed as a result of milling can be achieved using molecular dynamics to enable an in-depth understanding of the mechanism and the kinetics of the amorphisation process that can arise for example from accumulated defects as a result of milling.

The evaluation of the pharmaceutical performances such as the dissolution rate the solubility and the bioavailability of the API can be carried out to assess for the clinical performance of the API. However, this was not assessed in this work since the primary focus was to identify the mechanistic behaviour of the API instead of its clinical performances.

### 9.3. Reference

Aarathi, J. *et al.* (2018) ‘Growth and Characterization of  $\alpha$  and  $\beta$  Polymorphs of L-Glutamic Acid and its Anticancer and Antibacterial Application’, *Crystal Research and Technology*, 53(6), pp. 1–10. doi: 10.1002/crat.201700190.

Abouhakim, H. (2016) *BREAKAGE BY INTENT A STRUCTURAL AND MATERIAL UNDERSTANDING OF BREAKAGE*. Transfer Viva Report.

Abouhakim, H. *et al.* (2016) *Recrystallization of L- glutamic acid to the  $\beta$  -polymorph at a 20 L scale CAPE 5921M*.

Abouhakim, H., Nilsson Lill, S. O., *et al.* (2020) ‘The crystal structure, morphology and mechanical properties of diaquabis(omeprazole)magnesium dihydrate’, *Acta Crystallographica Section B*. International Union of Crystallography (IUCr), 76, pp. 275–284. doi: 10.1107/s2052520620001249.

Abouhakim, H., J. Quayle, M., *et al.* (2020) ‘Mechanically Induced Amorphization of Diaquabis(Omeprazole)-Magnesium Dihydrate’, *Crystal Growth & Design*. American Chemical Society (ACS), 0(0). doi: 10.1021/acs.cgd.0c00770.

Abramov, Y. A. (2016) *Computational pharmaceutical solid state chemistry*. John Wiley & Sons, Inc. Available at: <https://www.vlreader.com/Reader?ean=9781119229193> (Accessed: 17 October 2019).

Alex, T. C. *et al.* (2016) ‘Mechanical Activation of Al-oxyhydroxide Minerals–A Review’, *Mineral Processing and Extractive Metallurgy Review*, 37(1), pp. 1–26. doi: 10.1080/08827508.2015.1055626.

Alzghoul, A. *et al.* (2014) ‘Experimental and Computational Prediction of Glass Transition Temperature of Drugs’, *JOURNAL OF CHEMICAL INFORMATION AND MODELING*, 54, pp. 3396–3403. doi: 10.1021/ci5004834.

Arteaga, P. A. *et al.* (1993) ‘Use of nanoindentation to assess potential attrition of particulate solids’, *Tribology International*, 26(5), pp. 305–310. doi: 10.1016/0301-679X(93)90066-A.

Asachi, M. *et al.* (2017) ‘Assessment of Near-Infrared (NIR) spectroscopy for segregation measurement of low content level ingredients’, *Powder Technology*, 320, pp. 143–154. doi: 10.1016/j.powtec.2017.07.003.

Aulton, M. E. (2007) *Aulton’s pharmaceuticals : the design and manufacture of medicines*. 3rd edn. Edinburgh;New York; Churchill Livingstone. Available at: [https://leeds.primo.exlibrisgroup.com/discovery/fulldisplay?docid=alma991016416669705181&context=L&vid=44LEE\\_INST:VU1&lang=en&search\\_scope=My\\_Inst\\_CI\\_not\\_edsco&aptor=Local\\_Search\\_Engine&tab=AlmostEverything&query=any,contains,Pharmaceutics](https://leeds.primo.exlibrisgroup.com/discovery/fulldisplay?docid=alma991016416669705181&context=L&vid=44LEE_INST:VU1&lang=en&search_scope=My_Inst_CI_not_edsco&aptor=Local_Search_Engine&tab=AlmostEverything&query=any,contains,Pharmaceutics) The science (Accessed: 22 October 2019).

Avolio, R. *et al.* (2012) ‘A multitechnique approach to assess the effect of ball milling on cellulose’, *Carbohydrate Polymers*. Elsevier, 87(1), pp. 265–273. doi: 10.1016/J.CARBPOL.2011.07.047.

Babu, B. (2008) *Physically based model for plasticity and creep of Ti-6Al-4V*. Available at: <http://pure.ltu.se/portal/files/2290341/LTU-LIC-0840-SE.pdf>.

Backhurst, J. R. Harker, J.H. Richardson, J. F. (2002) *Coulson and Richardson's Chemical Engineering Volume 5 - Solutions to the Problems in Chemical Engineering from Volume 2 (5th Edition) and Volume 3 (3rd Edition)*. Elsevier. Available at: [https://app.knovel.com/web/toc.v/cid:kpCRCEVS01/viewerType:toc//root\\_slug:coulson-and-richardsons](https://app.knovel.com/web/toc.v/cid:kpCRCEVS01/viewerType:toc//root_slug:coulson-and-richardsons) (Accessed: 23 October 2019).

Bae, Sunwoo *et al.* (2014) 'Structure and properties of porous TiNi-based alloys produced by SHS and sintering for biomedical applications View project Porous TiNi material View project Planetary Ball Mill Process in Aspect of Milling Energy 유성밀 프로세스와 밀링에너지', *Journal of Korean Powder Metallurgy Institute*, 21(2). doi: 10.4150/KPMI.2014.21.2.155.

Bai, Y. *et al.* (2014) 'Energy calculation model of ball kinematics based on ball mill coal load', *International Journal of Innovative Computing, Information and Control*, 10(5), pp. 1715–1726.

Baird, J. A., Van Eerdenbrugh, B. and Taylor, L. S. (2010) 'A Classification System to Assess the Crystallization Tendency of Organic Molecules from Undercooled Melts'. doi: 10.1002/jps.22197.

Bajcinca, N., Perl, R. and Sundmacher, K. (2011) *Convex optimization for shape manipulation of multidimensional crystal particles*, *Computer Aided Chemical Engineering*. Elsevier. doi: 10.1016/B978-0-444-53711-9.50171-1.

Baláž, P. (2008) *Mechanochemistry and Nanoscience, Mechanochemistry in Nanoscience and Minerals Engineering*. Berlin, Heidelberg: Springer Berlin Heidelberg. doi: 10.1007/978-3-540-74855-7\_1.

Baláž, P. *et al.* (2013) 'Hallmarks of mechanochemistry: from nanoparticles to technology †', *Chem. Soc. Rev.*, 42, pp. 7571–7637. doi: 10.1039/c3cs35468g.

Bandyopadhyay, R. and Grant, D. J. W. (2002) 'Plasticity and Slip System of Plate-Shaped Crystals of L-Lysine Monohydrochloride Dihydrate', *Pharmaceutical Research*, 19(4), pp. 491–496. Available at: <https://link.springer.com/content/pdf/10.1023%2FA%3A1015151830473.pdf> (Accessed: 13 May 2019).

Barth, A. (2007) 'Infrared spectroscopy of proteins', *Biochimica et Biophysica Acta - Bioenergetics*, pp. 1073–1101. doi: 10.1016/j.bbabi.2007.06.004.

Bauer, J. F. (2009) 'Pharmaceutical Solids: Size, Shape, and Surface Area', *Journal of Validation Technology*, (Winter), pp. 37–44.

Bauer Jhon (2009) 'Pharmaceutical Solids: Size, Shape, and Surface Area', *Journal of Validation Technology*, pp. 37–44. Available at: <https://pdfs.semanticscholar.org/c25a/dd74a8c9172a9bae939f831b840c5a73dbff.pdf> (Accessed: 8 October 2019).

Behjani, M. A. *et al.* (2017) 'An investigation on process of seeded granulation in a continuous drum granulator using DEM', *Advanced Powder Technology*. Elsevier B.V., 28(10), pp. 2456–2464. doi: 10.1016/j.appt.2017.02.011.

Behjani, M. A. (2018) *Numerical Simulation of Segregation of Formulated Powder Mixtures*. University of Leeds.

Berkovitch-Yellin, Z. (1985) *Toward an ab Initio Derivation of Crystal Morphology*, *J. Am. Chem. Soc.* Available at: <https://pubs.acs.org/sharingguidelines>.

Beyer, T. (2001) 'The Prediction, Morphology, and Mechanical Properties of the Polymorphs of Paracetamol', *Journal of the American Chemical Society*, 123(13), pp. 5086–5094.

Bhatt, P. M. (2017) 'Tautomeric polymorphism in omeprazole', *Chemical Communications*, (20), p. 2057. Available at: <http://www.rsc.org/suppdata/cc/b7/b700506g/b700506g.pdf> (Accessed: 20 December 2017).

Bhugra, C. and Pikal, M. J. (2008) 'Role of Thermodynamic, Molecular, and Kinetic Factors in Crystallization from the Amorphous State', *Journal of Pharmaceutical Sciences*, 97(4), pp. 1329–1349. doi: 10.1002/jps.21138.

Bibi, S. *et al.* (2015) 'A preliminary investigation to group disparate batches of licit and illicit diazepam tablets using differential scanning calorimetry', *Analytical Methods*. Royal Society of Chemistry, 7(20), pp. 8597–8604. doi: 10.1039/c5ay01711d.

Birju, Kumar Kakumanu, V. and Bansal, A. K. (2006) 'Review Analytical Techniques for Quantification of Amorphous/ Crystalline Phases in Pharmaceutical Solids', *Journal of Pharmaceutical Sciences*, 95(8), pp. 1641–1665. doi: 10.1002/jps.20644.

Bochevarov, A. D. *et al.* (2013) 'Jaguar: A high-performance quantum chemistry software program with strengths in life and materials sciences', *International Journal of Quantum Chemistry*, 113, pp. 2110–2142. doi: 10.1002/qua.24481.

Boldyrev, V. V. and Tkáčová, K. (2000) 'Mechanochemistry of Solids: Past, Present, and Prospects', *Journal of Materials Synthesis and Processing*. Kluwer Academic Publishers-Plenum Publishers, 8(3/4), pp. 121–132. doi: 10.1023/A:1011347706721.

Boldyrev, V. V. (2006) 'Mechanochemistry and mechanical activation of solids', *Russian Chemical Reviews*, 75(177). doi: 10.1070/RC2006v075n03ABEH001205.

Boldyreva, E. (2013) 'Mechanochemistry of inorganic and organic systems: What is similar, what is different?', *Chemical Society Reviews*. The Royal Society of Chemistry, 42, pp. 7719–7738. doi: 10.1039/c3cs60052a.

Borissova, A. *et al.* (2009) 'In Situ Measurement of Solution Concentration during the Batch Cooling Crystallization of L-Glutamic Acid using ATR-FTIR Spectroscopy Coupled with Chemometrics In Situ Measurement of Solution Concentration during the Batch Cooling Crystallization of L -Gl'. doi: 10.1021/cg7010265.

Brittain, H. G. (2002) 'Effects of mechanical processing on phase composition', *Journal of Pharmaceutical Sciences*, 91(7), pp. 1573–1580. doi: <http://dx.doi.org/10.1002/jps.10115>.

Burmeister, C. F. and Kwade, A. (2013) 'Process engineering with planetary ball mills', *Chemical Society Reviews*, 42(42), pp. 7660–7667. doi: 10.1039/c3cs35455e.

Byrn, S. R., Zografu, G. and Chen, X. S. (2017) 'Solid-State Properties and Pharmaceutical Development', in *Solid State Properties of Pharmaceutical Materials*. John Wiley & Sons, Inc., pp. 1–21. doi: 10.1002/9781119264408.ch1.

Cameron F. Holder and Raymond E. Schaak (2019) 'Tutorial on Powder X-ray Diffraction for Characterizing Nanoscale Materials', *ACS Nano*, 13, pp. 7359–7365. doi: 10.1021/acsnano.9b05157.

Chamarthy, S. P. and Pinal, R. (2008) 'The nature of crystal disorder in milled pharmaceutical materials', *Colloids and Surfaces A: Physicochemical and Engineering Aspects*, 331(1), pp. 68–75. doi: 10.1016/j.colsurfa.2008.06.040.

Chamayou, A. and Dodds, J. A. (2007) 'Chapter 8 Air Jet Milling', *Handbook of Powder Technology*, 12(33), pp. 421–435. doi: 10.1016/S0167-3785(07)12011-X.

Chan, H. K. and Doelker, E. (1985) 'Drug Development and Industrial Pharmacy Polymorphic Transformation of Some Drugs Under Compression POLYMORPHIC TRANSFORMATION OF SOME DRUGS UNDER COMPRESSION', *DRUG DEVELOPMENT AND INDUSTRIAL PHARMACY*, 11(3), pp. 315–332. doi: 10.3109/03639048509056874.

Chauruka, S. R. *et al.* (2015) 'Effect of mill type on the size reduction and phase transformation of gamma alumina', *Chemical Engineering Science*. Elsevier, 134, pp. 774–783. doi: 10.1016/j.ces.2015.06.004.

Chauruka, S. R. (2015) *Effect of Milling on Size Reduction and Microstructural Changes to Gamma-Alumina The*. The University of Leeds.

*Chemistry: IR of amino acids* (2016). Available at: <http://openchemistryhelp.blogspot.com/2012/12/ir-of-amino-acids.html> (Accessed: 28 December 2019).

Chieng, N. *et al.* (2009) 'Physical characterization and stability of amorphous indomethacin and ranitidine hydrochloride binary systems prepared by mechanical activation', *Eur J Pharm Biopharm*, 71, pp. 47–54. doi: 10.1016/j.ejpb.2008.06.022.

Chikhaliya, V. *et al.* (2006) 'The effect of crystal morphology and mill type on milling induced crystal disorder', *European Journal of Pharmaceutical Sciences*, 27(1), pp. 19–26. doi: 10.1016/j.ejps.2005.08.013.

Clark, S. J. *et al.* (2005) 'First principles methods using CASTEP', *Z. Kristallogr*, 220, pp. 567–570. Available at: [www.accelrys.com/references/castep/](http://www.accelrys.com/references/castep/). (Accessed: 23 August 2019).

Colombo, I., Grassi, G. and Grassi, M. (2009) 'Drug mechanochemical activation', *Journal of Pharmaceutical Sciences*. Elsevier Masson SAS, 98, pp. 3961–3986. doi: 10.1002/jps.21733.

Colombo, I., Grassi, G. and Grassi, M. (2009) 'Drug Mechanochemical Activation', *Journal of Pharmaceutical Sciences*, 98, pp. 3961–3986. doi: 10.1002/jps.21733.

- Craig, D. Q. M. (1997) 'Pharmaceutical Materials Science - Resuscitation or', pp. 119–126.
- Crowley, K. J. and Zografi, G. (2002) 'Cryogenic Grinding of Indomethacin Polymorphs and Solvates: Assessment of Amorphous Phase Formation and Amorphous Phase Physical Stability'. doi: 10.1002/jps.10028.
- Cyberphysics - Young's Modulus* (2009). Available at: [https://www.cyberphysics.co.uk/topics/forces/young\\_modulus.htm](https://www.cyberphysics.co.uk/topics/forces/young_modulus.htm) (Accessed: 11 November 2019).
- Datta, S. and Grant, David J.W. (2004) 'Crystal structures of drugs: Advances in determination, prediction and engineering', *Nature Reviews Drug Discovery*. Nature Publishing Group, pp. 42–57. doi: 10.1038/nrd1280.
- Datta, S. and Grant, David J W (2004) 'CRYSTAL STRUCTURES OF DRUGS: ADVANCES IN DETERMINATION, PREDICTION AND ENGINEERING', 42. doi: 10.1038/nrd1280.
- Descamps, M. *et al.* (2007) 'Transformation of Pharmaceutical Compounds upon Milling and Comilling: The Role of Tg', *J. Pharm. Sci.*, 96, pp. 1398–1407. doi: 10.1002/jps.20939.
- Descamps, M. *et al.* (2015) 'The amorphous state of pharmaceuticals obtained or transformed by milling: Sub-Tg features and rejuvenation', *Journal of Non-Crystalline Solids*, 407, pp. 72–80. doi: 10.1016/j.jnoncrysol.2014.08.055.
- Descamps, M. and Willart, J. F. (2016) 'Perspectives on the amorphisation/milling relationship in pharmaceutical materials', *Advanced Drug Delivery Reviews*. Elsevier B.V., 100, pp. 51–66. doi: 10.1016/j.addr.2016.01.011.
- Docherty, R. *et al.* (1991) 'Application of Bravais-Friedel-Donnay-Harker, attachment energy and Ising models to predicting and understanding the morphology of molecular crystals', *Journal of Physics D: Applied Physics*, 24(24), pp. 89–89.
- Dudognon, E. *et al.* (2006) 'Formation of budesonide/ $\alpha$ -lactose glass solutions by ball-milling', *Solid State Communications*, 138(2), pp. 68–71. doi: 10.1016/j.ssc.2006.02.007.
- EDEM (2020) *EDEM - The leading Discrete Element Method (DEM) software*. Available at: <https://www.edemsimulation.com/> (Accessed: 12 July 2020).
- El-Azazy, M. (2019) 'Introductory Chapter: Infrared Spectroscopy - A Synopsis of the Fundamentals and Applications', in *Infrared Spectroscopy - Principles, Advances, and Applications*. IntechOpen. doi: 10.5772/intechopen.82210.
- Elamin, A. A. *et al.* (1994) 'Increased metastable solubility of milled griseofulvin, depending on the formation of a disordered surface structure', *International Journal of Pharmaceutics*, 111(2), pp. 159–170. doi: 10.1016/0378-5173(94)00132-4.
- Ertel, K. D. and Carstensen, J. T. (1988) 'Chemical, physical, and lubricant properties of magnesium stearate', *Journal of Pharmaceutical Sciences*, 77(7), pp. 625–629. doi: 10.1002/jps.2600770715.
- Fayed, M. E. (Muhammad E. . and Otten, L. (Lambert) (1997) *Handbook of powder science*

& technology. Chapman & Hall.

Florence, A. T. and Attwood, D. (2011) ‘Solids’, in *Physicochemical Principles of Pharmacy*, pp. 7–42. doi: 10.1002/jps.2600720336.

Fouad, E. A. *et al.* (2009) ‘Preparation and investigation of acetyl salicylic acid-glutamic acid complex: A novel oral delivery system’, *Digest Journal of Nanomaterials and Biostructures*, 4(2), pp. 299–308.

Friščić, T. and Jones, W. (2009) ‘ReViews Recent Advances in Understanding the Mechanism of Cocrystal Formation via Grinding’, *CRYSTAL GROWTH & DESIGN*, 9(3), pp. 1621–1637. doi: 10.1021/cg800764n.

Gaillac, R., Pullumbi, P. and Coudert, F.-X. (2016) ‘ELATE: an open-source online application for analysis and visualization of elastic tensors’, *Journal of Physics: Condensed Matter*, 28(27), p. 275201. doi: 10.1088/0953-8984/28/27/275201.

Gavezzotti, A. (2005) ‘Calculation of lattice energies of organic crystals: the PIXEL integration method in comparison with more traditional methods’, *Zeitschrift für Kristallographie - Crystalline Materials*, 220(5/6). doi: 10.1524/zkri.220.5.499.65063.

Ghadiri, M., Kwan, C. C. and Ding, Y. (2007) ‘Chapter 14 Analysis of Milling and the Role of Feed Properties’, in *Handbook of Powder Technology*, pp. 605–634. doi: 10.1016/S0167-3785(07)12017-0.

Graeser, K. A. *et al.* (2009) ‘Correlating thermodynamic and kinetic parameters with amorphous stability’, *European Journal of Pharmaceutical Sciences*, 37, pp. 492–498. doi: 10.1016/j.ejps.2009.04.005.

Guinot, S. and Leveiller, F. (1999) ‘The use of MTDSC to assess the amorphous phase content of a micronised drug substance’, *International Journal of Pharmaceutics*, 192(1), pp. 63–75. doi: 10.1016/S0378-5173(99)00273-2.

De Gusseme, A. *et al.* (2008) ‘Ordering and disordering of molecular solids upon mechanical milling: The case of fananserine’, *Journal of Pharmaceutical Sciences*, 97, pp. 5000–5012. doi: <http://dx.doi.org/10.1002/jps.21472>.

Gustavsson Anders, Kjellbom Kristina, Y. I. (1997) ‘Omeprazole sodium salt’. United States. Available at: <https://patents.google.com/patent/EP1856101A2/en?q=EP1856101A2> (Accessed: 18 March 2018).

Halme, A. *et al.* (2019) ‘Utilizing Crystal Structures for Predicting Impact of Mechanical and Surface Properties on Particle Fracture’, *Crystal Growth & Design*. American Chemical Society, 19, pp. 3670–3680. doi: 10.1021/acs.cgd.8b01867.

Hammond, R. B., Pencheva, K. and Roberts, K. J. (2012) ‘Structural variability within, and polymorphic stability of, nano-crystalline molecular clusters of l-glutamic acid and D-mannitol, modelled with respect to their size, shape and “crystallisability”’, *CrystEngComm*, 14(3), pp. 1069–1082. doi: 10.1039/c1ce06174g.

Hasegawa, M., Honma, T. and Kanda, Y. (1990) ‘Effect of mill diameter on the rate of initial

- grinding in vibration ball mills', *Powder Technology*. doi: 10.1016/0032-5910(90)80125-I.
- Hirayama, N. *et al.* (1980) 'Structure of  $\alpha$  Form of L-Glutamic Acid.  $\alpha$ - $\beta$  Transition', *Bulletin of the Chemical Society of Japan*, pp. 30–35. doi: 10.1246/bcsj.53.30.
- Hirokawa, S. (1955) 'A new modification of L-glutamic acid and its crystal structure', *Acta Crystallographica*. International Union of Crystallography, 8(10), pp. 637–641. doi: 10.1107/s0365110x55001990.
- Hogan, S. E. and Buckton, G. (2000) 'The quantification of small degrees of disorder in lactose using solution calorimetry', *International Journal of Pharmaceutics*. Elsevier, 207(1–2), pp. 57–64. doi: 10.1016/S0378-5173(00)00527-5.
- Horiba (2019) *Understanding Particle Size Distribution Calculations - HORIBA*. Available at: <https://www.horiba.com/scientific/products/particle-characterization/education/general-information/data-interpretation/understanding-particle-size-distribution-calculations/> (Accessed: 3 December 2019).
- Hossain Shariare, M. *et al.* (2012) 'Prediction of the Mechanical Behaviour of Crystalline Solids', *Pharma Res*, 29, pp. 319–331. doi: 10.1007/s11095-011-0543-1.
- Hui *et al.* (2015) 'Overview of milling techniques for improving the solubility of poorly water-soluble drugs', *asian journal of pharmaceutical sciences*, p. ) 255 e274. Available at: [http://ac.els-cdn.com/S1818087615000100/1-s2.0-S1818087615000100-main.pdf?\\_tid=2f07907e-31b9-11e7-b5a8-00000aab0f6b&acdnat=1494005888\\_a4d0e4c87b7e80caa8bf244987c92256](http://ac.els-cdn.com/S1818087615000100/1-s2.0-S1818087615000100-main.pdf?_tid=2f07907e-31b9-11e7-b5a8-00000aab0f6b&acdnat=1494005888_a4d0e4c87b7e80caa8bf244987c92256).
- Hull, D. and Bacon, D. J. (2011) *Introduction to Dislocations*. Fifth. Liverpool: Elsevier Ltd.
- Hultman, I., Stenhoff, H. and Liljeblad, M. (2007) 'Determination of esomeprazole and its two main metabolites in human, rat and dog plasma by liquid chromatography with tandem mass spectrometry', *Journal of Chromatography B: Analytical Technologies in the Biomedical and Life Sciences*, 848(2), pp. 317–322. doi: 10.1016/j.jchromb.2006.10.074.
- INSTRON (2020) *Instron Vickers Test - Instron*. Available at: <https://www.instron.com.es/en/our-company/library/test-types/hardness-test/vickers-test>.
- Instruments, T. (2020) *Differential Scanning Calorimeters*. Available at: <https://www.tainstruments.com/products/thermal-analysis/differential-scanning-calorimeters/>.
- Jakobs, B. S. *et al.* (2000) 'New method for faecal fat determination by mid-infrared spectroscopy, using a transmission cell: An improvement in standardization', *Annals of Clinical Biochemistry*. Royal Society of Medicine Press Ltd, 37(3), pp. 343–349. doi: 10.1258/0004563001899258.
- James, S. L. *et al.* (2012) 'Mechanochemistry: opportunities for new and cleaner synthesis', *Chemical Society Reviews*, 41, pp. 413–447. doi: 10.1039/c1cs15171a.
- Johanson, K. (2014) 'Review of new segregation tester method by Dr. Kerry Johanson, P.E.', *Powder Technol*. Elsevier, 257, pp. 1–10. doi: 10.1016/j.powtec.2014.02.021.

- Karmwar, P. *et al.* (2012) 'Effect of different preparation methods on the dissolution behaviour of amorphous indomethacin', *European Journal of Pharmaceutics and Biopharmaceutics*, 80(2), pp. 459–464. doi: 10.1016/j.ejpb.2011.10.006.
- Kaushal, A. M., Chakraborti, A. K. and Bansal, A. K. (2008) 'FTIR Studies on Differential Intermolecular Association in Crystalline and Amorphous States of Structurally Related Non-Steroidal Anti-Inflammatory Drugs', *Molecular pharmaceutics*, 5, pp. 937–945. doi: 10.1021/mp800098d.
- Khan, S. *et al.* (2011) 'In-Process Monitoring and Control of Supersaturation in Seeded Batch Cooling Crystallisation of L-Glutamic Acid: From Laboratory to Industrial Pilot Plant', *Organic Process Research & Development*. American Chemical Society, 15(3), pp. 540–555. doi: 10.1021/op100223a.
- Kocich, R. and Lukáč, P. (2015) 'SPD Processes - Methods for Mechanical Nanostructuring', in *Handbook of Mechanical Nanostructuring*. Wiley, pp. 237–262. doi: 10.1002/9783527674947.ch11.
- Kwan, C. C. *et al.* (2004) 'Development of a novel approach towards predicting the milling behaviour of pharmaceutical powders', *European Journal of Pharmaceutical Sciences*, 23(4–5), pp. 327–336. doi: 10.1016/j.ejps.2004.08.006.
- Kwan, C. C. *et al.* (2005) 'Analysis of the milling rate of pharmaceutical powders using the Distinct Element Method (DEM)', *Chemical Engineering Science*, 60(5), pp. 1441–1448. doi: 10.1016/j.ces.2004.10.002.
- Lefebvre, C. *et al.* (2008) 'Polymorphic Transitions of Carbamazepine During Grinding and Compression', *Drug Development and Industrial Pharmacy*, 12(11–13), pp. 1913–1927. doi: 10.3109/03639048609042617.
- Lehmann, M. S., Koetzle, T. F. and Hamilton, W. C. (1972) 'Precision neutron diffraction structure determination of protein and nucleic acid components. I. Crystal and molecular structure of the amino acid L-alanine', *Journal of the American Chemical Society*, pp. 2657–2660. doi: 10.1021/ja00763a016.
- Lehmann, Mogens S., Koetzle, T. F. and Hamilton, W. C. (1972) 'Precision neutron diffraction structure determination of protein and nucleic acid components. VIII: the crystal and molecular structure of the B-form of the amino acid L-Glutamic acid', *Journal of Crystal and Molecular Structure*, 2(5–6), pp. 225–233. doi: 10.1007/BF01246639.
- Li, Y. *et al.* (2013) 'Solubility of omeprazole sulfide in different solvents at the range of 280.35–319.65 K', *Journal of Solution Chemistry*. doi: 10.1007/s10953-013-0110-y.
- Lill, S. O. N. and Siegbahn, E. M. (2009) 'An Autocatalytic Mechanism for NiFe-Hydrogenase: Reduction to Ni(I) Followed by Oxidative Addition', *Biochemistry*, 48, p. 1057. doi: 10.1021/bi801218n.
- Loh, Z. H., Samanta, A. K. and Sia Heng, P. W. (2015) 'Overview of milling techniques for improving the solubility of poorly water-soluble drugs', *Asian Journal of Pharmaceutical Sciences*, 10(4), pp. 255–274. doi: 10.1016/j.ajps.2014.12.006.

Luz-Lima, C. *et al.* (2016) ‘ $\alpha$ -l-Glutamic acid under high pressure: Phase transitions studied by Raman spectroscopy’, *Vibrational Spectroscopy*, 86, pp. 343–349. doi: <http://dx.doi.org/10.1016/j.vibspec.2016.08.012>.

M. J. Frisch and G. W. Trucks and H. B. Schlegel and G. E. Scuseria and M. A. Robb and J. R. Cheeseman and G. Scalmani and V. Barone and G. A. Petersson and H. Nakatsuji and X. Li and M. Caricato and A. V. Marenich and J. Bloino and B. G. Janesko and R. G. J. A. and J. E. P. and F. O. and M. J. B. and J. J. H. and E. N. B. and K. N. K. and V. N. S. and T. A. K. and R. K. and J. N. and K. R. and A. P. R. and J. C. B. and S. S. I. and J. (2016) *Gaussian16 Revision*, Gaussian Inc. Wallingford CT. Gaussian Inc. Wallingford CT.

Mahlin, D. and Bergström, C. A. S. (2013) ‘Early drug development predictions of glass-forming ability and physical stability of drugs’, *European Journal of Pharmaceutical Sciences*, 49, pp. 323–332. doi: 10.1016/j.ejps.2013.03.016.

Malvern (2015) *A basic guide to particle characterization*. Available at: [https://www.cif.iastate.edu/sites/default/files/uploads/Other\\_Inst/Particle Size/Particle Characterization Guide.pdf](https://www.cif.iastate.edu/sites/default/files/uploads/Other_Inst/Particle_Size/Particle_Characterization_Guide.pdf) (Accessed: 2 September 2020).

Malvern Instruments Ltd (2012) ‘A basic guide to particle characterization’, *Inform White Paper*, pp. 1–26.

MalvernPanalytical (2013) ‘Mastersizer 3000’, 0.

Markovic, N. *et al.* (2006) ‘Physical and thermal characterisation of chiral omeprazole sodium salts’, *J. Pharm. Biomed*, 42, pp. 25–31. doi: 10.1016/j.jpba.2005.12.039.

MASROOR, M., SHEIBANI, S. and ATAIE, A. (2016) ‘Effect of milling energy on preparation of Cu–Cr/CNT hybrid nano-composite by mechanical alloying’, *Transactions of Nonferrous Metals Society of China (English Edition)*. doi: 10.1016/S1003-6326(16)64239-5.

Mazel, V. *et al.* (2011) ‘Polymorphic transformation of anhydrous caffeine under compression and grinding: a re-evaluation.’, *Drug Development and Industrial Pharmacy*, 37(7), pp. 832–840. doi: 10.3109/03639045.2010.545416.

*Mercury User Guide and Tutorials 2018 CSD Release* (2017). Available at: <http://www.ccdc.cam.ac.uk> (Accessed: 29 December 2018).

Mishra, M. K., Ramamurty, U. and Desiraju, G. R. (2015) ‘Solid Solution Hardening of Molecular Crystals: Tautomeric Polymorphs of Omeprazole’, *Journal of the American Chemical Society*, 137(5), pp. 1794–1797. doi: 10.1021/JA512817F&PMID=25634429.

Mohamed, M. E. and Mohammed, A. M. A. (2013) ‘Experimental and Computational Vibration Study of Amino Acids’, *International Letters of Chemistry, Physics and Astronomy ISSN*, 1(10), pp. 1–47. Available at: [www.ilcpa.pl](http://www.ilcpa.pl).

Müller, F. and Polke, R. F. (1999) ‘From the product and process requirements to the milling facility’, in *Powder Technology*. Elsevier Sequoia SA, pp. 2–13. doi: 10.1016/S0032-5910(99)00112-6.

Murakami, F. S. *et al.* (2009) ‘Physico-chemical solid-state characterization of omeprazole

sodium: Thermal, spectroscopic and crystallinity studies', *Journal of Pharmaceutical and Biomedical*, 49, pp. 72–80. doi: 10.1016/j.jpba.2008.10.005.

Natelson, D. (2015) *Nanostructures and nanotechnology*. Cambridge: Cambridge University Press.

Neikov, O. D. (2009a) *Mechanical Alloying, Handbook of Non-Ferrous Metal Powders*. Elsevier Ltd. doi: 10.1016/B978-1-85617-422-0.00003-3.

Neikov, O. D. (2009b) *Processing of Powders and Processing Equipment, Handbook of Non-Ferrous Metal Powders*. Elsevier Ltd. doi: 10.1016/B978-1-85617-422-0.00011-2.

Neikov, O. D. (2009) *Handbook of Non-Ferrous Metal Powders - Technologies and Applications - 2.2 Crushing and Grinding Equipment - Knovel*. 1st edn. Great Britain : Elsevier . Available at: [https://app.knovel.com/web/view/swf/show.v/rcid:kpHNFMPA1/cid:kt006QPXL2/viewerType:pdf/root\\_slug:handbook-non-ferrous?cid=kt006QPXL2&page=7&b-toc-cid=kpHNFMPA1&b-toc-root-slug=handbook-non-ferrous&b-toc-url-slug=mechanical-crushing-grinding&b-toc-title](https://app.knovel.com/web/view/swf/show.v/rcid:kpHNFMPA1/cid:kt006QPXL2/viewerType:pdf/root_slug:handbook-non-ferrous?cid=kt006QPXL2&page=7&b-toc-cid=kpHNFMPA1&b-toc-root-slug=handbook-non-ferrous&b-toc-url-slug=mechanical-crushing-grinding&b-toc-title) (Accessed: 25 January 2017).

Ohishi, H. *et al.* (1989) 'Structure of 5-methoxy-2-[4-methoxy-3,5-dimethyl-2-pyridinylmethyl]sulfinyl-1H-benzimidazole (omeprazole)', *Acta Crystallographica Section C*, 45(12), pp. 1921–1923. Available at: [http://scripts.iucr.org/cgi-bin/sendsupfiles?as0219&file=as0219\\_52104sup1.pdf&mime=application/pdf](http://scripts.iucr.org/cgi-bin/sendsupfiles?as0219&file=as0219_52104sup1.pdf&mime=application/pdf) (Accessed: 4 December 2018).

Olusanmi, D. *et al.* (2011) 'The breakage behaviour of Aspirin under quasi-static indentation and single particle impact loading: Effect of crystallographic anisotropy', *International Journal of Pharmaceutics*. Elsevier B.V., 411(1–2), pp. 49–63. doi: 10.1016/j.ijpharm.2011.03.039.

OTSUKA, M. and KANENIWA, N. (1983) 'Hygroscopicity and solubility of noncrystalline cephalixin.', *CHEMICAL & PHARMACEUTICAL BULLETIN*. The Pharmaceutical Society of Japan, 31(1), pp. 230–236. doi: 10.1248/cpb.31.230.

Otsuka, M., Otsuka, K. and Kaneniwa, N. (1994) 'Relation Between Polymorphic Transformation Pathway During Grinding and the Physicochemical Properties of Bulk Powders for Pharmaceutical Preparations', *DRUG DEVELOPMENT AND INDUSTRIAL PHARMACY*, 20, pp. 1649–1660. doi: 10.3109/03639049409050205.

Otsuka Makoto and Kaneniwa Nobuyoshi (1983) 'Effect of Grinding on the Degree of Crystallinity of Cephalixin Powder', *Chem.Pharm.Bull.*, 31(4489). Available at: [https://www.jstage.jst.go.jp/article/cpb1958/31/12/31\\_12\\_4489/\\_pdf](https://www.jstage.jst.go.jp/article/cpb1958/31/12/31_12_4489/_pdf) (Accessed: 8 February 2017).

Otte, A. and Carvajal, M. T. (2011) 'Assessment of Milling-Induced Disorder of Two Pharmaceutical Compounds', *Journal of Pharmaceutical Sciences*. Elsevier Masson SAS, 100(5), pp. 1793–1804. doi: 10.1002/jps.22415.

Palanisamy, D. and Karuppanan, S. (2016) 'Nucleation Control and Growth of Metastable ??-

l-Glutamic Acid Single Crystals in the Presence of l-Phenylalanine', in *Procedia Engineering*. doi: 10.1016/j.proeng.2015.08.1108.

Parrott, E. L. (1974) 'Milling of pharmaceutical solids', *Journal of Pharmaceutical Sciences*. Elsevier Masson SAS, 63(6), pp. 813–829. doi: 10.1002/jps.2600630603.

Perry, R. H., Green, D. W. and Maloney, J. O. (1997) *Perry's chemical engineers' handbook*. McGraw-Hill.

Prasad, K. V. R., Sheen, D. B. and Sherwood, J. N. (2001) 'Fracture property studies of paracetamol single crystals using microindentation techniques', *Pharmaceutical Research*, 18(6), pp. 867–872. doi: 10.1023/A:1011005016677.

Purdue University (2010) *Scanning Electron Microscope*. Available at: <https://www.purdue.edu/ehps/rem/rs/sem.htm> (Accessed: 29 June 2017).

Putra, O. D. (2016) 'Crystal Structure Determination of Dimenhydrinate after More than 60 Years: Solving Salt–Cocrystal Ambiguity via Solid-State Characterizations and Solubility Study', *Crystal Growth & Design*, 16(9), pp. 5223–5229. doi: 10.1021/acs.cgd.6b00771.

Reddy, M. S. *et al.* (2004) 'AMORPHOUS HYDRATES OF ESOMEPRAZOLE MAGNESIUM AND PROCESS FOR THE PREPARATION THEREOF'. United State: Koilkonda Purandhar. Available at: <https://patentimages.storage.googleapis.com/ba/ab/1d/fd4870c3b55de5/US20040167173A1.pdf> (Accessed: 22 August 2018).

Reimer, L. (1998) *Scanning Electron Microscopy*. Berlin, Heidelberg: Springer Berlin Heidelberg (Springer Series in Optical Sciences). doi: 10.1007/978-3-540-38967-5.

Renata Toplak Casar, L. (SI) (2013) 'Process for the Preparation of Esomeprazole Magnesium Dihydrate'. Available at: <https://patentimages.storage.googleapis.com/18/31/b8/b9f93fffb2a2c2/US8362259.pdf>.

RETSCH (2019) *Planetary Ball Mill PM 100 - RETSCH - highest fineness*. Available at: <https://www.retsch.com/products/milling/ball-mills/planetary-ball-mill-pm-100/function-features/> (Accessed: 2 December 2019).

Rhodes, M. (2008) *Introduction to Particle Technology*. Chichester, UK: John Wiley & Sons, Ltd. doi: 10.1002/9780470727102.

Roberts, K. (2016) 'PEME 5365M Pharmaceutical Formulation and Analysis Lecture Notes # 2 Pharmaceutical Science, Formulation and Processes', in *University of Leeds*.

Roberts, R. J., Rowe, R. C. and York, P. (1994) 'The relationship between indentation hardness of organic solids and their molecular structure', *Journal of Materials Science*. Kluwer Academic Publishers, 29(9), pp. 2289–2296. doi: 10.1007/BF00363416.

Roberts, R. J., Rowe, R. C. and York, P. (1995) 'The Relationship between the Fracture Properties, Tensile- Strength and Critical Stress Intensity Factor of Organic-Solids and Their Molecular-Structure', *International Journal of Pharmaceutics*, 125(1), pp. 157–162.

Romain Gaillac (2016) 'ELATE: an open-source online application for analysis and visualization of elastic tensors', *Journal of Physics: Condensed Matter*, 28(27), p. 275201. doi: 10.1088/0953-8984/28/27/275201.

Science, W. I. of (2016) *Defect in crystals*. Available at: [https://www.weizmann.ac.il/materials/igorl/sites/materials.igorl/files/uploads/3\\_-\\_defects\\_in\\_crystals\\_exe.pdf](https://www.weizmann.ac.il/materials/igorl/sites/materials.igorl/files/uploads/3_-_defects_in_crystals_exe.pdf) (Accessed: 11 November 2019).

Shah, U. V *et al.* (2015) 'Effect of milling temperatures on surface area, surface energy and cohesion of pharmaceutical powders'. doi: 10.1016/j.ijpharm.2015.08.061.

Shakhtshneider, T. P. (1997) 'Phase transformations and stabilization of metastable states of molecular crystals under mechanical activation', *Solid State Ion.*, 101, pp. 851–856. doi: 10.1016/S0167-2738(97)00224-5.

Shakhtshneider, T. P. and Boldyrev, V. V (1993) *Phase Transformations in Sulfathiazole During Mechanical Activation*, *Drug Dev Ind Pharm.* doi: 10.3109/03639049309069341.

Shakhtshneider, T. P. and Boldyrev, V. V (1993) 'Drug Development and Industrial Pharmacy Phase Transformations in Sulfathiazole During Mechanical Activation PHASE TRANSFORMATIONS IN SULFATHIAZOLE DURING MECHANICAL ACTIVATION', *Drug Dev Ind Pharm*, 19(16), pp. 2055–2067. doi: 10.3109/03639049309069341.

Sheldrick, George M (2015) 'Crystal structure refinement with SHELXL', *Acta Cryst C*, 71, pp. 3–8. doi: 10.1107/S2053229614024218.

Sheldrick, George M. (2015) '*SHELXT* – Integrated space-group and crystal-structure determination', *Acta Crystallographica Section A Foundations and Advances*. International Union of Crystallography, 71(1), pp. 3–8. doi: 10.1107/S2053273314026370.

Skieneh, J. *et al.* (2016) 'Crystallization of Esomeprazole Magnesium Water/Butanol Solvate', *Molecules*. Multidisciplinary Digital Publishing Institute, 21(5), p. 544. doi: 10.3390/molecules21040544.

Snow, Richard H. Luckie, P. T. (1979) 'Annual Review of Size Reduction', *Powder Technol.*, pp. 31–46.

Stephenson, G. A., Forbes, R. A. and Reutzel-Edens, S. M. (2001) 'Characterization of the solid state: quantitative issues', *Advanced Drug Delivery Reviews*, 48, pp. 67–90. Available at: [www.elsevier.com](http://www.elsevier.com) (Accessed: 19 October 2017).

Storey, R. A. and Ymen, I. (2011) *Solid state characterization of pharmaceuticals*. John Wiley & Sons.

Sun, C. C. (2008) 'On the identification of slip planes in organic crystals based on attachment energy calculation', *Journal of Pharmaceutical Sciences*, 97(8), pp. 3456–3461. doi: 10.1002/jps.21234.

Sun, C. C. and Kiang, Y.-H. (2008) 'On the Identification of Slip Planes in Organic Crystals Based on Attachment Energy Calculation', *Journal of Pharmaceutical Sciences*, 97(8), pp. 3456–3461. doi: 10.1002/jps.21234.

- Sun, W. J., Kothari, S. and Sun, C. C. (2018) 'The relationship among tensile strength, Young's modulus, and indentation hardness of pharmaceutical compacts', *Powder Technol.* Elsevier B.V., 331, pp. 1–6. doi: 10.1016/j.powtec.2018.02.051.
- Takacs, L. (2013) 'The historical development of mechanochemistry', *Chemical Society Reviews*. The Royal Society of Chemistry, 42, pp. 1–46. doi: 10.1039/c2cs35442j.
- Takahashi, Y. *et al.* (1984) 'Effects of grinding and drying on the solid-state stability of ampicillin trihydrate', *Chem. Pharm. Bull.*, 32, pp. 4963–4970.
- Takahashi, Y. *et al.* (1985) 'Polymorphism of fostedil: Characterization and polymorphic change by mechanical treatments', *Drug Development and Industrial Pharmacy*, 9045(February). doi: 10.3109/03639048509057685.
- Tan, D. and García, F. (2019) 'Main group mechanochemistry: from curiosity to established protocols', *Chemical Society Reviews*. Royal Society of Chemistry, pp. 2274–2292. doi: 10.1039/c7cs00813a.
- Tse, J. S. (1992) 'Mechanical instability in ice Ih. A mechanism for pressure-induced amorphization', *The Journal of Chemical Physics*, 96(7), pp. 5482–5487. doi: 10.1063/1.462732.
- Turner, M. J. *et al.* (2015) 'Energy frameworks: Insights into interaction anisotropy and the mechanical properties of molecular crystals', *Chemical Communications*. Royal Society of Chemistry, 51(18), pp. 3735–3738. doi: 10.1039/c4cc09074h.
- Turner, T. D. *et al.* (2020) 'Measuring the Particle Packing of L-Glutamic Acid Crystals through X-ray Computed Tomography for Understanding Powder Flow and Consolidation Behavior', *Crystal Growth & Design*. doi: 10.1021/acs.cgd.9b01515.
- Vanarase, A. U. *et al.* (2013) 'Development of a methodology to estimate error in the on-line measurements of blend uniformity in a continuous powder mixing process', *Powder Technol.*, 241, pp. 263–271. doi: 10.1016/j.powtec.2013.02.012.
- Varin, R. A. *et al.* (2009) 'Synthesis of nanocomposite hydrides for solid-state hydrogen storage by controlled mechanical milling techniques', *Journal of Alloys and Compounds*, 483(1–2), pp. 252–255. doi: 10.1016/j.jallcom.2008.07.207.
- Vegt, O. M. de (2007) *Jet milling from a particle perspective - Predicting particle fracture based on mechanical material properties*. Ph.D. Thesis, Rijksuniversiteit Groningen, Groningen, The Netherlands.
- Wang, C. and Sun, C. C. (2018) 'Identifying Slip Planes in Organic Polymorphs by Combined Energy Framework Calculations and Topology Analysis', *Crystal Growth and Design*, 18(3), pp. 1909–1916. doi: 10.1021/acs.cgd.8b00202.
- Wang, C. and Sun, C. C. (2019) 'Computational Techniques for Predicting Mechanical Properties of Organic Crystals: A Systematic Evaluation', *Molecular Pharmaceutics*. American Chemical Society, 16(4), pp. 1732–1741. doi: 10.1021/acs.molpharmaceut.9b00082.
- Winn, D. and Doherty, M. F. (2000) 'Modeling Crystal Shapes of Organic Materials Grown

from Solution', *AIChE*, 46(7), p. no-no. doi: 10.1002/chin.200102268.

Wu, H. *et al.* (2010) 'Phase Transformations of Glutamic Acid and Its Decomposition Products', *Crystal Growth & Design*, 10(2), pp. 988–994. doi: 10.1021/cg901303a.

Wu, X. *et al.* (2013) 'Fabrication of highly fluorescent graphene quantum dots using L-glutamic acid for in vitro/in vivo imaging and sensing', *Journal of Materials Chemistry C*, 1, p. 4676. doi: 10.1039/c3tc30820k.

Yihong Qiu, Yisheng Chen, Geoff G.Z. Zhang, Lawrence Yu, R. V. M. (2017) *Developing Solid Oral Dosage Forms | ScienceDirect*. Academic Press. Available at: <https://www.sciencedirect.com/book/9780128024478/developing-solid-oral-dosage-forms> (Accessed: 20 October 2019).

Young, P. M. *et al.* (2007) 'The Influence of Mechanical Processing of Dry Powder Inhaler Carriers on Drug Aerosolization Performance', *Association J Pharm Sci*, 96, pp. 1331–1341. doi: 10.1002/jps.20933.

Yu, L. (2001) 'Amorphous pharmaceutical solids: preparation, characterization and stabilization', *Advanced Drug Delivery Reviews*, 48(1), pp. 27–42. doi: 10.1016/S0169-409X(01)00098-9.

Yuan, S. *et al.* (2018) 'A dislocation climb/glide coupled crystal plasticity constitutive model and its finite element implementation', *Mechanics of Materials*. Elsevier B.V., 118, pp. 44–61. doi: 10.1016/j.mechmat.2017.12.009.

Zhou, D. *et al.* (2002) 'Physical Stability of Amorphous Pharmaceuticals: Importance of Configurational Thermodynamic Quantities and Molecular Mobility', *Journal of Pharmaceutical Sciences*. New Castle, DE, TA Instruments, 91(8), pp. 1863–1872. doi: 10.1002/jps.10169.

Zielke, R. H. F. (1985) 'Mechanical Activation of Pharmaceutical Systems', *Pharmaceutical Research*, 2(6), pp. 302–306.